Engineering Spinal Fusion

Evaluating Ceramic Materials for Cell Based Tissue Engineered Approaches

Clayton Ellis Wilson

Orthopaedie

Universitair Medisch Centrum Utrecht

Engineering Spinal Fusion
Evaluating Ceramic Materials for Cell Based Tissue Engineered Approaches

C. E. Wilson

ISBN: 978-94-6108-241-1
Design and layout by Clayton Wilson
Printed by Gildeprint Drukkerijen - www.gildeprint.nl

The research described in this thesis was financially supported by a grant from the Dutch Technology Foundation (STW) under project number UGN.4966 entitled "Tissue engineered hybrid bone for spinal fusion" which started in January 2000. This project was a collaboration between the Department of Orthopaedics at the University Medical Center Utrecht and IsoTis S.A.

Financial support for the reproduction of this thesis was generously provided by the following organizations:
CellCoTec B.V.
PoroGen B.V.

Engineering Spinal Fusion

Evaluating Ceramic Materials for Cell Based Tissue Engineered Approaches

Technische benadering van Wervelfusies

Onderzoek naar Keramische dragers voor cel-gerelateerde botgroei
(met een samenvatting in het nederlands)

Proefschrift

ter verkrijging van de graad doctor aan de Universiteit Utrecht op gezag van de rector magnificus, prof.dr. G.J. van der Zwaan, ingevolge het besluit van het college voor promoties in het openbaar te verdedigen op vrijdag 23 december 2011 des ochtends te 10.30 uur

door

Clayton Ellis Wilson

geboren op 14 april 1967 te Prosser, Verenigde Staten van Amerika

Promotoren: prof. dr. W.J.A. Dhert
prof. dr. C.A. van Blitterswijk
prof. dr. J.D. de Bruijn

Publications Contributing to this Thesis

Design and fabrication of standardized hydroxyapatite scaffolds with a defined macro-architecture by rapid prototyping for bone-tissue-engineering research.
Wilson CE, de Bruijn JD, van Blitterswijk CA, Verbout AJ, Dhert WJA. *J Biomed Mater Res A*. 2004 Jan 1;68(1):123–32.

Evaluating 3D bone tissue engineered constructs with different seeding densities using the alamarBlue™ assay and the effect on in vivo bone formation.
Wilson CE, Dhert WJA, van Blitterswijk CA, Verbout AJ, de Bruijn JD. *J Mater Sci Mater Med*. 2002 Dec;13(12):1265-9.

Scaffolds with standardized macro-architecture fabricated from several calcium phosphate ceramics using an indirect rapid prototyping technique.
Wilson CE, van Blitterswijk CA, Verbout AJ, Dhert WJA, de Bruijn JD. *J Mater Sci Mater Med*. 2011 Jan;22(1):97-105.

Comparison of four calcium phosphate ceramic scaffolds with standardized macro-architectures in a bone tissue engineering model.
Wilson CE, Kruyt MC, van Blitterswijk CA, Verbout AJ, de Bruijn JD, Dhert WJA.
Manuscript in preparation

Accessible volume of three-dimensional macroporous scaffolds: a micro-computed tomography alternative for low pressure mercury intrusion porosimetry.
Wilson CE, Laib A, Woodfield TBF, Pieper JS, de Wijn JR, de Bruijn JD, van Blitterswijk CA, Verbout AJ, Dhert WJA
Manuscript in preparation

A new in vivo screening model for posterior spinal bone formation: comparison of ten calcium phosphate treatments.
Wilson CE, Kruyt MC, de Bruijn JD, van Blitterswijk CA, Oner FC, Verbout AJ, Dhert WJA. Biomaterials. 2006 Jan;27(3):302-14.

The effect of cell-based bone tissue engineering in a goat transverse process model.
Kruyt MC, Wilson CE, de Bruijn JD, van Blitterswijk CA, Oner FC, Verbout AJ, Dhert WJA. Biomaterials. 2006 Oct;27(29):5099-106.

Table of Contents

1

Introduction and aims

Bone Grafting

Bone grafting is a commonly applied orthopaedic procedure used to treat bone fractures, non-unions and defects as well as achieve therapeutic arthrodesis, such as in spinal fusions. More than 500,000 bone grafting procedures are performed annually in the United States alone, with spinal fusions accounting for approximately half of these procedures.[103, 104, 213] Globally, bone grafting procedures are easily double the US figure and as much as 2.2 million by some estimates.[95] Approximately 90% of procedures utilize either autologous or allogeneic bone tissue.

The Autologous Bone Graft

The autologous bone graft, or autograft, is the golden standard for bone grafting procedures. The success of the autograft is attributed to a combination of osteoconductive, osteoinductive and osteogenic properties. Unfortunately, applying autografts has some significant limitations. First of all, because the autograft is obtained from healthy functional tissue, the amount of autograft bone tissue that can be safely harvested is limited. This harvest typically necessitates a second surgical site, such as the iliac crest or fibulae, and extents the duration of the overall surgical procedure. The harvest of autologous bone also has associated complications with donor site pain being the most common complaint.[15, 18, 255] There is a clear need for alternatives to the autograft. The osteoconductive, osteoinductive and osteogenic properties of autografts are the attributes by which potential alternatives are judged.

Alternatives to the Autograft

Allografts represent tissues transplanted between genetically non-identical individuals of the same species. Allogeneic bone grafts, or allografts, and associated products, e.g. demineralized bone matrix (DBM) and machined bone, are the second most commonly applied bone grafting materials. Allografts are generally considered to have osteoconductive and osteoinductive properties. Modern processing and screening techniques virtually eliminate immunogenic responses and the likelihood of disease transfer, however, reports of infections associated with allografts means the possibility of disease transfer cannot be discounted completely.[4, 5, 32, 50, 134, 184, 231] Furthermore, the processing methods used may influence the osteoconductive and osteoinductive properties of allograft materials.[32, 98, 194] Finally, insufficient donor numbers means there is inadequate allograft material to meet the increasing demand for grafting procedures.[104]

Biomaterials are also an alternative. Although many different biomaterials, both from natural and synthetic origins, have been proposed as bone graft substitutes over the past few decades, including metals, bamboo, wood, plaster, coral and others, the most common biomaterials currently applied as bone graft substitutes are based on calcium phosphate ceramics.[36, 82, 95, 162, 163] Most notable are hydroxyapatite (HA), which forms the mineral component of bones and teeth, beta-tricalcium phosphate (β-TCP), and mixtures of these two, known as biphasic calcium phosphate (BCP). These materials have well established biocompatibility and are generally considered to possess osteoconductive properties.[43, 68, 91, 124, 162] These materials have also been shown to have osteoinductive qualities.[206, 257, 258, 261]

The disadvantages of the autologous bone grafts, and the limitations and or risks of the current substitutes, means that an alternative which can provide the osteoconductive, osteoinductive and osteogenic capabilities of autografts would be highly desirable.[24] Tissue engineering of bone offers this potential.

Tissue Engineering

Tissue engineering was originally defined at a 1988 National Science Foundation (USA) workshop as “the application of principles and methods of engineering and life sciences toward fundamental understanding of structure/function relationships in normal and pathological mammalian tissue and development of biological substitutes to restore, maintain or improve tissue functions.” In addition, the concurrently developing field of biomimetics has been described, with specific regard to regenerative medicine, as “an interdisciplinary field that combines information from the study of biological structures and their functions with physics, mathematics, chemistry and engineering in the development of principles that are important for the generation of novel synthetic materials and organs.”[3] The merger of these disciplines has resulted in tissue engineering being more recently defined as “the application of biomimetics toward the development of biological substitutes that restore, maintain or improve tissue function.”[41]

Bone Tissue Engineering

Some 45 years ago, long before tissue engineering was defined as a discipline, two critical discoveries were reported which laid the foundation on which current bone tissue engineering strategies are based:

First, in 1965 Urist et al. reported the induction of bone formation by bone morphogenic proteins (BMPs). Since then, sustained research and development programs have ultimately resulted in clinical studies using BMPs in spinal fusion

applications and for treating long bone non-unions.[30, 37, 89, 138] Although numerous studies have demonstrated the safe application of BMPs,[7] the extremely high local doses of BMP used present a potential risk with ectopic bone formation, osteolysis, neck swelling and other complications being reported.[22, 221, 243]

Second, although the osteogenic capacity of bone marrow had been demonstrated previously,[38, 67] in 1966 Friedenstein et al. identified a population of osteoprogenitor cells within adult human bone marrow biopsies that demonstrated osteogenic capacity.[88] This adherent population of cells, referred to as colony forming unit fibroblasts (CFU-F's) by Friedenstien and his colleagues,[85] have subsequently been studied extensively and are commonly referred to as Mesenchymal Stem Cells (MSC's)[40] and Bone Marrow Stromal Cells,[17] among other names. These cell demonstrate stem cell like characteristics and can be culture expanded. These cells will be primarily referred to as Bone Marrow Stromal Cells (BMSC's) throughout this thesis.

The Hybrid Construct

Associating BMSC's with porous scaffolds to create a "hybrid construct," has been utilized since the earliest efforts to demonstrate the osteogenic capacity of culture expanded cells.[72, 99, 114] From the most basic, practical point-of-view, associating cells with porous scaffolds provides a means by which cells can be localized. This is particularly important for in vivo studies when the implanted cells, or resulting tissue, need to be retrieved after an implantation period. A logical choice of scaffold material was calcium phosphate ceramics. This is due to their extensive use in orthopaedics as bone graft substitutes or extenders and their proven biocompatibility and established osteoconductive nature. A particularly important characteristic of osteoconduction in calcium phosphates is bonding osteogenesis, the direct bonding of bone to the material surface without and interposed fibrous tissue layer.[54, 56, 57, 93, 190]

The feasibility of hybrid constructs consisting of porous calcium phosphate ceramic scaffolds and bone marrow stromal cells has been demonstrated in small and large animal studies[12, 33, 141, 147, 195] and a vast amount of work has been performed to develop bone tissue engineering strategies based on these hybrid constructs.[39, 81, 106, 188, 224] However, this work has yet to produce definitive clinical studies demonstrating the efficacy of bone tissue engineering for orthopedic applications currently treated with autografts.[179] The classic tissue engineering concept of using BMSCs and scaffolds to build a tissue is being superseded by the view of BMSCs as drug-delivery transplants that influence tissue generation via dynamic paracrine effects.[191]

First heralded as a regenerative therapy for skeletal tissue repair, MSCs have recently been shown to modulate endogenous tissue and immune cells. Preclinical studies of the mechanism of action suggest that the therapeutic effects afforded by MSC transplantation are short-lived and related to dynamic, paracrine interactions between MSCs and host cells.

Obstacles to Clinical Bone Tissue Engineering with Hybrid Constructs

The most apparent difficulty to applying hybrid constructs clinically is their size. It is situations that required the generation or replacement of reasonably large volumes of bone that necessitate autologous bone grafting in the first place and are therefore target applications for bone tissue engineering. Rodent models, in particular immunocompromised mice, have been well accepted as proof-of-concept models to demonstrate osteogenicity of hybrid constructs.[39, 73, 99, 114, 141, 145] However, increasing construct size from the small fraction of a cubic centimeter (cc) used in mice to the multiple cubic centimeters required for clinical relevance has serious consequences. Being non-vascularized, hybrid constructs rely on diffusion for oxygen supply and nutrient exchange. The diffusion characteristics of the hybrid construct create gradients that influence cell proliferation and viability.[59, 168, 174, 200] The little information available in the literature regarding nutrient diffusion suggest a broad acceptable depth range from 100 to 5000 µm. Diffusion properties of hybrid constructs are, of course, greatly influenced by the structural characteristics of the scaffold and tissue formation within the structure.

A second difficulty to overcome is the large wound created for implantation of clinically relevant hybrid constructs. In the case of bone tissue engineering this will involve both bone tissue and the surrounding or interposed soft tissues. The result is a combination of wound healing and fracture repair responses. Neither wound healing nor fracture repair utilize or require cells within the wound bed during the 2 to 3 days.[10, 132, 181] Implanting a hybrid construct with a large number of progenitor cells into the fresh wound bed may be incompatible, or at least temporally mismatched, with the normal cellular involvement in wound and fracture healing.

Spinal Fusion

Introduction to Spinal Fusion

Spinal fusion procedures account for the largest single use of bone grafts with approximately ¼ million procedures performed per annum in the US.[27, 104] The standard treatment is posterolateral fusion (PLF) and applies instrumented fixation with either pedicle or intervertebral screws plus bilateral autologous bone grafts

between the transverse processes with a total volume of roughly 15cc. The development of metal and polymer cages has played a role in facilitating techniques which aim to provide improved mechanically stability by creating a fusion in the anterior spine where the bulk of compressive loads are carried.[143, 225, 263] Anterior interbody fusion (AIF) applies cage into the disc space between the vertebral bodies from an anterior approach, typically with 4 to 6cc of graft material.[225] Posterior lumbar interbody fusion (PLIF) applies smaller cages, typically with graft material, into the disc space from a posterior approach but suffers from compromised stability (compared to AIF) due to the facetectomy required to place the cages.[263]

Models of Spinal Fusion and their Limitations

Numerous animal models for evaluating spinal fusion been described.[74, 137, 152, 215, 217] These models are typically functional in nature, i.e. they aim to demonstrate functional fusions or nonunions at one or more spinal levels. Their functional nature means that follow-up times are long, typically one condition per animal is evaluated and the animal numbers required are high. Left/right comparisons of two conditions are possible but any mismatch in fusion rate between the sides can have biomechanical consequences that may render the results misleading. While functional models are essential for evaluating the feasibility and safety of new treatments, these models are highly inefficient for screening the multiple parameters typically evaluated during the development of new materials and techniques.

Obstacles to Applying Hybrid Constructs for Spinal Fusion

The application of bone tissue engineering with hybrid constructs to spinal fusion bears the same difficulties as described generally above for clinically relevant bone defects. Spinal fusion aims to generate a relatively large volume of bone at the site of a large, freshly created wound bed. Furthermore, the goal of spinal fusion and joint arthrodesis in general, is to generate this bone in the space between two bony sites that is normally occupied by soft tissues such as muscle or cartilage. The application of tissue engineering to spinal fusion, particularly with regard to PLF, may be regarded as both orthotopic and ectopic.[216] In order to overcome these obstacles and reach the clinical application of hybrid constructs for spinal fusion applications, a significant amount of research and development will be required to optimize this strategy.

Calcium Phosphate Ceramic Scaffolds

Background and Biological Relevance

Calcium phosphates are salts of the tribasic phosphoric acid H_3PO_4, forming compounds containing $H_2PO_4^-$, HPO_4^{2-} or PO_4^{3-} ions. Of these ions, HPO_4^{2-} and PO_4^{3-} occur in biologically important compounds. The most critical of these are the apatites. Apatites have the chemical formula $Ca_5(PO_4)_3X$ where X can be a number of different ions including, for example, OH- (hydroxyapatite) or F- (fluoroapatite) ions. Coupled substitutions are common in apatites and it is a carbonate (CO_3) containing hydroxyapatite like salt that forms the mineral component of bones and teeth as well as assorted pathological calcifications. Several non-apatitic calcium phosphates are also of interest to medical scientists either from there structural similarities to biological apatites (alpha-tricalcium phosphate, alpha-TCP), there formation upon heating of biological apatites (beta-tricalcium phosphate, beta-TCP) or as precursors in the biomineralization process of biological apatites (octacalcium phosphate, OCP). A thorough review of the structure and chemistry of apatites and other calcium phosphates has been compiled by Elliot. [82]

Manufacturing Methods

Porous ceramics for medical applications have been produced for decades. The methods employed for their production can be generally designated as either conversion or synthetic methods.

Conversion methods start with a naturally occurring precursor with a desired porous structure. Typically, thermal and/or chemical processes are applied which convert the material of the precursor into the desired calcium phosphate material while maintaining the original structure. One of the most well-known conversion methods is the hydrothermal exchange, or Replamineform, process. The process is used to convert the skeleton of natural reef corals into hydroxyapatite or other materials[211, 242]. Methods have also been described which convert or replicate trabecular bone samples using thermal or impregnation/casting processes, respectively.[171, 229] One of the primary motivations for developing the aforementioned methods is to produce bone graft substitutes, or scaffolds, with organic architectures that appear very similar or are identical to the cancellous bone that is being replaced or grafted.

A number of different methods have been described for the fabrication of porous ceramics by synthetic or man-made processes. The application of a foaming agent within a ceramic slurry system followed by drying and thermal sintering can

produce highly porous ceramics.[204, 220, 228] Alternatively, admixing or slip casting of porogens in a ceramic slurry and their subsequent removal has also been used to produce porous ceramics. The porogen may either be particulates, [31, 233] such as wax or naphthalene beads, or a second immiscible phase as in the process of dual-phase mixing.[169] The slip casting of reticulate polymer sponges has also been described and, depending on the structure of the precursor foam chosen, can yield structures very similar to those produced by conversion methods.[250]

While the careful choice of precursor structure in conversion methods and control of process parameters in synthetic methods may provide some consistency with regard to porosity and pore structure, these methods ultimately result in complex macroporous architectures of a random nature. The complexity and variability of these structures makes them difficult to define quantitatively.[118]

Influence of Physical and Chemical Calcium Phosphate Properties on BMSCs

The interaction between bone marrow stromal cells and calcium phosphate ceramics depends on physical properties (i.e. surface reactivity, dissolution, and precipitation), chemical composition, surface topography and porous structure, with considerable interaction between many of the properties. These properties, or there consequences, influence the attachment, proliferation and differentiation of associated cells in hybrid constructs.[19]

Calcium phosphate ceramics in general undergo surface dissolution followed by precipitation of a carbonated apatite layer.[21, 53, 61, 77, 199, 262] The presence of proteins influences the precipitation process and organic compounds are incorporated within this newly formed layer and may account for the attachment and stimulation of bone marrow stromal cells.[20, 116, 256, 259] The dissolution-precipitation behavior can affect proliferation, differentiation and maturation of cells.[14, 60, 61, 139, 238] Altering the calcium/phosphorous ratio has in impact on the dissolution-precipitation behavior as does the differences in crystallinity.[76, 77, 161, 162, 164] The surface energy of calcium phosphates also greatly influences the initial cell attachment and spreading and affects collagenous matrix deposition.[203]

Consequences of Scaffold Structural Characteristics on Bone Tissue Engineering

Calcium phosphate scaffolds for bone tissue engineering are typically macroporous in nature, often with superimposed microporosities and/or surface topographies. These macro- and micro-structural features of scaffolds have consequences on bone tissue engineering.

Macroporosity and Interconnectivity

Important functional characteristics of hybrid constructs are influenced by pore size distribution and the 3-dimensional (3D) interconnecting porous architecture. Studies of the osteoconduction of bone into macroporous calcium phosphate materials has yielded a rough consensus for pore sizes between 100 and 400 µm are optimal for bone ingrowth,[26, 120, 125, 133, 218] however, bone conduction into cylindrical channels as small as 50 µm has been described.[43] Porosity and interconnectivity of the porous network are also critical with regard to osteocondution.[155] Bone morphogenic protein (BMP) induced osteogenesis has also been examined with pore size,[233] porous structure[154] and overall scaffold geometry[131, 207] all influencing ectopic bone formation in HA scaffolds.

Cellular processes such as attachment, proliferation, migration, extra-cellular matrix production and perhaps even differentiation are accommodated and even influenced by macroporous structure.[105, 180, 207, 222, 261, 264] The amount of bone formed, the kinetics of this bone formation and the pattern of vascular invasion are influenced by porosity and the interconnectivity of the porosity.[176] The porosity must also provided sufficient diffusion of nutrients and waste products throughout the scaffold for the short term maintenance of the implanted cells and support formation of new vascular networks for long term survival. A range of pore diameters from tens of microns to greater than 500 µm[135, 237] may be appropriate depending on the application. Therefore, an adequate method for assessing the macroporous environment must describe the pore volume that is accessible from an exterior surface of the scaffold via pores of a relevant size and also convey the 3D structure of the accessible porosity to the viewer.

Surface Topography and Microporosity

The microscopic features of the ceramic scaffolds, either surface textures or micro-porosity, also influences cellular activity. Cells cultured on microgrooved surfaces exhibit contact guidance, or orientation, in relation to the microgrooves. This guidance appears to be independent of the surface chemistry while more subtle measures show cell morphology remains influenced by surface chemistry.[172] Comparing microtextured surfaces (including posts, grooves and smooth surfaces) of the same material concluded that micro-textures influence osteoprogenitor cell morphology, attachment, migration and proliferation.[177] Cells cultured on scaffolds with surface microconcavities demonstrated better cell-scaffold interactions with quicker differentiation, bone tissue formation and vascularization.[102] The presence of surface micropores within macroporous structures, and the consequent increase in specific surface area, may be responsible for the osteoinductive properties of

some calcium phosphate scaffolds by selectively triggering relevant cells into the osteogenic lineage.[111, 112, 258, 261] The culture of osteoblast-like cells on the microporous surface of macroporous scaffold has demonstrated that the micropores play a role in cellular anchorage and attachment.[11]

Developing Tissue Engineering for Spinal Fusion using Hybrid Constructs

There is an established need for new bone graft substitutes that obviate the need for autologous bone grafting, particularly in spinal fusion. Ideally, these new grafts would behave similarly to autografts and posses the same osteoconductive, osteoinductive and osteogenic properties as autografts. Bone tissue engineering using hybrid constructs, composed of calcium phosphate ceramic scaffolds seeded with bone marrow stromal cells, has the potential to meet these requirements. However, developing this hybrid construct strategy for spinal fusion applications presents numerous challenges that will need to be overcome.

Aims of this Thesis

The principal aim of this thesis is to advance the development of tissue engineered posterolateral spinal fusion applications by investigating the relationship between calcium phosphate ceramic scaffold materials and tissue engineered ectopic and orthotopic bone formation. Building on the established relationships between various calcium phosphate materials and their osteoconductive and osteoinductive properties, it is hypothesized that similar relationships may exist with regard to tissue engineered bone formation using calcium phosphates. The limited ability of traditional manufacturing methods to produce (or reproduce) standardized porous ceramic morphologies and the lack of spinal fusion screening models necessitated the development of novel model systems to discretely evaluate ectopic and orthotopic tissue engineered bone formation with a focus on posterolateral spinal fusion applications. The posterolateral model was chosen over interbody models because of an expected advantage in discriminating the long-term effects of tissue engineering from osteoconduction.

Chapters of this thesis and detailed aims

Standardized ceramic scaffolds for evaluation of ectopic bone formation

Chapter 2 presents a method for manufacturing hydroxyapatite scaffolds with designed and reproducible porous structure using an indirect rapid prototyping method. The ability of these scaffolds to support BMSC attachment and subsequent proliferation is examined with an Alamar Blue assay in **Chapter 3**. The rapid prototyping method was then extended to produce standardized scaffolds

from several different calcium phosphate materials. **Chapter 4** describes this method and characterizes the chemical and physical properties the resulting scaffolds. Tissue engineered ectopic bone formation in these scaffolds is evaluated in **Chapter 5** using a goat paraspinal muscle implantation model. **Chapter 6** presents a micro computed tomography for evaluating the accessible volume of porous scaffolds.

Specific research questions addressed in the development and application of standardized ceramic scaffolds included:

- *Can rapid prototyping technology reproducibly manufacture standardized ceramic scaffolds with essentially identical macroporous architectures?*
- *Will the chemical and/or physical properties of the ceramic materials be influenced by the manufacturing method?*
- *Will standardized scaffolds support tissue engineering with bone marrow stromal cells?*
- *Will standardized scaffolds be effective in determining the influence of different materials on ectopic tissue engineered bone formation?*

Screening models for bone formation in posterolateral lumbar spinal fusion

Chapter 7 introduces a standardized screening model for early bone formation in lumbar spinal fusion. This model examined bone formation between planar plates of 10 different calcium phosphate ceramics including the same chemistries evaluated in Chapters 4 and 5. **Chapter 8** extends this model system to examine the influence of BMSC tissue engineering of bone formation in traditionally manufactured porous scaffolds of the same four calcium phosphate chemistries as in Chapters 4 and 5.

Specific research questions addressed in the development and application of these screening models included:

- *Can a screening model be designed that is specifically relevant to posterolateral spinal fusion?*
- *Will this screening model be effective in determining the influence of different materials on tissue engineered orthotopic and ectopic bone formation?*
- *Is the tissue engineering of porous calcium phosphates with BMSCs likely to improve posterolateral spinal fusion?*

2

Design and fabrication of standardized hydroxyapatite scaffolds with a defined macro-architecture by rapid prototyping for bone tissue engineering research

C. E. Wilson[1], J. D. de Bruijn[2], C. A. van Blitterswijk[2,3], A. J. Verbout[1] and W. J. A. Dhert[1]

J Biomed Mater Res A. 2004 Jan 1;68(1):123-32

[1] *Department of Orthopaedics, University Medical Center Utrecht, Utrecht, The Netherlands*
[2] *IsoTis NV, Bilthoven, The Netherlands*
[3] *Institute for Biomedical Technology, University of Twente, Enschede, The Netherlands*

Abstract

This investigation describes the production and characterization of calcium phosphate scaffolds with defined and reproducible porous macro-architectures and their preliminary *in vitro* and *in vivo* bone tissue engineered response. Fugitive wax molds were designed and then produced by a Rapid Prototyping technique. An aqueous hydroxyapatite slurry was cast in these molds. After sintering at 1250 °C and cleaning, dimensional and material characterizations of the scaffolds were performed. The resulting scaffolds represented the design and their dimensions were remarkably consistent. A texture inherent to the layer-by-layer production of the mold was impressed onto vertical surfaces of the scaffolds. The surface roughness (R_a) of the textured surface was significantly greater then that of the non-textured surfaces. Material analyses revealed a ß-TCP phase in addition to hydroxyapatite for the molded ceramics. Non-molded control ceramics exhibited only hydroxyapatite. Thirty scaffolds were seeded with culture expanded goat Bone Marrow Stromal Cells (BMSCs), and implanted subcutaneously in nude mice for 4 or 6 weeks. Histology revealed mineralized bone formation in all scaffolds for both implantation periods. After 4 weeks, bone was primarily present as a layer on scaffold surfaces. After 6 weeks, the surface bone formation was accompanied by bone budding from the surface and occasional bridging of pores. This budding and bridging bone formation was almost always associated with textured scaffold surfaces. However, the area percentage of bone in pores was similar for the 4 and 6 week implantation periods.

Introduction

Calcium phosphate ceramics, in particular hydroxyapatite (HA), have been widely investigated as porous bone fillers.[46] The biocompatibility,[68] osteoconductive[43, 91, 124] and, under specific conditions, osteoinductive[206, 258, 261] qualities of these ceramics have been well established. The development of Tissue Engineered (TE) bone, typically through the association of Bone Marrow Derived Stromal Cells (BMSCs) and a scaffold material, has capitalized on these qualities, making porous calcium phosphate ceramics popular for bone TE research.[12, 65, 100, 189]

Porous ceramics can be produced using various methods including conversion from natural structures and by completely synthetic techniques. Conversion methods start with a naturally occurring structure, such a coral[211, 242] or trabecular bone,[171, 229] which are converted to the final composition while maintaining the original architecture. Completely synthetic techniques employ several very different methods for creating pores. These methods include the foaming of ceramic slurries,[204, 220, 228] slip casting of reticulate polymer sponges,[250] addition of organic particles to ceramic powders[31, 233] and dual-phase mixing of polymer and ceramic slurries.[169] All these techniques result in macroporous architectures of a random nature, and thus, the resulting architectures are not designed. Furthermore, the complex nature of these structures makes them difficult to define quantitatively.[118]

The complexity and lack of control over the structure of traditional porous ceramics has several consequences regarding the optimization of bone tissue engineering. In order to optimize scaffold architectures, parameters defining the structure must be isolated and their impact on the outcome variables determined. Isolating and predicting the value of parameters, such as pore diameter, interconnectivity, surface area and others, is difficult, if not impossible, to accomplish with the techniques described above. Therefore, when traditional ceramics are used to investigate tissue engineering parameters the effect of varying scaffold structures is difficult to eliminate. Despite these limitations, some knowledge has been gained regarding porous HA structures. Osteoconduction has received the most attention with the consensus being that pore sizes between 100 and 400 µm are optimal for bone ingrowth,[26, 120, 125, 218] however, bone conduction into cylindrical channels as small as 50 µm has been described.[43] Additionally, the interconnectivity of the porous network is also critical.[79, 123, 155] Bone morphogenic protein (BMP) induced osteogenesis has also been examined with pore size,[233] porous structure[154] and overall scaffold geometry[131, 207] all influencing ectopic bone formation in HA scaffolds.

To support both scaffold and, more generally, bone TE optimization studies, a fabrication technique that allows the accurate reproduction of designed scaffold architectures is needed. Rapid prototyping (RP) refers to a variety of technologies capable of producing three-dimensional (3D) physical models from 3D computer data sets. The use of rapid prototyping techniques has been suggested for producing scaffolds with defined architectures,[128, 252] although these have typically focused on polymeric materials. Recently, HA implants with designed porous structures have been produced using fugitive molds made by stereolithography,[48, 167] a RP technique that builds models by scanning a photo-curable epoxy resin with a laser. These molds were filled with a "reactive ceramic suspension" and, once cured, the mold and organic components of the suspension were pyrolyzed and the ceramic sintered. Various geometries have been produced by this technique with porosities between 26 and 52% and channel sizes from 366 to 968 µm.

The objective of the current study was to develop a manufacturing technique utilizing RP technology to produce standardized HA scaffolds with defined architectural parameters. The consistency of the designed macroporous architecture and reproducibility of the microstructure were examined in the resulting scaffolds as well as the material composition and preliminary *in vivo* bone tissue engineering response.

Materials and Methods (outlined in Figure 2.1)

Implant design and mold production.

The criteria for our standard scaffold design were: porosity of approximately 50%, channel/pore diameter within the range described in literature, overall size appropriate for implantation in small animals, exterior dimensions that allow identification and orientation of implant axes during histological processing, and fabricated from hydroxyapatite. Using these criteria the following specifications were defined: a parallelepiped with exterior dimensions of 2.8 x 3.6 x 5.2 mm and an intersecting network of 400 x 400 µm square cross-section channels oriented along the orthogonal axes and separated by 400 µm from each other and the outside edges. Sacrificial molds, capable of producing six scaffolds each, were designed using the Rhinoceros computer aided design software (Robert McNeel & Associates, USA) on a personal computer (Dell Inc., USA) running Windows 2000 (Microsoft Corp., USA). The mold model was scaled to account for the 20% shrinkage we expected from previous experience. Two parallel surfaces of the molds were open to allow slurry infiltration through the mold. Multiple copies of the mold were produced using the ModelMaker II rapid prototyping system (Solidscape Inc., USA). This system constructs models by sequentially depositing material in

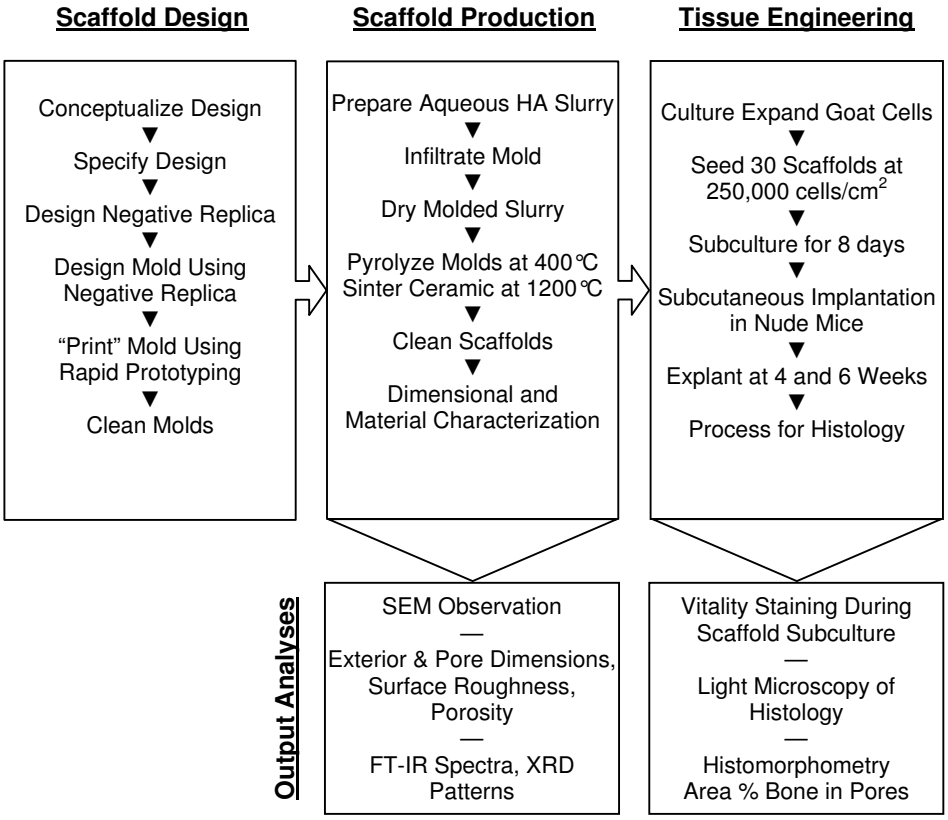

Figure 2.1: Flow Diagram of Study Design divided into three components: Scaffold Design, Scaffold Production and Tissue Engineering. Output analyses are shown below their respective component.

thin parallel-planar layers. Each layer is formed by jetting small droplets of both build and support materials. The build material forms the actual mold and the support material reinforces the build material during the RP process. Each layer is milled to a specified thickness, 0.0508 mm in our case, prior to deposition of the next layer. This layer-by-layer process continues until the entire mold is constructed. The construct is then taken from the machine and the support material removed by a solvent (BIOACT™ VSO, Petroferm, USA).

Scaffold fabrication and characterization.

A previously described aqueous slurry system was used.[169] In brief, commercially available HA powder (Merck Eurolab BV, The Netherlands) was calcined in air at 1000 °C using a heating and cooling rate of 100 °C/hour with no holding period. An aqueous ceramic slurry was prepared by slowly admixing 67.1 wt% calcined HA powder to a mixture of 28.6 wt% demineralized water, 2.6 wt% ammonia solution

(25%, Merck) and 1.5 wt% deflocculant (Dolapix, Aschimmer & Schwarz GmbH, Germany). When a homogenous blend was obtained, 0.15 wt% of binder (CMC, Pomosin BV, The Netherlands) was incorporated into the mixture. The slurry was stored in a covered beaker until its use later the same day.

The molds were filled using a simple vacuum device. Millex®-GV syringe driven filter units (25 mm, Millipore S.A., France) were divided in half and the filter paper removed. An open face of each mold was secured against the perforated interior surface of a filter half by circumferentially wrapping both with wax laboratory film. The mold/filter constructs were attached to 50 ml syringes (Fig. 2.2) and flushed with demineralized water. The beaker containing the slurry was placed on a Porex vibrating table (Renfert, Germany), and the slurry drawn slowly into the molds. The mold was then placed on a sheet wax laboratory film and the syringe and filter half removed. The molds were allowed to air dry overnight at room temperature and were further dried for 24 hours at 50 ℃ in air. Excess slurry was allowed to dry in the beaker, processed identically to the molded ceramics, and served as controls when examining material properties.

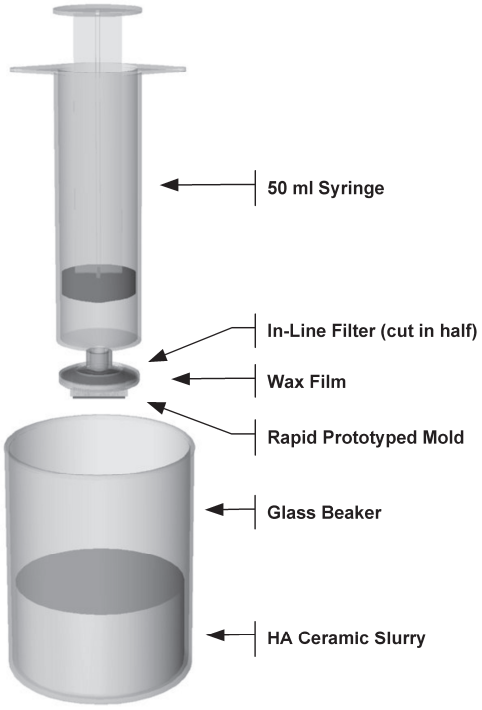

Figure 2.2: Schematic of mold infiltration device.

Pyrolysis of the mold and other organic components, as well as final sintering of the ceramic scaffolds, was conducted in air in a high temperature furnace (Nabertherm 1400, Germany) using the following temperature profile: 200 min. to 200 °C, 400 min. to 400 °C, 180 min. at 400 °C, 510 min. to 1250 °C, 480 min. at 1250 °C and 750 min. to room temperature. Excess ceramic was often present on the scaffold faces corresponding to the open sides of the molds. This was removed using a rotary polisher (LaboPol-5, Struers, Denmark) with 1200 grit waterproof silicon carbide paper (Struers). The scaffolds were cleaned by ultrasound for 15 minutes each in acetone, 100% ethanol and finally demineralized water. After air drying at 50 °C, the scaffolds were steam sterilized for 20 minutes at 121 °C.

The exterior scaffold dimensions were measured using a digital caliper (CD-15C, Mitutoyo Ltd., United Kingdom). Scanning Electron Microscopy (ESEM, XL 30 ESEM-FEG, Philips, The Netherlands) was used to investigate the architecture and surface micro-structure of three scaffolds. The interior surfaces of the scaffolds were exposed using a rotary polisher with 1200 grit waterproof silicon carbide paper. Two surface types were apparent from ESEM observations, smooth and textured (see results below). Laser profilometry (Microfocus, UBM, Germany) was used to measure the average roughness (R_a) of these surfaces. Five measurements of both smooth and textured interior surfaces of three scaffolds were made using a scan line length of 0.3 mm. Measurements of the textured surfaces was made perpendicular to the texture. Differences between surface types and scaffolds were determined by single factor ANOVA with a significance level of $p<0.05$. Apparent porosity of the scaffolds was determined by comparing the apparent density of each scaffold (dry weight / measured volume) and the theoretical density of HA (3.156 g/cm^3).[2] Specimens of molded and non-molded sintered ceramic were evaluated by Fourier Transformed Infrared Spectroscopy (FT-IR, Spectrum 1000, Perkin-Elmer, USA) and X-ray diffraction (XRD, Miniflex, Rigaku, Japan) to evaluate composition and phase purity.

In vitro and in vivo evaluation of scaffolds seeded with BMSCs.

Goat BMSCs were obtained from an iliac wing bone marrow aspirate. The aspirate was plated and culture expanded in standard culture media[64] consisting of *alpha*-MEM (Gibco, Scotland) with 15% (v/v) fetal bovine serum (FBS, Gibco), 0.2 mM L-ascorbic acid-2-phosphate (AsAP, Sigma-Aldrich Chemie BV, The Netherlands), 2.0 mM L-glutamine (Life Technologies BV, The Netherlands), antibiotics (100 U/ml each penicillin and streptomycin) and 1ng/ml of basic fibroblastic growth factor (bFGF, Sigma-Aldrich). The adherent cells were cryo-preserved at the end of the first passage. Within 6 months, the cryo-preserved cells were thawed and replated in standard culture medium. When confluent, the cells were trypsinized and a cell

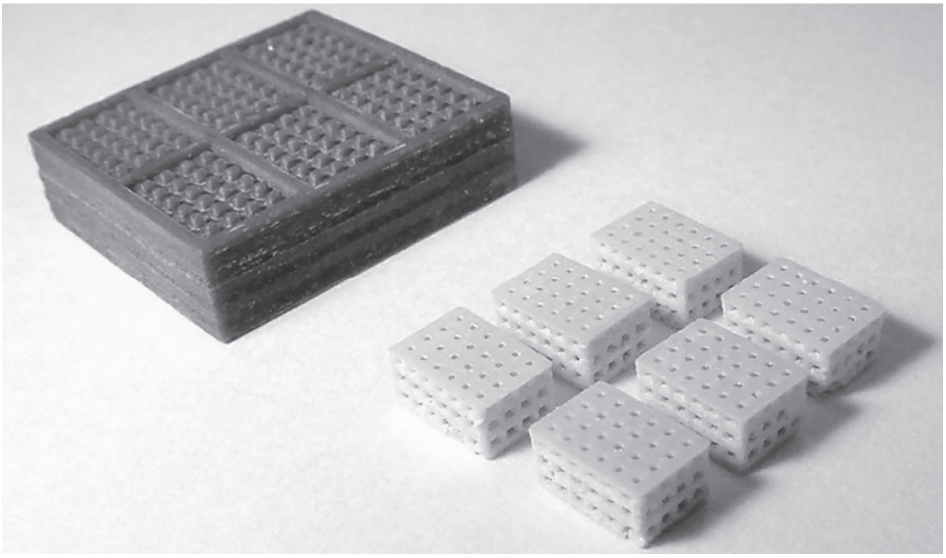

Figure 2.3: A rapid prototyped mold and six scaffolds produced by such a mold.

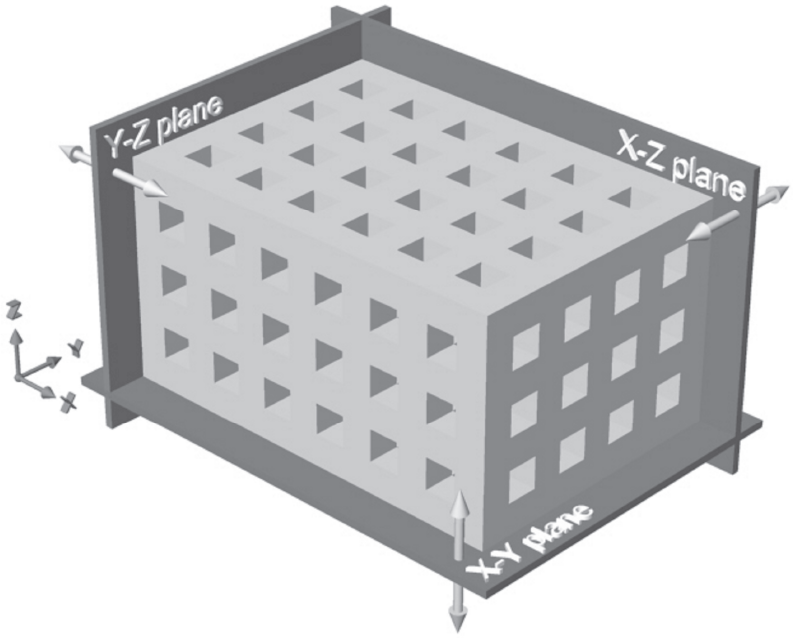

Figure 2.4: Schematic of the scaffold as designed and the three orthogonal planes used to define the scaffold surfaces throughout the text.

suspension of $5x10^5$ cells/ml prepared. Thirty scaffolds were divided equally between five sterile 10 ml tubes for seeding. A 0.5 ml volume of cell suspension ($2.5x10^5$ cells) per scaffold was added to each tube for a total of 3.0 ml per tube. Seeding was conducted for six hours on a roller bank (2 rpm) in an incubator (37 ℃, humidified atmosphere with 5% CO_2). The constructs were subsequently cultured in 25-well plates using standard culture medium supplemented with 10 nM dexamethasone and 10 mM β-glycerophosphate (both Sigma-Aldrich). The medium was refreshed every other day. On days 1, 4 and 7 after seeding, four scaffolds were utilized for *in vitro* analysis. Two were stained with the tetrazolium dye 3-(4,5-dimethylthiazol-2-yl)-2,5-diphenyl-2*H*-tetrazolium bromide (MTT, Sigma-Aldrich) to indicate vital cells and the other two with trypan blue (Sigma-Aldrich) to indicate non-vital cells. The remaining scaffolds were cultured for 7 days and then implanted subcutaneously in the backs of nude mice for 4 or 6 weeks. Three scaffolds each were implanted into two mice for the 4-week implantation time and two scaffolds each were implanted into six mice for the 6-week implantation time. After the implantation periods, the mice were killed and the implants removed and fixed overnight in 1.5% glutaraldehyde/0.14M sodium cacodylate buffer (pH 7.2-7.4). The samples were dehydrated by ethanol series and embedded in methyl-methacrylate (MMA, Merck, Germany). After polymerization, the embedded samples were sectioned at ±10μm using a sawing microtome (Leica, Germany) and stained with methylene blue and basic fuchsine (both Sigma-Aldrich). Bone formation within scaffolds was observed by light microscopy and measured by histomorphometry (KS400, Zeiss, Switzerland). The total area was established as the maximum rectangular area within the boundaries of the scaffold material. Scaffold and bone areas were measured and pore area and the percent of pore area occupied by bone (%bone) were calculated. Although the intent of this study was not to test differences in bone formation, ANOVA using a nested design (implantation period[mouse]) was used to compare the average %bone between implantation periods.

Results

Scaffold fabrication and characterization.

The molds and resulting scaffolds (Fig. 2.3) are discussed in the following text using the orthogonal plane explained in Fig. 2.4. Table 2.1 summarizes the physical measurements of the scaffolds (calculated and expected values). The expected values for the scaffold dimensions, volume and porosity were calculated from the computer model used to design the molds. The theoretical weight of the scaffolds was calculated by multiplying the scaffolds ceramic volume (determined from the computer model) with the theoretical density of HA (3.156 g/cm^3). Recall

Table 2.1: Measurements of exterior scaffold dimensions and weight (n=12) as well as calculated values for volume, porosity and shrinkage.

		Measured or Calculated (± SD)			Theoretical or Expected	% Diff.
Exterior Dimensions (mm)	x	5.03	±	0.066	5.20	-3.22
	y	3.50	±	0.037	3.60	-2.69
	z	2.68	±	0.042	2.80	-4.29
Volume (mm^3)		47.25	±	1.114	52.42	-9.86
Weight (mg)		71.23	±	4.185	96.35	-26.07
Porosity (%)		52.26	±	2.163	41.76	25.14
Shrinkage (%)	x	22.58	±	1.021	20.00	12.88
	y	22.15	±	0.817	20.00	10.74

Comparison to theoretical or expected values with percent difference. Measurements in the z-direction were between polished surfaces, therefore, shrinkage was not calculated in this direction.

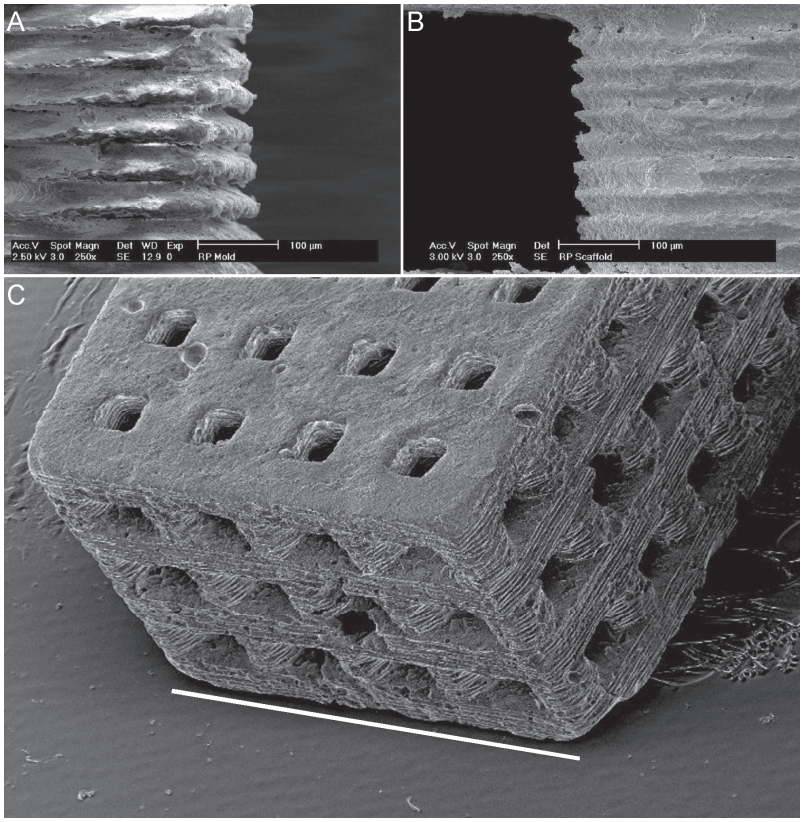

Figure 2.5: ESEM micrographs of (**A**) RP mold texture, (**B**) resulting scaffold texture and (**C**) perspective view of a typical scaffold showing smooth horizontal and textured vertical surfaces as well as semi-spherical surface pores. Width of scaffold, indicated by white bar, is approximately 3.6 mm.

that measurements in the z-direction (Table 2.1) were made between surfaces polished to remove excess ceramic and, therefore, do not represent the 'as molded' dimensions. For this reason, shrinkage in the z-direction and volumetric shrinkage were not calculated.

Distinctive texturing resembling a series of parallel ridges and valleys was observed in SEM micrographs of mold and scaffold surfaces parallel to the x-z and y-z planes (Fig. 2.5). Some pores (semi-spherical, 50 to 150 µm) and protuberances (extending 15 to 50 µm) were seen on the textured surfaces. Tightly packed ceramic grains (2 to 10 µm, Fig. 2.6) and a small amount of micro-porosity (5 to 10 µm) were revealed at high magnification. The cross-sectional channel geometry was dependant upon direction. Channels running in the x- and y-directions were square in cross section with textured vertical (z-direction) surfaces and smooth horizontal surfaces. Channels running in the z-direction were rounded with no apparent texturing. Surface texture and pore dimensions are contained in Table 2.2. Average surface roughness measurements ($R_{a,}$ Table 2.3) demonstrated significant differences between smooth and textured surfaces both within and between scaffolds. No difference was found between scaffolds for the same surface type.

The XRD patterns (Fig. 2.7) revealed several small peaks, associated with ß-TriCalcium Phosphate (ß-TCP) formation in the molded specimens, which were not exhibited in the non-molded specimens. Additionally, peaks associated with OH^- groups were diminished in the FT-IR spectra of molded versus non-molded specimens (Fig. 2.8).

In vitro and in vivo evaluation of scaffolds seeded with BMSCs.

One day after seeding, vital cells were attached to all scaffold surfaces but were concentrated on textured regions of the exterior surfaces. By day 4, cells were evenly distributed on exterior surfaces and were forming multi-layers. Interior surfaces were also covered with cells with a slightly decreasing density gradient toward scaffold centers. By day 7, cell density on the exterior surfaces had increased with many exterior channel openings completely blocked by cell layers. Cell density on interior surfaces also increased but the decreasing gradient towards scaffold centers remained. Trypan blue stain revealed few non-vital cells throughout the scaffolds with only a slight increase observed from day 1 to 7.

Histology revealed bone formation in all scaffolds at all time points (Fig. 2.9). After 4 weeks (Fig. 2.9c-d), scaffolds were full of tissue and well vascularized. Bone formation typically presented as a thin layer (20-80 µm) on the interior surfaces of

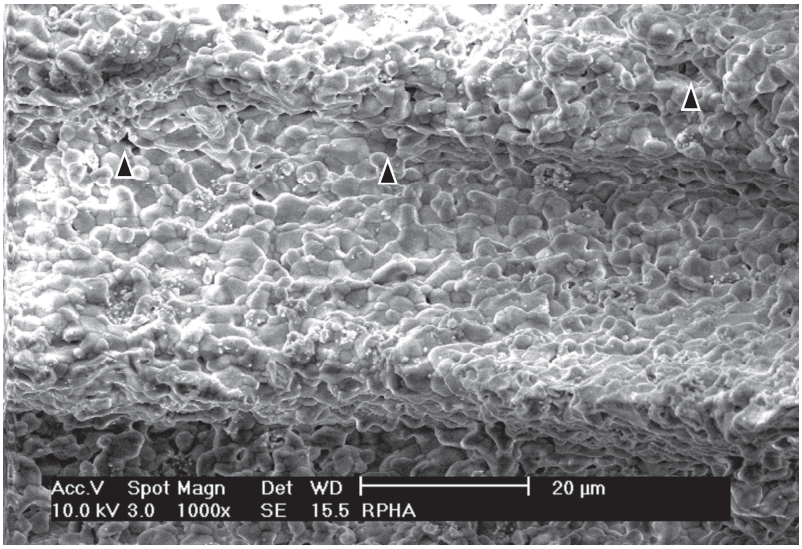

Figure 2.6: High magnification ESEM micrograph of scaffold surface showing grain structure and micro-porosity (examples indicated by ►). The surface texture is also visible in the image (running horizontally).

Table 2.2: Pore and micro-texture measurements.

			Value (µm ± SD)		
Pore Dimensions	x-y plane	x-direction	286	±	15
		y-direction	280	±	16
	x-z plane	x-direction	352	±	28
		z-direction	339	±	17
	y-z plane	y-direction	394	±	24
		z-direction	376	±	30
Micro Texture	Peak to Peak		41.2	±	1.4
	Valley Depth		25.9	±	2.3

Table 2.3: Surface roughness measurements (R_a) for smooth and textured surfaces of three scaffolds.

	Surface Roughness (R_a ± SD)					
Scaffold	Smooth			Textured		
1	0.68	±	0.21	1.69	±	0.40
2	0.94	±	0.14	1.81	±	0.81
3	0.70	±	0.20	1.67	±	0.38
Average	0.78	±	0.21	1.72	±	0.53

Measurements were made perpendicular to texture.

the scaffolds. Osteoid tissue occasionally provided early indications of bone budding away from the scaffold surfaces. After 6 weeks (Fig. 2.9e-f), mineralized bone tissue was frequently observed budding away from scaffold surfaces and regularly bridged channels. Budding bone formation almost always occurred on textured surfaces and rarely on smooth surfaces. No difference was detected in %bone (Table 2.4) between the 4 and 6 week implantation periods.

Discussion and Conclusions

The present study demonstrates the application of Computer Aided Design and Rapid Prototyping technologies for the production of HA scaffolds with a defined macro-architecture. Fugitive molds were designed and manufactured in wax material using a commercially available RP system. As with most RP systems, a physical model is created by sequential, layer by layer addition of material. However, several unique features of this RP system make it particularly useful for producing detailed fugitive molds. First, this RP process uses both build and support materials, allowing overhangs and internal voids to be created. Second, the build material has a very low coefficient of thermal expansion (CTE), thus minimizing the risk of fracture due to CTE mismatch with the ceramic during pyrolysis. Third, deposited layers are milled to a specified thickness, providing not only a smooth surface for deposition of the subsequent layer but also unmatched control of spatial resolution in the build (z) direction.

The molds exhibited a characteristic surface texture as a result of the RP production process. As mentioned above, each layer of the mold was constructed by jetting molten droplets of build material, which flatten and spread when they strike the surface. As a result, the edges defined by the build material have a convex rounded profile, resulting in a characteristic texturing of all mold surfaces shaped by multiple print layers (Figure 2.5a). Therefore, as molds are built up vertically layer by layer, this results in a texture on the vertical surfaces (x-z and y-z planes) which is subsequently cast into the ceramic. The rounded corners of channels running in the z-direction (cross-sections parallel to the x-y plane) are explained by the pooling of adjacent droplets prior to solidification, resulting in rounding of both inside and outside corners within the printed layers. These rounded mold corners are then cast into the resulting ceramic scaffolds and observed in channels running parallel to the z-direction.

The shrinkage of the ceramic system was slightly greater than expected. This may result from a small amount of residual water remaining in the molds after cleaning, which could effectively reduce the HA loading of the slurry, resulting in greater

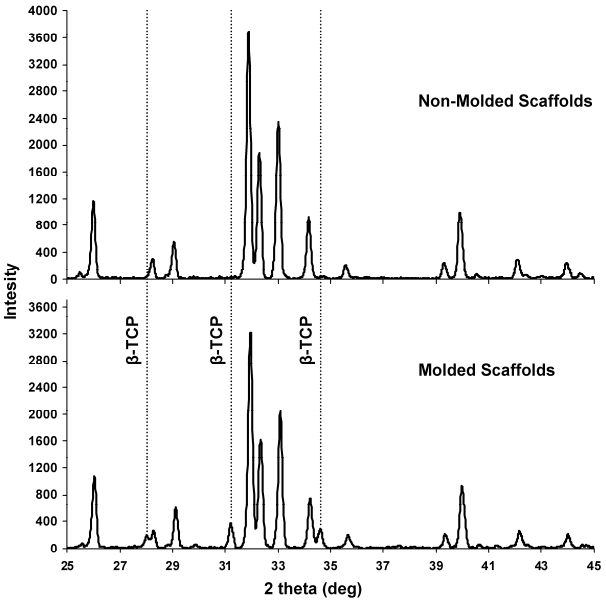

Figure 2.7: XRD patterns of non-molded (top) and molded (bottom) ceramics. Vertical lines indicate additional peaks present in the molded specimens only. These are associated with β -TCP formation.

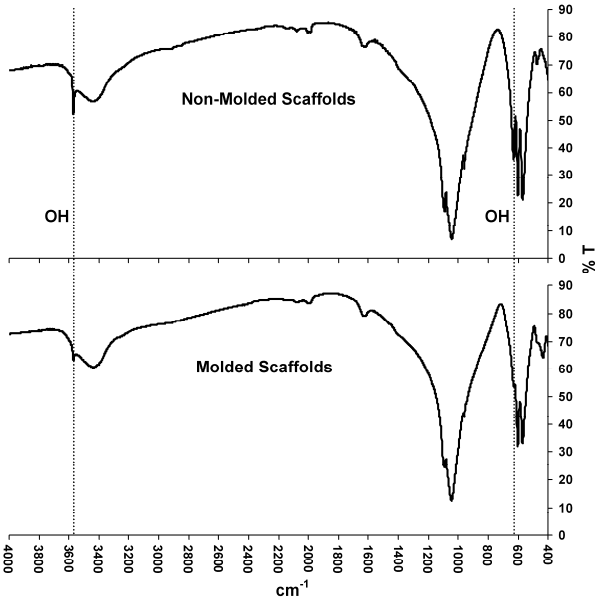

Figure 2.8: FT-IR spectra of non-molded (top) and molded (bottom) ceramics. Vertical lines indicate OH^- associated peaks that are reduced in the molded specimens.

shrinkage during drying and sintering. This shrinkage may have several consequences with respect to the resulting scaffolds: (1) The dimensions of the scaffolds can be somewhat smaller than predicted which is reflected not only in measurements of the exterior dimensions (Table 2.1) but also in measurements of pore and surface texture dimensions (Table 2.2). (2) If shrinkage is due to a decreased HA loading of the slurry, this may also explain the lower than expected weight of the scaffolds. For example, if one assumes that the shrinkage is 10% more than expected in each direction, then the volumetric shrinkage would be approximately 27% greater than expected. If this excess shrinkage were entirely due to decreased HA loading then you could expect the weight of the scaffold to be approximately 27% lower than expected. This corresponds well to the actual shrinkage and weight date for the scaffolds. However, the porosity of the scaffolds is higher than expected, indicating that the lower weight is not simply due to the smaller size of the scaffold. It is likely that the surface texture and defects within the ceramic also contribute to the increased porosity and decreased weight.

Compositional analysis by XRD indicated the presence of a ß-TCP phase in addition to an HA phase only after molding. This was supported by the FT-IR spectra which indicate a reduction in size of the OH^- peaks in the molded specimens compared to the non-molded specimens. This is consistent with the chemical formulas in which HA has 2 OH groups and ß-TCP none.[82] Since molded and non-molded specimens were identically treated with the exception of the molding process, it is likely that the presence of ß-TCP after molding results from the exposure of the HA slurry to the mold material. However, the mechanism is not clear and requires further investigation.

Histology revealed mineralized bone in all specimens, predominantly as a layer on interior surfaces of the scaffolds. This is similar to TE induced bone formation in porous ceramics as described by other researchers.[12, 100, 189] While there was no difference in the amount of bone after 4 and 6 weeks of implantation, the budding of mineralized tissue away from scaffold surfaces and the complete bridging of pores were seen only after 6 weeks. Of particular interest is the association of this budding and bridging behavior with textured scaffold surfaces. These surfaces may influence bone formation in several ways. First, the textured surfaces may influence cell distribution in terms of cells per unit surface area. Secondly, Chang et al. has shown that elevated concentrations of calcium and phosphate are important for *in vitro* mineralization.[44] They also suggest that HA enhanced bone formation *in vivo* may be via a similar mechanism due to the degradation of HA and the resulting increase in calcium and phosphate concentrations. Following this line of thinking, it is reasonable to assume that the increased surface area of the textured

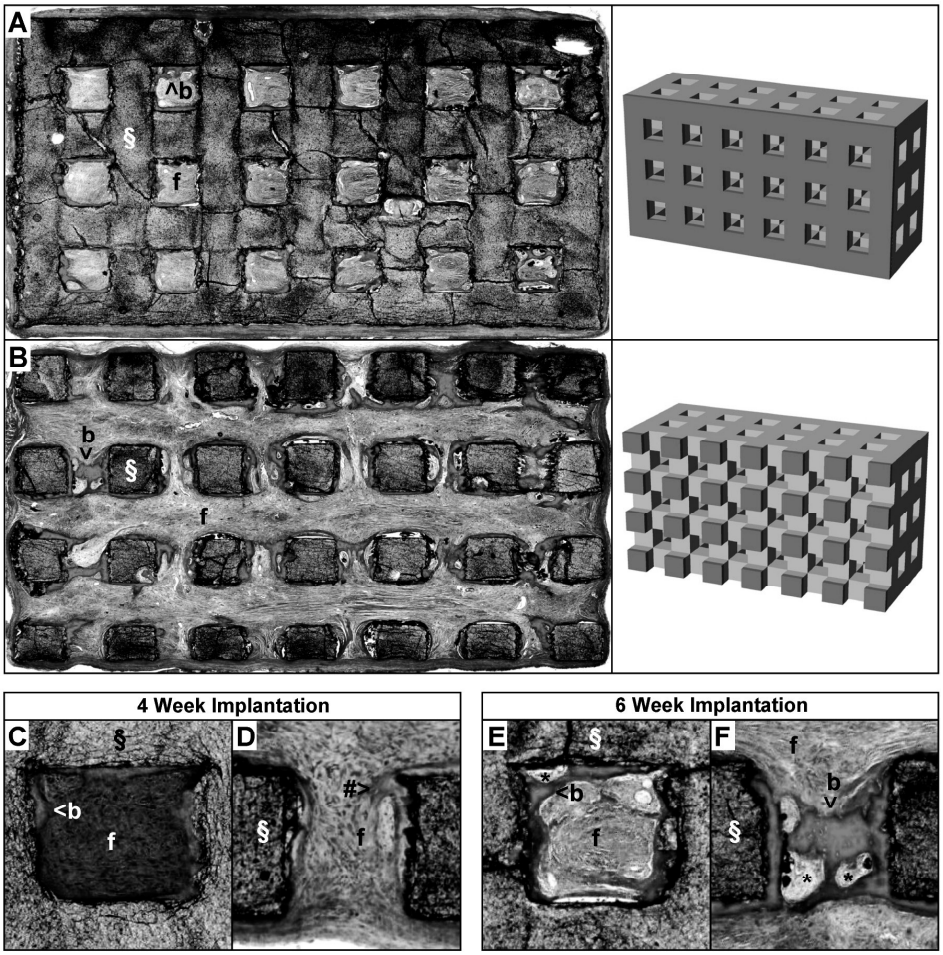

Figure 2.9: Light micrographs of methylene blue/basic fuchsine stained histological sections. Pores/channels are approximately 350 to 400 µm across. **A** and **B**, full sections from mouse 3 (see Table 4) after 6 weeks implantation with schematic representations of the sections to the right. Scaffold material (gray, **§**), fibrous tissue (purple, **f**), and mineralized bone tissue (red, **b>**) are visible. **C** and **D**, enlargements of 4 week histology. Bone tissue is primarily on scaffold surfaces with some early indications of bone budding away from surface (**#>**). **E** and **F**, enlargements of 6 week histology. Surface bone formation most common with frequent budding away from surface and encapsulation of fat or marrow like tissue (*). *(See color image on page 195)*

Table 2.4: Histomorphometry of scaffolds presented as the area % bone in pores for each scaffold and totaled for each implantation period (mean ± SD).

Implant Period	Mouse Number	Number of Scaffolds	Area % Bone (Mean ± SD)
4 Week	1	3	5.49 ± 3.48
4 Week	2	3	6.86 ± 3.23
		4 Week Total	6.11 ± 3.28
6 Week	1	1	6.70 ± 1.54
6 Week	2	2	6.80 ± 2.09
6 Week	3	2	14.57 ± 4.75
6 Week	4	2	2.14 ± 1.36
6 Week	5	2	4.97 ± 2.66
6 Week	6	2	2.07 ± 0.89
		6 Week Total	6.16 ± 5.05

scaffold surfaces results in more dissolution, and therefore, more calcium and phosphate release at these surfaces.

In conclusion, we have described a method for fabricating ceramic scaffolds with defined and reproducible 3-dimensional porous architectures using a rapid prototyping technique. In combination with culture expanded goat BMSCs, ectopic bone formation was demonstrated in all constructs. Additionally, the texture inherent to specific surfaces of the scaffolds appears to be important for the budding of bone formation away from the surface.

Acknowledgements

The authors would like to thank The Netherlands Technology Foundation for financial support (grant UGN.4966). We also thank Ellen van Leeuwen (Technical University of Eindhoven) and Dr. ShiHong Li (IsoTis N.V.) for their assistance.

3

Evaluating 3D bone tissue engineered constructs with different seeding densities using the alamarBlue™ assay and the effect on in vivo bone formation

C. E. Wilson[1], W. J. A. Dhert[1], C. A. van Blitterswijk[2,3], A. J. Verbout[1] and J. D. de Bruijn,[2]

J Mater Sci Mater Med. 2002 Dec;13(12):1265-9

[1] *Department of Orthopaedics, University Medical Center Utrecht, Utrecht, The Netherlands*
[2] *IsoTis NV, Bilthoven, The Netherlands*
[3] *Institute for Biomedical Technology, University of Twente, Enschede, The Netherlands*

Abstract

Bone tissue engineering using patient derived cells seeded onto porous scaffolds has gained much attention in recent years. Evaluating the viability of these 3D constructs is an essential step in optimizing the process. The alamarBlue™ assay was evaluated for its potential to follow in vitro cell proliferation on architecturally standardized hydroxyapatite scaffolds. The impact of the alamarBlue™ assay and seeding density on subsequent in vivo bone formation was investigated. Twelve scaffolds were seeded with various densities from 250 to $2.5x10^6$ cells/scaffold and assay by alamarBlue™ at 5 time points during the 7 day culture period. Twelve additional scaffolds were seeded with $2.5x10^5$ cells/scaffold. 2 control and 2 alamarBlue™ treated scaffolds were subcutaneously implanted into each of 6 nude mice for 6 weeks. Four observers ranked bone formation using a pair wise comparison of histological sections form each mouse. The alamarBlue™ assay successfully followed cell proliferation, however, the diffusion kinetics of the 3D constructs must be considered. The influence of in vitro alamarBlue™ treatment on subsequent in vivo bone formation cannot be ruled out but was not shown to be significant in the current study. The alamarBlue™ assay appears to be quite promising for evaluating a maximum or end-point viability of 3D tissue engineered constructs. Finally, higher seeding densities resulted in more observed bone formation.

Introduction

The combination of patient own cells and porous ceramic scaffolds to produce three-dimensional hybrid osteogenic constructs is a common theme in bone tissue engineering research[12, 65, 100, 189]. Tracking the survival/activity of cells on scaffolds from the time they are seeded until implantation may be helpful to the optimization of these cell/scaffold constructs. The alamarBlue™ (aB) assay (Biosource International, USA) uses an oxidation-reduction indicator that both fluoresces and changes color in response to chemical reduction of growth medium resulting from metabolic activity. There are several advantages of the alamarBlue™ assay over other methods: The alamarBlue™ assay can assess both proliferation and viability. The assay is also very simple to implement and is not toxic. Therefore, the same culture can be evaluated at several time points and potentially used for additional purposes following alamarBlue™ assay. This method has been used in a variety of proliferation and viability studies[25]. Of specific interest to the current work, alamarBlue™ has been used to monitor the number of melanoma cells adhering to hydroxyapatite beads coated with synthetic peptides[97]. Additionally, the toxicity of Tumor Necrosis Factor Alpha (TNF-α) and actinomycin on an osteoblastic cell line (MC3T3-E1) has been investigated by alamarBlue™ [96]. Based upon these data, it can be speculated that the alamarBlue™ assay could be of value in (bone) tissue engineering research to evaluate cell growth and viability on scaffolds that can subsequently be implanted. However, so far no data are available on its feasibility and safety in bone tissue engineering using 3-dimensional (3D) scaffolds. Therefore, the aim of the current study is to determine whether alamarBlue™ can be used to evaluate the proliferation of bone marrow derived cells seeded at various densities onto 3D porous hydroxyapatite scaffolds and to establish if the assay affects subsequent *in vivo* bone production.

Materials and Methods

Standardized hydroxyapatite (HA) scaffolds with dimensions of 2.8 x 3.6 x 5.2 mm and an intersecting network of 400 µm channels were produced using a rapid prototyped negative replica method developed by the authors[245]. Briefly, a negative mold of the desired scaffold was designed on a personal computer using Computer Aided Design software (Rhinoceros, Robert McNeel & Associates, USA). This design was then fabricated in wax material using a commercially available Rapid Prototyping (RP) system (ModelMaker II, Solidscape Inc., USA). The resulting molds were infiltrated with an aqueous HA slurry and allowed to air dry. The ceramic filled molds were then heated to 1250 °C in an air filled high temperature furnace (Nabertherm 1400, Germany) with a heating and cooling rate of 100 °C per hour. This resulted in complete pyrolysis of the mold material and sintering of

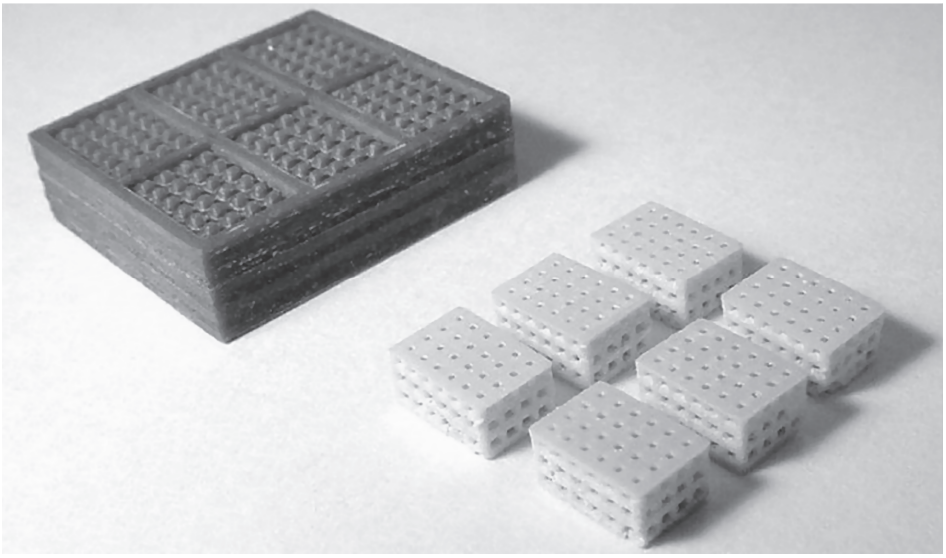

Figure 3.1: Example of rapid prototyped mold (upper left) and the six hydroxyapatite scaffolds resulting from such a mold (lower right).

the ceramic. Examples of a rapid prototyped mold and the scaffolds produce by such a mold are shown in Figure 3.1. A total of 30 scaffolds were produced for this experiment. Twenty-four scaffolds were used for the tissue engineering study with 12 used for the alamarBlue™ (aB) assay and 12 serving as controls for subsequent bone formation analysis. The remaining six scaffolds were used to determine if the aB assay is influenced by the HA scaffold material.

Passage one cryo-preserved goat bone marrow cells, obtained from an iliac wing biopsy, were thawed and replated in standard culture medium consisting of *alpha*-MEM (Gibco, Scotland) with 15% (v/v) fetal bovine serum (FBS, Gibco), 0.2 mM L-ascorbic acid-2-phosphate (AsAP, Sigma-Aldrich Chemie BV, The Netherlands), 2.0 mM L-glutamine (Life Technologies BV, The Netherlands), antibiotics (100 U/ml each penicillin and streptomycin) and 1ng/ml of basic fibroblastic growth factor (bFGF, Sigma). When confluent, the cells were trypsinized and a cell suspensions of 1.0 $x10^6$ and $2.5x10^5$ cells/ml prepared.

The 12 scaffolds for the aB assay were seeded at various concentrations, with 4 scaffolds seeded at $2.5x10^5$ cells/scaffold and two scaffolds each seeded at 250, 2500, 25000 and $2.5x10^6$ cells/scaffold. The 12 control scaffolds were all seeded at $2.5x10^5$ cells/scaffold. Seeding of all scaffolds was done in pairs in sterile 10 ml tubes. Each scaffold pair was covered with 2 ml of fluid consisting of the

appropriate volume of cell suspension for the desired concentration, made up to 2 ml with standard culture medium as needed. Dynamic seeding for six hours was conducted by placing the tubes on a roller bank at approximately 2 rpm in an incubator at 37 °C and humidified an atmosphere with 5% CO_2. All scaffolds were sub-cultured for 7 days in 25-well bacteriological plates with 3 ml/well of standard culture medium supplemented with 0.1 mM dexamethasone and 0.5 mg/ml β-glycerophosphate (both Sigma).

On days 1, 2, 3, 5 and 7 after seeding, the aB test scaffolds were replenished with medium containing 10% AB. After incubating for 0 (background), 2, 4 and 6 hours, the medium surrounding each scaffold was agitated by repetitive pipetting and 200µl was withdrawn from the aliquots and placed in a 96 well plate. Additionally, 6 non-seeded scaffolds were treated and analyzed identically to the seed scaffolds to determine if the HA material influenced the aB assay. The plate was covered with aluminum foil and placed on the counter for one hour to equilibrate with room temperature. The plate was then analyzed by fluorometer (Perkin-Elmer, USA) as prescribed by the manufacturer of the aB assay. All scaffolds, including controls, were then refreshed with new medium. Eight days after seeding, these same scaffolds were implanted into 6 nude mice with 2 control and 2 aB treated scaffolds of different seeding densities in each mouse.

Scaffolds were removed after six weeks of implantation and fixed overnight in 1.5% glutaraldehyde/0.14M cacodylate buffer (pH 7.2-7.4). After rinsing in PBS, the samples were dehydrated using a graded ethanol series and embedded in methyl-methacrylate (MMA, Merck, Germany) for undecalcified histology. During histological processing, a control scaffold from mouse one was lost. The embedded samples were sectioned at 10µm for light microscopy using a sawing microtome (Leica, Germany) and stained with methylene blue (Sigma) and basic fuchsine (Sigma). Sections were digitized using an Eclipse E600 light microscope (Nikon, Japan) configured with a digital video camera connected to a personal. Four observers judged *in vivo* bone formation within mice by a blinded pair-wise comparison that ranked images from one scaffold as having more, less or similar amounts of bone compared to images from another scaffold. This resulted in 33 comparisons for each observer, 3 for mouse one (lost scaffold) and 6 for each of the other five mice. These 33 comparisons consisted of 5 possible conditions that were tabulated separately: **A**) comparison of a control scaffold to an aB treated scaffold with a lower seeding density, **B**) comparison of a control scaffold to an aB treated scaffold with a higher seeding density, **C**) comparison of two aB treated scaffolds (always different seeding densities), **D**) comparison of a control scaffold

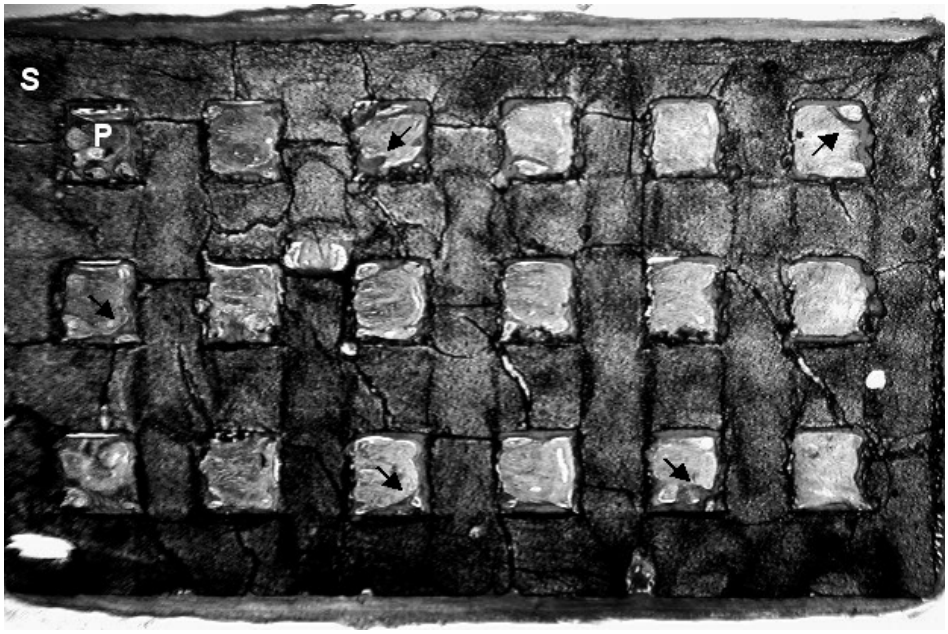

Figure 3.2: Example of histology. The scaffolds (S) forms a continuous lattice containing a 3x6 array of pores (P). Bone is present on the periphery of all pores. Some of this bone is indicated by the black arrows. *(See color image on page 196)*

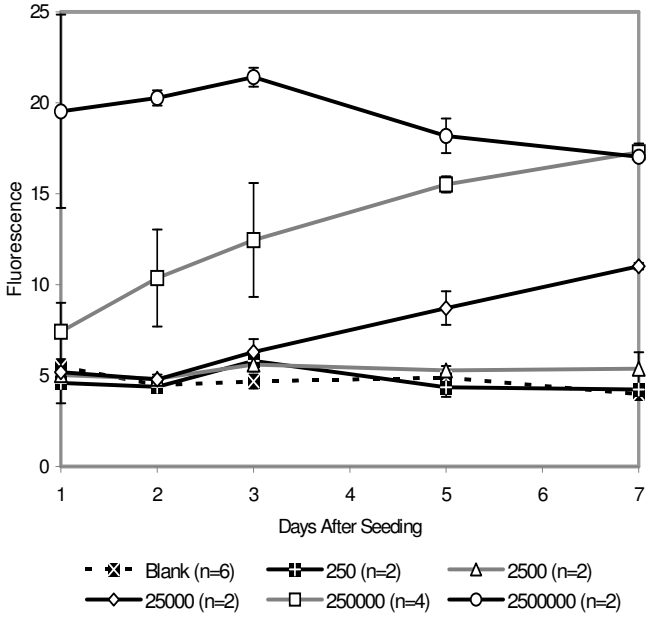

Figure 3.3: alamarBlue™ assay result for the entire 7 day culture period as a function of seeding density. Incubation time = 4 hours. Error bars indicate standard deviation.

to an aB treated scaffold with the same seeding density, and finally **E**) comparison of two control scaffolds (always the same seeding densities).

Separate statistical analyses of evaluation conditions **A**, **B**, **C** and **D** were conducted using a Chi-square Goodness of Fit test assuming a uniform distribution of observations. Similarly, analysis of the combined results of all observations between scaffolds with different seeding densities, evaluation conditions **A**, **B** and **C**, was also performed. Observations were averaged by the number of observers and a significance of 0.05 was set.

Results

Figure 3.3 shows the aB results after 4 hours of incubation for the different seeding densities over the 7 day test period. From day 1 to day 7, the aB assay showed an overall decrease in the cellular activity of scaffolds seeded with $2.5x10^6$ cells and increase in cellular activity for scaffolds seeded with $2.5x10^5$ and $2.5x10^4$ cells. Little response was seen at lower seeding densities. By day 7, the aB readings for scaffolds with the two highest seeding densities, $2.5x10^6$ and $2.5x10^5$ cells/scaffold, were nearly identical. Similar plots were obtained from the 2 and 6 hour incubation times, however, 1 hour of incubation did not adequately resolve the increased activity over the 7 day period of the scaffolds seeded with $2.5x10^4$ cells. The aB assays of the 6 non-seeded scaffolds indicated no influence of the HA material.

An example of the histology in shown in Figure 3.2. Table 3.1 contains scaffold treatments and comparisons made as well as each observers results and the evaluation condition of each comparison. Of the 33 comparisons made, the observers were in complete agreement in 19 comparisons, 3 observers agreed in 8 comparisons and the decision was split in 6 comparisons. In 5 of the 6 split decisions, 2 observers were in agreement on which scaffold contained more bone and the other 2 observers indicated that the bone formation was similar. It should be noted that of the 24 scaffolds implanted 22 exhibited bone formation, although the amount was widely varied. The two scaffolds which did not yield bone were the aB treated scaffolds in mouse 4. As a result, all four observers ranked these scaffolds as similar.

The results for each of the 5 evaluation conditions are contained in Table 3.2 and the statistical analyses of these results in Table 3.3. For evaluation condition **A**, the control scaffolds had higher seeding densities than the aB treated scaffolds. Observers indicated that the controls had more bone formation in 77% of the comparisons. This outcome was statistically significant ($p = 0.015$). Similarly, for

Table 3.1: Raw data showing scaffold treatments, comparisons made to evaluate bone formation, observer results for the comparisons and the evaluation condition of each comparison.

Mouse	Scaffolds compared			Scaffold with more bone (S = same)				Eval. Cond.[2]
	# (SD, cond.)	to	# (SD, cond.)[1]	Obs. 1	Obs. 2	Obs. 3	Obs. 4	
1	1 (2.5×10^5, CT)	to	2 (250, AB)	1	1	1	1	A
	1 (2.5×10^5, CT)	to	4 (2.5×10^5, AB)	4	4	4	4	D
	2 (250, AB)	to	4 (2.5×10^5, AB)	4	4	4	4	C
2	1 (2.5×10^5, CT)	to	2 (25000, AB)	1	1	1	1	A
	1 (2.5×10^5, CT)	to	3 (2.5×10^5, CT)	1	1	1	1	E
	1 (2.5×10^5, CT)	to	4 (2.5×10^5, AB)	S	1	1	S	D
	2 (25000, AB)	to	3 (2.5×10^5, CT)	S	3	S	3	A
	2 (25000, AB)	to	4 (2.5×10^5, AB)	4	4	4	4	C
	3 (2.5×10^5, CT)	to	4 (2.5×10^5, AB)	4	4	4	4	D
3	1 (2.5×10^5, CT)	to	2 (25000, AB)	1	1	1	1	A
	1 (2.5×10^5, CT)	to	3 (2.5×10^5, CT)	1	1	1	1	E
	1 (2.5×10^5, CT)	to	4 (2.5×10^5, AB)	1	1	1	1	D
	2 (25000, AB)	to	3 (2.5×10^5, CT)	3	3	3	3	A
	2 (25000, AB)	to	4 (2.5×10^5, AB)	4	4	4	4	C
	3 (2.5×10^5, CT)	to	4 (2.5×10^5, AB)	3	3	3	S	D
4	1 (2.5×10^5, CT)	to	2 (2500, AB)	1	1	S	S	A
	1 (2.5×10^5, CT)	to	3 (2.5×10^5, CT)	3	3	3	3	E
	1 (2.5×10^5, CT)	to	4 (2.5×10^5, AB)	1	1	S	S	D
	2 (2500, AB)	to	3 (2.5×10^5, CT)	3	3	3	3	A
	2 (2500, AB)	to	4 (2.5×10^5, AB)	S	S	S	S	C
	3 (2.5×10^5, CT)	to	4 (2.5×10^5, AB)	3	3	3	3	D
5	1 (2.5×10^5, CT)	to	2 (2500, AB)	1	1	1	1	A
	1 (2.5×10^5, CT)	to	3 (2.5×10^5, CT)	1	1	1	1	E
	1 (2.5×10^5, CT)	to	4 (2.5×10^6, AB)	4	4	1	4	B
	2 (2500, AB)	to	3 (2.5×10^5, CT)	3	2	2	S	A
	2 (2500, AB)	to	4 (2.5×10^6, AB)	4	4	2	4	C
	3 (2.5×10^5, CT)	to	4 (2.5×10^6, AB)	4	4	S	4	B
5	1 (2.5×10^5, CT)	to	2 (250, AB)	1	1	S	1	A
	1 (2.5×10^5, CT)	to	3 (2.5×10^5, CT)	1	1	S	1	E
	1 (2.5×10^5, CT)	to	4 (2.5×10^6, AB)	4	1	4	4	B
	2 (250, AB)	to	3 (2.5×10^5, CT)	3	3	S	S	A
	2 (250, AB)	to	4 (2.5×10^6, AB)	4	4	4	4	C
	3 (2.5×10^5, CT)	to	4 (2.5×10^6, AB)	S	4	4	4	B

SD = seeding density (cells/scaffolds), Grp = aB for alamarBlue and CT for control
There are 5 evaluation conditions: A = CT scaffold compared to aB scaffold with lower seeding density; B = CT scaffold compared to aB scaffold with higher seeding density; C = Two aB scaffolds with different seeding densities compared; D = CT scaffold compared to aB scaffold with same seeding density; E = Two CT scaffolds compared (same seeding densities).

evaluation condition **B**, the aB treated scaffolds had higher seeding densities than the controls and observers indicated that the aB scaffolds had more bone formation in 75% of the comparisons. However, this effect was not significant. When two aB treated scaffolds of different seeding densities were compared, evaluation condition **C**, observers indicated that the scaffold with the higher seeding density had more bone for 79% of comparisons. This result was statistically significant ($p = 0.044$). However, for evaluation condition **D,** where control and aB treated scaffolds with the same seeding densities were compared, control scaffolds showed more bone in 54% of observations compared to aB scaffolds showing more bone in 29%

Table 3.2: Bone formation observations grouped by evaluation condition.

Bone formation	Obs. 1	Obs. 2	Obs. 3	Obs. 4	Total
Evaluation condition A:					
Control scaffold compared to aB scaffold with lower seeding density					
Control more	10	10	6	8	34
aB more	0	1	1	2	4
Same	1	0	4	1	6
Evaluation condition B:					
Control scaffold compared to aB scaffold with higher seeding density					
Control more	0	1	1	0	2
aB more	3	3	2	4	12
Same	1	0	1	0	2
Evaluation condition C:					
Two aB scaffolds with different seeding densities (SD) compared					
Higher SD more	5	5	4	5	19
Lower SD more	0	0	1	0	1
Same	1	1	1	1	4
Evaluation condition D:					
Control scaffold compared to aB scaffold with same seeding density					
Control more	4	5	4	2	15
aB more	2	2	2	2	8
Same	1	0	1	3	5
Evaluation condition E:					
Two Control scaffolds compared (same seeding densities)					
Different	5	5	4	5	19
Same	0	0	1	0	1

Table 3.3: Statistical analyses for evaluation conditions **A**, **B**, **C** and **D** as well as the pooled results of **A**, **B** and **C**.

	A	B	C	D	A + B + C
Summed observations	34	2	19	15	65
	4	12	1	8	7
Averaged observations (4 observers)	8.50	0.50	4.75	3.75	16.25
	1.00	3.00	0.25	2.00	1.75
Chi-square goodness of fit statistic	5.921	1.786	4.050	0.533	11.681
p-value	0.015	0.181	0.044	0.466	0.001

of observations. However, this difference was not significant. Finally, all but one observation indicated that there was a difference in bone formation when control scaffolds were compared, evaluation condition **E**.

The results of all comparisons between scaffolds with different seeding densities, evaluation conditions **A**, **B** and **C**, were pooled to more sensitively evaluate the impact of seeding density on bone formation. Observations were grouped by seeding density, either higher or lower, and averaged by the number of observers. Observers indicated that the scaffold with higher seeding density had more bone 77% of the time. This is statistically significant ($p = 0.001$).

Discussion and Conclusions

The original goals for this research were twofold: First, to evaluate the potential of aB to observe proliferation of several densities of bone marrow derived cells seeded onto architecturally standardized HA scaffolds. Secondly, to determine whether aB influences bone formation in these scaffolds following implantation.

The aB results for the scaffolds with the two highest seeding densities, and possibly even the next lowest density, appear to be converging to a common value. This suggests that the proliferation rate of cells on the scaffolds with the two highest seeding densities was different and that there is a maximum number of viable cells that can be maintained on these scaffolds. In order to determine this with certainty, the time course of the experiment must be expanded. However, when interpreting these results, one must consider the 3-dimensional nature of the scaffolds and changes in the diffusion kinetics due to cell propagation and extracellular matrix production over the course of this experiment. The aB assay relies on cellular metabolism of the aB indicator. For 2-dimensional cultures and cell suspensions it is reasonable to think that most cells have uniform access to the aB indicator. The aB results for these culture types are, therefore, related directly to cell number. For cultures on 3-dimensional porous substrates this assumption may not be so reasonable. This situation is further complicated over long culture periods as cells and extracellular matrix buildup within the pores of the substrate. The diffusion properties of the cell/scaffold construct are likely to change during the culture period and, therefore, the access of cells to the aB indicator and the diffusion of the metabolized product back to the surrounding medium is also likely to change. Consequently, the contribution cells make to the aB assay may diminish the deeper the cell is within the 3-dimentional construct.

Exposure of the tissue engineered scaffolds to aB certainly did not prevent subsequent bone formation *in vivo*. This is substantiated by 10 of the 12 aB treated scaffold exhibiting bone formation. However, when control and aB treated scaffolds of the same seeding density were compared, evaluation condition **D**, approximately 54% of observations indicated more bone in control scaffolds compared to 29% of observations that indicated more bone in aB treated scaffolds. Although this difference is not significant ($p = 0.466$), the influence, if any, that aB has on the amount of bone formation is difficult to ascertain from the observer data. Other researchers have shown that aB is non-toxic and does not appear to affect the function of lymphocytes in culture[8]. In the current experiment the exposure of cultures to aB was very high, approximately 15% of the 7 day culture period.

Lowering this exposure by minimizing the number of assay points and/or the incubation time may make aB an effective tool for determining a maximum or end-point viability for 3D tissue engineered constructs. Additionally, when standardized scaffolds are used, as in this study, differences in diffusion kinetics are normalized making this assay very useful for monitoring the influence any parameter has on the vitality of 3D cultures *in vitro*. Continuing research with this assay method will determine its true usefulness for tissue engineering studies.

A consequence of the current experimental design is the possibility to compare bone formation in scaffolds with different seeding densities. The idea that seeding density may influence bone formation in tissue engineered constructs may seem intuitive, however, little data has been presented to support this conclusion. Yuan et al. [260] demonstrated that scaffolds seeded with 50,000 cells showed significantly more bone formation compared to scaffolds seeded with 5,000 cells ($p < 0.05$). In the current study, when scaffolds of different seeding densities were compared, the observation that the scaffold with the higher seeding density contained more bone was significantly more common ($p = 0.001$) than the converse observation.

To summarize, aB successfully followed cell proliferation on 3D porous HA scaffolds, although, the diffusion kinetics of the constructs must be considered. The assay appears well suited for determining a maximum or end-point viability for 3D tissue engineered constructs. The influence of in vitro aB treatment on subsequent in vivo bone formation cannot be ruled out but was not shown to be significant in the current study. Finally, higher seeding densities resulted in more observed bone formation.

Acknowledgements

This research was supported by the Dutch Technology Foundation STW under project number UGN.4966. The authors would like to thank Edwin Martens from the Department of Biostatistics at Utrech University for his assistance with the statistical analyses.

4

Scaffolds with a standardized macro-architecture fabricated from several calcium phosphate ceramics using an indirect rapid prototyping technique

C. E. Wilson[1], C. A. van Blitterswijk[3], A. J. Verbout[1], W. J. A. Dhert[1,4] and J. D. de Bruijn[2]

J Mater Sci Mater Med. 2011 Jan;22(1):97-105. Epub 2010 Nov 11

[1] Department of Orthopaedics, University Medical Center Utrecht, P.O. Box 85500, 3508 GA Utrecht, The Netherlands;
[2] Department of Materials, Queen Mary University of London, Mile End Road, London E1 4NS, United Kingdom
[3] Institute for Biomedical Technology, Department of Tissue Regeneration, University of Twente, PO Box 217, 7500 AE, Enschede, The Netherlands
[4] Faculty of Veterinary Medicine, Utrecht University, Yalelaan 1, 3584 CL Utrecht, The Netherlands

Abstract

Calcium phosphate ceramics, commonly applied as bone graft substitutes, are a natural choice of scaffolding material for bone tissue engineering. Evidence shows that the chemical composition, macroporosity and microporosity of these ceramics influences their behavior as bone graft substitutes and bone tissue engineering scaffolds but little has been done to optimize these parameters. One method of optimization is to place focus on a particular parameter by normalizing the influence, as much as possible, of confounding parameters. This is difficult to accomplish with traditional fabrication techniques. In this study we describe a design based rapid prototyping method of manufacturing scaffolds with virtually identical macroporous architectures from different calcium phosphate ceramic compositions. Beta-tricalcium phosphate, hydroxyapatite (at two sintering temperatures) and biphasic calcium phosphate scaffolds were manufactured. The macro- and micro-architectures of the scaffolds were characterized as well as the influence of the manufacturing method on the chemistries of the calcium phosphate compositions. The structural characteristics of the resulting scaffolds were remarkably similar. The manufacturing process had little influence on the composition of the materials except for the consistent but small addition of, or increase in, a beta-tricalcium phosphate phase. Among other applications, scaffolds produced by the method described provide a means of examining the influence of different calcium phosphate compositions while confidently excluding the influence of the macroporous structure of the scaffolds.

Introduction

Calcium phosphate ceramics have seen extensive clinical application as synthetic bone fillers and graft extenders.[35, 36, 183] The biocompatibility as well as osteoconductive and osteoinductive properties of these ceramics have been well documented.[43, 68, 91, 109, 110, 124, 206, 256, 258] Bone Tissue Engineering research has capitalized on these qualities, making porous calcium phosphate ceramics a popular choice of scaffold.[12, 65, 100, 189]

Porous ceramics for medical applications have been manufactured for decades using a variety of traditional methods. Conversion of natural structures, such as coral,[211, 242] and trabecular bone[229] yield porous ceramics with organic architectures that appear very similar to that of the bone that is being replaced. Synthetic manufacturing methods such as foaming,[204, 220, 228] dual-phase mixing[169] and the slip-casting of polymer foams and particles,[31, 233, 250] may also be used to produce porous ceramics. However, conversion and synthetic techniques result in highly complex macroporous structures that are difficult to define quantitatively. Despite the complex nature of the porous ceramics produced by conventional means, quite some information is available regarding the influence the porous structure has on osteoconduction,[26, 79, 119, 120, 125, 135, 155, 218] BMP induced osteogenesis[131, 154, 207, 233] and osteoinduction.[109, 111]

Rapid prototyping (RP), also termed free form fabrication, refers to a variety of technologies capable of producing three-dimensional (3D) physical constructs directly from 3D computer aided models. In recent years, rapid prototyping has been proposed for the production of both scaffolds with controlled porous architectures[122, 128, 252] as well as porous implants with patient specific geometries.[45, 48, 167] Several rapid prototyping techniques have been developed to produce ceramic scaffolds for bone tissue engineering research.[47, 78, 219, 246]

The aim of the current study was to produce porous ceramic scaffolds from different calcium phosphate materials with sufficiently similar macroporous architectures as to be able to reasonably eliminate the macroporous architecture as a confounding variable in future tissue engineering studies. The scaffolds were produced by casting four different calcium phosphate materials into identical molds produced using a rapid prototyping technique. The resulting macroporous structures as well as the chemistry before and after manufacture were evaluated.

Materials and Methods

Scaffold Design and Mold Fabrication

Scaffolds were designed and molds fabricated as described previously.[246] Briefly, the scaffolds specifications called for an interconnecting network of 400 µm square cross-section channels oriented along the orthogonal axes and separated from each other and the exterior by 400 µm. Six, four and three channels were incorporated in the X, Y and Z axis directions, resulting in overall design dimensions of 5.2 x 3.6 x 2.8 mm, respectively. A schematic of such a scaffold is shown in Figure 4.1. Molds, with cavities for the production of six scaffolds each, were designed using the Rhinoceros® computer aided design software (Robert McNeel & Associates, USA). The mold model was scaled to account for shrinkage of approximately 20% during thermal processing demonstrated previously by our hydroxyapatite ceramics. This resulted in pre-thermal processing scaffold dimensions of 6.5 x 4.5 x 3.5 mm in the X, Y and Z axis directions. Multiple copies of the mold were produced using a ModelMaker II rapid prototyping system (Solidscape Inc., USA).

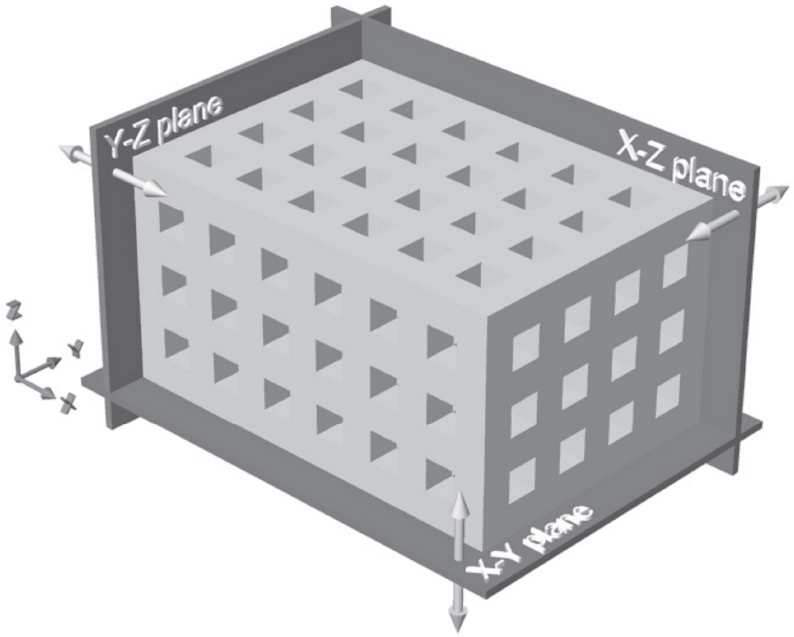

Figure 4.1: Schematic of the designed scaffolds including the three orthogonal planes used to define the scaffold surfaces.

Ceramic Slurries

Ceramic scaffolds were manufactured to achieve four conditions through combinations of calcium phosphate ceramic compositions and sintering temperatures as outlined in Table 4.1. Hydroxyapatite powder (HA, Merck, Germany), beta-tricalcium phosphate powder (TCP, Merck, Germany) and biphasic calcium phosphate powder (BCP, weight% 85/15 HA/TCP, IsoTis SA) were obtained commercially. The HA and TCP raw powders were calcined by heating from ambient to 900 °C at a rate of 100 °C/hour and then cooled naturally with no dwell period. Aqueous slurries of HA, TCP and BCP powders were prepared as previously described for the production of cast plates.[247] In brief, the slurry components detailed below were slowly admixed until a homogenous blend was achieved. The HA and TCP slurries consisted of 67.1 wt% calcined HA powder, 28.6 wt% demineralized water, 2.6 wt% ammonia solution (25%, Merck), 1.5 wt% deflocculant (Dolapix, Aschimmer & Schwarz GmbH, Germany). Once a homogeneous blend was obtained, a CMC binder was added (0.15 wt%, Pomosin BV, The Netherlands) to the HA slurry and the slurry further mixed until homogeneous. The BCP slurry consisted of 56.4 wt% ceramic powder, 37.6 wt% demineralized water, 3.9 wt% ammonia solution and 2.1 wt% deflocculant. No binder was added to the TCP and BCP slurries. All slurries were stored in covered beakers until there use within the same day.

Scaffold Fabrication

The molds were filled using a simple vacuum device.[246] Millex®-GV filter units (25 mm, Millipore S.A., France) were divided in half and the filter paper removed to expose the perforated interior surface. The open face of a mold was carefully placed against the interior surface of a filter half and secured by circumferentially wrapping with wax laboratory film. The mold/filter constructs were attached to 50 ml syringes and flushed with demineralized water. During casting, the beakers containing slurry were placed on a Porex vibrating table (Renfert, Germany). This assisted in mold filling by importing shear energy and thus lowering the viscosity of the pseudoplastic (shear thinning) slurries. The molds were filled by submerging the open face of each mold in slurry and then drawing vacuum pressure using the syringe. The molds were then placed on a sheet wax laboratory film and the syringes and filter halves removed. The molds were allowed to air dry overnight at room temperature and were then further dried for 24 hours at 50 °C in air. Excess slurry from each ceramic composition was processed identically to the molded ceramics to serve as controls when examining material chemistry and to further examine the previously observed influence of the rapid prototyping wax on the material composition.[246]

Table 4.1: Scaffold dimensions, shrinkage, volume, weight and apparent porosity of scaffolds compared to the solids in slurry and sintering temperature during manufacturing.

Material	Solids in Slurry (wt%)	Sintering Temp. (C°)	Exterior Dimensions (mm ± SD)	Shrinkage (from 'as molded', %)	Volume (mm^3 ± SD)	Weight (mg ± SD)	Apparent porosity (% ± SD)
HA h	67.1	1250	x: 5.05 ± 0.05 y: 3.48 ± 0.03 z: 2.73 ± 0.03	x: 22.35 y: 22.68	47.92 ± 0.87	76.16 ± 2.89	49.65 ± 1.76
HA l	67.1	1150	x: 6.14 ± 0.05 y: 4.23 ± 0.13 z: 3.26 ± 0.11	x: 5.48 y: 6.04	84.92 ± 3.17	73.82 ± 5.40	72.39 ± 1.27
BCP	56.4	1150	x: 5.45 ± 0.05 y: 3.73 ± 0.06 z: 2.90 ± 0.06	x: 16.21 y: 7.86	58.96 ± 1.38	48.86 ± 2.33	73.72 ± 1.03
TCP	67.1	1150	x: 6.05 ± 0.04 y: 4.15 ± 0.13 z: 3.21 ± 0.09	x: 6.88 y: 7.86	80.53 ± 3.05	69.49 ± 4.54	72.54 ± 1.10

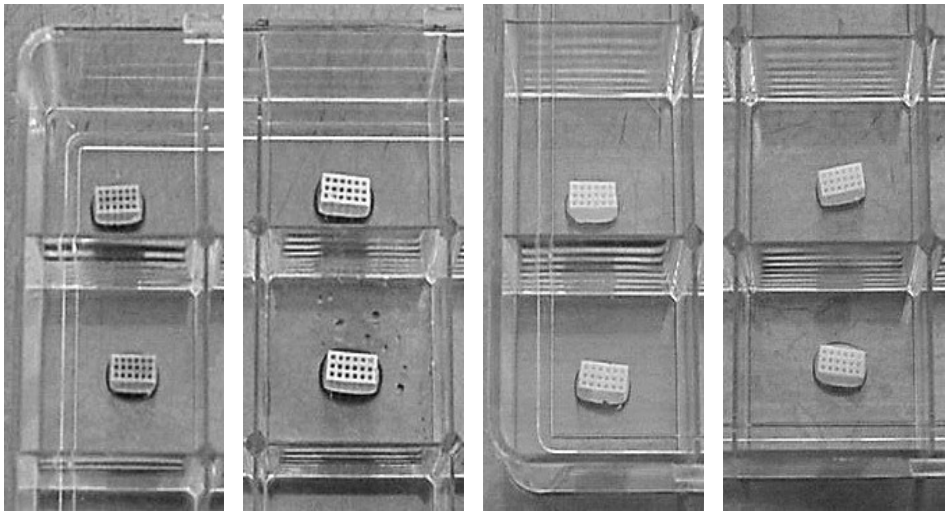

Figure 4.2: The four ceramic compositions all in 25 well plates. Note the similarity of the scaffold structures and the differences in the scaffold colors. *(See color image on page 196)*

Debinding and sintering of the ceramics were performed in two steps in a high temperature furnace (Nabertherm 1400, Germany). Debinding of all ceramics was performed by heating at a rate of 0.5 °C/minute to 400 °C and then cooling naturally with no dwell period. The ceramics were then sintered using a 600 minute heating phase with a 480 minute dwell period at the final sintering temperature followed by natural cooling. One set of HA scaffold was sintered at 1250 °C, designate HA h, while a sintering temperature of 1150 °C was used for a second set of HA scaffolds, designate HA l, as well as all of the TCP and BCP scaffolds. Excess ceramic, occasionally present on the scaffold faces corresponding to the open sides of the molds, was removed using a rotary polisher (LaboPol-5, Struers, Denmark) with 1200 grit waterproof silicon carbide paper (Struers). The ceramics were cleaned by ultrasound for 15 minutes each in acetone, 100% ethanol and deionized water, and then dried in air at 50 °C.

Scaffold Characterization

The exterior scaffold dimensions were measured using a digital caliper (CD-15C, Mitutoyo Ltd., United Kingdom) and used to calculate the shrinkage resulting from the combined debinding and sintering processes. Scanning electron microscopy (SEM, XL 30 ESEM-FEG, Philips, The Netherlands) was used to examine the macro-architecture and surface micro-structure of the scaffolds. The dimensions of the macroporosity were measured in each of the orthogonal planes (Figure 4.1). The apparent porosity of the scaffolds was determined by comparing the apparent density of each scaffold (dry weight / measured volume) and the theoretical density of HA (3.156 g/cm^3),[108] TCP (3.14 g/cm^3) and BCP (85% HA, 15% TCP). The chemistry of raw ceramic powder, calcined ceramic powder, non-molded sintered ceramic and molded scaffolds were evaluated by X-ray diffraction (XRD, Miniflex, Rigaku, Japan). Finally, the potential contamination of the ceramics by residues from the wax mold material was investigated by performing energy-dispersive X-ray spectroscopy (EDX, XL 30 ESEM-FEG, Philips, The Netherlands) on the surface of cast and non-cast (not exposed to wax mold material) ceramics specimens.

Results

The manufacturing process resulted in scaffolds with remarkably similar structural appearances (Figure 4.2). Scaffold dimensions, shrinkage, volume, weight and apparent porosity values are summarized in Table 4.1. The high sintering temperature HA scaffolds exhibited the greatest shrinkage and lowest apparent porosity. The BCP scaffolds also demonstrated considerable shrinkage but maintained a high apparent porosity similar to the low sintering temperature HA

Table 4.2: Pore dimensions by orthogonal plane (refer to Figure 1).

Material	Pore Dimensions (µm ± SD)		
	x-y plane	x-z plane	y-z plane
HA h	x: 286 ± 15 y: 280 ± 16	x: 353 ± 28 y: 339 ± 17	x: 394 ± 24 y: 376 ± 30
HA l	x: 414 ± 44 y: 416 ± 34	x: 470 ± 37 y: 496 ± 21	x: 484 ± 29 y: 486 ± 27
BCP	x: 366 ± 24 y: 377 ± 18	x: 444 ± 47 y: 433 ± 20	x: 432 ± 37 y: 414 ± 42
TCP	x: 405 ± 43 y: 408 ± 33	x: 460 ± 36 y: 486 ± 21	x: 474 ± 29 y: 476 ± 26

and TCP scaffolds. The low sintering temperature HA and TCP scaffolds exhibited the lowest shrinkage. In order to evaluate whether the various treatments influenced the ratio of macroporosity to total porosity, computer models of the porous scaffolds were created using the measured exterior and macropore dimensions in Tables 4.1 and 4.2, respectively. These computer models were used to calculate the approximate volume of the macroporosity. Table 4.3 shows the volumes approximated by the computer models for the various treatments and compares the macroporosity to the apparent porosity. Shrinkage in the z-direction and volumetric shrinkage were not calculated since the respective surfaces were manually polished to remove excess ceramic and therefore do not represent the 'as cast' properties.

Table 4.3: Scaffold volumes and macroporosity calculated form computer model compared to the measured total apparent porosity and other porosity (difference between macro and apparent porosity).

Material	Total Volume (mm^3)	Material Volume (mm^3)	Pore Volume (mm^3)	Macro-porosity (%)	Apparent Porosity (%)	Other Porosity (%)
HA h	47.98	31.78	16.19	33.75	49.65	15.90
HA l	84.67	50.19	34.48	40.72	72.39	31.67
BCP	58.95	34.82	24.14	40.94	73.72	32.78
TCP	80.60	48.08	32.51	40.34	72.54	32.20

SEM images of the resulting scaffolds are shown in Figure 4.3. These scaffolds are discussed in the following text using the axes and orthogonal planes depicted in Figure 4.1. A distinctive texture of parallel ridges and valleys was observed in SEM micrographs on all vertical scaffold surfaces, i.e. surfaces parallel to the x-z and y-z planes. This texture is an impression of the rapid prototyped mold and a consequence of the layer-by-layer manufacturing of the mold. The cross-sectional geometry of the channels was dependant upon the orientation of the channel. Channels running in the x- and y-directions were square in cross section with

textured vertical surfaces and smooth horizontal surfaces. Channels running in the z-direction were rounded with no apparent texturing. Again, this is a consequence of the mold manufacturing process.

The surface microporosity of the scaffolds, as observed by SEM, varied with material composition and sintering temperature (Figure 4.3). The BCP scaffolds exhibited a spectrum of surface microporosity features from approximately 1 to 10 µm in size. The surface features of the low sintering temperature HA scaffolds were similar to the BCP with perhaps somewhat less and smaller surface microporosity, approximately 0.5 to 5 µm. The high sintering temperature HA scaffolds exhibited smoother surfaces with very little microporosity. The TCP material, in contrast to the other materials sintered at low temperatures, appeared very similar to the high sintering temperature HA with very little surface microporosity.

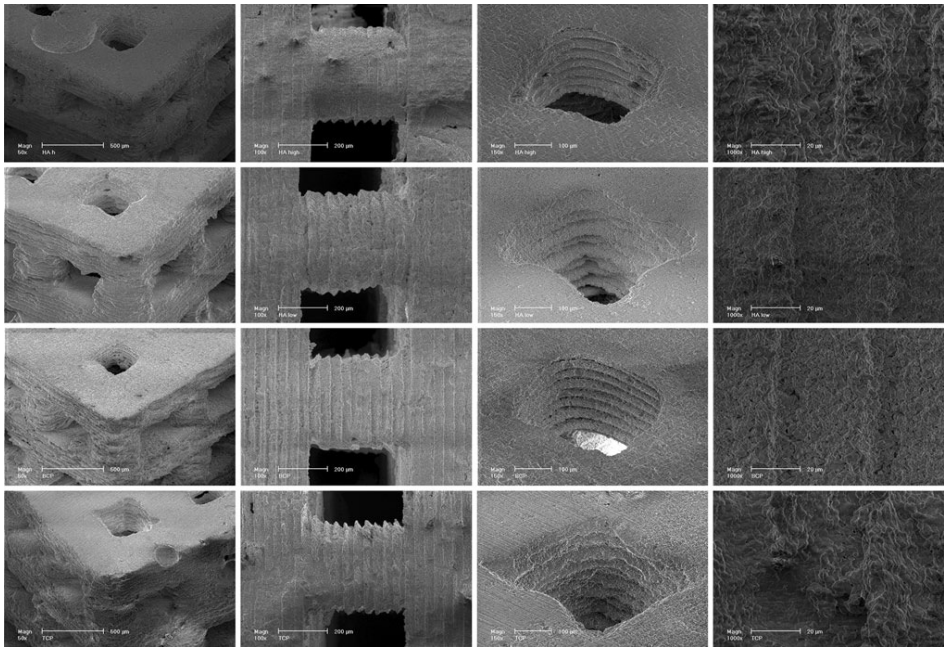

Figure 4.3: SEM micrographs of the four scaffold materials. Rows top to bottom: HA h, HA l, BCP and TCP. First column: Perspective view of scaffolds at 50X magnification (bar = 50 µm). Second column: Scaffold structures at 100X magnification (bar = 200 µm). Note the regular surface texture on the scaffolds. Third column: Scaffold pores at 150X magnification (bar = 200 µm). Fourth column: Scaffold surfaces at 1000X magnification (bar = 20 µm).

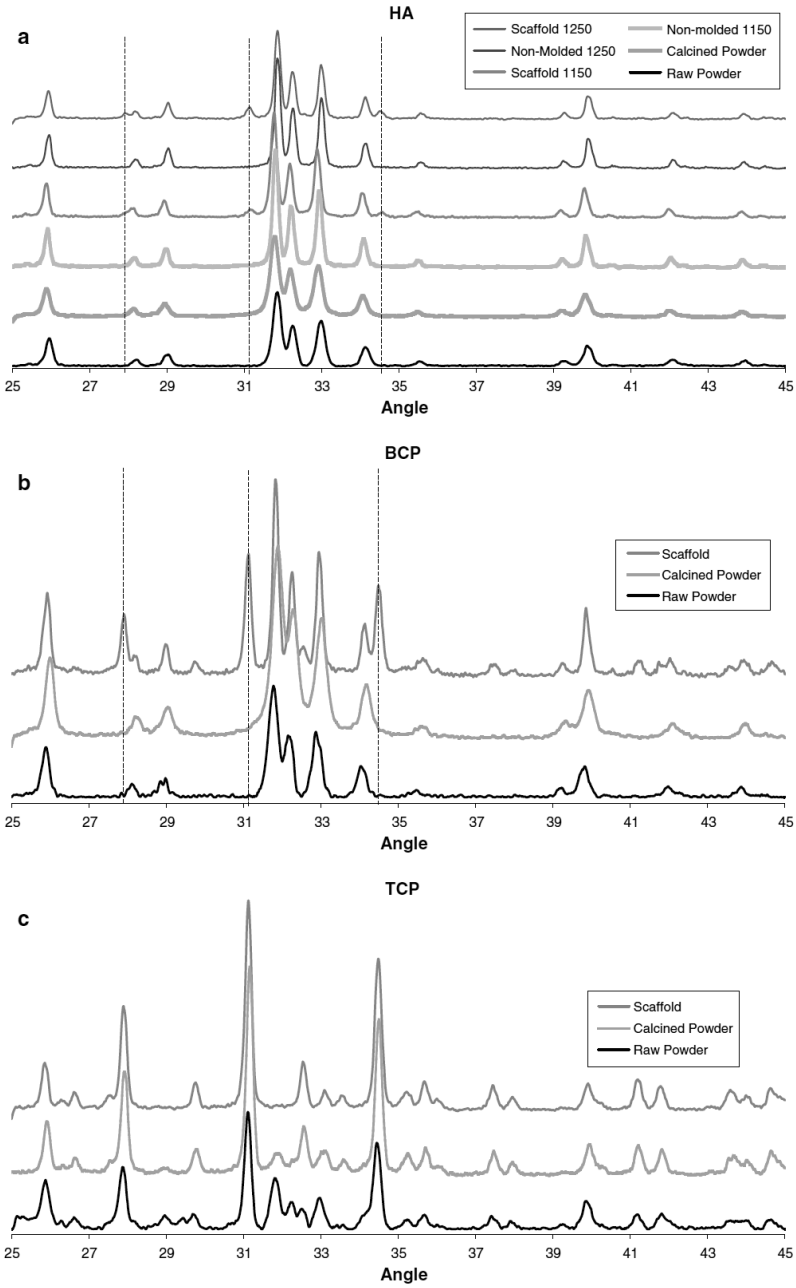

Figure 4.4: XRD patterns of **a**)HA h (1250) and HA l (1150), **b**) BCP and **c**) TCP. Shown are XRD patterns of the raw powder, calcined powder and molded ceramics (scaffolds). XRD patterns of non-molded ceramics are also shown in **a**) for the HA h (1250) and HA l (1150) materials. Vertical dotted lines indicate additional peaks associated with beta-TCP formation that are only present in the molded specimens (scaffolds).

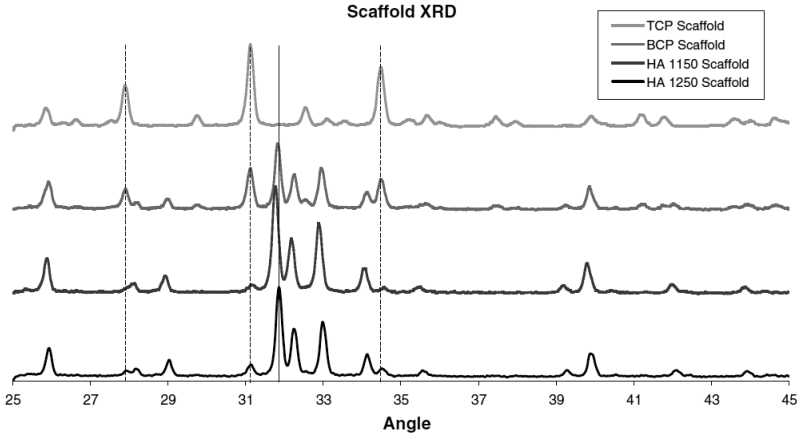

Figure 4.5: XRD patterns of the four scaffold materials. Vertical dotted lines indicate beta-TCP peaks which form in the HA and BCP material as a result of the molding process.

The XRD patterns for the different ceramic chemistries, shown in Figure 4.4, were generally as expected. Figure 4.4a shows the patterns for the HA ceramic raw powder, calcined powder, non-molded material sintered at 1150 ℃, scaffolds sintered at 1150 ℃, non-molded material sintered at 1250 ℃, and scaffolds sintered at 1150 ℃. Several peaks associated with TCP formation were observed in the patterns for the cast HA scaffold materials at both the 1150 ℃ and 1250 ℃ sintering temperatures (vertical lines in Figure 4.4a). The BCP ceramics also demonstrated these TCP peaks in the cast scaffolds (Figure 4.4b, vertical lines). The TCP ceramics exhibited changes, relative to the raw powder, that were consistent with the calcination and sintering process temperatures (Figure 4.4c). The XRD patterns for the four scaffold conditions are shown in Figure 4.5 for clarity. EDX of the surfaces of both cast and non-cast ceramic specimens showed identical spectra consistent with the calcium phosphate materials. There was no evidence of contamination from the wax mold material.

Discussion and Conclusions

The present study demonstrates the application of Computer Aided Design and Rapid Prototyping technologies for the production of ceramic scaffolds from different chemistries but with defined, virtually identical, macro-architectures. Other than producing macroporosities with pore dimension in the range suggested in the literature for osteoconduction, i.e. between 50 to 500 mm,[26, 43, 120, 125, 218] we did not attempt to produce optimal or ideal porous structures. The purpose of this study was to manufacture porous scaffolds in which the macroporous architecture was designed and sufficiently similar to be able to reasonable exclude the macroporous architecture as a confounding variable in future research studies. The material

chemistries and thermal processing methods employed in this study were chosen to provide continuity with materials used in past and ongoing research.[94, 146, 150, 153, 246, 247]

Although the visual appearance of the scaffolds was similar with regard to structure, there were differences in shrinkage and therefore the macroporous dimensions. As expected from our previous work, a sintering temperature of 1250 ℃ resulted in a shrinkage of just over 22% for the HA material compared to approximately 6% shrinkage for HA and TCP sintered at 1150 ℃. The relatively large shrinkage of 16 to 17 % for the BCP scaffolds, also sintered at 1150 ℃, can almost completely be accounted for by the lower solids loading of the BCP slurry (56.4 wt%) compared to the HA and TCT slurries (67.1 wt%). The lower solids loading was necessary to achieve appropriate rheological properties for the casting of scaffolds from slurries of the non-calcined BCP powder. Interestingly, the apparent porosity of BCP scaffolds was very similar to the TCP and low sintering temperature HA scaffolds despite the much higher shrinkage (Table 4.2). Comparing the porosity resulting from the measured macroporous structure to the total apparent porosity, Table 4.3, reveals that the a much greater proportion of the apparent porosity of the high sintering temperature HA is likely due to the macroporosity compared to the lower sintering temperature materials. This indicated greater densification due to the higher sintering temperature. The BCP, TCP and low sintering temperature HA all had similar proportions of macroporosity despite the much higher shrinkage of the BCP material.

The texture exhibited on the vertical surfaces of the scaffold (ref. Figure 4.1), as well as the rounded nature of the macropores in the z-direction, are a consequence of the rapid prototyping technique used to manufacture the molds. This technique jets molten droplets of wax material, which flatten and spread when they strike the surface, to build each layer of the molds. As molds are built up vertically layer by layer, this results in a texture on the vertical surfaces (x-z and y-z planes) which is subsequently cast into the ceramic. The rounded corners of channels running in the z-direction (cross-sections parallel to the x-y plane) result from the coalescing or pooling of adjacent droplets prior to solidification, resulting in rounding of both inside and outside corners within the printed layers. These rounded mold corners are then cast into the resulting ceramic scaffolds and observed in channels running parallel to the z-direction.

Compositional analyses by XRD were largely as expected. The XRD patterns for the HA and BCP scaffolds indicated that a TCP phase had been introduced. Since the XRD patterns of the non-molded specimens did not show the TCP phase and

the molded and non-molded materials were treated identically with the exception of the molding process, it is likely that the presence of TCP phase after molding results from the exposure of the HA and BCP materials to the wax mold material itself, despite elemental analysis of cast and non-cast specimens demonstrated there was no direct contamination of the ceramics by the mold material. The mechanism for this is not clear but is consistent with our previous findings for HA materials.[246]

In conclusion, we have demonstrated a rapid prototyping method for fabricating ceramic scaffolds with virtually identical, 3-dimensional, macroporous architectures from different calcium phosphate ceramics. Scaffolds produced by this method will not only enhance research aimed at optimizing macroporous architectures and material compositions but will improve many other aspects of tissue engineering research by eliminate differences in macroporous structure as a confounding variable.

Acknowledgements

The authors would like to thank The Netherlands Technology Foundation for financial support (grant UGN.4966). We also thank Ellen van Leeuwen (Technical University of Eindhoven) and Dr. ShiHong Li (IsoTis N.V.) for their assistance.

5

Comparison of four calcium phosphate ceramic scaffolds with standardized macro-architectures in a bone tissue engineering model

C. E. Wilson[1], M. C. Kruyt[1], C. A. van Blitterswijk[3], A. J. Verbout[1], J. D. de Bruijn[2] and W. J. A. Dhert[1,4]

[1] Department of Orthopaedics, University Medical Center Utrecht, P.O. Box 85500, 3508 GA Utrecht, The Netherlands;
[2] School of Engineering & Materials Science, Queen Mary University of London, Mile End Road, London E1 4NS, United Kingdom;
[3] Institute for Biomedical Technology, Department of Tissue Regeneration, University of Twente, PO Box 217, 7500 AE, Enschede, The Netherlands;
[4] Faculty of Veterinary Medicine, Utrecht University, Yalelaan 1, 3584 CL Utrecht, The Netherlands

Abstract

Calcium phosphate ceramics are commonly applied as bone graft substitutes and are therefore a common choice as scaffold material for bone tissue engineering. The chemical composition, macroporosity and microporosity of these ceramics are known to influence their behavior as bone graft substitutes and bone tissue engineering scaffolds. In this investigation, a rapid prototyping technique was used to fabricate scaffolds with nearly identical structures and macroporous architectures from four different calcium phosphate chemistries, HA prepared at high and low sintering temperatures, BCP and TCP. Bone marrow stromal cells from 10 Dutch milk goats were culture expanded. Single scaffolds of each material type were per-operatively seeded with bone marrow stromal cells in autologous blood plasma and implanted autologously in individual intramuscular pockets in the paraspinal muscles. Control scaffolds seeded only with autologous plasma were also implanted. Fluorochrome markers were administered at 3, 5 and 7 weeks to monitor the bone formation dynamics and the animals were sacrificed at 9 weeks after implantation. The addition of cells to TCP scaffolds dramatically increased the amount of degradation observed during the implantation period. In 6 of 10 animals, both the BCP and low sintering temperature HA (HAl) scaffolds yielded remarkably similar bone formation. Light and epifluorescent microscopy demonstrated that bone formation typically originated on scaffold surfaces, regularly from the textured surface resulting from the manufacturing technique, and progressed into the pore space. No other scaffold conditions yielded bone.

Introduction

Calcium phosphate (CaP) ceramics, due to their compositional similarity to bone mineral, have been commonly applied as bone graft substitutes. The biocompatibility[70], osteoconductive[43, 91, 124] and osteoinductive[20, 206, 257, 261] qualities of these ceramics have been well established. These same characteristics have also made CaP ceramics a popular choice of scaffold material for bone Tissue Engineering (TE) research. However, despite almost two decades of work[100, 189], little progress has been made toward the clinical application of bone TE using the combination of bone marrow stromal cells (BMSCs) and porous CaP ceramic scaffolds. Scaling bone TE toward clinically relevant sized grafts will require a greater understanding of the complex interactions between the biological and biomaterial components of scaffold based bone TE and how these interactions, within the recipient environment, may be utilized and optimized to achieve desirable outcomes. Of the many parameters that influence these interactions, the biomaterial composition and porous structure of the scaffolds are among the few that we can manipulate directly.

Typically, the porous CaP ceramics used clinically as bone graft substitutes and as scaffolds for bone TE research have been produced by either conversion or conventional, non-designed based synthetic techniques. Conversion methods start with a naturally occurring structure, such a coral[211, 242] or trabecular bone,[171, 229] and converted these to the final composition while maintaining the original architecture. Conventional synthetic techniques include the foaming of ceramic slurries,[204, 220, 228] slip casting of polymer sponges,[250] addition and subsequent removal of organic porogens in ceramic powders[31, 233] and dual-phase mixing of polymer and ceramic slurries.[169] The macroporous architectures that result from these processes are not constrained by design but rather reflect the uncertainty of the processes themselves in their structure. Indeed, the complex nature of these structures makes them difficult to define quantitatively.[118]

Rapid prototyping (RP) refers to a variety of technologies capable of producing three-dimensional (3D) physical models from 3D computer data sets. The use of RP techniques have been extensively discussed as methods for producing scaffolds with defined architectures[122, 128, 252] as well as porous implants with patient specific geometries.[45, 48, 167] Several RP techniques have been developed to produce CaP ceramic scaffolds for bone tissue engineering research.[47, 78, 219, 246] Typically, there have been two purposes of using RP methods to produce TE scaffolds with designed porous structures; either to enable the controlled manipulation of the porous structure to examine the influence on the bone TE or

simply to provide a reference scaffold with consistent size, shape and porous architecture.[246]

In the present study we examine ectopic (intramuscular) bone formation, with and without added BMSCs, in scaffolds with a single, designed, macroporous structure produced from four different calcium phosphate materials using a rapid prototyping technique[246]. Use of sequential fluorochrome labeling enabled the dynamics of the bone formation to be evaluated and compared to bone formation in orthotopic model systems using the same calcium phosphate materials[247].

Materials and Methods

Experimental design

Approval was obtained from the Institutional animal care committee for a study in 10 adult Dutch milk goats. Bone marrow was harvested from each goat and the colony forming efficiency (CFE) of the aspirates determined. The BMSCs were culture expanded for two passages and then cryopreserved. Scaffolds with standardized porous architectures were prepared from four calcium phosphate chemistries. Per-operatively, just prior to implantation, autologous BMSCs were thawed, re-suspended in autologous blood plasma and seeded onto the scaffolds. Control scaffolds were seeded with plasma alone. One seeded and one control scaffold of each of the four materials were separately implanted bilaterally in intramuscular pockets in the paraspinal muscles of the 10 goats. To monitor the bone formation over time, fluorochrome markers were administered at 3, 5 and 7 weeks and the animals were sacrificed at 9 weeks after implantation. Bone formation was investigated by histology using epifluorescent and light microscopy.

Scaffolds

Manufacture and characterization of the ceramic scaffolds used in this study has been described in detail elsewhere.[244, 246] Briefly, wax molds, with cavities for the production of six scaffolds each, were designed using the Rhinoceros® computer aided design software (Robert McNeel & Associates, USA) and manufactured using a ModelMaker II rapid prototyping system (Solidscape Inc., USA). The molds were designed to create “as cast” scaffolds with an interconnecting network of 500 µm square cross-section channels oriented along the orthogonal axes and separated from each other and the exterior by 500 µm. Six, four and three channels were incorporated in the X, Y and Z axis directions resulting in overall dimensions of 6.5 x 4.5 x 3.5 mm, respectively. Four scaffold material conditions were achieved through combinations of calcium phosphate ceramic compositions and sintering temperatures. Aqueous slurries of hydroxyapatite powder (HA,

Merck, Germany), beta-tricalcium phosphate powder (TCP, Merck, Germany) and BCP powder (HA/TCP, weight% 85/15, IsoTis SA) were prepared, cast into the molds and dried. One set of HA scaffolds was sintered at 1250 °C, designate HAh, while a sintering temperature of 1150 °C was used for TCP, BCP and a second set of HA scaffolds, designate HAl. The resulting overall scaffold and pore dimensions were measured. Samples were evaluated by FTIR and XRD analysis to verify composition and phase purity. Characterization of surface features and microporosity was conducted with a scanning electron microscope (SEM; XL30 ESEM-FEG, Philips, Eindhoven, The Netherlands).

BMSCs culture and seeding conditions

After approval of the local animal care committee, ten adult female Dutch milk goats (24–36 months) were obtained at least 4 weeks prior to surgery. Bone marrow was aspirated (15 ml per iliac wing) as previously described, together with 100 ml venous blood for the preparation of Autologous Serum (AS)[149]. The venous blood was allowed to clot over night in a sterile bottle. The serum was then drawn off, heat inactivated for 30 min at 56-58 °C, filtered through a 0.2 µm filter and then frozen until use[149]. The proportion of BMSCs in the bone marrow aspirate was assessed by a colony forming efficiency (CFE) assay by culturing a fraction of the nucleated cells from each bone marrow aspirate[86]. The remainder of the aspirate was plated and cultured according a standardized protocol to retrieve and expand the BMSCs [149]. After the 2nd passage, the BMSCs were cryopreserved in 1 ml aliquots of 10^7 cells[254]. On the day of surgery, the frozen AS was thawed to 4 °C. The cryopreserved BMSCs were then thawed on ice, thoroughly washed with AS and finally re-suspended in AS at a concentration of 10^6 cells/ml. Cell viability was assessed by trypan blue exclusion method. Iced aliquots of 5.5 ml (5.5 x 10^6 BMSCs) were taken to the operating room. During surgery, the suspension was centrifuged at 300g, the supernatant decanted and the pellets re-suspended in 1 ml of autologous plasma that had been derived by ultracentrifugation of 10 ml peripheral blood[254]. Each scaffold was then drop-seeded with 76 µl of plasma, with or without BMSCs. This resulted in approximately 8 x 10^6 BMSCs/cm^3 of scaffold for the cell seeded condition. The plasma was allowed to clot on the scaffolds prior to implantation.

Surgical model and fluorochrome labeling

The surgical procedures were performed under standard conditions [149, 247]. After shaving and disinfecting the dorsal thoracolumbar area, a midline skin incision from T10-L5 was made to expose the paraspinal muscles. This allowed implantation of the intramuscular implants as well as spinal and iliac wing implants that will not be

discussed in the present paper. Bilateral intramuscular pockets were created by blunt dissection following separate fascia incisions in the paraspinal muscles (L1-3). Seeded and control scaffolds of each of the four materials were individually inserted into the pockets according a randomized scheme for a total of 8 implants per goat. The muscle fascia was closed with a non-resorbable suture to enable the implantation sites to be located for implant retrieval. The subcutis and skin were closed separately. Postoperative pain relief was provided by Buprenorphin (Shering-Plough, The Netherlands). Sequential fluorochrome markers were administered at three (Calcein Green, 10 mg/kg intravenously, Sigma, The Netherlands); five (Oxytetracyclin, Engemycine 32 mg/kg intramuscularly, Mycofarm, The Netherlands) and 7 weeks (Xylenol Orange, 80 mg/kg intravenously, Sigma, The Netherlands). At 9 weeks, the animals were killed by an overdose of pentobarbital (Organon, Oss, The Netherlands)[146].The implants were located using the non-resorbable sutures as a guide. The scaffolds were then carefully excised with a small amount of surrounding paraspinal muscles to minimize the potential risk of damage during explantation.

Histological processing and histomorphometry

The explanted samples were fixated in a solution of 4% glutaraldehyde and 5% paraformaldehyde. The samples were then dehydrated by ethanol series and embedded in methyl-methacrylate (MMA, Merck, Germany). After polymerization, the embedded samples were sectioned at ±10μm using a sawing microtome (Leica, Germany). Stained and unstained sections were evaluated using a light/fluorescent microscope (E600, Nikon, Japan) equipped with a quadruple filter block (XF57, dichroic mirror 400, 485, 558 and 640 nm, Omega Optics, The Netherlands). Sections stained with methylene blue and basic fuchsine (both Sigma-Aldrich) were observed by light microscopy to evaluate general tissue response and bone formation within the scaffolds. Unstained sections were observed by epifluorescence microscopy, using the quadruple filter block, to evaluate the presence or absence of the each of the fluorochrome labels, indicating the presence or absence of mineralizing tissue at the time the fluorochrome labels were administered. High resolution digital images of unstained sections were pseudocolored using Adobe Photoshop software, with the bone being colored red, the scaffold yellow, the pore space black and all else white. Histomorphometry was performed using KS400 software (version 3, Zeiss, Nussloch, Germany). A custom macro was developed to measure the total area, scaffold area, bone area, scaffold perimeter, bone perimeter and bone-to-scaffold contact length on the pseudocolored images. This data was used to calculate the pore area (Pore Area = Total Area – Scaffold Area), percent bone apposition (Contact% = [bone-to-scaffold contact length ÷ scaffold perimeter] × 100%) and

percent of bone area relative to available pore area (Bone Area % = [[Bone Area] ÷ [Total Area – Scaffold Area]] × 100%).

Results

Scaffolds

Characterization of the materials used in this study has been described in detail elsewhere.[244] The following is a brief summary of the results. Figure 5.1 depicts the scaffolds that were used for a single goat implantation in this study. Under SEM, the distinctive texturing of ridges parallel to the top and bottom surfaces of the scaffolds was noted as previously described (Figure 5.2)[244, 246]. This texturing is a

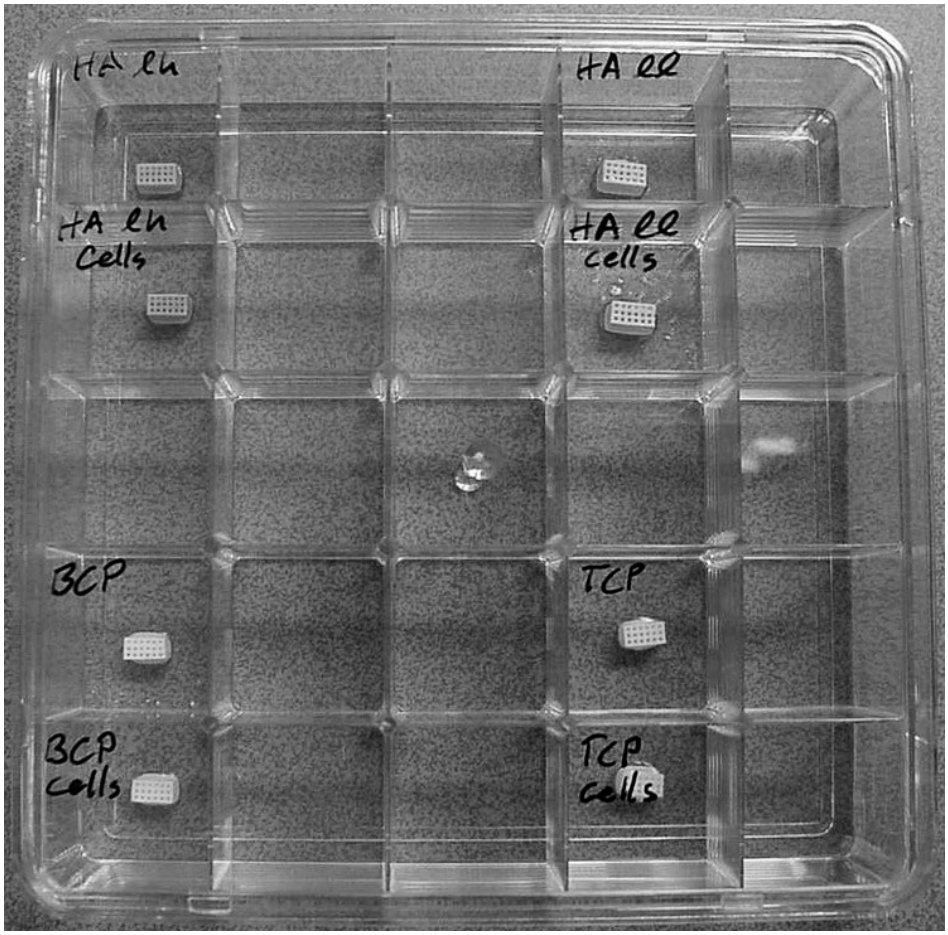

Figure 5.1: The four ceramic compositions in a 25 well plate. Note the similarity of the scaffold structures and the differences in the scaffold colors. *(See color image on page 197)*

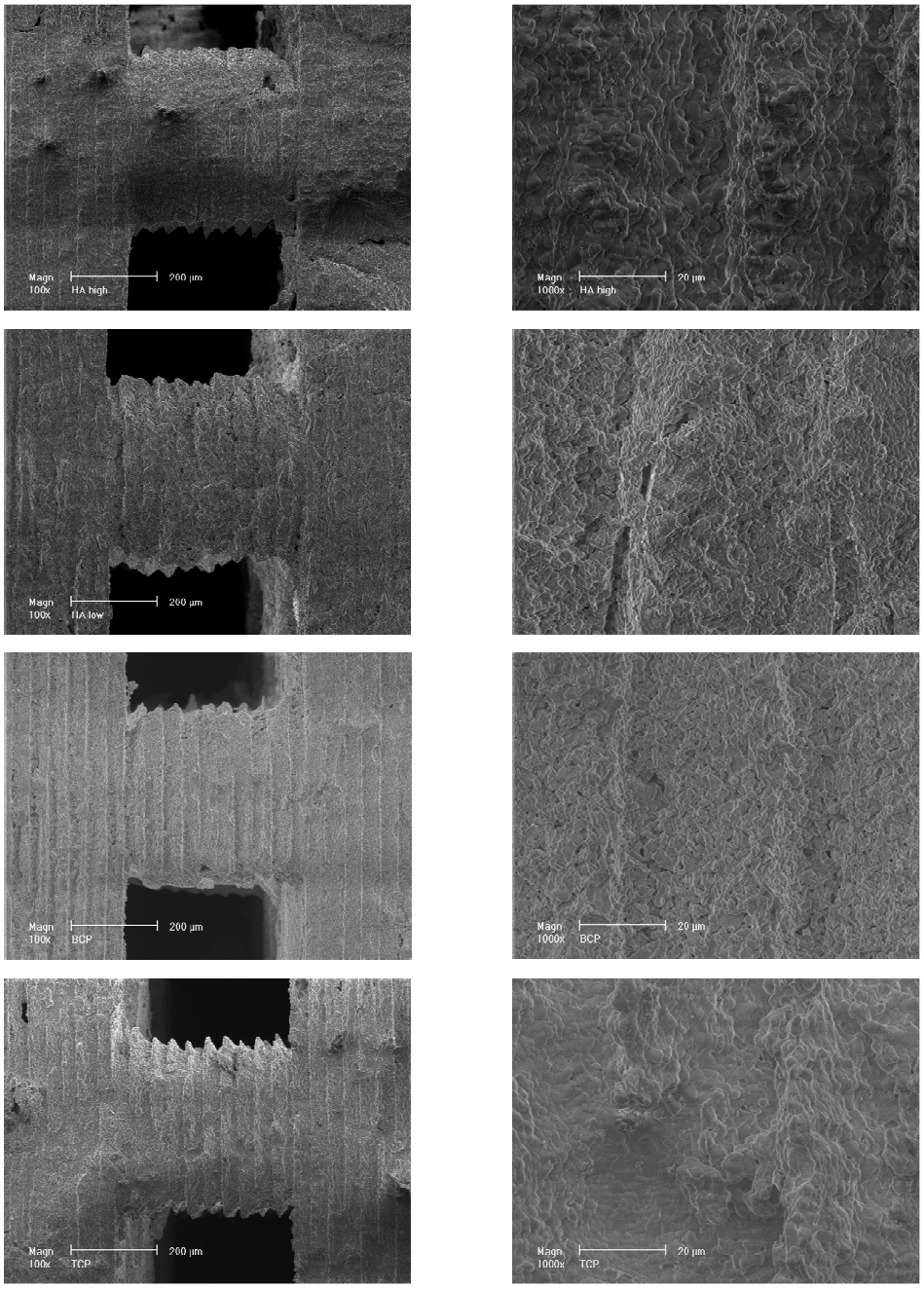

Figure 5.2: SEM micrographs of the four scaffold materials. From top to bottom: HA h, HA l, BCP and TCP. Left column: Scaffold structures at 100X magnification (bar = 200 µm). Note the regular surface texture on the scaffolds. Right column: Scaffold surfaces at 1000X magnification (bar = 20 µm).

Table 5.1: Slurry composition and sintering temperatures of scaffolds during manufacture compared to resulting scaffold weight, dimensions, shrinkage and apparent porosity.

Material	Ceramic in Slurry (wt%)	Sintering Temp. (C°)	Weight (mg±SD)	Exterior Dimensions (mm±SD)	Pore Dimensions (µm)	Shinkage (%)	Apparent Porosity (%±SD))
HA h	67.1	1250	76.16 ± 2.89	x: 5.05 ± 0.05 y: 3.48 ± 0.03 z: 2.73 ± 0.03	top: 283 ± 16 side: 361 ± 32	x: 22.35 y: 22.68	49.65 ± 1.76
HA l	67.1	1150	72.82 ± 5.40	x: 6.14 ± 0.05 y: 4.23 ± 0.13 z: 3.26 ± 0.11	top: 415 ± 39 side: 484 ± 31	x: 5.48 y: 6.04	72.39 ± 1.27
BCP	56.4	1150	78.86 ± 2.33	x: 5.45 ± 0.05 y: 3.73 ± 0.06 z: 2.90 ± 0.06	top: 372 ± 22 side: 432 ± 38	x: 16.21 y: 17.86	73.72 ± 1.03
TCP	67.1	1150	69.49 ± 4.54	x: 6.05 ± 0.04 y: 4.15 ± 0.13 z: 3.21 ± 0.09	top: 407 ± 38 side: 474 ± 30	x: 6.88 y: 7.86	72.54 ± 1.10

result of the layer-by-layer rapid prototyping production process for the molds. Table 5.1 summarizes the scaffold compositions and sintering temperatures, measurements of the scaffold weights and dimensions as well as calculations for shrinkage and porosity. Differences in the sintering temperature, chemistry and slurry composition resulted in the different shrinkage characteristics of the ceramics. The surface microporosity of the scaffolds, as observed by SEM, also varied with material composition and sintering. The low sintering temperature HA and BCP scaffolds exhibited a similar spectrum of surface microporosity features ranging in size from approximately 1 to 10 µm for BCP and 0.5 to 5 µm for the HA. The high sintering temperature HA scaffolds exhibited smoother surfaces with very little microporosity. The TCP material, in contrast to the other low sintering temperature materials, appeared very similar to the high sintering temperature HA with very little surface microporosity. XRD and FT-IR analyses verified the composition and phase purity of the ceramics with the exception of several small peaks, associated with ß-TriCalcium Phosphate (ß-TCP) formation, in the HA (high and low sintering temperature) and BCP materials as previously described[244, 246].

In vitro results

The bone marrow aspirates yielded 5.6±1.5x10^6 (Mean±SD) nucleated cells/ml. The colony forming efficiency was 1.9±0.6 colonies per 100.000 cells. The adherent BMSCs proliferated well with a doubling time of 1.2±0.6 days. This allowed cryopreservation of 60–100 million BMSCs within 3 weeks after obtaining the aspirates. Trypan blue exclusion after thawing the cells indicated <5% dead cells. Following the per-operative re-suspension of cells in plasma, the plasma remained in a liquid state for 10–20 min before polymerizing, allowing good

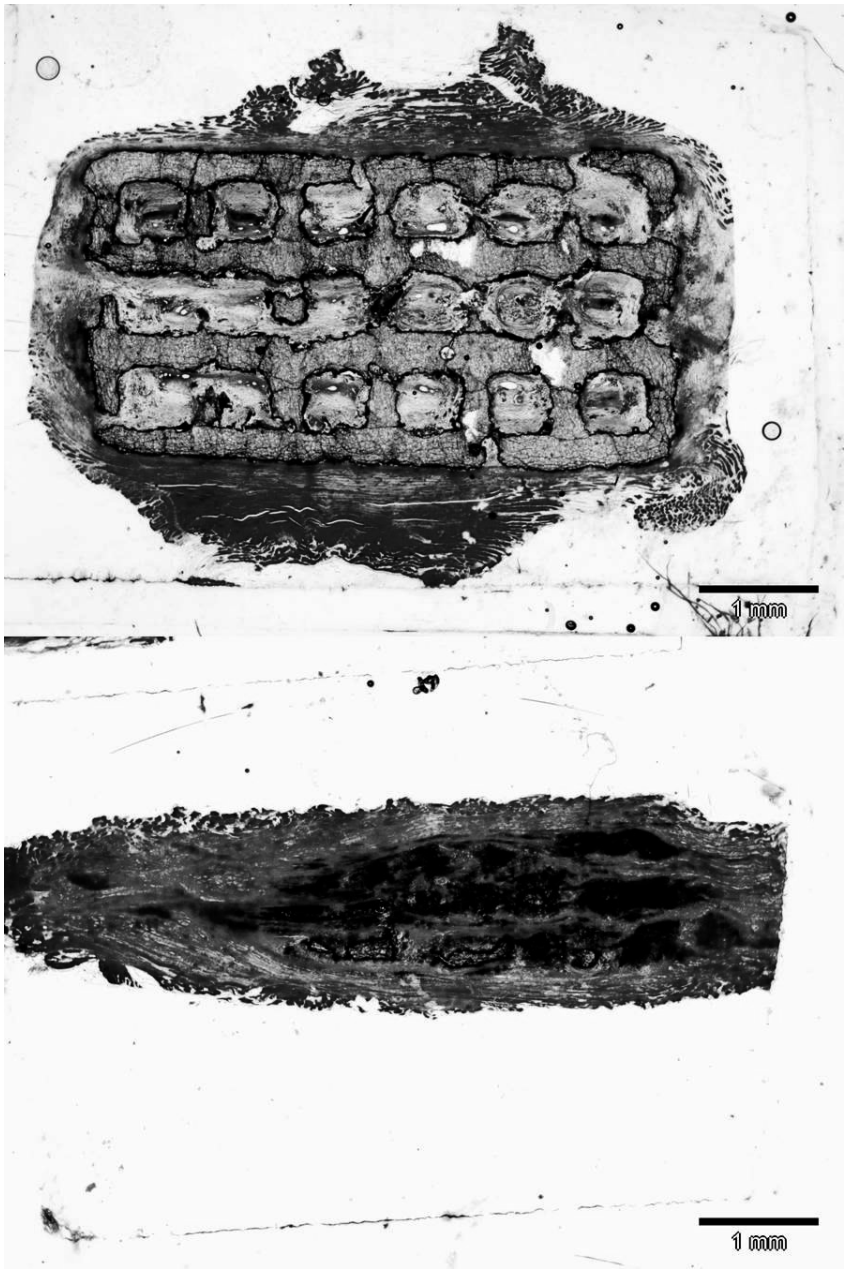

Figure 5.3: Light micrographs of methylene blue/basic fuchsin stained histological sections of TCP scaffolds with (top) and without (bottom) cells. This pattern of degradation was present in 9 of 10 pairs of TCP scaffolds. *(See color image on page 198)*

penetration of the scaffolds. SEM imaging and stereo microscopy of methylene blue stained constructs showed a homogeneous distribution of spherical cell aggregates throughout the interior of the scaffolds with more dense layers of cells at the upper and lower peripheries.

In vivo results.

All animals recovered well within two days of surgery and survived the follow-up period without difficulties. One of the 80 scaffolds implanted, a BCP scaffold without cells, could not be recovered at explantation.

Histology showed no signs of infection or adverse tissue reactions. All scaffolds remained largely intact with the exception of TCP. When not seeded with cells, TCP showed signs of degradation, demonstrated by enlargement and rounding of the pores as well as the loss of the surface texture. When seeded with cells, TCP was notably more degraded and, in all but one case (9/10), lost the typical orthogonal structural characteristics (Figure 5.3). Only the HAI and BCP materials seeded with cells showed bone formation, all other conditions did not exhibit bone. The HAI and BCP materials seeded with cells showed bone formation in 6 out of 10 animals, (Figure 5.4) and the bone formation was always paired, i.e. 6 goats exhibited bone formation in both these materials, 4 goats exhibited no bone formation in any scaffold. Mineralized bone tissue was in direct contact with the scaffold surface and frequently budded away from scaffold surfaces and bridged channels. Budding bone formation appeared to preferentially originate from the textured surfaces resulting from the rapid prototyping technique. Histomorphometry of the HAI and BCP materials containing bone yielded bone Area % values of 7.52 ± 3.94 and 10.54 ± 5.54, respectively (mean ± standard deviation), and Contact %s of 17.32 ± 9.03 and 16.24 ± 8.41, respectively (mean ± standard deviation). Neither bone Area % nor Contact % for the HAI and BCP materials were significantly different (Student's t-test, $\alpha = 0.05$). Epifluorescence microscopy of unstained sections of scaffolds containing bone demonstrated the dynamics of the bone formation. The early 3-week label, Calcein Green, was visible and observed closest, often directly apposed, to the scaffold surface. The 5-week label, Oxytetracyclin, and 7-week label, Xylenol Orange, were present and sequentially more distant from the surface, indicating surface mediated centripetal bone formation (Figure 5.5). This demonstrated the nucleation of bone formation at distinct sites on the scaffold surface which then progressed toward the pore interiors. This type of bone morphology was also evident in the stained histology (figure 5.4).

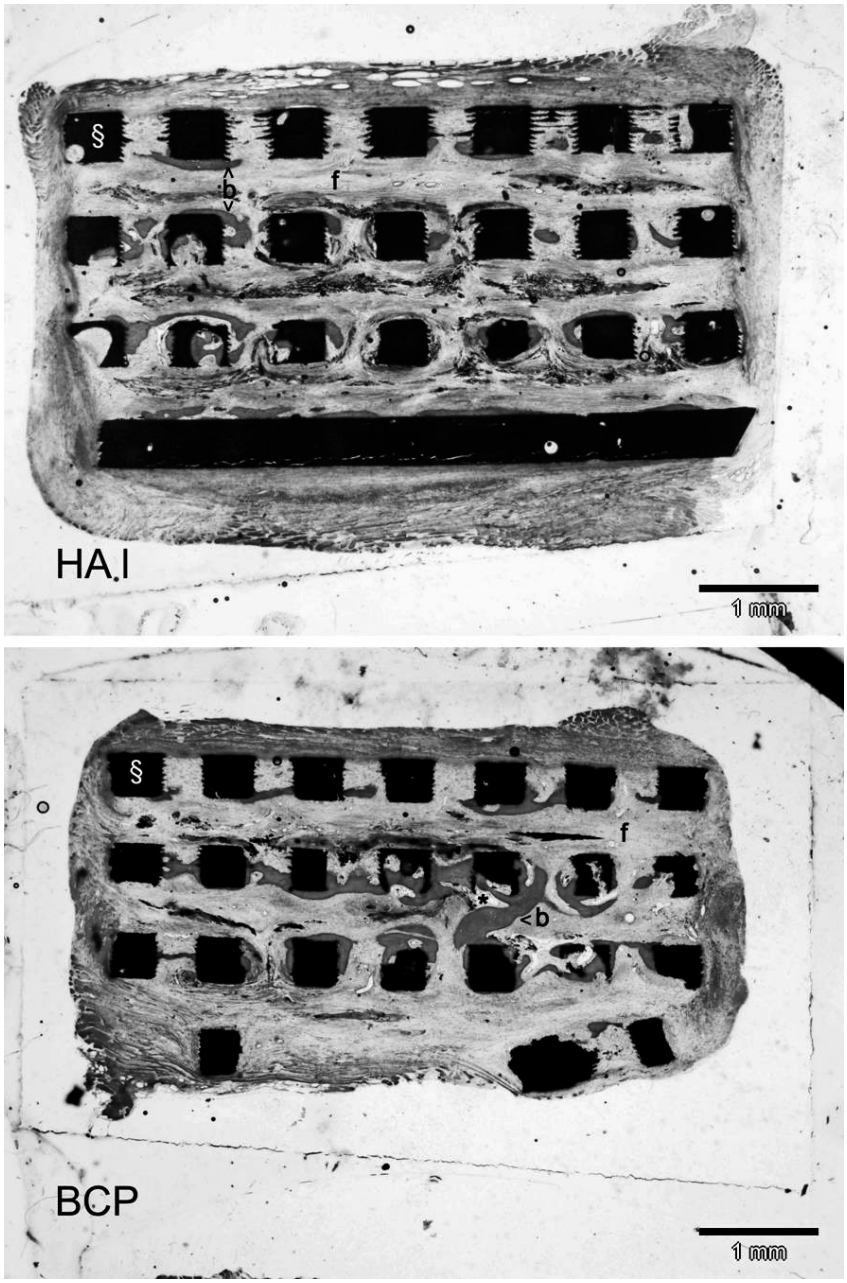

Figure 5.4: Representative light micrographs of methylene blue/basic fuchsin-stained histologic sections of bone formation in HA I (top) and BCP (bottom) scaffolds. Scaffold material (dark gray, §), fibrous tissue (purple, f), and mineralized bone tissue (red, b) are visible. Surface bone formation is most common, with frequent budding away from surface and encapsulation of fat or marrow-like tissue (*).
(See color image on page 199)

Discussion and Conclusions

The present study examines the influence of four different CaP ceramic compositions on ectopic tissue engineered bone formation in scaffolds with a size, shape and macroporous architecture sufficiently similar to reasonably discount these parameters as confounding variables. The macroporous structures used in this study, while within the pore size range suggested in the literature for osteoconduction,[26, 43, 120, 125, 218] do not represent an optimal or ideal porous structure for any particular application. The overall dimensions of the structure were chosen to enable implantation in animals as small as mice[245]. The CaP compositions used in this study were chosen to represent materials typically applied both clinically and in TE research and to provide continuity with materials used in our groups past and ongoing research.[94, 146, 150, 153, 246, 247] While the BCP material has been commonly applied within this work, the identical material compositions for all four scaffolds used in the present study have also been evaluated in two orthotopic models in the goat lumbar spine.[153, 247]

Although the visual appearance of the scaffolds in this study was similar with regard to structure, there were differences in shrinkage and, therefore, the macroporous dimensions (Table 5.1). The higher sintering temperature of the high temperature HA and the lower solids loading of the BCP were the primary contributors for the higher shrinkage of these materials. Conversely, the low sintering temperature and higher solids loading of the TCP and low temperature HA materials resulted in less shrinkage. Interestingly, the apparent porosity of the BCP scaffolds was very similar to the TCP and low sintering temperature HA scaffolds despite the much higher shrinkage of the BCP. This indicates that, for the same sintering temperature, these CaP materials ultimately reach a similar level of densification despite the initial lower solids loading of the BCP. This was further evaluated by determining the approximate values for total, material and pore volumes using the measured dimensions for the scaffolds and pores, and then calculating the macroporosity. The difference between this macroporosity and the measured apparent porosity provides an indication of the proportion of porosity attributable to micropores and unmeasured macro inclusions. Comparing these numbers for the different scaffold materials, Table 5.2 shows that while the volume measures for BCP were different from TCP and low sintering temperature HA, the porosity measures were all quite similar. Again, this indicates that the same level of densification was achieved during sintering in these materials, requiring greater shrinkage of the BCP materials due to the lower initial solids loading.

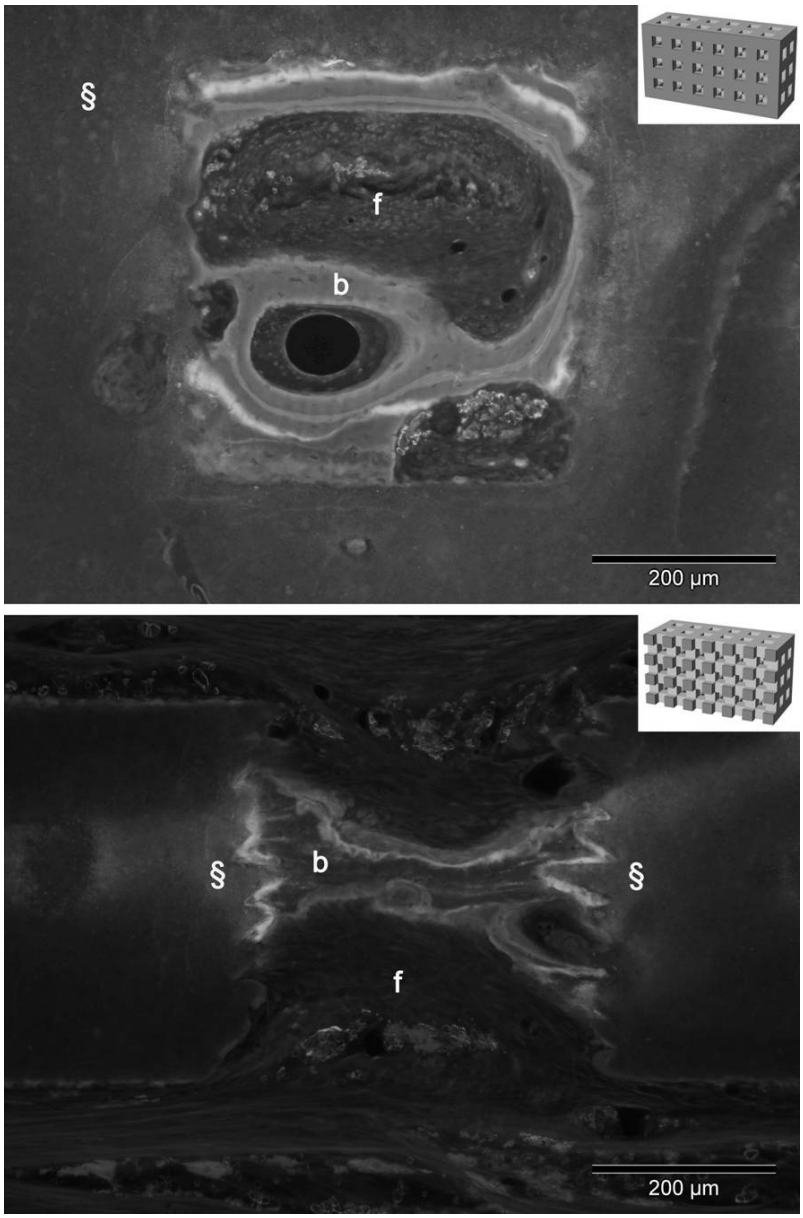

Figure 5.5: Epifluorescent microscopy images of fluorochrome markers. Top image shows a single pore containing fibrous tissue (f) and bone (b) that is completely surrounded by scaffold (§). The bottom image shows bone (b) between two scaffold struts. In both images the earliest label is green (3 weeks, calcein green), the intermediate label is yellow (5 weeks, oxytetracyclin) and the final label is orange (7 weeks, xylenol orange). Diffuse labeling of the scaffold material is also present. Inset drawings demonstrate general section configuration of the two images. *(See color image on page 200)*

Table 5.2: Scaffold volumes (Total, Material (ceramic) and Pore) and Macroporosity calculated form a computer model of the scaffolds compared to the measured total apparent porosity and the other porosity (difference between macro and apparent porosity).

Material	Total Volume (mm^3)	Material Volume (mm^3)	Pore Volume (mm^3)	Macro-porosity (%)	Apparent Porosity (%)	Other Porosity (%)
HA h	47.98	31.78	16.19	33.75	49.65	15.90
HA l	84.67	50.19	34.48	40.72	72.39	31.67
BCP	58.95	34.82	24.14	40.94	73.72	32.78
TCP	80.60	48.08	32.51	40.34	72.54	32.20

Scaffold material, addition of cells and individual animal all influenced the formation of mineralized bone in this study. Bone formation occurred only in the HAl and BCP ceramics seeded with cells. This bone formation occurred in 6 of the 10 animals and was always paired, i.e., 6 animals showed bone formation in both HAl and BCP and 4 animals showed no bone formation whatsoever. Compared to orthotopic conduction and tissue engineering[153] in a transverse goat spine model using the same four materials as the present study but produced by more traditional foaming and mixing methods, TCP and BCP consistently outperformed both high and low sintering temperature HA materials (HAh and HAl). Furthermore, the BCP, TCP and HAl materials all showed statistically significant responses in combination with BMSCs, demonstrating an increases in Contact % particularly in regions of the scaffold furthest from underlying bone bed[153]. Similarly, a model evaluating bone conduction from the decorticated transverse process into standardized channels between plates of these same four materials also concluded that BCP and TCP performed best followed closely by HAl, all of which were significantly better than HAh.[247] However, implantation of HAh scaffolds, identical to those described here, have demonstrated limited bone formation after six weeks of implantation subcutaneously in nude mice[246].

Surprisingly, the TCP scaffolds in the present study demonstrated no bone formation despite the relative success of this material in previous work. The addition of cells clearly influenced the degradation of the TCP scaffolds (Figure 5.3). Substantial degradation, resulting in a nearly complete loss of structure, was observed in 9 out of 10 TCP scaffolds seeded with cells. However, the 10 TCP scaffolds without cells, while demonstrating some signs of degradation, all maintained their shape and pore structure. While the organized open porosity and relatively small size of the scaffolds may encourage early and rapid degradation processes that may affect bone formation, the mechanism by which the cells have intensified the degradation of the TCP material is not clear. Histological examination after the nine week implantation period showed no observable signs

of an adverse response. Examining these materials at an earlier time point may help expose any cell or tissue processes involved.

Analysis of the fluorochrome labels demonstrated that bone nucleated at the scaffold surface and then progressed into the pore space. Furthermore, this bone nucleation appeared preferentially on textured surfaces. Since the addition of cells was required for bone to form, it is likely that added cells migrated to the scaffold surface and that areas of surface texture offered an environmental advantage to nucleate bone formation. The possibility that the added cells also recruited, or contributed to the recruitment of, systemic osteogenic cells that participated in the bone formation can not be eliminated. The resulting bone formation showed direct bonding of bone matrix with the material surface without an interposing fibrous tissue layer, so-called bonding osteogenesis.[56] Materials that elicit bonding osteogenesis are termed bioactive. The bioactive process for ceramic materials has been described [51, 62, 63, 140] in three basic steps: (1) the partial dissolution of the ceramic resulting in an increase in calcium and phosphate concentration in the local microenvironment; (2) precipitation of a carbonate calcium phosphate layer; (3) association and then incorporation of the precipitated layer with the organic matrix of newly formed bone. The formation of the prerequisite carbonate calcium phosphate layer is dependent upon the solubility of the ceramic substratum. It has been suggested that the bioactivity of ceramics may be influenced by the microenvironments created by microporosity and surface texture.[52, 258] Microporosity and surface texture can greatly increase the surface area of a ceramic, facilitating greater dissolution and enhancing the precipitation of the carbonate calcium phosphate layer. This may, for example, enable bone morphogenic proteins adsorbed on the surfaces to reach local concentrations greater than the threshold value needed to induce bone formation. [53, 206, 258] These surfaces may also enhance the adhesion, proliferation, differentiation and matrix deposition of osteogenic cells.[136, 157] Considering the specific materials described in this manuscript, the results suggest that the high sintering temperature HA (HAh) and TPC materials do not fulfill the requirements needed to elicit a bioactive process leading to bone formation. However, considering the relative success of TCP described elsewhere, further examination of the raw material used may be useful. The low sintering temperature HA (HAl) and BCP materials, in combination with the surface texture resulting from the rapid prototyping process, do elicit a bioactive process leading to bone formation.

In conclusion, the present study examines the tissue engineered ectopic (intramuscular) bone formation in scaffolds of four different calcium phosphate compositions with nearly identical macroporous structures designed and produced

using a rapid prototyping technique. The addition of BMSCs to TCP scaffolds dramatically increased the amount of degradation observed during the implantation period. In 6 of 10 animals, both the BCP and low sintering temperature HA (HAl) scaffolds yielded remarkably similar bone formation. No other scaffolds, with or without BMSCs, yielded bone. Therefore, in addition to being in a receptive animal, both an appropriate material type, either BCP or low sintering temperature HA, and the per-operative addition of BMSCs were required in order to yield bone formation.

Acknowledgements

The authors would like to thank The Netherlands Technology Foundation for financial support (grant UGN.4966). We also thank Ellen van Leeuwen (Technical University of Eindhoven) and Dr. ShiHong Li (IsoTis N.V.) for their assistance.

6

Accessible volume of three-dimensional macroporous scaffolds: a micro-computed tomography alternative for low pressure mercury intrusion porosimetry

C.E. Wilson[1], A. Laib[2], T.B.F. Woodfield[3], J.S. Pieper[4], J.R. de Wijn[6], J.D. de Bruijn[5], C.A. van Blitterswijk[6], A.J. Verbout[1] and W.J.A. Dhert[1,7]

[1] Department of Orthopaedics, University Medical Center Utrecht, P.O. Box 85500, 3508 GA Utrecht, The Netherlands;
[2] SCANCO Medical AG, Auenring 6-8, 8303 Bassersdorf, Switzerland;
[3] Centre for Bioengineering, University of Canterbury, Private Bag 4800, Christchurch 8020, New Zealand
[4] Isotis OrthoBiologics (Integra Orthobiologics), 2 Good Year, Irvine, CA 92618, United States of America
[5] School of Engineering & Materials Science, Queen Mary University of London, Mile End Road, London E1 4NS, United Kingdom
[6] Institute for Biomedical Technology, Department of Tissue Regeneration, University of Twente, PO Box 217, 7500 AE, Enschede, The Netherlands
[7] Faculty of Veterinary Medicine, Utrecht University, Yalelaan 1, 3584 CL Utrecht, The Netherlands

Abstract

The connectivity and accessibility of porosity within macroporous tissue engineering scaffolds is critical to their performance. Mercury intrusion porosimetry is the established technique for evaluating connectivity and accessibility, however, it is destructive and provides little insight regarding the geometrical distribution of these parameters. We describe a numerical method of approximating mercury intrusion porosimetry using volumetric micro-computed tomography data. This technique was evaluated against theoretical expectations in a packed sphere reference model. We further compared the numerical method to mercury intrusion by evaluating porous polymer scaffolds before and after a reticulation treatment to improve connectivity. The numerical method provided information similar to mercury intrusion and was as specific in determining the influence of the reticulation treatment. Furthermore, the numerical method enabled the evaluation and 3D visualization of accessible volumes in the scaffolds determined at various threshold diameters. While mercury intrusion remains an important tool for evaluating connectivity and accessibility, numerical techniques like the one described herein can provide complementary information, particularly when a non-destructive assessment of connectivity and accessibility is desired.

Introduction

Research in tissue engineering (TE) has increased dramatically in recent years with efforts currently underway to engineer numerous human tissues. The vast majority of tissue engineering techniques employ macroporous scaffolds that are functionalized with cells and/or bioactive factors. The characteristics of an ideal scaffold have been discussed by many and are generally accepted.[42, 49, 122, 127, 249, 251] One of these characteristics is an interconnecting macroporous network.

Porous Scaffolds and Interconnectivity

Interconnectivity, or simply connectivity, is the degree to which a single phase within a medium is joined to form continuous paths. When used to describe TE scaffolds, the term interconnectivity typically refers to the void space (pores, cracks, channels, etc.) within the scaffold material. However, interconnectivity has little practical meaning unless qualified by a cross-sectional dimension or pore size. The International Union of Pure and Applied Chemistry (IUPAC) classifies pores into three size ranges: micropores (~0.5 nm to 2 nm), mesopores (2 nm to 50 nm) and macropores (greater than 50 nm).[1] This classification, however, is rarely cited in biomaterials literature. More common are pore sizes defined in the context of the porous material being discussed. In general, macropores are defined as the larger pores within a scaffold, with sizes from tens of micrometers and larger. Micropores are typically defined as smaller pores, with dimensions of a few micrometers or smaller. Nanopores refer to an even smaller category of pore sizes. This paper describes techniques for characterizing the interconnectivity of porous structures with pore sizes greater than approximately 10 µm. Therefore, in this paper, the macro- and micro- prefixes refer to pore sizes greater than and less than roughly 10 µm, respectively.

Important functional characteristics of TE scaffolds are influenced by pore size distribution and the 3-dimensional (3D) interconnecting porous architecture. Cellular processes such as attachment, proliferation, migration, extra-cellular matrix production and perhaps even differentiation are accommodated and even influenced by the structure of this porosity.[105, 133, 176, 207, 222, 261, 264] The porosity must also provided sufficient diffusion of nutrients and waste products throughout the scaffold for the short term maintenance of the implanted cells and support formation of new vascular networks for long term survival. A range of pore diameters from tens of microns to greater than 500 µm[135, 237] may be appropriate depending on the application. Therefore, an adequate method for assessing the macroporous environment must describe the pore volume that is accessible from

an exterior surface of the scaffold via pores of a relevant size and also convey the 3D structure of the accessible porosity to the viewer.

The connectivity of porous biomaterials is often qualitatively described in biomaterials literature but rarely measured. Many researchers simply describe the observed porous morphology as interconnecting or open (or as non-interconnecting or closed, respectively) and may provide apparent interconnecting pore diameters as observed by light microscopy or SEM (scanning electron microscopy).[169, 173, 185, 201, 239] Quantitative methods that have been applied to characterizing porous biomaterials include stereological (2D imaging), permeation (fluidic) and 3D imaging (e.g. tomography) techniques.

Traditional stereology is the science of describing 3D geometric relationships by statistical inferences made from measurements on 2D images. Stereology is often applied in biology to describe the 3D relationships of features in a specimen from 2D microscopic sections. [212, 234] Stereology has also been used to measure properties such as porosity and pore size.[90] Several measures for connectivity have also been described including: Global Connectivity,[212] the number of cuts that can be made through a single phase of a 3D structure without separating it into two parts; Euler characteristic,[84, 212] the difference between the number of independent parts and the collective Global Connectivity; and, Interconnectivity Index (ICI),[159] a ratio of nodes, branches and free ends based on a morphological skeleton of the porous structure. However, the accuracy of stereological measures is dependant upon applying appropriate geometric correction factors, requiring an existing knowledge of the general shape of the features being measured.[234] Furthermore, only a small subset of geometric properties measured in 2D images have unambiguous, stereological relationships to geometric properties of the 3D structure from which the images were obtained[212]. This is particularly relevant to structures of arbitrary shape and complex connectivity. In other words, 3D and 2D connectivity are fundamentally different.[90] Finally, the 3D structure as it is understood by the observer is difficult to interpret from the representative indices provided by stereological measures. Therefore, metric and topological measures alone do not provide sufficient information to understand and visualize the 3D structure of a complex feature such as connectivity.

Permeation techniques utilize fluids (gases and/or liquids) to characterize porous structures. An ASTM standard[16] for the characterization and testing of biomaterial scaffolds for tissue engineered medical products suggests the use of two permeation techniques, porometry and porosimetry. Porometry measures the flow of a fluid completely across a porous structure. Measurements are therefore

constrained to through pores (pores that completely traverse the structure) and do not consider blind (dead end) pores. This method is governed by Darcy's Law and characterizes the permeability of a porous medium. Porometry provides little information regarding the structure of a porous medium. Porosimetry measures the intrusion of liquid into a porous structure that is open to the exterior of the material, treating through and blind pores similarly. Neither method can account for closed pores that are inaccessible to the test fluid.

Mercury Intrusion Porosimetry

Of the permeation techniques, mercury intrusion porosimetry (MIP) is the classic technique for characterizing porous materials and media. MIP is based on the principle that non-wetting liquids (contact angle > 90°) will intrude capillaries only under an applied pressure. Mercury is the fluid of choice because it is non-wetting and non-reactive to most materials. In 1921, Washburn derived an equation stating that the pressure, P, required to force a non-wetting liquid to enter a capillary of circular cross-section is inversely proportional to the diameter, d, of the capillary and directly proportional to the surface tension of the liquid, γ_{lv}, and the contact angle with the solid surface, θ.[240]

$$P = -4\gamma_{lv} \cos\theta / d$$

The Washburn equation describes the capillary pore diameter that mercury will intrude at a given pressure. Careful measurement of the volume of mercury entering a porous sample over a range of pressures enables the relationship between pore size and accessible porous volume to be calculated. A typical MIP test begins with a sample in an evacuated chamber. Mercury is then allowed to fill the chamber, completely surrounding the sample, while the vacuum is maintained. The pressure is then slowly increased stepwise while carefully monitoring the volume of mercury entering the sample container, i.e. volume intruding into the sample, during each pressure step. As the pressure increases, smaller and smaller pore diameters are intruded, conducting the mercury further into the porous system. Low pressure MIP, from vacuum to atmospheric pressure, intrudes capillary pores larger than approximately 12 µm in diameter and is therefore the technique used to characterize macroporous structures. Continued pressurization of the mercury in the sample chamber can evaluate pores as small as approximately 0.003 µm in diameter.[241] MIP has been applied to a variety of materials and is a common technique for characterizing the connectivity, porosity, pore size distribution and surface area of porous biomaterials. The effective pore diameter, also called the threshold or continuous pore diameter (but is not the "mean" pore diameter), may be determined from the largest differential intruded

volume and indicates where percolation has occurred.[6] Due to the use of highly toxic mercury, MIP must always be considered a destructive technique regardless of whether specimens are physically damaged or not. This is particularly so for biomaterials since complete removal of mercury from complex porous structures is difficult to guarantee.

When reporting MIP data it is important to understand the limitations of the technique and the assumptions required for data reduction. In order to calculate pore diameters using the Washburn equation, the structure is assumed to be composed capillary pores of circular cross-section.[241] MIP data reduction also assumes that the pore geometry is regular and that the pores are interconnected. When considering pore geometries where relatively large pore volumes are accessible through relatively small interconnections, MIP misrepresents the size of these pores as having the diameter of their interconnection. This bias is referred to as the “ink bottle” effect. Furthermore, the contact angle of mercury with most materials is generally considered constant at around 130 degrees and is the assumed value in most MIP tests. However, this is not always true. A different drying regimen for structural cement pastes caused a 13° change in contact angle and resulted in a 30% reduction in the diameter intruded at a given pressure.[248] The contact angle may also vary depending on surface roughness.[80] This is an important consideration when any treatment is applied to a scaffold that may alter its surface characteristics.

More recently, the use of MIP to evaluate compliant and/or fragile porous structures has been questioned. Compression and/or densification of these porous structures under the pressure applied during MIP analysis can result in the superimposition of an error onto the intrusion volume versus pressure data.[166] When studying hyperporous mineral aerogels, the distinct nature of an initial destructive compaction followed by intrusion of the compacted structure enabled Pirard et al. to establish a relationship between the applied pressure and the size of the collapsed pores, allowing extraction of pore size data.[196-198] However, Maquet et al. performed a similar evaluation of macroporous poly(L-lactide-*co*-ε-caprolactone) foams (mean pore diameters from 83 to 194 µm) and demonstrated simultaneous intrusion and densification of the foams during MIP. They concluded it was impossible to determine the relative contribution attributable to either intrusion or densification. Therefore, neither Washburn’s equation nor equations like those described by Picard et al. could be used to determine actual pore size distributions.[175]

Additional considerations relate specifically to the sensitivity and accuracy of low pressure MIP. During MIP, the volume of mercury intruded into the sample due to a pressure increase from P_i to P_{i+1} is equal to the volume of the pores in the associated size range d_i to d_{i+1} as determined from Washburn's equation.[241] It is important to note that due to the hyperbolic relationship between P and d, a step increase at low pressures results in a relatively large range of pore sizes being filled compared to the same step increase at higher pressures where in a much narrower range of pore sizes is filled. For example, assuming a mercury contact angle of 130 degrees and surface tension of 0.485 N/m, raising the pressure from 28.0×10^{-4} MPa to 36.0×10^{-4} MPa, a difference of 8.00×10^{-4} MPa, fills capillary pore diameters from approximately 450 to 350 µm, a range of 100 µm. When the pressure is raised from 992.0×10^{-4} MPa to 1000.0×10^{-4} MPa, also a difference of 8.00×10^{-4} MPa, pore diameters from 12.57 to 12.47 µm are filled, a range of only 0.100 µm. This results in relatively low sensitivity for low pressure MIP and large pores and comparatively higher sensitivity for higher pressures and small pores. To put this in perspective, low pressure MIP uses a pressure range of approximately one atmosphere (vacuum to 0.1 MPa) to measure all pore sizes larger than 12 µm. A pressure range of over 4000 atmospheres (0.1 to 414 MPa) is used to measure pore sizes from 12 µm to 0.003 µm. Equipment manufacturer compensate for the lack of sensitivity in low pressure MIP by using very fine pressure steps (typically 3.00×10^{-4} to 4.00×10^{-4} MPa) at the lowest pressures and more coarse steps as atmospheric pressure is approached and surpassed.

Finally, even with very sensitive pressure control and volume measurement equipment, the maximum pore diameter that can be accurately measured by low pressure MIP is limited due to the hydrostatic head or pressure of the mercury itself. For most purposes, this maximum is regarded as approximately 400 µm.[129] However, for samples having substantial height, the differential hydrostatic mercury pressure from the top to the bottom of the sample can be significant. The hydrostatic pressure difference for a 10 mm high sample equals 13.33×10^{-4} MPa or three to four times the magnitude of typical pressure steps used in low pressure MIP. Putting this in the context of our previous example regarding the sensitivity of low pressure MIP, a pressure increase from 28.0×10^{-4} to 36.0×10^{-4} MPa at the top of a 10 mm high sample fills 450 to 350 µm diameter pores. At the bottom of the sample the pressue includes the hydrostatic head and increases from approximately 41.3×10^{-4} to 49.3×10^{-4} MPa, filling pores as small as 250 µm. This can therefore impose substantial errors in the intruded volume measured as the result of a pressure step, particularly at lower pressures.

Microcomputed Tomography

X-ray microcomputed tomography (µCT) is a rapidly advancing technology that reconstructs 3D data sets, consisting of volume elements (voxels), from a series of planar radiographic images. Modern commercial systems are capable of nominal resolutions (voxel dimensions) of a few microns. The technique is non-destructive and, with special equipment, may be applied to *in vivo* specimens in small animals without untoward harm to the animal. Once data sets are obtained, numerous quantitative probes and/or visualization techniques may be applied. µCT has been used to evaluate, compare and quantify 3D architectural structures such as trabecular bone,[117, 156, 178, 210, 230] vasculature[23, 101, 209] and porous biomaterials including tissue engineering scaffolds.[84, 107, 170, 226, 236, 264] µCT may also complement molecular imaging in small animals[208] and high energy systems (i.e. linear accelerators) may be used for imaging at the cellular level.[158] Several authors have recently reported the use of µCT data sets for the quantitative assessment of interconnectivity and pore structures.[165, 182, 227] These methods iteratively apply three dimensional morphological erosion and dilation operations to progressively close pores or interconnections of increasing diameter. These morphological tools have the undesired affect of smoothing abrupt surface features, leading to potential data loss and errors in the measured volumes after applying the tools.

In this study we propose a µCT based alternative to low pressure MIP for evaluating the structure of macroporous scaffolds. This technique applies a distance transformation to the entire pore volume. A threshold pore size can then be used to evaluate the pore volume that is accessible form an exterior surface of the scaffold via pores equal to or larger than the threshold pore size. These values are termed the accessible volume (AV) for each pore size. A cumulative curve of AV versus threshold pore size is similar to the intrusion volume versus pore diameter resulting from MIP. The accessible volume is easily visualized via computer imaging to facilitate a more complete comprehension of the macroporous environment that is accessible through different pores sizes. This technique is applied to a reference model of packed ceramic spheres and also to two polymer scaffolds with similar porous structures. Common parameters, i.e. porosity and mean pore size, obtained from stereology, MIP and µCT are compared for the two polymer scaffolds.

Materials and Methods

Reference Model

Hydroxyapatite ceramic spheres were sieved to a diameter range of 400 to 500 µm. These spheres were densely packed in a glass tube and embedded in acrylic polymer to create a cylindrical reference model. The apparent packing density (volume percent) of spheres was calculated from overall volume and the weight and density of the ceramic material. The ceramic and acrylic phases of the reference model were both analyzed by the µCT technique and compared to theoretical expectations for the effective (percolation) diameter range for each phase. The minimum and maximum theoretical effective diameters for the acrylic phase were calculated as the diameter of the aperture between hexagonally packed 400 µm diameter spheres and the aperture between cubic or orthogonally packed 500 µm diameter spheres, respectively. The theoretical effective diameter range for the ceramic phase was based on the resolution of the µCT data. Ideally, the rigid ceramic spheres touch at point contacts. However, due to the finite resolution of µCT, the density value assigned to each voxel is an average for that volume. Where voxels overlap density gradients, i.e. the boundary between ceramic and acrylic phases, segmenting the data set allocates these voxels to just one phase. Segmenting the data set to isolate the radiopaque ceramic favors allocation of voxels to this phase. The results in an apparent increase in the radius of the ceramic spheres by up to one voxel dimension. Therefore, adjacent spheres may appear to overlap by up to two voxel dimensions. The diameter of the circular aperture between spheres created by this overlap is easily calculated. The minimum and maximum theoretical effective diameters for the ceramic phase were calculated using an overlap of one voxel dimension for 400 µm diameter spheres and two voxel dimensions for 500 µm spheres, respectively.

Porous Polymer Scaffolds

Porous scaffolds of a block co-polymer consisting of 55% hydrophilic poly(ethylene glycol)-terephthalate and 45% hydrophobic poly(butylene terephthalate) (PolyActive®, IsoTis SA, The Netherlands) were prepared by compression molding. Briefly, a homogenous mixture of 25 % (Vol) polymer resin and 75 % (Vol) NaCl salt crystals (sieved to between 400-600 µm) were placed in a 16 x 16 x 1 cm stainless steel mould and compressed to a pressure of 20,000 ±500 lbf/in^2. Under this pressure, the mould was heated to 220 ^{0}C and maintained at that temperature for 10 minutes. After cooling to room temperature, the salt crystals were statically leached from the polymer matrix using demineralised water. The scaffolds were dried at room temperature for 2 days and then in a vacuum oven at 50 °C for 16 hours. The result was a 10 mm thick block of porous, off white, pliable material.

Two cylindrical cores (17 mm in diameter by 10 mm in height) were cut from the center of the polymer block. One cylinder was not modified while the other was subjected to a reticulation treatment to improve the interconnectivity of the porous structure. This treatment was performed by quickly passing a volume of chloroform/isopropyl alcohol mixture (1:1 volume ratio), a marginal solvent for the polymer, through the porous structure by overpressure. The cylinders were then dried in a vacuum oven at 50 °C for 16 hours. The reticulation treated (RT) and non-treated (NT) cylinders were then cut into three uniformly sized discs. One set each of RT and NT samples were used for MIP, µCT and stereology measurements.

Mercury Intrusion Porosimetry

Low pressure MIP was performed by Micromeritics Instrument Corporation (Norcross, Georgia, USA) using an AutoPore IV 9500 system. The standard test set-up assumed a mercury contact angle of 130 degrees and a surface tension of 0.485 N/m. The reported data included pressure and surface area data versus intrusion volume and calculated pore diameter. Values for several parameters including average pore diameter and porosity were also reported. The actual mercury contact angle for NT and RT specimens was subsequently calculated as the average of ten independent measurements (DSA100, Krüss USA, Matthews, North Carolina, USA) and the intrusion data recalculated.

µCT

The reference model and scaffolds were measured without further preparation using a desktop µCT system (µCT-40, Scanco Medical, Bassersdorf, Switzerland; X-Ray voltage 45 kVp) at a resolution of 6 µm in all three spatial dimensions. 400 slices, covering a length of 2.4 mm, were scanned of each sample with 2048x2048 pixels per slice. Volumes of interest (VOI) were 6.0 mm in diameter and centrally located in order to exclude boundary effects at the cylinder walls. The resulting gray-scale images were segmented using a low-pass filter to remove noise and a fixed threshold to extract the ceramic phase of the reference model and the polymer phase of the scaffolds. These binary images were then inverted to enable characterization of the acrylic and void spaces, respectively

Accessible Volume from µCT data

An algorithm, termed DTVAL, was developed to mimic mercury intrusion porosimetry by attempting to answer the question: What volume is accessible from exterior surfaces through pathways with a specified cross-sectional dimension?

The following description considers the evaluation of the void volume within a scaffold. However, this procedure is easily applied to any segmented phase in a µCT dataset.

First, a distance transformation[117] was used to determine the distance of every voxel within the void space to the nearest scaffold surface. Each void voxel was then weighted with its distance value. This three-dimensional distance transformed image data set can then segmented by distance values. For example, if the data set were segmented for a specific threshold distance, D, all void voxels with a weighted value less than D would be removed and all void voxels with a weighted value of D or greater would remain. This results is a subset of the original void space broken at points where the local maximum weighted value drops below D. The local cross-sectional dimension at these points would be two times the threshold distance, 2D. A component labeling operation was then applied to remove all isolated components not connected to the exterior VOI surface. Thus, for each threshold distance D (threshold cross-sectional dimension 2D), the surviving structure consisted of a skeleton of the original void space continuously connected to the exterior VOI surface by voxels with a distance weighted value of *D* or larger. The accessible void volume for threshold distance D would be the volume of the original void space that surrounds this surviving skeleton. To calculated this , surfaces at the internal breaks of the skeleton structure were defined by iteratively growing the skeleton until it just fills the original void space. The volume of the original void space between the exterior VOI surface and the internal termination surfaces is the accessible void volume. The accessible surface area is calculated as the area of the original void surface demarcated by these surfaces.

Calculations on MIP and µCT data

The process described above was applied to the acrylic and ceramic phases of the reference model and to the void phase of the polymer scaffolds. It was repeated for threshold diameters in steps of 12.0 µm, twice the resolution of the µCT data. Accessible volume and accessible surface area, as well as intrusion volume from MIP, were plotted against the reverse log of threshold diameter, the standard way of representing MIP data. The regions of maximum slope, i.e. greatest incremental intrusion or change in accessibility, were calculated as the effective (percolation) diameters. The effect of the reticulation treatment on accessible pore volume was determined by calculating the difference between RT and NT data (RT – NT) for each threshold (pore) diameter for both the MIP and µCT data. The accessible volumes were visualized using standard 3D computer imaging techniques.

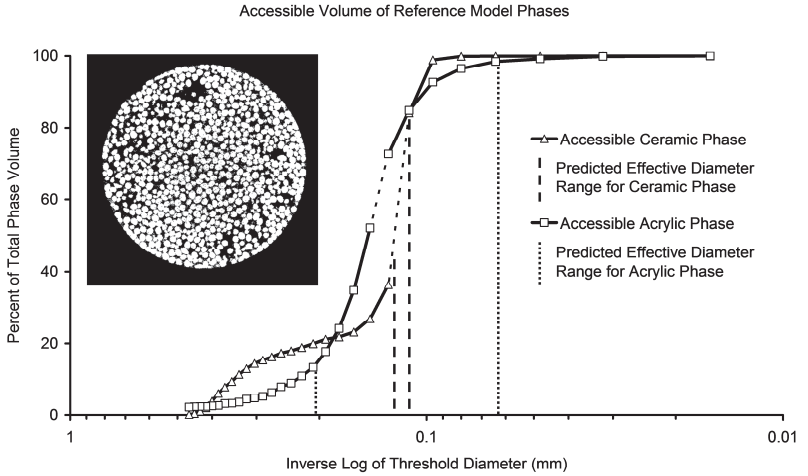

Figure 6.1: Cumulative accessible volume curves for both the ceramic and acrylic phases of the reference material as calculated by the DTVAL technique. Vertical lines indicated theoretical effective diameter determined from geometric predictions. Inset image is a cross-sectional image from the μCT data set and indicated the less than optimal packing efficiency.

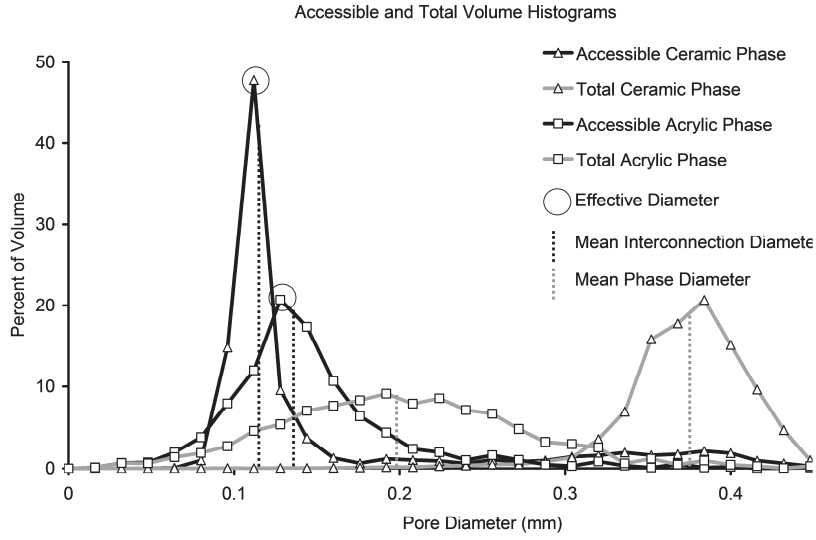

Figure 6.2: Phase diameter histograms derived from accessible (black) and total (gray) phase volume data obtained by μCT. Vertical dotted lines indicate the mean interconnection diameter of the accessible volume data (black) and mean phase diameters of the total phase volumes (gray). Effective diameters of each phase are circled.

Differentiating the accessible volume data sets yielded histograms of the accessible volumes associated with each threshold diameter. The maximums of the accessible volume histograms correspond to the maximum slopes and, therefore, the effective diameters of the accessible volume data sets. The mean interconnecting diameters were calculated as the means of the accessible volume histograms. Additionally, total volume data sets were obtained by omitting the component labeling operation of the DTVAL algorithm (section 2.5 above) that removed isolated components. Differentiating these data sets yielded threshold diameter histograms for the entire phase volume. The mean values of these total volume histograms were calculated as the mean (pore) diameters for the phases.

Microscopy and 2D stereology

The porous structures of the scaffolds were observed and imaged using a stereo microscope (SMZ-10A, Nikon) and digital camera (Retiga 1300, Q-Imaging). The scaffolds were then embedded in plastic (GMA, glycol methacrylate) and 15 ± 5 µm sections cut by microtome. Four sections of each scaffold type, RT and NT, were viewed by polarized light microscopy (Eclipse E600, Nikon) and digital images captured using a digital camera (Retiga 1300, Q-Imaging). Light areas in the images corresponded to scaffold material and dark areas with the embedding plastic. These images were segmented by manual thresholding to yield binary images with white being scaffold and black being pores (embedding plastic). Computer assisted stereology was performed using BioQuant Nova software (BioQuant, Nashville, USA). The software was calibrated using an identically obtained image of a micrometer. The Normal Histogram function was used to create 30 evenly spaced horizontal lines on the images. The histogram of each line contained a series of valleys (pores, black) and peaks (scaffold, white) with vertical walls. The distances across the valleys represented the linear intercepts for the pores. These were measured for each line and the mean intercept length of each scaffold determined as a measure of mean pore size. Additionally, the percent of segmented pore area to total area was calculated as a measure of porosity. For comparison, these same stereological measurements were also performed on four slices from the µCT data sets for the scaffolds.

Results

Reference Model

The accessible volume curves for both the ceramic and acrylic phases of the reference model as calculated by the DTVAL algorithm are shown in Figure 6.1. The pore diameter histograms for the accessible and total pore volumes of both the

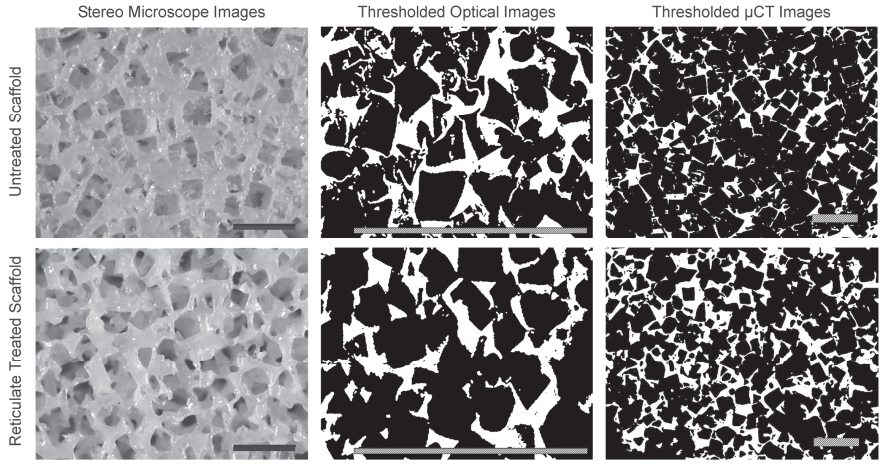

Figure 6.3: Images of polymer scaffolds before and after reticulation treatment (top and bottom rows, respictively). Columns from left to right: stereomicroscopic images of scaffolds, stereomicroscopic images after segmenting polymer and porosity by manual threshold, cross-sectional slice from µCT data after manual threshold. (bars = 1 mm)

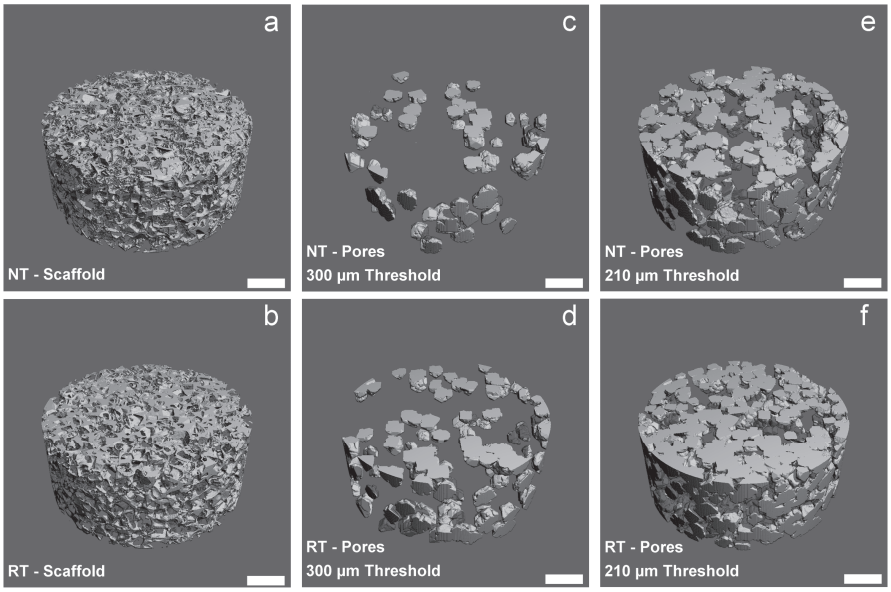

Figure 6.4: 3-dimension images before and after reticulation treatment (top and bottom rows, respictively) rendered from µCT data. Columns from left to right: image of entire polymer scaffold, image of pore volume accessible through pore diameters of 300 µm and larger, image of pore volume accessible through pore diameters of 210 µm and larger. (bars = 1 mm)

ceramic and acrylic phases are shown in Figure 6.2. Physical measurements and image slices from the µCT data set indicated that the packing efficiency of the ceramic spheres was not ideal (inset, Figure 6.1). The apparent packing efficiency was 63% and the µCT measured packing efficiency was nearly 61%, less than an ideal value of approximately 68% for a single sphere diameter. The effective and mean interconnection diameters measured from the accessible volume data and the mean phase diameters measured from the total phase volume data corresponded well with the theoretical values. These values are depicted in Figures 6.1 and 6.2 and summarized in Table 6.1. The difference between mean interconnecting and mean phase diameters was relatively large for the ceramic phase as compared to the acrylic phase. This was predicted by the theoretical calculations for the reference model and helps explain why there is an initial step in accessible volume for the ceramic phase (form approximately 0.400 to 0.200 mm) and not for the acrylic phase. This step is due to spheres that intersect the boundary of the VOI with volumes accessible from the exterior through openings comparatively larger than the interconnection diameters between spheres. This effect is much less pronounced in the acrylic phase due to the relatively smaller difference between the mean interconnecting and mean pore diameters.

Table 6.1: Summary of measured values and geometric predictions (in mm) for the reference model.

µCT Calculations	Effective Diameter	Mean Interconnection Diameter		Mean Phase Diameter	
Acrylic Phase	0.128	0.137		0.198	
Ceramic Phase	0.112	0.113		0.374	
Geometric Predictions		Interconnection Diameter Range		Phase Diameter Range	
		low	high	low	high
Acrylic Phase		0.062	0.207	0.090	0.366
Ceramic Phase		0.097	0.133	0.400	0.500

Polymer Scaffolds

Stereo microscopy images of NT and RT scaffolds as well as examples of segmented images from embedded sections and µCT image slices used for stereological measurements are shown in Figure 6.3. By visual observation, reticulation treatment of the scaffolds resulted in a smoothing of the scaffold surface, removal of small or loosely attached polymer pieces and the apparent enlargement of the interconnecting apertures between pores.

Examples of 3D images from µCT for both NT and RT scaffolds are provided in Figure 6.4. Comparing images of NT and RT scaffold structures (Figure 6.4a & 6.4b) reveals visible differences. The NT scaffold shows debris and remnant

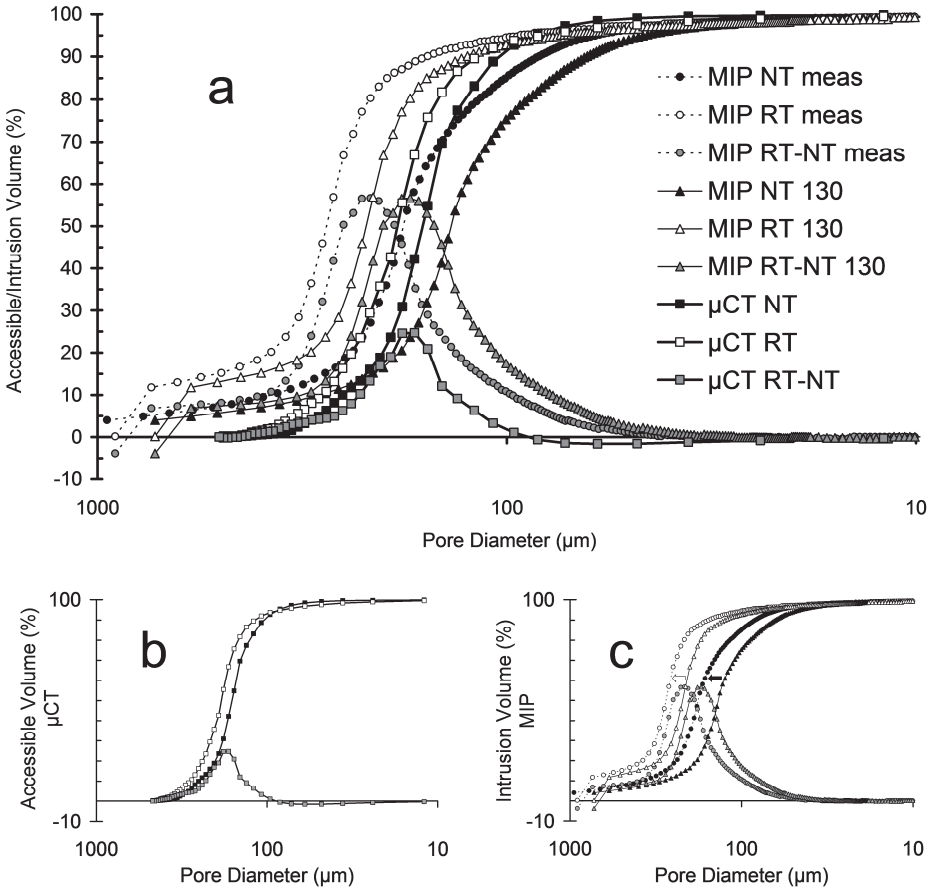

Figure 6.5: Cumulative DTVAL accessible volume (µCT) and intrusion (MIP) curves for non-treated (NT) and reticulate treated (RT) scaffolds as well as treatment difference curves (RT-NT). Plot A shows all data for comparison purposes while plots B and C show only the µCT and MIP data, respectively. MIP data calculated using assumed contact angle (130) and measured contact angels (meas).

Table 6.2: Measured values for polymer scaffolds.

		Effective Pore Diameter (µm)		Mean Pore Diameter (µm)		Porosity (%)	
Method	Source	NT	RT	NT	RT	NT	RT
µCT	Total Pore Volume	–	–	248	267	82	75
	Accessible Pore Volume	144	180	166	188	–	–
MIP	As Reported	134	212	127	178	80	74
	Calculated	–	–	217	316	–	–
Stereology	Microscopic Sections	–	–	231	352	71	77
	µCT Slices	–	–	261	274	81	71

polymer material in the pores whereas the pores of the RT scaffold appear clean and relatively free of remnant material. Images of the accessible pore volumes calculated by the DTVAL technique for the NT and RT scaffolds at threshold diameters of 300 and 210 µm (Figure 6.4c through 6.4f) are also shown. These images clearly demonstrate a difference in accessible volume both between the two pore (threshold) diameters examined and as a result of the reticulation treatment.

Intrusion volume from MIP and accessible volume from µCT were plotted against the inverse log of pore (threshold) diameter for both RT and NT scaffolds in Figure 6.5. Curves representing the difference between treatments (RT – NT) for both MIP and µCT are also shown. The location of peaks in the difference curves indicates the pore diameter where the reticulation treatment had the greatest influence and the resulting difference in intrusion/accessible volumes. Figure 6.5a presents all data to enable comparison. Figures 6.5b and 6.5c show the µCT and MIP data separately for clarity.

The measured contact angles (± standard deviation) for the NT and RT scaffolds were 147.3 ± 0.6 and 143.5 ± 0.4, respectively. Referring to the Washburn equation, an increase in the contact angle results in a proportional increase in the calculated pore diameters, or a shift to the left in Figure 6.5. Recalculating the MIP pore diameters using the measured contact angles resulted in 30% and 25% increases in the calculated pore diameters for the NT and RT scaffolds, respectively. The arrows in Figure 6.5c indicate the shift in the intrusion curves as a result of the different contact angles.

Pore diameter histograms for accessible and total volumes from µCT and intrusion volumes from MIP are plotted in Figure 6.6a and 6.6b. Mean pore diameters (from µCT total volume data) and mean interconnecting pore diameters (from µCT accessible volume and MIP data) were calculated from these data. Peaks in the accessible volume (µCT) and intrusion (MIP) curves indicate the effective pore sizes. These data, including porosity measurements, are compared to stereological measures in Table 6.2. Plots of accessible surface area, as well as treatment difference, are shown in Figure 6.7 and exhibit similar characteristics to those for accessible volume (Figure 6.5).

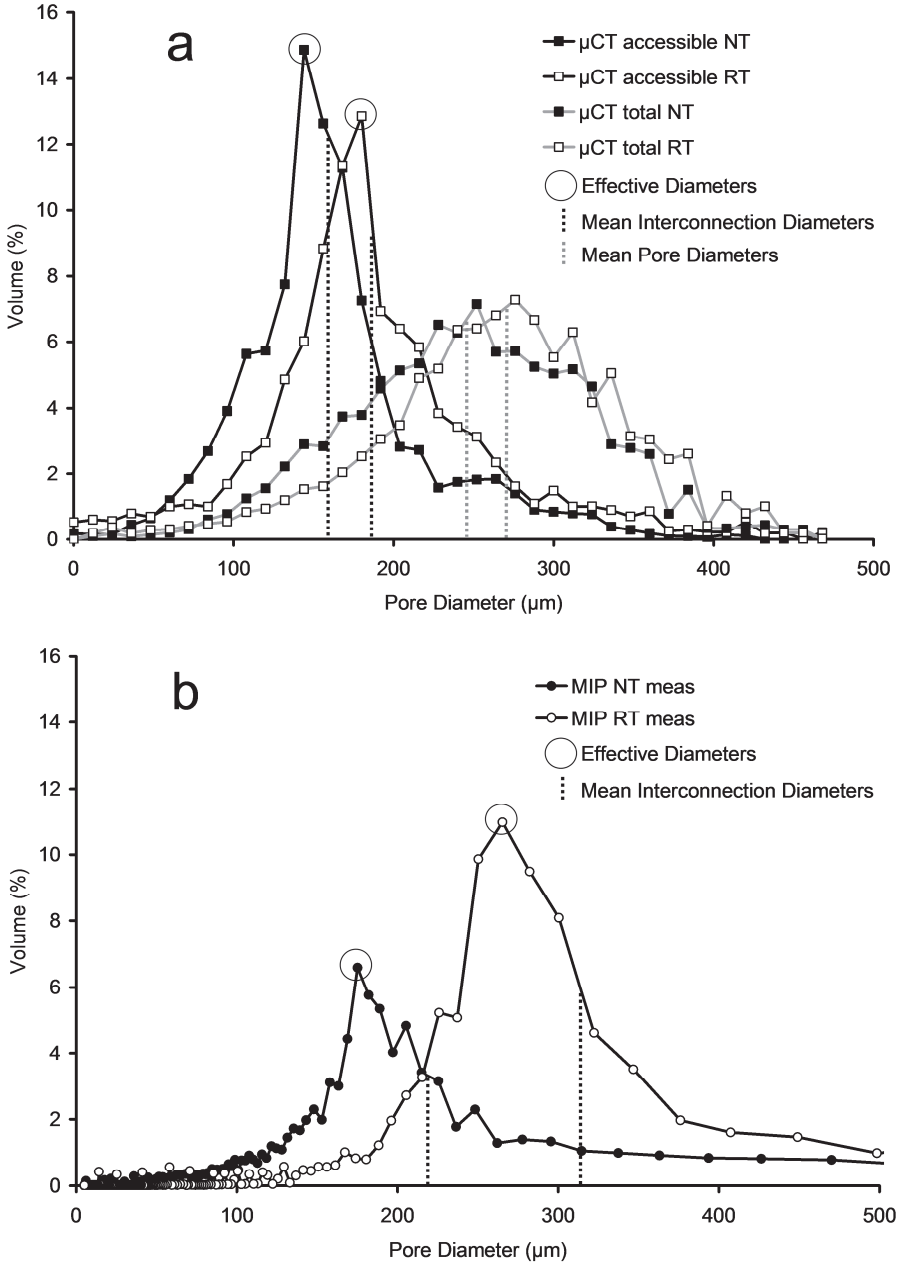

Figure 6.6: Pore diameter histograms for non-treated (NT) and reticulate treated (RT) scaffolds. Plot A derived from DTVAL data for accessible (black) and total (gray) pore volumes with mean interconnection diameters and mean pore diameters indicated by vertical lines, respectively. Plot B from reported MIP intrusion data with mean interconnection diameters indicated. Effective diameters are circled.

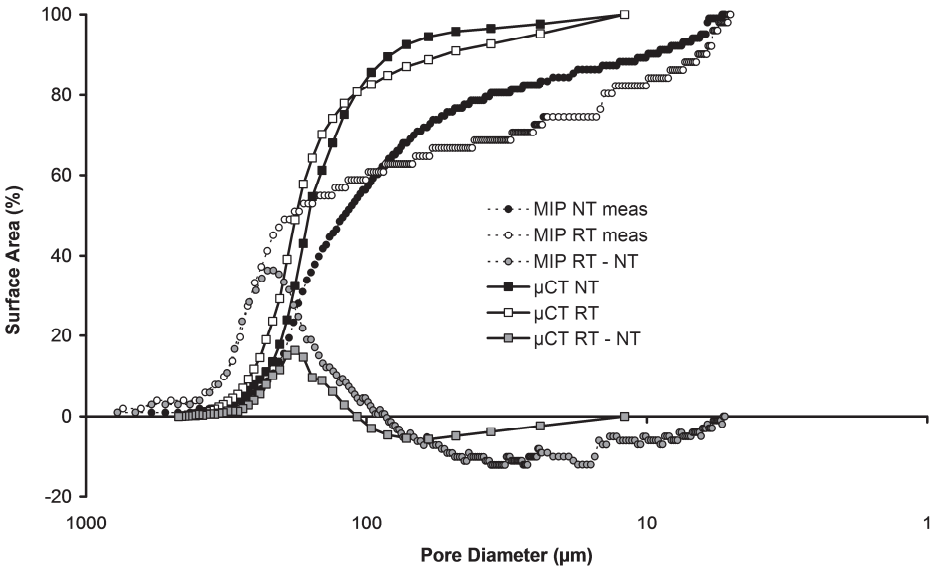

Figure 6.7: Cumulative accessible surface areas calculated from µCT and MIP data for non-treated (NT) and reticulate treated (RT) polymer scaffolds as well as treatment difference curves (RT-NT).

Discussion

The technique described in this paper processes µCT data sets to provide both qualitative and quantitative information regarding the interconnectivity and accessibility of macroporous structures. When applied to the reference material the DTVAL technique generated data consistent with geometric expectations for both the acrylic and ceramic phases. Less than optimal packing efficiency was accurately identified and values for interconnecting and mean phase diameters fell centrally within the ranges predicted by geometric calculations. Application of the DTVAL technique to the polymer scaffolds also provided useful information about their structure, interconnectivity and accessibility as well as the influence of the reticulation treatment on these properties. Low pressure MIP, stereology and the µCT technique provided similar information regarding porosity, effective pore diameter and mean (interconnecting) diameter. The influence of the reticulation treatment on scaffold accessibility, emphasized by the bell shaped treatment difference curves in figure 6.5, are comparable for MIP and µCT, however, the magnitude of the influence identified by µCT was approximately half that identified by MIP. Additionally, using the measured contact angles versus the assumed value of 130 degrees resulted in a 25% to 31% increase in the calculate pore sizes from the MIP data.

μCT based techniques, including DTVAL, are constrained by the finite resolution of the μCT system used. The minimum pore diameter that can be evaluated is at lease twice the volumetric resolution of the μCT data set. However, a key benefit to the μCT based technique is that it is nondestructive. The technique may be applied to scaffolds prior to implantation and possibly during (with in vivo μCT equipment) and after implantation as well, enabling measured structural properties to be related to biological responses. Furthermore, the technique enables 3-dimensional visualization of the accessible volumes, providing critical information that cannot be conveyed by simple measurements of graphs. Finally, once μCT data sets have been acquired, any number of visualization and quantification tools can be applied and reapplied to them.

Conclusions

The μCT based DTVAL technique presented herein provides a useful tool for evaluating the interconnectivity and accessibility of macroporous scaffolds. The technique provides similar information as MIP but in a nondestructive manor, enabling subsequent use of the material being evaluated.

Acknowledgements

The authors would like to thank The Netherlands Technology Foundation (STW) for financial support (grant UGN.4966).

7

A new in vivo screening model for posterior spinal bone formation: comparison of ten calcium phosphate ceramic material treatments

C.E. Wilson[1], M.C. Kruyt[1], J.D. de Bruijn[2,3], C.A. van Blitterswijk[3], F. C. Oner[1], A.J. Verbout[1] and W.J.A. Dhert[1]

[1] *Department of Orthopaedics, University Medical Center Utrecht, The Netherlands;*
[2] *Queen Mary, University of London, Mile End Road, London E1 4NS, United Kingdom;*
[3] *Institute for Biomedical Technology, University of Twente, PO Box 217, 7500 AE Enschede, The Netherlands*

Abstract

This study presents a new screening model for evaluating the influence of multiple conditions on the initial process of bone formation in the posterior lumbar spine of a large animal. This model uses cages designed for placement on the decorticated transverse process of the goat lumbar spine. Five conduction channels per cage, each be defined by a different material treatment, are open to both the underlying bone and overlying soft tissue. The model was validated in ten adult Dutch milk goats, with each animal implanted with two cages containing a total of ten calcium phosphate material treatments according to a randomized complete block design. The ten calcium phosphate ceramic materials were created through a combination of material chemistry (BCP, TCP, HA), sintering temperature (low, medium, high), calcination and surface roughness treatments. To monitor the bone formation over time, fluorochrome markers were administered at three, five and seven weeks and the animals were sacrificed at nine weeks after implantation. Bone formation in the conduction channels was investigated by histology and histomorphometry of non-decalcified sections using traditional light and epifluorescent microscopy. According to both observed and measured bone formation parameters, materials were ranked in order of increasing magnitude as follows: low sintering temperature BCP (rough and smooth) ≈ medium sintering temperature BCP ≈ TCP > calcined low sintering temperature HA > non-calcined low sintering temperature HA > high sintering temperature BCP (rough and smooth) > high sintering temperature HA (calcined and non-calcined). These results agree closely with those obtained in previous studies of osteoconduction and bioactivity of ceramics thereby validating the screening model presented in this study.

Introduction

Since the first investigations by Albee[9] nearly a century ago, posterior spinal fusion has become a commonly performed procedure for many orthopaedic and neurosurgical indications. The autologous bone graft is the golden standard for achieving a bony bridge between transverse processes. Despite the success of autologous grafts, bone harvest requires an extra operative procedure which incurs additional costs and carries inherent risks, such as donor site morbidity.[18, 255] Therefore, substitutes for the autograft are actively being investigated. Synthetic biomaterials, such as calcium phosphate ceramics, are attractive as bone grafts substitutes due to their unlimited supply and ease of sterilization and storage. The osteoconductive nature of calcium phosphate ceramics has been well established.[92, 121, 130] Commercially available ceramic bone graft substitutes are currently utilized in posterior spinal fusion primarily as bone graft extenders.[35] These materials have also been validated for use as bone graft substitutes for instrumented posterior spinal fusion in children and young adults.[71, 160, 202] Emerging technologies for spinal fusion, including bone inducing growth factors such as bone morphogenic proteins (BMP) and cell based bone tissue engineering, are also utilizing porous calcium phosphate ceramics as carriers and/or scaffolds.[149, 152, 214] Furthermore, the recent identification of certain calcium phosphate materials with the inherent ability to induce bone formation is also of great potential for spinal fusion applications.[206, 261] This increasing interest necessitates a relevant and efficient model, preferably in a large animal, for screening materials and conditions to support the more rapid development and optimization activities. Numerous posterior spinal fusion models have been described,[137, 215] however, these models are typically functional in nature, i.e. they aim to create a functional fusion of one or more spinal levels, and utilize porous granules of material. While these types of models are essential for evaluating new treatments, they are inefficient for the screening of multiple parameters. Additionally, it is difficult to ascertain how and why materials and treatments behave differently using the traditional functional models.

The purpose of the current study was to introduce and validate a new screening model for the simultaneous evaluation of multiple conditions on the initial process of bone formation. This model was inspired by the well-established multi-channel cage model of Spivak et al.[223] for evaluating intramedullary bone formation in the dog, but adapted for use on the transverse processes of the goat lumbar spine. The cages for this study were designed to hold five material conditions each. In the current study, two cages were implanted in each animal allowing ten material conditions to be evaluated. The ten material conditions examined included

differences in material phases, sintering temperatures, surface roughness and calcination treatments.

Materials and Methods

Experimental design

A total of 10 adult Dutch milk goats were used following approval of the institutional animal care committee. Two spinal cages containing a total of ten bone conduction channels (five per cage), each of a different ceramic material condition, were implanted bilaterally on the transverse process of the L4 vertebrae of each goat according to a randomized complete block design. To monitor the bone formation over time, fluorochrome markers were administered at three, five and seven weeks and the animals were sacrificed at nine weeks after implantation. Bone formation into conduction channels was investigated by histology and histomorphometry of non-decalcified sections using epifluorescent and light microscopy.

Cages

Polyacetal cages were designed for fixation to the transverse process of the goat lumbar spine. Each cage consisted of two side walls, two end pieces, four stainless steel machine screws for cage assembly and two self-tapping bone screws to attach the cage to the transverse process. Ridges on the cage side walls were designed to separate five pairs of material plates to create five bone conduction channels. These channels were open to both the underlying bone and overlying soft tissues (Figure 7.1), had cross sections of 0.8 by 5.0 mm and were 8.0 mm in length. The polyacetal components were sterilized by soaking in 80% ethanol for at least 20 minutes and the metal screws were sterilized by autoclave.

Materials

Ceramic plates were manufactured to achieve ten conditions through a combination of ceramic composition, calcinations, sintering temperature and

Table 7.1: Material conditions by calcination temperature, sintering tempurature and surface roughness.

Ceramic material	Calcination temp.	Sintering temp.	Surface
BCP r h r	n/a (**r**aw)	1300℃ (**h**igh)	**r**ough
BCP r h s	n/a (**r**aw)	1300℃ (**h**igh)	**s**mooth
BCP r m s	n/a (**r**aw)	1200℃ (**m**ed)	**s**mooth
BCP r l r	n/a (**r**aw)	1150℃ (**l**ow)	**r**ough
BCP r l s	n/a (**r**aw)	1150℃ (**l**ow)	**s**mooth
TCP r l s	n/a (**r**aw)	1150℃ (**l**ow)	**s**mooth
HA l h s	900℃ (**l**ow)	1250℃ (**h**igh)	**s**mooth
HA l l s	900℃ (**l**ow)	1150℃ (**l**ow)	**s**mooth
HA r h s	n/a (**r**aw)	1250℃ (**h**igh)	**s**mooth
HA r l s	n/a (**r**aw)	1150℃ (**l**ow)	**s**mooth

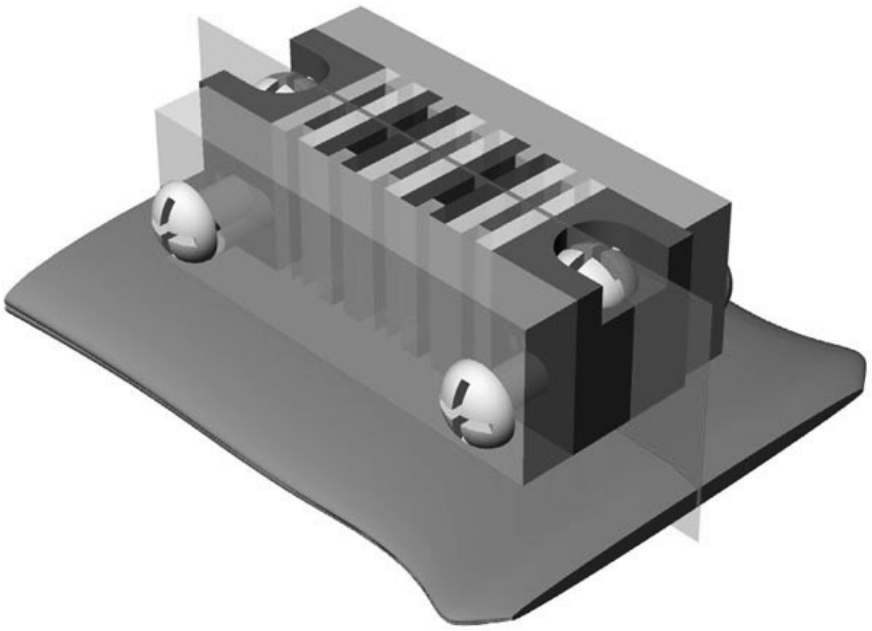

Figure 7.1: Computer generated image of conduction cage placed on a transverse process. The sectioning plane used for histology is indicated. *(See color image on page 201)*

surface roughness, as specified in Table 7.1. Hydroxyapatite powder (HA, Merck, Germany), beta-tricalcium phosphate powder (TCP, Merck, Germany) and BCP powder (HA/TCP, weight% 80/20, IsoTis SA) were obtained commercially. A portion of HA powder was calcined by heating from ambient to 900 °C at a rate of 100 °C/hour and then cooling naturally with no dwell period. Aqueous slurries of calcined HA, raw HA, raw TCP and raw BCP powders were prepared by the slow admixing of components. The calcined HA slurry consisted of 67.1 wt% calcined HA powder, 28.6 wt% demineralized water, 2.6 wt% ammonia solution (25%, Merck), 1.5 wt% deflocculant (Dolapix, Aschimmer & Schwarz GmbH, Germany), and 0.15 wt% of binder (CMC, Pomosin BV, The Netherlands) added once a homogenous blend was obtained. The raw HA, TCP and BCP slurries consisted of 56.4 wt% ceramic powder, 37.6 wt% demineralized water, 3.9 wt% ammonia solution and 2.1 wt% deflocculant. No binder was added to the raw powder slurries. Cubes of approximately 12x12x12 mm were cast from these slurries and allowed to air dry for 12 hours at ambient temperature followed by 24 hours in an air filled oven at 50 °C. Debinding of the ceramics was performed by heating at a rate of 0.5 °C/minute to 400 °C and then cooling naturally with no dwell period. The ceramic cubes were then sintered using a 600 minute heating phase and a 480 minute dwell period at the appropriate sintering temperature (Table 7.1) followed by

natural cooling. Plates with dimensions of 7.0 mm by 8.0 mm by 1.1 mm were cut from sintered blocks using a sawing microtome (Leica, Germany). All plates were polished to 0.95±0.03 mm in thickness using a rotary polisher and 1200 grit silicon carbide paper (Struers, Denmark) ensuring both sides of the plate were polished. Rough surfaces were created by unidirectionally abrading both sides of the plates on 120 grit paper. The plates were cleaned by ultrasound for 15 minutes each in acetone, 100% ethanol and demineralized water. After air drying at 50 °C, the scaffolds were sterilized by autoclave. Verification of the composition and phase purity of the plates was performed by FTIR and XRD analysis. Characterization of surface features and microporosity was conducted via scanning electron microscope (SEM) observation.

Implantation and fluorochrome labeling

Following the approval of the institutional animal care committee, ten adult female Dutch milk goats, aged 24 to 36 months, were acquired and allowed to acclimate for at least four weeks. Prior to the surgical procedure, two spinal cages for each animal were aseptically assembled with the ten material conditions arranged according to a randomized complete block design. The surgical procedures were performed under general inhalation anesthesia of a halothane gas mixture (Sanofi, The Netherlands) preceded by detomidine sedation (Pfizer, The Netherlands). After shaving and disinfecting the thoracolumbar region, a central skin incision, from approximately T8 to L5, was made to expose the muscle fascia. This incision supported implantation of the spinal implants as well as intramuscular and iliac implants that are not discussed in the present manuscript. Bilateral muscle incisions were then made and retracted to expose both transverse processes of the L4 vertebrae. The processes were decorticated using an angled bone rasp. Care was taken to ensure the even decortication of a flat surface with an area sufficient for placement of a cage. One cage was placed on each transverse process and pilot holes were drilled under saline irrigation. Two stainless steel self-tapping screws were then inserted to firmly attach each cage. Light finger pressure was applied to the top of each cage just prior to muscle closure to ensure the ceramic plates were in contact with the underlying bone. The muscle fascia was closed with non-resorbable sutures and the skin closed in two layers with resorbable sutures. Buprenorphin (Shering-Plough, The Netherlands) was administered for postoperative pain relief. Sequential fluorochrome markers were administered at three, five and seven weeks after implantation. Calcein Green (10 mg/kg intravenously, Sigma, The Netherlands) was administered at either three or seven weeks, Xylenol Orange (80 mg/kg intravenously, Sigma, The Netherlands) was correspondingly administered at either seven or three weeks and Oxytetracyclin (Engemycine 32 mg/kg intramuscularly, Mycofarm, The Netherlands) was always

administered at 5 weeks. At nine weeks, the animals were sacrificed by an overdose of pentobarbital (Organon, The Netherlands) and the implants retrieved.

Histological processing and histomorphometry

The explanted samples were fixed in a solution of 4% glutaraldehyde and 5% paraformaldehyde. Fixed samples were dehydrated by ethanol series and embedded in polymethylmethacrylate. Two centrally located (Figure 7.1) 10 µm thick sections were cut from each sample using a sawing microtome (Leica, Germany). The first section remained unstained for epifluorescence microscopy and the second section was stained with methylene blue and basic fuchsin for routine histology. The general tissue response, bone formation and fluorochrome markers were evaluated using a light/fluorescence microscope (E600, Nikon, Japan) equipped with a quadruple filter block (XF57, dichroic mirror 400, 485, 558 and 640nm, Omega Optics, The Netherlands). High resolution, low magnification (4x), digital fluorescent micrographs were made of unstained sections for histomorphometry. High resolution digital scans of the stained sections were made for histomorphometry using a photographic film scanner (Dimage Scan Elite 5400, Minolta, Japan). Histomorphometry was performed using a PC-based system with the KS400 software (version 3, Zeiss, Germany). A custom macro was developed to measure the height of bone in each channel (bone height), percentage of available space occupied by bone in each channel (bone area%) and the length of direct contact between bone and ceramic in each channel (contact length). Bone height was effectively measured at three, five, seven and nine weeks by measuring the maximum height of each fluorochrome marker in the fluorescence images and the maximum bone height on the digital images of the stained sections.

Statistics

Box plots were used to display statistics of the measured parameters. To review, a box plot displays the lower, median and upper quartiles as well as the minimum and maximum of a data set. The box depicts the interquartile range and encompasses the middle 50% of the data values. The whiskers extend from the box to the minimum and maximum values. Observation between 1.5 and 3 times the interquartile range are outliers and observations greater than 3 times the interquartile range are extreme outliers. The data were subsequently analyzed by ANOVA for randomized complete block design with a post hoc Tukey's HSD ($\alpha = 0.05$) to determine differences between material conditions. Partial correlation coefficients between measured parameters (nine week bone height, bone area% and contact length) were also calculated.

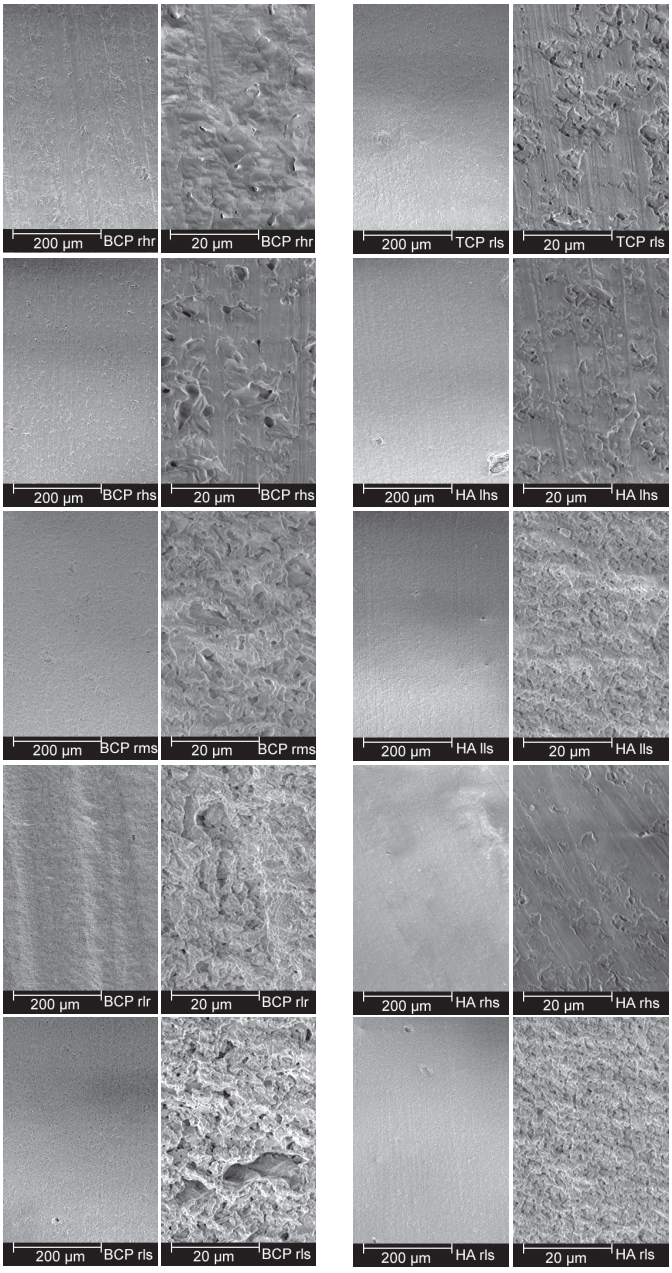

Figure 7.2: Low and high magnification SEM micrographs of each of the ceramic materials used in this study. Material name and magnification are indicated in data bar at bottom of each image. BCP materials are in left hand columns going from high sintering temperature (top) to low sintering temperature (bottom). Similarly, TCP and HA materials are in the right hand columns. Refer to table 1 for specific material condition associated with material name.

Results

Materials

The XRD patterns and FTIR spectra of the ceramic materials were indicative of the expected materials and demonstrated no extraneous phase impurities. As expected, lower sintering temperatures resulted in more amorphous materials, as demonstrated by broader peaks in the XRD patterns. Conversely, higher sintering temperatures resulted in more crystalline materials. No influence as a result of powder pre-calcinations was noted in the XRD patterns and FTIR spectra of the HA materials. SEM observations of the surface characteristics of the ceramic plates revealed general differences that correlated with material and sintering temperature (Figure 7.2). The low and medium sintering temperature BCP materials exhibited a spectrum of surface micro- and macroporosity features from approximately 1 to 20 µm in size. In comparison, the high sintering temperature BCP materials displayed much less surface porosity features. The effect of the surface roughening procedure on the low and high sintering temperature BCP materials is apparent at lower magnifications (100x). The roughing resulted in wide gouges with a deep appearance for the low sintering temperature BCP while the high sintering temperature BCP exhibited relatively narrow and shallow scratches. At higher magnification (1000x), little difference was apparent between the rough and smooth surfaces for low sintering temperature BCP. However, the roughened high temperature BCP material demonstrated a generally coarse surface texture as compared to the smooth high temperature BCP. The surface features of the low sintering temperature HA materials did not appear to be influenced by the calcination treatment and displayed much more uniform surface microporosity, approximately 0.5 to 2 µm in size, in relation to the low temperature BCP materials. At the higher sintering temperature the HA material exhibited much smoother surfaces with little microporosity, however, the calcination treatment appeared to increase the surface microporosity and texture somewhat. The TCP material, in contrast to the other materials sintered at low temperatures, exhibited very different surface micro-features with intermixing patches of microporosity and smooth surfaces in near equal proportions.

in vivo results

There were no surgical complications and all cages were attached firmly to the underlying transverse process at retrieval. No macroscopic or microscopic indications of infection were found.

Histological observations of stained sections clearly revealed greater bone formation in low and medium sintering temperature materials compared to high

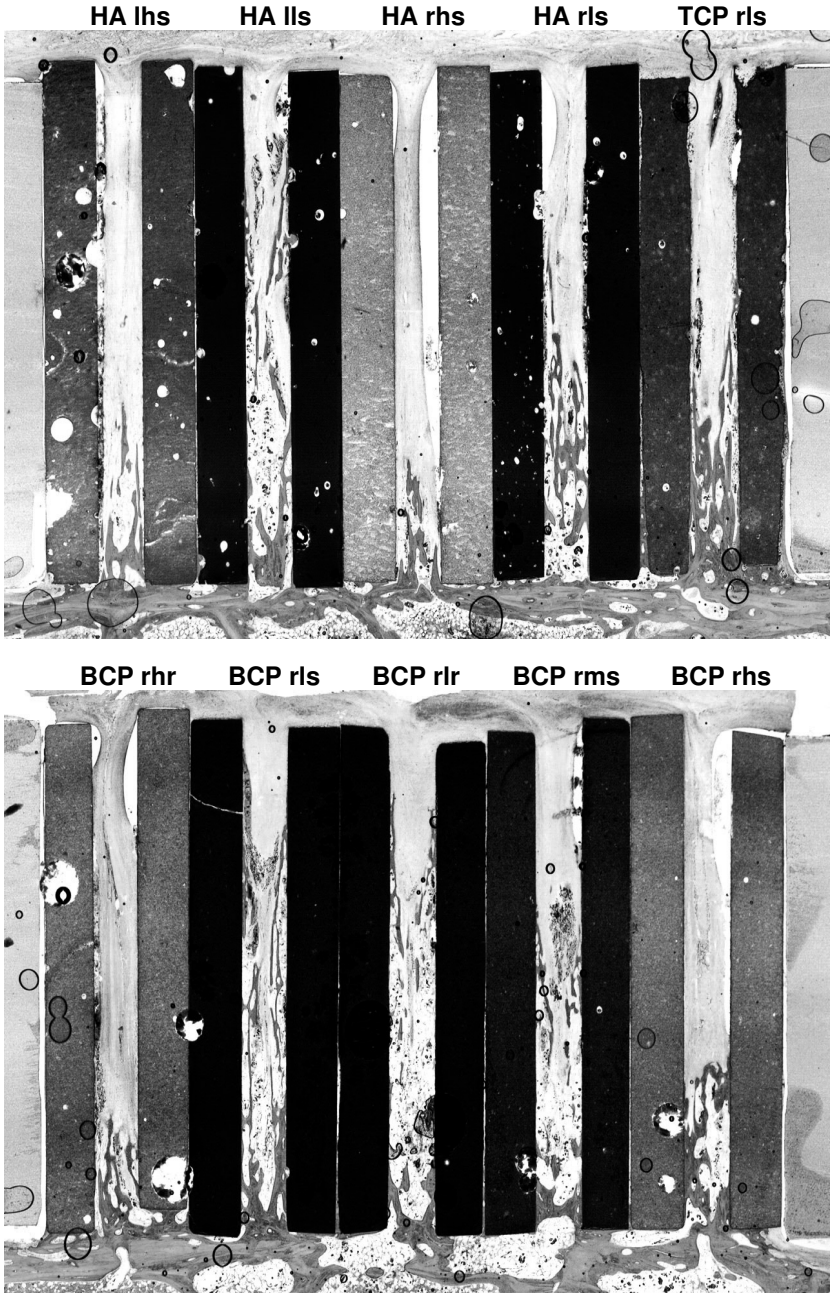

Figure 7.3: Stained (methylene blue/basic fuchsine) histological sections. Bone is stained pink/red and the ceramic plates light to dark gray. The transverse processes are at the bottom the images and the polymer cage is visible at the extreme right and left of the images. Material treatment label (ref. table 1) is indicated above the conduction channels created by pairs of material plates.
(See color image on page 202)

sintering temperature materials with regard to bone area. Additionally, these materials demonstrated increased bone heights in the channels and displayed numerous sites of direct contact between bone and ceramic. In contrast, high sintering temperature BCP and HA materials had notably lower bone areas and heights in the channels with virtually no contact between bone and ceramic (Figure 7.3). Although the amount of bone formation in the TCP channels was similar to that of the low sintering temperature BCP and HA materials, the trabecular like structures appeared thicker in comparison, particularly in close proximity to the transverse process. Also noteworthy was the visible degradation of the TCP material, particularly toward the channel end furthest from the transverse process. Pre-calcination of the HA powder and roughening of BCP surfaces demonstrated no observable influence compared to corresponding material and sintering conditions. Finally, the appearance of the ceramic materials themselves in the stained histological sections was noticeably different. In general, low sintering temperature materials appeared much darker compared to the lighter gray of the high sintering temperature materials (Figure 7.3). The exception was the TCP material, which had a distinctly lighter appearance compared to the other low sintering temperature materials.

Epifluorescent microscopy of the sequential fluorochrome labels revealed the dynamics of bone formation in the channels (Figure 7.4). All three labels were present in the healing bone of the transverse process. However, the first label (three weeks) was not always present within the bone in the ceramic channels. The second (five week) and third (seven week) labels were always present within bone in the channels. The fluorochrome labels indicated that the bone formation occurred in two manners, as a spur from the underlying transverse process or via nucleation of bone formation at distinct sites on the ceramic surface. The spur type bone formation had a centrally located early label (three or five weeks) that did not connect with the ceramic surface within a channel. This early bone formation was then at least partially surrounded by a layer of bone containing a later label, which may or may not contact the ceramic surface. This was the primary mode of bone formation in the high sintering temperature HA materials. The nucleation type bone formation presented as distinct sites where an early label was directly apposed or very near the ceramic surface. The order of fluorochrome labels then indicated that bone formation started at the surface and progressed toward the channel interior. Although these surface bone nucleation sites were often not connected by bone lying on the ceramic surface they were almost always connected by thin, trabecular like struts of bone lying away from the ceramic surface in the channel interior. This type of bone morphology was seen in the stained histology (Figure 7.3). The nucleation type of bone formation was most prominent in the low and medium

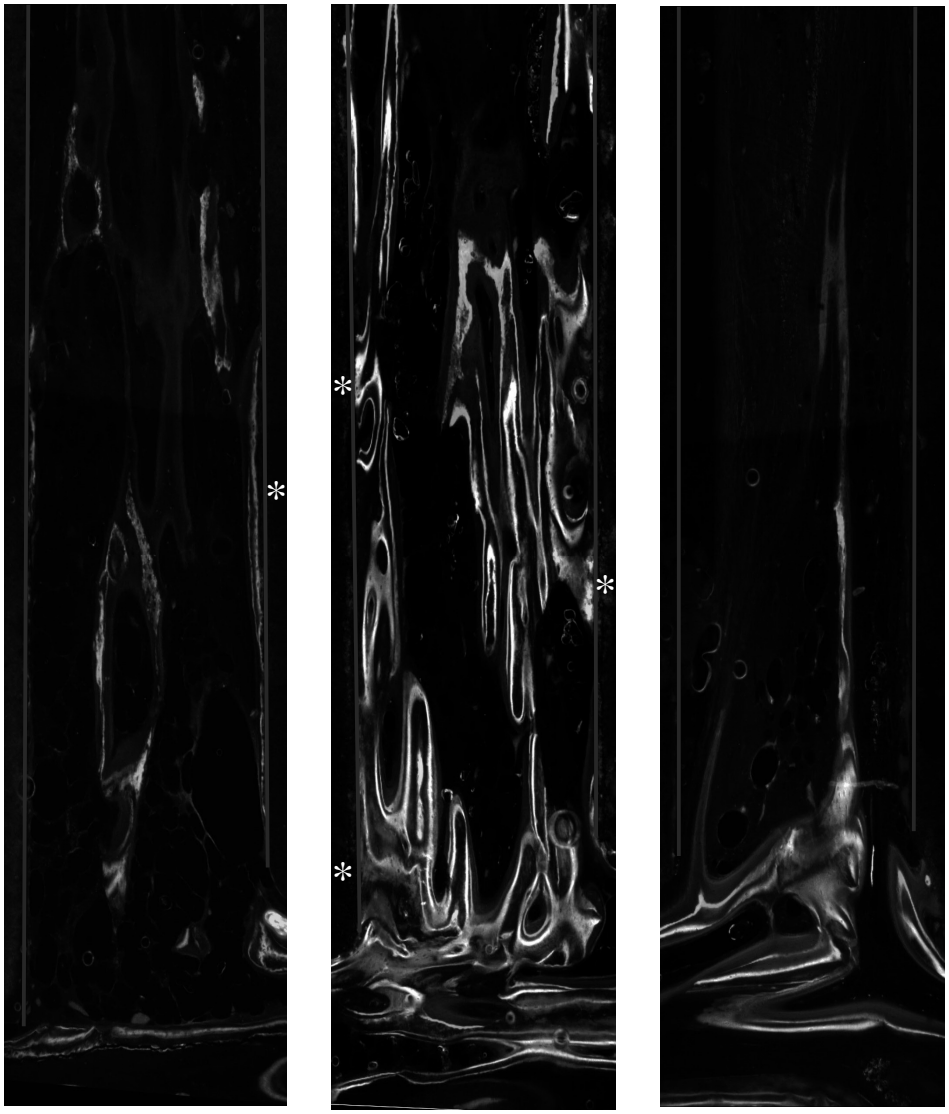

Figure 7.4: Epifluorescent microscopy images of fluorochrome markers. Label at bottom of each image indicates the goat number and material treatment. In all three images the earliest label is green (3 weeks, calcein green), the middle label is yellow (5 weeks, oxytetracyclin) and the final label is orange (7 weeks, xylenol orange). Vertical blue lines indicate the approximate location of the ceramic surface. Examples of bonding osteogenesis are indicated by an *. *(See color image on page 203)*

sintering temperature materials and was the exclusive means of bone formation at distances of more than a few millimeters from the transverse processes.

Histomorphometric data were analyzed graphically and statistically. Box plots of bone height at three, five, seven and nine weeks, shown in Figure 7.5, demonstrate the progression of bone formation for the different material conditions. At three weeks, the high sintering temperature BCP materials (BCP rhr, BCP rhs) and, in particular, the high sintering temperature HA materials (HA lhs, HA rhs) exhibited inferior bone height compared to the six lower sintering temperature materials (BCP rms, BCP rlr, BCP rls, TCP rls, HA lls and HA rls). All materials exhibited progressively greater bone height in the channels as the implantation period increased. However, the six lower sinter temperature materials continued to outperform the higher sintering temperature materials. Comparing nine week bone height results with contact length and bone area%, a common pattern is apparent (see also Figure 7.6). The two low temperature BCP ceramics (BCP rls and BCP rlr), the medium temperature BCP ceramic (BCP rms) and the TCP ceramic (TCP rls) yield the highest mean values for all measurements. This is followed by the two low temperature HA materials (HA lls and HA rls), then the two high temperature BCP materials (BCP rhs and BCP rhr) and, finally, the two high temperature HA materials (HA lhs and HA rhs). Statistical analyses were performed on the bone height, contact length and bone area% measurements at the end point of the nine week implantation period, and demonstrated highly significant ($p < 0.01$) differences within all three parameters. Post-hoc, pair wise comparisons using Tukey's HSD test were performed to illustrate the significant differences between the ten material treatments for the three measurements. Figure 7.7 graphically depicts these results. The material treatments in Figure 7.7 have been generally ordered by their mean values and in the groupings suggested by the box plots. The same sequence is used for the three parameters to enable easier comparison of the significance patterns. Although the results are actually mirrored around the diagonal, displaying only the results above the diagonal enables the charts to be interpreted in a row-wise manner. In this case, when significance is indicated by a shaded block at the intersection of a row and column, the value for the material treatment represented by the row is always significantly greater than the value for the material treatment represented by the column. In general, there is a notable similarity between the significance patterns for the three parameters with material type and sintering temperature being the primary reasons for significant differences. Calcination of the HA powder consistently resulted in higher measurement means compared to the non-calcined (raw powder) ceramics with the same final sintering temperature (HA lls and HA rls, HA lhs and HA rhs). Additionally, the combination of pre-calcination with low sintering temperature

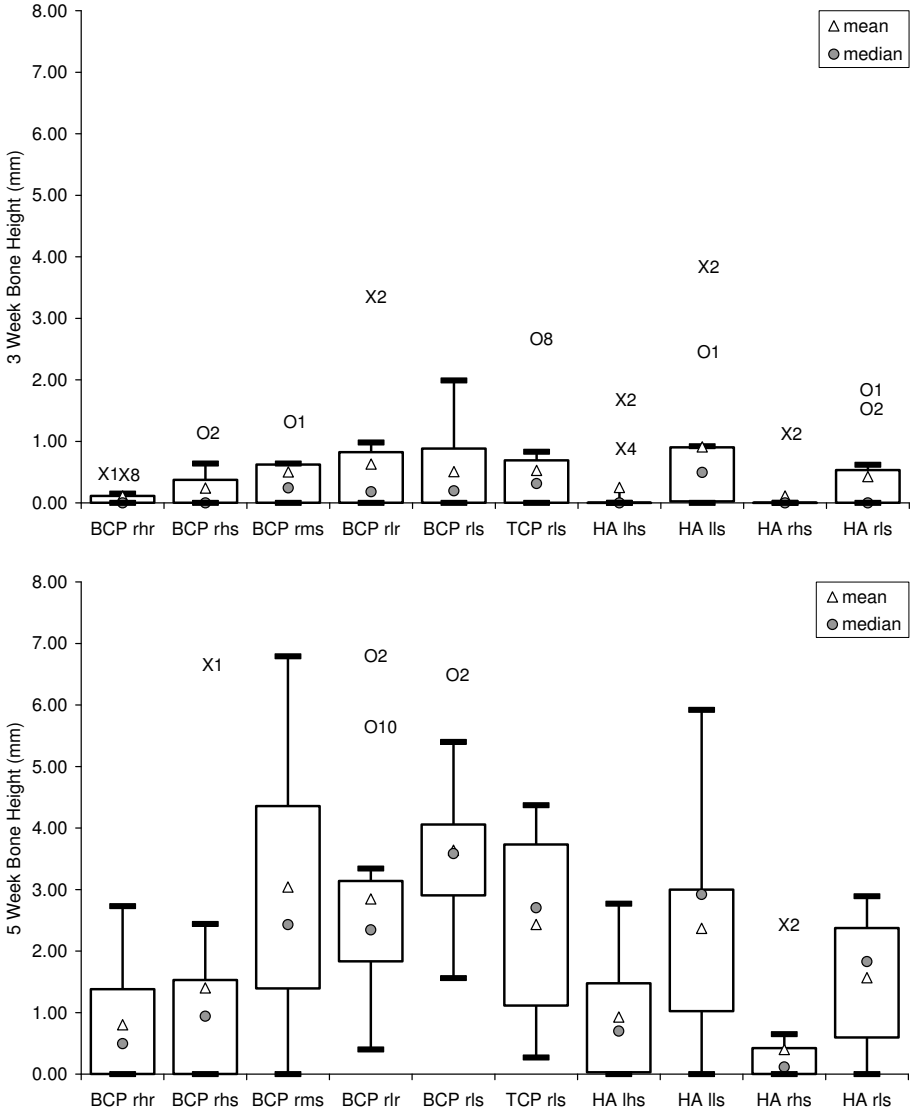

Figure 7.5: Box plots of bone height at 3, 5 and 7weeks, measured on fluorescent images, and at 9 weeks, measured on stained histology. The symbol "**O**" indicates and outlier and the symbol "**X**" indicates an extreme outlier. The number following these symbols indicates the animal associated with the measurement.

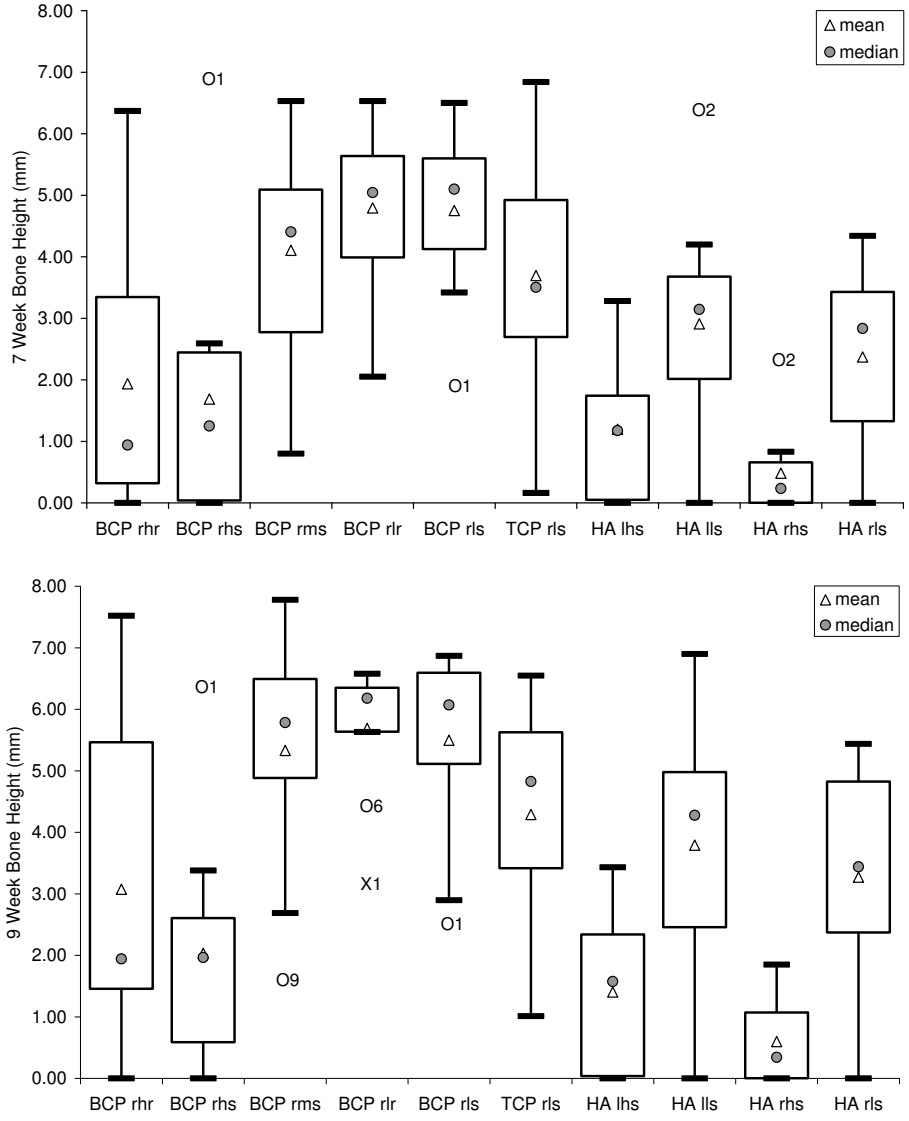

Figure 7.5: (continued)

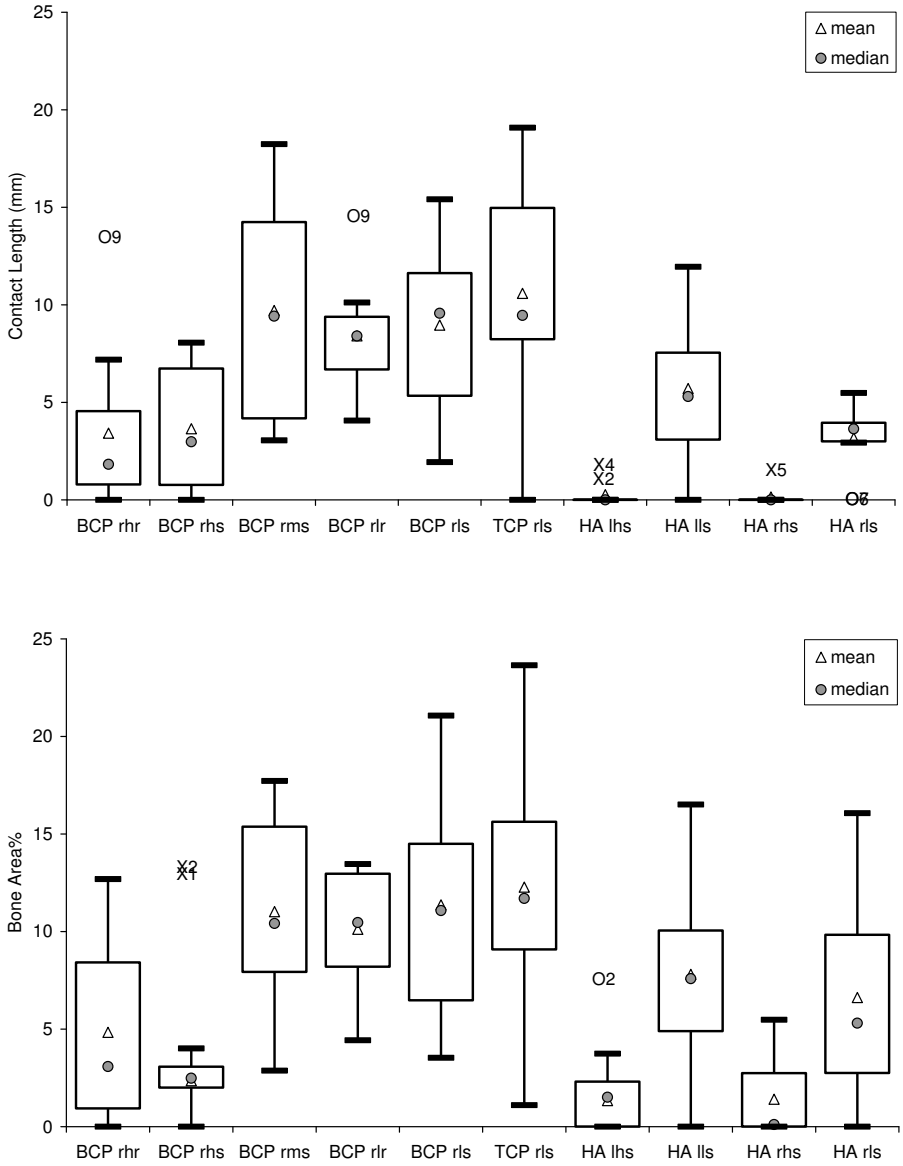

Figure 7.6: Box plots of bond contact length and bone area% measured on stained histology. The symbol "**O**" indicates and outlier and the symbol "**X**" indicates an extreme outlier. The number following these symbols indicates the animal associated with the measurement.

yielded significantly higher values for all three measurements than both of the high sintering temperature HA materials. However, the use of raw powder with a low sintering temperature did not demonstrate these significances. Roughening of the low and high temperature BCP surfaces had little influence compared to smooth surfaces. Finally, a partial correlation test between measured parameters was performed while controlling for material condition and revealed highly significant correlations ($p<0.01$) between all three measured parameters.

Discussion

We demonstrated in the current manuscript a new screening model that concerns early bone formation from the decorticated transverse process of the goat lumbar spine. The observed bone formation occurred by two modes depending upon the material treatment and manifested as either a spur extending from the underlying transverse process or via nucleation of bone formation at distinct sites on the ceramic surface. The spur type bone formation was not dependent upon the surface of an implant. This type of bone formation has been labeled as bone ingrowth. In this study, bone ingrowth occurred in all materials but was the dominate mode of bone formation in the high sintering temperature ceramics, particularly the HA materials. The nucleation type bone formation was the dominant mode of bone formation in the lower sintering temperature ceramics and was observed to be highly surface dependant. This is termed osteoconduction and is described as the growth or spreading of bone over a surface. However, bone matrix does not have the intrinsic ability to grow or spread once formed. Therefore, it is a population of migratory osteogenic cells that are conducted along a surface and must be responsible for the bone formation. Once these cells begin producing matrix, they stop migrating.[58] Thus, osteoconduction may be defined as the spreading of bone over a surface preceded by the ordered migration of differentiating osteogenic cells. An important aspect of osteoconduction is the direct bonding of bone matrix with the material surface without an interposing fibrous tissue layer, so-called bonding osteogenesis.[56]

Materials that elicit a bonding osteogenesis response are termed bioactive. The bioactive process for ceramic materials has been covered in detail elsewhere.[51, 62, 63, 140] and is described by several basic steps: (1) the partial dissolution of the ceramic resulting in an increase in calcium and phosphate concentration in the local microenvironment; (2) precipitation of a carbonate calcium phosphate layer; (3) association and then incorporation of the precipitated layer with the organic matrix of newly formed bone. The formation of the prerequisite carbonate calcium phosphate layer is dependent upon the solubility or resorbability of the ceramic

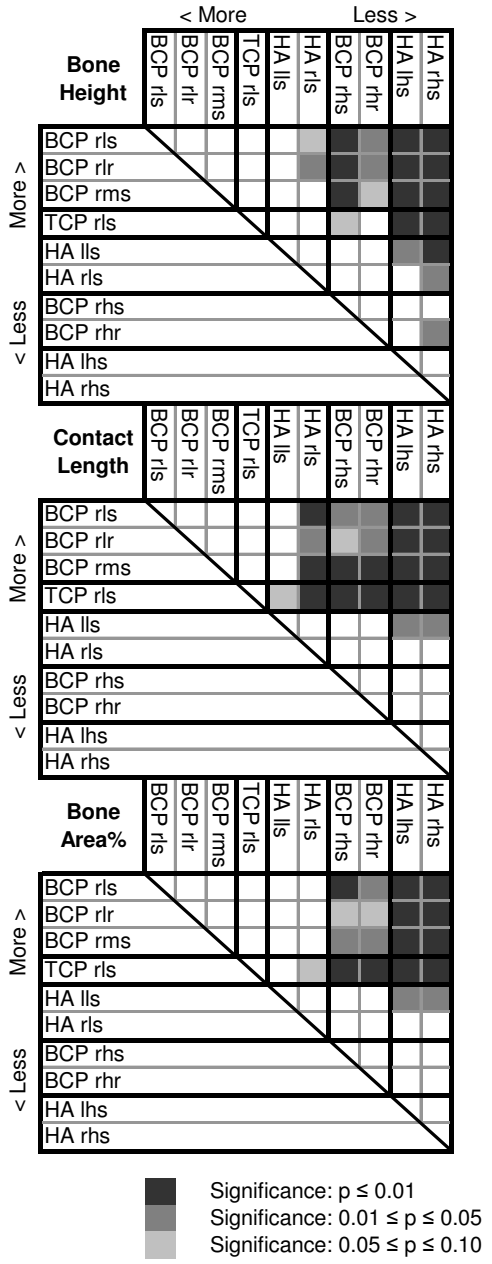

Figure 7.7: Graphical representation of Tukey's HSD post hoc test to determine significant differences between material treatments. These charts are interpreted in a row wise manner. When a shaded area lies at the intersection of a row and column, the material treatment represented by the row has a significantly higher mean than the material represented by the column. The legend at the bottom indicates the significance levels associated with the three shades of grey.

substratum. For example, BCP ceramics become more resorbable and exhibit a greater abundance of precipitated carbonate calcium phosphate when the ratio of β-TCP to HA is increased.[53, 164] Sintering also influences solubility with higher temperatures, thereby decreasing the solubility. This imparts a more detailed solubility range to the BCP and HA materials as a result of the sintering temperatures used in their production. Furthermore, microporosity has also been suggested as an important factor in the bioactivity of ceramics.[52, 258] Microporosity can greatly increase the surface area of a ceramic, facilitating greater dissolution and, therefore, enhancing the precipitation of the carbonate calcium phosphate layer. Additionally, microporosity may enable bone morphogenic proteins adsorbed on their surface to reach local concentrations greater than the threshold value needed to induce bone formation.[53, 206, 258] Microporous surfaces may also enhance the adhesion, proliferation, differentiation and matrix deposition of osteogenic cells.[136, 157]

Although dissolution characteristics were not assessed in this study, well established data regarding the dissolution characteristics of calcium phosphate materials[69, 82] may be used to order the expected solubility of the ceramics in this study. The overall dissolution characteristics result from the interaction of material chemistry, sintering temperature and microporosity. The solubility order based on chemistry alone is: TCP >> BCP > HA. It is important to note that the BCP material in this study is approximately 80% HA. Therefore, based on chemistry alone, the BCP is likely to behave more similarly to HA than to TCP. Considering sintering temperature, the solubility of the BCP and HA materials can be ordered as follows: BCP (low) > BCP (medium) > BCP (high) and HA (low) > HA (high). Higher sintering temperatures increase the crystallinity (reduce vacancies in crystal lattice) and increase crystal grain size, both of which reduce solubility. Finally, the ceramics can be ordered based on the amount of surface microporosity as determined by SEM observation: BCP (low sintering temp.) > BCP (medium sintering temp.) > HA (low sintering temp.) > TCP > BCP (high sintering temp.) > HA (high sintering temp.). Microporosity was generally associated with lower sintering temperatures. However, microporosity can only modulate the solubility of a material by changing the surface area. Therefore, the solubility of materials used in this study will be in line with the predictions made from chemistry and sintering temperature with microporosity increasing the solubility of the lower sintering temperature materials. We can predict the following solubility order with some certainty: TCP > BCP (low) > BCP (medium) > BCP (high) > HA (high). The low sintering temperature HA cannot be precisely placed in this order, however, we know that it will be less soluble than BCP (low) and more soluble than HA (high).

While all the materials in this study have been previously described as bioactive[55, 70, 75, 163] and did exhibit areas of direct bone bonding, observations and measures of this activity varied with material conditions. These variations in bioactivity agreed very well with the literature cited in the previous paragraphs. As a rule, the bioactivity, as determined by observation and histomorphometry, correlated accurately with the expected solubility of the ceramics. Low and medium sintering temperature BCP materials (BCP rls, BCP rlr and BCP rms) and the single TCP material (TCP rls) yielded similar but significantly higher values for bone height (9 week), contact length and bone area% compared to HA and, in most cases, BCP materials sintered at high temperatures (HA lhs, HA rhs, BCP rhs and BCP rhr). The low sintering temperature HA materials (HA lls and HA rls), while not achieving the same mean values as TCP and the low and medium temperature BCP materials, attained greater values than the high temperature materials.

Several specific observations from the current study are of particular interest. First, osteoconductive and bioactive qualities were virtually absent from the high sintering temperature materials. Second, TCP, despite noticeably less surface microporosity, performed as well as the low and medium sintering temperature BCP materials (TCP was also sintered at low temperature). This suggests that microporosity may not play as critical a role in bioactivity as suggested by others,[136, 157, 258] and that another property of the material, such as solubility, is more essential. TCP was certainly the most soluble material in the current study as it was the only material with observable degradation. Third, the bioactivity of low sintering temperature HA materials was improved by using calcined HA powder as compared to raw HA powder. The reason for this is not clear, however, it is know that calcination treatment provides a more spherical powder morphology.[192] This may result in a more interconnected microporosity in the ceramic plates made from calcined powder as compared to raw powder. This, in turn, would enhance the solubility characteristics of this material and the subsequent precipitation of a carbonate calcium phosphate layer. Finally, the surface roughness imparted on the low and high sintering temperature BCP materials had no observed or measured influence on bone formation. The high magnification SEM observations indicate a likely reason for this. The roughening protocol used in this study did not appreciably impact the surface roughness at the micro scale and therefore did not appreciably alter any material parameters related to bioactivity.

It is difficult to ignore the similarity, both in appearance and definition, between osteoconduction and osteoinduction.[152, 253] Urist defined osteoinduction as the mechanism of cellular differentiation towards bone of one tissue due to the physiochemical effect of contact with another tissue.[235] At the time, only tissues,

such as demineralized bone matrix and uroepithelium, were known to have this ability. More recently, some synthetic biomaterials have also been recognized as osteoinductive, i.e. they can induce bone formation at extraskeletal locations.[66, 205, 258] Bone formation in both osteoconduction and osteoinduction relies upon differentiated bone cells producing bone matrix which is then mineralized. The critical difference between the phenomena is the population of cells involved. Osteoconduction can draw upon a population of osteoprogenitor cells in adjacent bone tissue. Osteoinduction relies upon a population of cells available either in the local tissue (e.g. muscle or subcutaneous tissue) or systemically. Despite this difference, the mechanisms involved are likely to be very similar and insights into these mechanisms will be beneficial to understanding both phenomena.

The new model presented in this paper provides an efficient means of screening the influence of parameters on the process of early bone formation in a large animal and at a clinically relevant location. This model is easily applied and readily adaptable to the materials and treatments of interest. The model, as demonstrated in this manuscript, not only allows the performance of the materials/treatments to be gauged but may also enable the fundamental processes involved in bone formation to be studied.

Conclusions

The current study validates a new model for screening multiple material conditions that is clinically relevant for posterior spinal fusion. This model facilitates the use of completely randomized block designs and supporting statistics. Clearly demonstrated are the differences, both observed and measured, between ten calcium phosphate ceramics with regard to the initial process of bone formation from the goat transverse process.

Acknowledgements

The authors would like to thank The Netherlands Technology Foundation (STW, grant UGN.4966) and the Anna Foundation for their financial support.

8

The effect of cell-based bone tissue engineering in a goat transverse process model

Moyo C. Kruyt[1], Clayton E. Wilson[1,2], Joost D. de Bruijn[2,3], Clemens A. van Blitterswijk[2], Cumhur F. Oner[1], Abraham J. Verbout[1], Wouter J.A. Dhert[1]

[1] *Department of Orthopaedics, G05.228, University Medical Center Utrecht, PO Box 85500, 3508 GA Utrecht, The Netherlands*
[2] *Institute for Biomedical Technology, Twente Universit, Enschede, The Netherlands*
[3] *Queen Mary University of London, Mile End Road, London, UK*

Abstract

A disadvantage of traditional posterolateral spinal fusion models is that they are highly inefficient for screening multiple conditions. We developed a multiple-condition model that concentrates on the initial process of bone formation from the transverse process and not on a functional fusion. The effect of bone marrow stromal cells (BMSCs) in four different porous ceramic scaffolds was investigated in this setting. Polyacetal cassettes were designed to fit on the goat transverse process and house four different ceramic blocks, i.e: hydroxyapatite (HA) sintered at 1150 ℃ and 1250 ℃; biphasic calcium phosphate (BCP) and tricalcium phosphate (TCP). Goat BMSCs (n = 10) were cultured and per-operatively seeded autologeously on one of two cassettes implanted per animal. The cassettes were bilaterally mounted on the dorsum of decorticated L2-processes for 9 weeks. To asses the dynamics of bone formation, fluorochrome labels were administered and histomorphometry focused on the distribution of bone in the scaffolds. A clear difference in the extent of bone ingrowth was determined for the different scaffold types. An obvious effect of BMSC seeding was observed in three of four scaffold types, especially in scaffold regions adjacent to the overlying muscle. Generally, the BCP and TCP scaffolds showed better osteoconduction and an increased response to BMSCs administration. In conclusion the model provides a reliable and highly efficient method to study bone formation in cell-based tissue engineering. An effect of cell administration was obvious in three of the four scaffold materials.

Introduction

Posterior lateral spinal fusion (PLF), by bridging the transverse processes with bone, is a well-known, successful procedure in orthopedic surgery. Many investigations over several decades have been performed to elucidate the exact mechanism[9, 126, 232] and to characterize conditions to optimize the rate of fusion.[29, 83, 113, 142, 193] Much research has also focused on techniques to obviate the need for autologous bone grafts, the current gold standard, by developing alternative grafts with comparable or better fusion rates. An impressive amount of literature concerns the discussion and validation of good animal models for these purposes[27, 152, 217] and hundreds of functional studies concerning potential autologous graft substitutes have been published so far.[152] Although many aspects of the mechanism of PLF remain unclear, e.g. the role of viable cells in the autologous bone graft, there is consensus on the initial processes of bone bridge formation. New bone originates from the two thoroughly decorticated transverse processes and progresses by a combination of osteoconduction, osteoinduction and osteogenesis through the graft material. In time, the two bone frontiers meet to create a functional fusion.[28, 232] Typically, a non-union is located at this meeting point as a result of excessive motion, soft tissue interposition or preliminary graft resorption.[83] The vast majority of studies are performed with functional models that focus on fusion or non-fusion. While these types of models are essential for evaluating advanced techniques and comparing these to the gold standard, they are highly inefficient for the screening of multiple parameters as is typically needed during the development of new materials and techniques. The reason for this is that (1) only one condition per animal is normally used in order to prevent an interaction bias especially as fusion on one side would effect the fusion rate on the contralateral side; (2) if the outcome parameter is the rate of fusion, relatively high numbers of animals are required to achieve a reasonable power, since such data is non-parametric; and (3) long follow-up times to allow spinal fusion are required in these studies.

Cell-based bone tissue engineering is a technique that needs to be further developed in clinically sized orthotopic models, as the translation from ectopic models to orthotopic function has been very difficult.[151] The concept of this technique is to combine osteogenic cells with an appropriate porous scaffold to form a so called ‘‘hybrid construct’’. Already in the 1960s it was shown that bone marrow derived stromal cells (BMSCs), were capable of osteogenesis ectopically in mice. Especially when combined with porous scaffolds, these constructs could theoretically yield enormous amounts of bone.[86-88] Many groups have investigated this technique further and some remarkable achievements have been reported.[13,

[34, 151, 186, 195] However, both fundamental and practical aspects of the technique have not been elucidated. Fundamentally, it has not yet been proven that cells can survive in clinically sized transplants. Therefore, new bone formation by the implanted cells remains speculative. Practically, many different scaffold types, cell types, and seeding strategies have been advocated. These need to be compared to optimize the technique.[148, 187, 254] Recently, we introduced a goat transverse process model to investigate bone conduction in multiple conditions simultaneously.[247] The current study evaluates the use of an adapted version of this model, to provide a quantifiable means to simultaneously screen the effect of different bone tissue engineering conditions on the initial process of bone growth from the transverse processes. We investigated four different scaffold types and the effect of cell administration to these scaffolds.

Materials and methods

Experimental design

Institutional animal care committee approval was obtained for a study in 10 adult Dutch milk goats. Bone marrow was harvested from each goat and the colony forming efficiency (CFE) of the aspirates determined. The BMSCs were culture expanded for two passages and then cryopreserved. Blocks of four different porous ceramic materials were prepared. Two spinal cassettes per goat, each holding a complete set of the four different ceramic materials separated by Teflon sheets, were implanted bilaterally on the transverse process of the L2 vertebrae of the 10 goats (Fig. 8.1). In the operating theatre, just prior to implantation, thawed, autologous BMSCs were resuspended in autologous blood plasma and used to impregnate the ceramics in one of the cassettes. Close apposition of all four ceramic blocks to the underlying bone was ensured by thoroughly decorticating and flattening the processes before mounting the cassettes. To monitor the bone formation over time, fluorochrome markers were administered at 3, 5 and 7 weeks and the animals were sacrificed at 9 weeks after implantation. Bone formation was investigated by histology and histomorphometry using epifluorescent and light microscopy. The effects of scaffold material and BMSCs were assessed by measuring the percent of material surface with bone apposition. The distribution of bone was examined by applying histomorphometry to upper, middle and lower regions of interest within each ceramic block.

Cassettes

Polyacetal cassettes, designed for fixation to the transverse processes of the goat lumbar spine, were described in a previous bone conduction model.[247] Each cassette consisted of two sidewalls, two end pieces, four stainless steel screws for

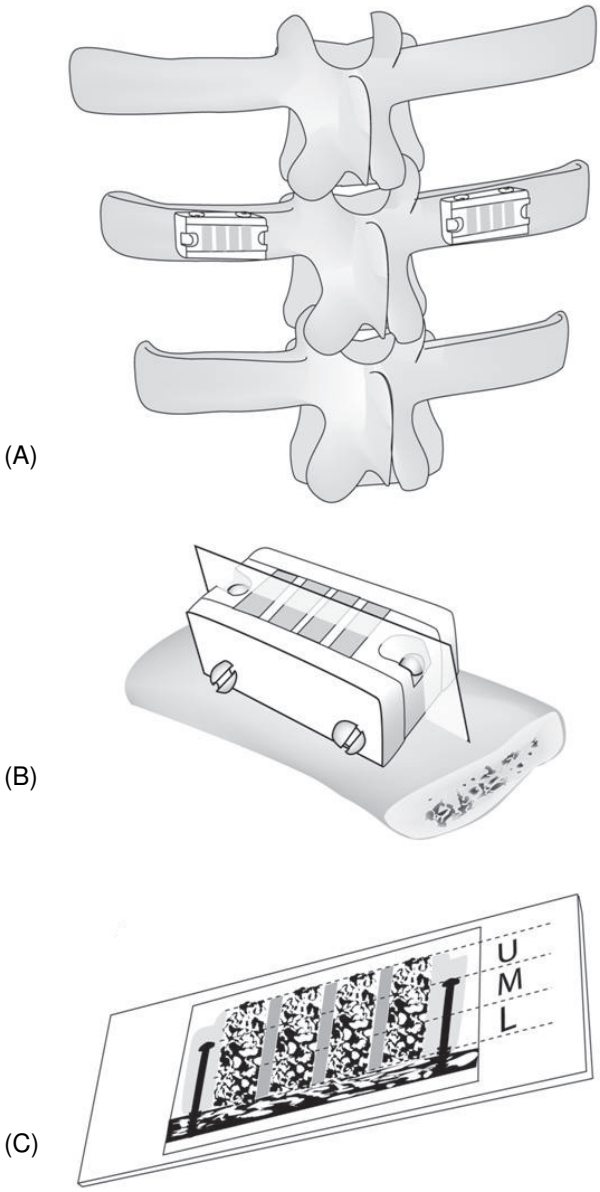

Figure 8.1: Cartoon of the model. (A) Position of the cassettes with the four scaffolds on the goat's bilateral L2 processes. (B) Cassette on the removed process in more detail. The plain that was used for histomorphometry is indicated. (C) Section as it was used for histomorphometry (see also Fig. 8.3(a)). The four scaffold blocks separated by Teflon sheets can be recognized within the cassette. Dotted lines indicate the upper (U) middle (M) and lower (L) thirds that were analyzed separately.

assembly and two self-tapping screws to attach the cassette to the decorticated transverse process. Four 8 × 7 × 3 mm porous ceramic blocks (also called scaffolds) separated by 0.5 mm thick Teflon® sheets fitted tightly within each cassette. After mounting of the cassette on the process, the scaffolds were only open to the underlying bone and overlying soft tissues. The polyacetal components were sterilized by soaking in 70% ethanol for at least 20 min and the screws were sterilized by autoclave.

Scaffolds

Four porous calcium phosphate ceramic materials were examined in this study: Biphasic Calcium Phosphate (BCP, IsoTis Orthobiologics, Irvine, USA), beta-TriCalcium Phosphate (TCP, Progentix, Bilthoven, The Netherlands) and Hydroxyapatite (HA) prepared by the authors at two sintering temperatures (Table 8.1). The BCP material had an 80/20 weight percent ratio of HA/TCP, respectively. Both the BCP and TCP materials were approximately 65% porous, including 10-20% microporosity (<10 µm pores), with a pore size of 200–800 µm. The HA materials were produced from commercially available HA powder (Merck, Germany). The raw HA powder was pre-calcined at 900 °C and bulk porous blocks of HA material were produced with a pore size ranging from 60 to 120 µm, using a dual-phase mixing process described previously.[169] The HA blocks were sintered at either 1150 or 1250 °C (HA1150 and HA1250, respectively) to create micro-structural and physiochemical differences.[144] Scaffolds, measuring 8 × 7 × 3 mm, were cut for all four materials, cleaned in an ultrasonic bath and sterilized by autoclave. Samples were withheld for verification of the composition and phase purity by FTIR and XRD analysis. Characterization of surface features and microporosity was conducted with a scanning electron microscope (ESEM; XL30 ESEM-FEG, Philips, Eindhoven, The Netherlands). Prior to implantation, two cassettes per animal were aseptically assembled with complete sets of the four scaffold materials. The order of materials between the cassettes was reversed to enable the same medial to lateral positioning of materials when the cassettes were implanted bilaterally on transverse processes of the L2 vertebrae.

BMSCs culture and seeding conditions

After approval of the local animal care committee, ten adult female Dutch milk goats (24–36 months) were obtained at least 4 weeks prior to surgery. Bone marrow was aspirated (15 ml per iliac wing) as previously described, together with 100 ml venous blood for the preparation of Autologous Serum (AS).[149] The proportion of BMSCs in the aspirate was assessed by a CFE assay.[86] Fractions of 5×10^6 nucleated cells of each goat were cultured with standard medium[149] in two

Table 8.1: Physicochemical characteristics of the different scaffolds.

Scaffold type	HA / TCP ratio (%)	Sintering temp. (°C)	Porosity (%)	Pore size range (µm)
HA1250	100/0	1250	33	60-120
HA1150	100/0	1150	33	60-120
BCP	80/20	1200	55	200-800
TCP	0/100	1150	55	200-800

25 cm^2 flasks (Nunc, Roskilde, Denmark, 10^5 cells/cm^2) and refreshed every 3 days. When colonies appeared after 8 or 9 days, the medium was washed away with PBS and the colonies were fixated with 8% formaline. The colonies were stained with methylene blue and counted under an inverted microscope. The remainder of the aspirate was plated and cultured according a standardized protocol to retrieve and expand the BMSCs.[149] After the 2nd passage, the BMSCs were cryopreserved in 1 ml aliquots of 10^7 cells.[148] At the day of surgery, the frozen AS was thawed to 4 °C. The cryopreserved cells were then thawed on ice, thoroughly washed with AS and finally resuspended in AS at a concentration of 10^6/ml. Cell viability was assessed by trypan blue exclusion method. Iced aliquots of 5.5 ml (5.5×10^6 BMSCs) were taken to the operation room. During surgery, the suspension was centrifuged at 300g, medium was decanted and the pellets were resuspended in 1 ml autologous plasma that had been derived by ultracentrifugation of 10 ml peripheral blood.[148] One ml of plasma, with or without BMSCs, was drop-seeded on the cassettes containing the four ceramic blocks (= 8×10^6 BMSCs/cm^3) and the plasma was allowed to polymerize. An additional cell-seeded cassette was prepared and analyzed for cell distribution by methylene blue staining and SEM imaging.

Surgical model

The surgical procedures were performed under standard conditions.[149, 247]. After shaving and disinfection of the dorsal thoracolumbar area, a midline skin incision from T10-L5 was made to expose the paraspinal muscles. This allowed implantation of the spinal implants as well as intramuscular and iliac wing implants that will not be discussed in the present paper. Bilateral incisions were then made through the paraspinal muscles to expose the transverse L2-processes. The processes were decorticated using an angled bone rasp until a flat, bleeding surface was obtained. One cassette was screwed to each process. Finger pressure was applied to the top of the blocks in the cassette prior to muscle closure to ensure direct contact of all blocks with the underlying bone. The muscle fascia, subcutis and skin were closed separately. Postoperative pain relief was provided by Buprenorphin (Shering-Plough, The Netherlands). Sequential fluorochrome

markers were administered at three (Calcein Green, 10 mg/kg, Sigma, The Netherlands); five (Oxytetracyclin, Engemycine 32 mg/kg, Mycofarm, The Netherlands) and 7 weeks (Xylenol Orange, 80 mg/kg Sigma). At 9 weeks, the animals were killed by an overdose of pentobarbital (Organon, Oss, The Netherlands) and the implants retrieved by removing the transverse processes.

Histological processing and histomorphometry

The explanted samples were fixated in a solution of 4% glutaraldehyde and 5% paraformaldehyde, dehydrated by ethanol series and embedded in polymethylmethacrylate. Two centrally located 10 μm thick sections were cut from each sample using a sawing microtome (Leica, Nussloch, Germany). The first section remained unstained for epifluorescence microscopy and the second section was stained with methylene blue and basic fuchsin. Tissue response, bone formation and the fluorochrome markers were evaluated using a light/fluorescence microscope (E600, Nikon, Japan) equipped with a quadruple filter block (XF57, dichroic mirror 400, 485, 558 and 640 nm, Omega Optics, The Netherlands). The presence or absence of the each of the fluorochrome labels was evaluated for the upper (closest to muscle), middle and lower (adjacent to the transverse process) thirds of the scaffolds to assess bone mineralization at the time of fluorochrome administration in these areas. High-resolution digital scans of the stained sections were made for histomorphometry using a photographic film scanner (Dimage Scan Elite 5400, Minolta, Japan). Subsequently blinded scans were pseudocolored, bone red and scaffold green, using Adobe Photoshop 7.0 on a commercial PC. Histomorphometry was performed using KS400 software (version 3, Zeiss, Nussloch, Germany). A custom macro was developed to measure the area of interest, the area of scaffold, the area of bone, the scaffold outline available for bone apposition and the contact length of bone and scaffold.[151] This allowed the calculation of the percent bone in available space, Bone area% = ((bone area) ÷ (total area - scaffold area)) × 100% and the percent bone apposition, Contact% = (bone-to-scaffold contact length ÷ scaffold outline) × 100%. The Contact% was shown to be more sensitive, as new bone exclusively forms by apposition on the scaffold surface.[151] Additionally, the measurements were performed separately for the upper, middle the lower thirds of the scaffolds (see Fig. 8.1) to investigate bone distribution specifically. The distribution of new bone in the cell-seeded condition is of particular interest since cell survival especially deep within the middle portion of the scaffold is uncertain. Furthermore, ectopic (upper part) and orthotopic (lower part) constituents can be discerned, which is important considering a significant difference in the effect of cell-based tissue engineering that was observed between these locations in previous work.[151]

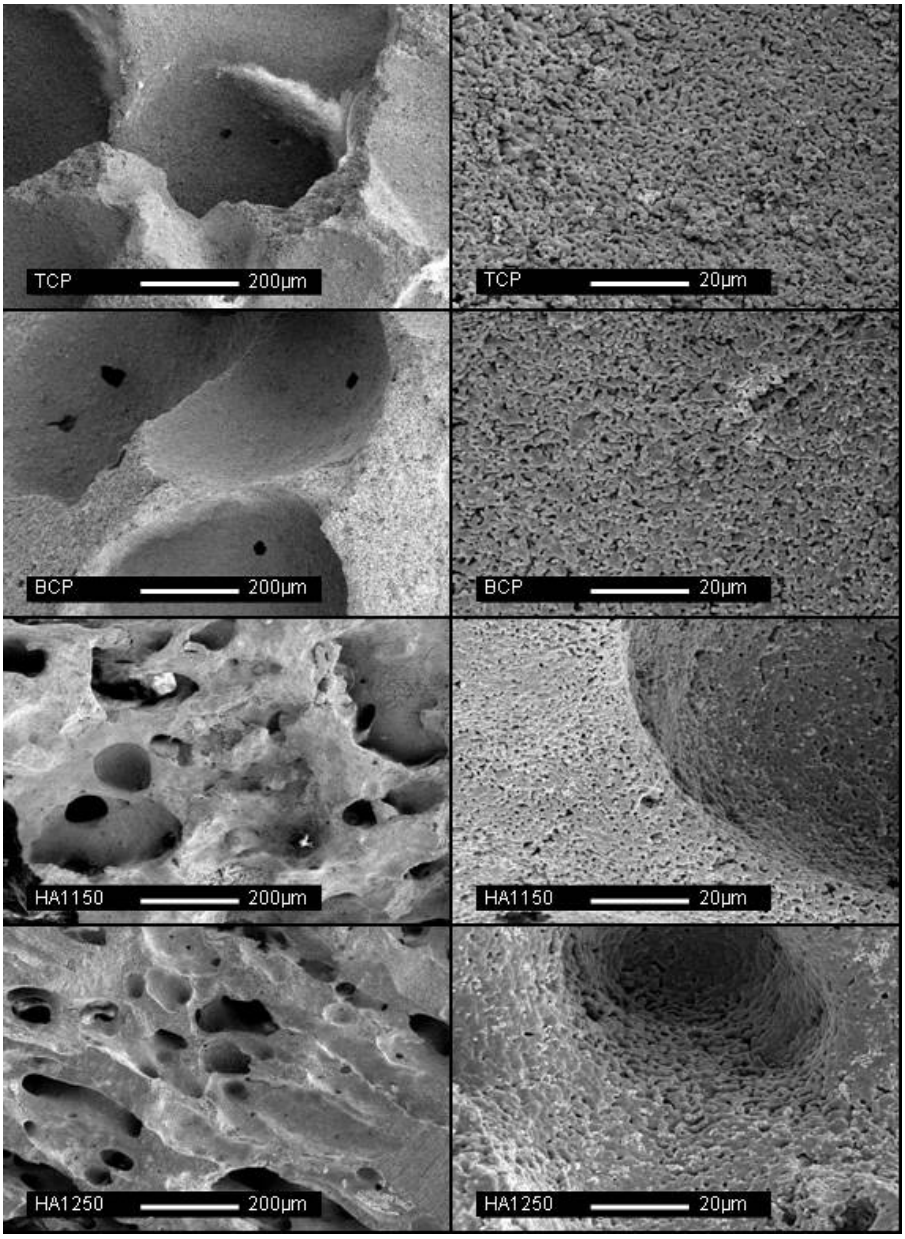

Figure 8.2: SEM micrographs of the four material conditions (rows) at low and high magnifications (left and right columns, respectively). Scale bar length and material condition indicated within black scale bar in each image.

Statistics

To enable comparison with previous work and the work of others, the Bone area% was calculated and graphically displayed. The Contact% (percent bone apposition on the available scaffold surface) was used for comparative statistics within this study. SPSS version 12.01 software was used to evaluate the normality of the data distribution and to perform further statistical analyses (significance was assumed when $p < 0.05$). The effect of the scaffold type was analyzed for both the cell-seeded and control condition by repeated measurements. This was done for the complete block as well as for the lower, middle and upper thirds. Post-hoc test were done with Bonferroni correction. The effect of cell seeding was analyzed with a two-sided paired student *t*-test.

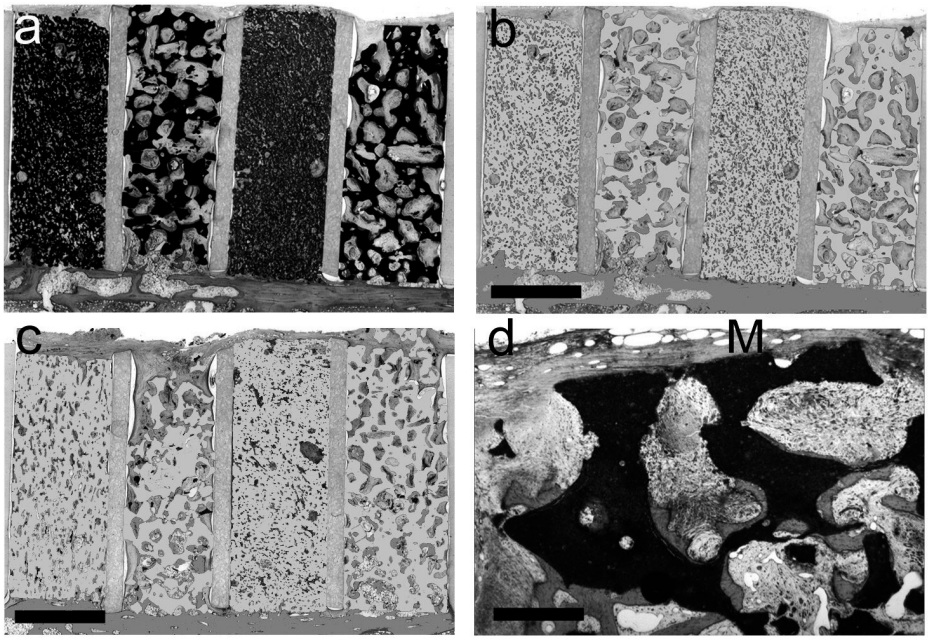

Figure 8.3: Histology. (a) Low-magnification image of the midsection through a BMSC-impregnated cassette. All four ceramic blocks separated by Teflon sheets can be discerned. From left to right: HA1150; TCP; HA1250 and BCP. An obvious difference in pore size can be observed, as well as a preference of bone (red) for apposition in the larger pores. Note the good integration of all materials from the underlying transverse process (Bar = 3 mm). (b) Pseudocolored version of image 8.3a (green = scaffold, red = bone). Note the homogeneous distribution of bone throughout the BCP and TCP scaffolds (Bar = 3 mm). (c) Pseudocolored image of the control cassette (not seeded with BMSCs) in the same animal. The order of materials is the same. Note bone is much less in the upper parts (Bar = 3 mm). (d) High-magnification image of the upper part of TCP with BMSCs. Abundant bone (red) is present within the concavities Typically no bone was found at the peripheral straight surface next to muscle (M) (Bar = 600 µm). *(See color image on page 204)*

Results

In vitro results

XRD and FTIR analysis of the materials confirmed the phase purity of the HA and TCP scaffolds and the biphasic nature of the BCP scaffolds. SEM imaging (not quantified) confirmed that both the macroporous and microporous structures of the TCP and BCP materials were very similar. The macroporous structures of the two HA materials were also similar to each other, however, higher magnification SEM revealed more microporosity inherent to the lower sintering temperature of HA1150. Furthermore, the TCP and BCP exhibited more microporous structure than either of the HA materials. (Fig. 8.2).

The bone marrow aspirates yielded $5.6 \pm 1.5 \times 10^6$ (Mean ± SD) nucleated cells/ml. The colony forming efficiency was 1.9 ± 0.6 colonies per 100,000 cells. The adherent BMSCs proliferated well with a doubling time of 1.2 ± 0.6 days. This allowed cryopreservation of 60-100 million BMSCs within 3 weeks after obtaining aspirates. Trypan blue exclusion after thawing the cells indicated <5% dead cells. Following the per-operative resuspension of cells in plasma, the plasma remained in a liquid state for 10-20 min before polymerizing, allowing good penetration of the scaffolds. SEM imaging and stereo microscopy of methylene blue stained constructs showed a homogeneous distribution of spherical cell aggregates throughout the interior of the scaffolds with more dense layers of cells at the upper and lower peripheries.

In vivo results

All animals recovered well within two days of surgery and survived the follow-up period without difficulties. Upon explantation, the cassettes were found firmly attached to the underlying transverse processes, even after removing the bone screws.

Histology showed no signs of infection or adverse tissue reactions. All scaffold blocks remained largely intact although some signs of degradation were observed for the TCP material. The HA materials had comparable pore sizes and distributions as did the BCP and TCP materials. The pores in the HA scaffolds were obviously smaller and appeared to be less interconnected than those in the BCP and TCP scaffolds (Fig. 8.3). The general appearance of new bone was similar in all conditions and locations and bone was always in close contact to the scaffold surface with osteoblasts lining the new bone at the luminal side. In the control condition (no BMSCs) bone apposition was obviously the result of ingrowth from the underlying bone (osteoconduction). Both HA materials showed only a

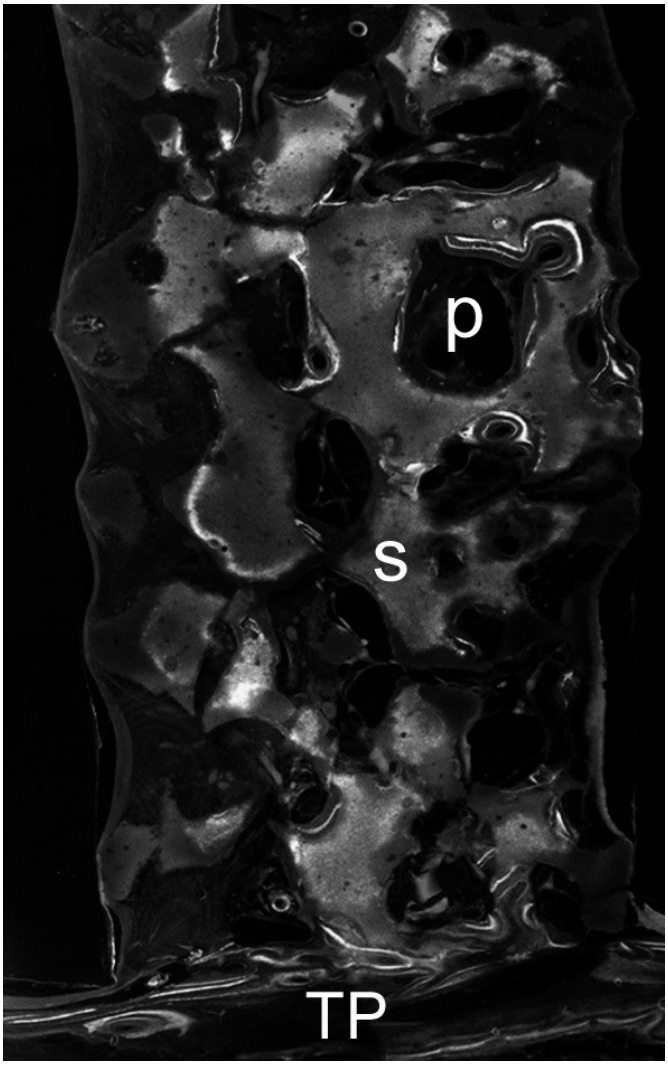

Figure 8.4: Fluorescent microscopy. Composite image of the lower half of a BCP scaffold (s) without BMSCs. The green (3 weeks) yellow (5 weeks) and orange (7 weeks) labels are present in the lower area and in the underlying transverse process (TP) In the highest areas only the orange label is present indicating bone had grown by conduction. (p = pore). *(See color image on page 205)*

small amount of bone in the lower part of the scaffolds immediately adjacent to the underlying transverse processes. In contrast, bone integration in the BCP and TCP appeared far greater, occasionally reaching the upper third of the scaffolds (the part in contact to the overlying muscle). Regarding the BMSC-seeded scaffolds, the HA1250 appeared similar. The upper part of the HA1100 occasionally showed islands of bone. The most obvious effect of BMSCs administration was found in the BCP and TCP scaffolds that were almost completely covered by bone (Fig. 8.3).

Fluorescent microscopy of growth dynamics of the control condition confirmed bone had grown from the underlying bone towards the upper part of the scaffolds by conduction, as the early label (given at 3 weeks) was only present in the lower part (Fig. 8.4). In general, bone conduction was slower in the HA scaffolds. This was most obvious for the HA1250 where no early mineralization was detected and bone was limited to the lower third of the scaffold. In the BCP and TCP scaffolds, mineralization had already occurred in the lower third at 3 weeks. By 5 weeks, bone had reached the middle third and in 4 of 10 goats the 7 weeks label was observed in the upper third. In the BMSC-seeded constructs, the HA1250 did not show any effect, whereas in the HA1150 scaffolds the 5-week label was observed in the upper third in 3 of 10 goats. In the BCP and TCP scaffolds, bone formation in the upper third was always present by 5 weeks and in 3 of 10 already at 3 weeks. This indicates early, BMSC-related, osteogenesis. Interestingly, mineralization in the middle occurred later, often only the 7-week label was observed, suggesting the absence of BMSC-related bone formation.

Histomorphometry of the control condition showed total bone apposition (Contact%) was comparable for the two HA materials, HA1250 = 1.3 ± 1.8 and HA1150 = 2.3 ± 1.2 (Mean ± SD). This was significantly ($p < 0.01$) less than bone apposition for the BCP = 11.2 ± 3.9 and TCP = 15.7 ± 8.6, which were comparable (Table 8.2 and Fig. 8.5). Regarding the BMSC condition, bone apposition in HA1250 was similar to the controls, with 1.5 ± 1.2% in the total scaffolds, limited to the lower parts of the scaffolds. In the HA1150 seeded with BMSCs, more total bone was observed (5.4 ± 5.6%), although not significantly different compared to the control condition or HA1250. However, in the upper third of the HA1150 scaffolds, significantly more bone contact was present as compared to the control ($p = 0.04$, see Table 8.2). The BCP and TCP scaffolds were comparable in total bone Contact% (BCP = 23.6 ± 8.4% and TCP = 23.7 ± 9.5%), which was significantly more than the control conditions (BCP $p < 0.01$, TCP $p = 0.03$). When considering the lower third of the scaffolds, the effect of BMSCs was only significant for BCP ($p < 0.01$). In the upper third however, both BCP and TCP exhibited a highly significant effect of the BMSCs ($p < 0.01$). In the middle third of

Table 8.2: Bone apposition on the four different scaffolds calculated from the percent scaffold surface occupied by bone (= Contact%, mean ± SD).

Scaffold type	Total scaffold		Lower 3rd		Middle 3rd		Upper 3rd	
	Control	BMSCs	Control	BMSCs	Control	BMSCs	Control	BMSCs
HA1250	1.3 ± 1.8	1.5 ± 1.2	3.5 ± 4.7	4.0 ± 3.0	<1	<1	<1	<1
HA1150	2.1 ± 1.2	5.4 ± 5.6	5.5 ± 2.7	10.7 ± 10.1	<1	1.8 ± 3.1	<1	3.8 ± 4.7*
BCP	11.2 ± 3.9	23.6 ± 8.4*	24.8 ± 8.2	42.5 ± 15.2*	7.0 ± 3.7	10.3 ± 4.3	<1	14.1 ± 7.0*
TCP	15.7 ± 8.6	23.7 ± 9.5*	35.6 ±18.7	42.3 ± 11.1	9.2 ± 6.0	11.3 ± 6.0	2.2 ± 3.4	10.6 ± 6.8*

Apposition in the total scaffold and in the lower (close to underlying bone), middle and upper (close to overlying muscle) thirds. The BCP and TCP consistently showed more bone apposition than the HA's ($p<0.01$). Asterisks (*) indicate a significant effect of the BMSCs.

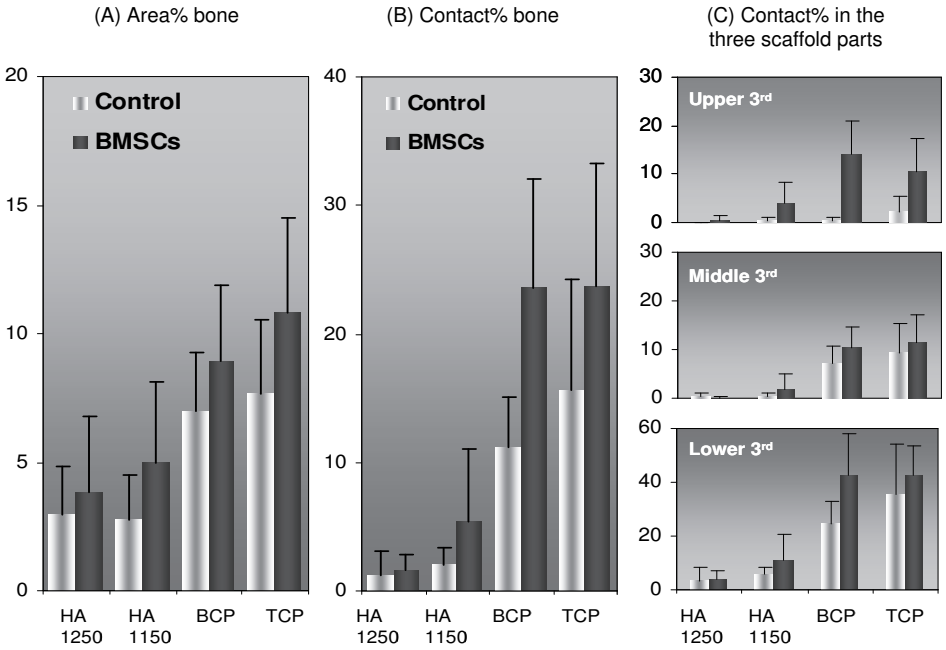

Figure 8.5: (A) The Area% bone in the available space of the whole scaffolds (n = 10) with or without BMSCs. Error bars indicate the standard deviation. (B) The percent available surface of the same scaffolds as in (A), that is covered with bone (Contact%). Note that the effect of BMSCs is more pronounced when using this parameter as compared to the Area%. (C) The Contact% in the upper, middle and lower parts of the scaffold. Note the impressive effect of the BMSCs in the upper part as compared to the middle and lower part. In the lower part the maximum Contact% is twice as much for both conditions.

the BCP and TCP, bone formation was comparable and not significantly influenced by the BMSCs.

Discussion

The current study investigated eight conditions of bone tissue engineering with porous ceramic scaffold blocks by using an adapted version of the earlier described transverse process model.[247] While this model does not attempt to create a spinal fusion, it does illustrate the initial bone formation processes relevant to posterolateral spinal fusion. The described study compared different scaffold types and assessed the effect of BMSCs on bone formation in these scaffolds. We did not attempt to identify optimal scaffold characteristics, although the model appears suitable for this purpose, particularly if single parameters can be isolated. Irrespective of the underlying mechanism, we demonstrated that the type of scaffold significantly influenced bone ingrowth from the transverse processes (osteoconduction) as well as BMSC-related bone formation (osteogenesis) which was most obvious at the submuscular side. In general, the TCP and BCP scaffolds performed far better than the HA scaffolds. This finding may be due to the chemical compositions, the different macro- and microporosities and possible other factors influencing the local micro-environment with respect to dissolution/reprecipitaton and surface characteristics for cell attachment.[144, 247] Little difference could be proven between the HA scaffolds, however, compared to HA1250, HA1150 consistently showed more bone formation and a significant effect of cell seeding in the upper third of the scaffold.

The effect of BMSC administration was most obvious in the upper third of the BCP and TCP scaffolds. In the lower third, closest to the underlying bone, a modest effect from BMSCs was observed only in the BCP. This is confusing and cannot be explained easily. Apparently, the effect of BMSCs administration is more pronounced in non-bony area's (ectopical), an observation that we have made in previous studies.[151] A possible explanation for this may be that only a maximal percentage of bone apposition can be reached in the scaffolds, possibly due to vascularization limitations. When this percentage is reached within the study period in the lower parts by osteoconduction alone, additional cell-based bone apposition will be minimal and irrelevant. In the middle thirds, no effect of cell administration was observed with regard to either the amount of bone or the presence of an early fluorochrome label. This is likely the result of decreased cell survival due to the greater distance required for oxygen and nutrient diffusion from the overlying muscle or underlying bone. However, based on literature, cell survival should have been restricted to only a superficial 300–500 µm layer.[115] If that is what happened,

it can be speculated that only these superficial BMSCs formed bone that subsequently progressed by osteoconduction, similarly as from the underlying transverse process in our control condition. However, contradictory to this hypothesis is the presence in the current study of the early 3 week fluorochrome label at a depth far greater than 500 µm. Obviously, adequate BMSC labeling studies are required to determine what exactly happens to the cells.

Although BMSCs administration was not shown to be effective in areas close to bone, in areas away from bone (more ectopical) the effect was impressive. Therefore, especially in posterior lateral spinal fusion where the majority of non-unions occur in between the processes, BMSC administration may be of great value. However, this was not evaluated in this study.

Conclusions

In the current study we have shown the effect of BMSCs in a transverse process model that allowed screening of 2×4 conditions. Although this is not a posterior spinal fusion model, it illustrates the initial bone formation processes that are relevant for posterior spinal fusion. The BCP and TCP porous scaffolds appeared most favorable as compared to the HA scaffolds with respect to both osteoconduction and cell-based osteogenesis. The effect of BMSCs was always more pronounced in the submuscular area as compared to the area adjacent to the transverse process. Probably improved cell survival and the absence of osteoconduction were responsible for these observations. Future studies will be required to elucidate the fate of the BMSCs and to investigate the feasibility of cell-based bone tissue engineering as an alternative for the autologous bone graft in posterior spinal fusion.

Acknowledgements

The authors acknowledge The Netherlands Technology Foundation (STW; Grant UGN.4966) for financial support. We also thank Maarten Terlou from the Image Analysis department of the University Utrecht for developing the software used for histomorphometry.

9

Summary and Discussion

In the current thesis we focus our attention on calcium phosphate ceramic scaffolds and their use as tissue engineering scaffolds in ectopic and orthotopic environments related to posterolateral spinal fusion. The macro- and micro-features of calcium phosphate ceramics that are known to influence cell behavior may eventually be capitalized upon to improve tissue engineering performance. However, these same features may represent confounding variables when performing the research to develop a tissue engineering strategy. To this end, a theme throughout much of the current work has been the normalization of these factors to provide standardized, reproducible model systems to enhance the research and development efforts.

Standardized ceramic scaffolds for evaluation of ectopic bone formation

The porous calcium phosphate ceramics used by us and others for tissue engineering research at the beginning of the current work were adopted from materials used clinically as bone fillers or grafts. This was, and still is, well justified, however, the manufacturing methods for these materials had changed little over the preceding decades and typically yielded highly complex porous structures. Understanding that various aspects of these porous structures, such as pore size and connectivity, can influence their osteoconductive and osteoinductive properties led us to look for novel manufacture methods that offered greater control. Rapid prototyping, also an emerging field at the time, presented an interesting proposition for implementing direct design control in ceramic scaffold manufacturing and led to our first research question.

Can rapid prototyping technology reproducibly manufacture standardized ceramic scaffolds with essentially identical macroporous architectures?

Our first step in answering this question was to design our concept of a standardized scaffold. This design incorporated our current knowledge of the osteoconductive and osteoinductive properties of porous ceramics and their relationship to porosity as well as our desire to apply the resulting scaffolds in small and large animal models. Our analysis of the available rapid prototyping technologies indicated that an indirect manufacturing method, whereby rapid prototyping was used to generate sacrificial wax molds which would then be used to cast the ceramics, offered the best means for successfully and reproducibly fabricating scaffolds according to this design. **Chapter 2** describes the design of our standardized scaffold and demonstrates the indirect rapid prototyping method for manufacturing HA scaffolds according to this design. **Chapter 4** extended this method to include the manufacture four different calcium phosphate scaffolds: low

and high sintering temperature HA, BCP and TCP. All scaffolds produced by this method demonstrated essentially identical macro-porous architectures. All scaffolds exhibited detailed impressions of the uniform surface texture inherent to the rapid prototyped wax molds. This texture occurred on specific surfaces of the scaffolds (and molds) as a consequence of the rapid prototyping process while the remaining surfaces were smooth. The dimensions, volume, weight and apparent porosity were all highly reproducible for each material type. Differences between material types were the result of different levels of volumetric shrinkage and these differences in shrinkage were attributed to the solids loading and sintering temperatures used to prepare the ceramics. We concluded that the size, shape and macroporous architectures of these scaffolds were sufficiently similar to discount these parameters as confounding variables in studies examining the influence of the four ceramic materials on ectopic bone formation.

Chapter 6 was an exercise in the description and measurement of porosity, interconnectivity and accessibility of macroporous structures. We demonstrated a 3D micro-CT analysis that was modeled after traditional mercury intrusion porosimetry. The method yielded similar results as mercury intrusion porosimetry for macroporos polymer materials but with improved capabilities for measuring macroporosities larger than a few hundred microns in diameter. Furthermore, the volume of the macroporosity accessible via pores smaller than or equal to a threshold diameter could be three-dimensionally visualized and measured using this method. Although not applied elsewhere in this thesis, this method is certainly applicable to calcium phosphate materials. The non-destructive and non-intrusive nature of this method enables its application to materials destined for animal implantation as well as the explanted results. Such a tool may be very useful in the localization and characterization of scaffold features that influence bone tissue engineering.

Will the chemical and/or physical properties of the ceramic materials be influenced by the manufacturing method?

Chapter 2 and **Chapter 4** both compared the chemical composition of scaffolds to control materials that had been processed in parallel but without exposure to the rapid prototyped wax molds. XRD analysis demonstrated the introduction of a TCP phase in HA and BCP scaffolds compared to the control materials. Elemental analysis by EDX of scaffold and control material surfaces showed identical spectra without evidence of contamination from the wax mold material. The introduction of the TCP phase is likely the result of the casting of the ceramics in the rapid prototyped wax molds but the exact mechanism is not clear.

Will standardized scaffolds support tissue engineering with bone marrow stromal cells?

Staining of vital and non-vital cells in **Chapter** 2 visually demonstrated that goat BMSCs seeded onto standardized HA scaffolds attached within one day and the number of vital cells increased at four and seven days. Seeded and sub-cultured constructs implanted subcutaneously in nude mice for either four or six weeks all demonstrated bone formation. This bone formation was primarily a thin layer on the surface after four weeks and was accompanied by budding bone formation and occasional pore bridging after six weeks. Budding bone formation was associated with textured surfaces and rarely occurred on smooth surfaces. The area percentage of bone was similar at the four and six weeks. **Chapters 3** expanded on this by using the alamarBlue assay to evaluate the cellular activity of HA scaffolds seeded at different BMSC densities over a seven-day period. This demonstrated that changes in the cellular activity (reduction of alamarBlue) of scaffolds were dependent on the initial seeding density. The activity of scaffolds with the highest seeding density of 2,500,000 cells/scaffold decreased moderately and converged at seven days with the increasing cellular activity of scaffolds seeded with 250,000 cells/scaffold. Lower seeding densities showed moderate (25,000 cells/scaffold) or no (2,500 and 250 cells/scaffold) increase in activity over the seven-day period. The convergence of the two highest seeding densities suggests that there may be a maximum or equilibrium cell activity that can be supported by a given scaffold and its environmental conditions. Furthermore, the dense layer of cells and extracellular matrix observed on the exterior of the scaffolds after seven days likely influences this maximum or equilibrium by inhibiting diffusion into the scaffolds. Due to the non-toxic nature of the alamarBlue assay, the same scaffolds as studied by the assay were subsequently implanted in nude mice along with control scaffolds seeded at 250,000 cells/scaffold (identically treated but without exposure to alamarBlue). Histological observations revealed that the influence of the alamarBlue assay on subsequent bone formation was not significant but could not be completely discounted. More importantly, bone formation was observed in scaffolds seeded at all seeding densities and the amount of bone observed increased with higher seeding densities.

The combined results of **Chapters 2**, **3** and **4** demonstrated that the standardized scaffolds manufactured by our indirect rapid prototyping method were reproducible, biocompatible and supported tissue engineering using sub-cultured goat BMSCs in nude mice.

Chapter 5 aimed to answer the question: *Will standardized scaffolds be effective in determining the influence of different materials on ectopic tissue engineered bone formation?*

Tissue engineered and empty controls of the standardized HA (low and high sintering temperature), BCP and TCP scaffolds described in Chapter 4 were implanted in goat paraspinal muscles for 9 weeks. Per-operative seeding of the tissue engineered scaffolds with cryo-preserved autologous BMSCs was implemented based on studies within our group which showed similar bone yields in scaffolds that were pre-cultured for seven days.[148, 149] Histological examination of explanted scaffolds revealed that the addition of cells, scaffold material, and the individual animal in which the scaffolds were implanted all influenced the formation of bone tissue.

None of the control scaffolds in this study showed bone formation. In other words, these scaffolds in this animal model did not demonstrate osteoinductive properties. HA, BCP and TCP have all shown osteoinductive potential in large animals, even goats. However, despite having similar chemical and microporous characteristics to these inductive materials, the small scaffold volume and easily accessible, regular porous structure of our standardized scaffolds may not have supported development of the niche environments needed to elicit osteoinductivity in this animal model.

Neither the TCP nor high sintering temperature HA showed bone formation when seeded with BMSCs. TCP is generally considered quite promising with regard to demonstrated tissue engineering and osteoinductive potential and performed well in the orthotopic models presented in this thesis. However, the addition of cells to TCP scaffolds substantially increased the degradation of the scaffolds compared to non-seeded controls. Nine of ten seeded TCP scaffold showed a nearly complete loss of structure whereas all ten non-seeded controls maintained their structure. The addition of cells also did not lead to bone formation within the high sintering temperature HA scaffolds. This contrasts with the consistent bone formation as early as 4 weeks seen in **Chapters 2** and **3** when identical scaffolds were implanted in nude mice. Despite the different tissue engineering methods used, pre-cultured versus per-operative seeding, this demonstrates the divergent results that different animal models can yield as well as highlights the potential difficulties in interpreting and applying such results to the clinical situation.

The addition of BMSCs to our standardized scaffolds did result in bone formation in the low sintering temperature HA and BCP materials. The bone formation was

similar in these two materials and resembled the surface mediated budding bone formation seen previously in mice (Chapter 2) with a similar preference for the textured scaffold surfaces. Interestingly, bone formation in this study was animal dependant. Either bone occurred in both the low sintering temperature HA and BCP tissue engineered scaffolds within an animal (six or ten animals) or no bone formation occurred in any scaffold (four of ten animals). The administration of fluorochrome labels at 3, 5 and 7 weeks following implantation enabled the dynamics of the resulting bone formation to be observed. The earliest administered label was most often observed as discrete locations of bone formation directly or closely apposed to the textured surface of the scaffolds. The subsequent labels showed the bone formation propagating away from these early nucleation sites both alone the scaffold surface and into the pore space.

Screening models for bone formation in posterolateral spinal fusion

The aim of posterior lateral spinal fusion is to create a bony bridge between adjacent transverse processes. The vast majority of studies concerning posterior lateral fusion have utilized functional models, which evaluate whether or not a fusion is achieved and may consider the rate of fusion. These functional models are essential for evaluating and comparing new techniques to current standards but are highly inefficient for screening the multiple parameters typically screened during the development of new materials and techniques.

Can a screening model be designed that is specifically relevant to posterolateral spinal fusion?

A fully successful posterior lateral spinal fusion requires the formation of a viable bony fusion between two or more adjacent transverse processes. The fusion therefore involves both the bone of the transverse processes and the muscle tissue in the intertransverse space between the processes. To achieve the fusion, surgeons decorticate the transverse processes and place the graft material in a muscle pocket that traverses the space between the processes. **Chapters 7** and **8** describe and validate two variants of a large animal (goat) screening model designed specifically to engage both the bone and muscle aspects of posterior lateral spinal fusion. The screening model uses cages with closed sides but open top and bottom surfaces. The multiple test specimens, compartmentalized within each cage, extend from the bottom to the top surfaces of the cage. During the surgical procedure, the paraspinal muscles of the goats are retracted and the exposed transverse processes of lumbar spine are decorticated. The cages are then affixed to decorticated processes and the muscle tissue closed over the cage.

The bottom surface of the cages, and materials within the cages, are in directly apposed to the decorticated bone whereas the top surfaces of the cages and materials are in direct contact with the paraspinal muscle tissue. This enables the efficient and controlled screening of multiple conditions in an environment relevant to early bone formation processes in posterolateral spinal fusion. The two variants of this model described in this thesis examine the influence of material condition alone under idealized circumstances as well as the influence of tissue engineering in clinically relevant graft materials.

Chapter 7 addresses the research question: *Will this screening model be effective in determining the influence of different materials on tissue engineered orthotopic and ectopic bone formation?*

The screening model examined the influence of material condition alone on the early bone formation processes under controlled conditions. The model creates five uniform conduction channels of five different material conditions per cage by separating two plates of each material by a small distance. Implanting 2 cages per animal in ten different animals enabled the influence of the ten different material conditions to be compared using a randomized complete block statistical design. Furthermore, the addition of fluorochorme labels at 3, 5 and 7 weeks followed by explantation at 9 weeks enabled the dynamics of the initial bone formation processes to be observed and measured. The ten calcium phosphate ceramic materials compared material chemistry (BCP, TCP, HA), sintering temperature (low, medium, high), calcination and surface roughness treatments. This model demonstrated a clear correlation between the expected solubility of the ceramic materials and the bone forming potential over the time course of the study. Materials with a higher expected solubility (TCP and the lower sintering temperature BCP and HA materials) showed superior bioactivity with preferential bone formation by surfaced medicated osteoconduction with bonding osteogenesis and, in most cases, significantly more bone formation compared to their less soluble counterparts. This effect increased over the time course of the study as indicted by measures of fluorochrome label height and was prominent at the end point by measures of bone area and contact percent. Conversely, the least soluble, high sintering temperature, materials were virtually devoid osteoconductive and bioactive qualities with bone formation primarily by ingrowth from the underlying bone and little direct apposition to the material surfaces. Finally, we also demonstrated that the use of pre-calcined raw material significantly improved the bone forming capacity of low sintering temperature HA material. In conclusion, this model is an efficient and reliable method for screening material conditions in an environment relevant to posterior lateral spinal fusion.

Chapter 8 used a variant of the cage model to address our final research question: *Is the tissue engineering of porous calcium phosphates with BMSCs likely to improve posterolateral spinal fusion?*

The cages were adapted to enable four material blocks to be partitioned within each cage. The influence of tissue engineering using cryopreserved autologous BMSCs was examined in porous blocks of HA (high and low sintering temperature), BCP and TCP. Two cages, one seeded and one control, were implanted on decorticated transverse processes of the lumbar spine with fluorochrome labels administered at 3, 5 and 7 weeks followed by explantation at 9 weeks. Analysis of the histology focused on the dynamics and distribution of bone within upper (adjacent to muscle), middle and lower (adjacent to bone) thirds of the scaffolds. Histomorphometry of control scaffolds demonstrated that bone contact percent for both the high and low sintering temperature HA materials was significantly lower compared to the BCP and TCP materials. This is consistent with the results of the conduction cage model in **Chapter 7**. Total bone formation in the tissue engineered high and low sintering temperature HA materials were not significantly different from controls. However, tissue engineering resulted in significantly more bone contact in the upper third of the low sintering temperature HA scaffolds. Tissue engineering significantly increased the total bone contact in the BCP and TCP materials compared to controls. Considering the influence of BMSCs in the three regions, BCP alone showed modest but significant improvement in the lower third, neither BCP nor TCP benefited from BMSCs in the middle third, and both BCP and TCP exhibited highly significant increases in the upper third. These measurements yield a surprising and important conclusion. In this model, the addition of BMSCs did not affect bone formation in areas close to the underlying bone (more orthotopic) but the effect in areas furthest from the underlying bone (more ectopic) was impressive and significant. Therefore, it is reasonable to conclude that the addition of BMSCs may be beneficial to posterior lateral spinal fusions where the majority of non-unions occur in the intertransverse space between the processes. Further studies would be needed to evaluate this and, based on the results of this study, BCP and TCP would be the good candidate materials.

Conclusions

The principal aim of this thesis was to advance the development of tissue engineered posterior lateral spinal fusion by investigating the potential of calcium phosphate ceramic scaffold materials to support tissue engineered bone formation. The studies that make up this thesis have accomplished the aim in two ways.

First, the *in vivo* model systems described (**Chapters 4**, **7** and **8)** all incorporated at least four common materials; HA (low and high sintering temperature), BCP and TCP. All demonstrated that high sintering temperature HA had the lowest bioactivity. This material was also the least affected by the addition of BMSCs. Except for TCP in the ectopic scaffold model (**Chapter 4**), all models showed BCP and TCP to be the most bioactive. These materials were also the most affected by the addition of BMSCs. Not only does this suggest BCP and TCP to be very good candidate materials for further development but the consistency of the results between these models and with the available literature supports their validity.

Second, the models we have developed demonstrate reliable and efficient tools for screening multiple conditions in relevant environments. It is our hope that these tools will be utilized and adapted to support further research to advance our knowledge and accelerate the development of bone tissue engineering solutions for spinal fusion and other applications.

10

Samenvatting in het Nederlands

In dit poefschrift onderzoeken we calciumfosfaat keramieken en de mogelijkheid deze als dragers te gebruiken voor tissue engineering in ectopische en orthotopische locaties gerelateerd aan posterolaterale spinale fusie. Wanneer we weten welke macro-en micro-eigenschappen van calciumfosfaat keramieken het cel gedrag beïnvloeden, kan dit gebruikt worden om de prestaties van bot tissue engineering te verbeteren. Bij het onderzoek naar de optimale strategie van tissue engineering kunnen deze variabelen echter ook verstorend werken. Daarom is een belangrijk onderdeel van het huidige werk gericht op de normalisering van deze factoren tot gestandaardiseerde, reproduceerbare modelsystemen.

Gestandaardiseerde keramische dragers voor de evaluatie van ectopische botvorming

Aan het begin van dit onderzoek hebben we gebruik gemaakt van poreuze calciumfosfaat keramieken die ook in de kliniek werden toegepast als botvullers of z.g.n. grafts. Hoewel dit een logische benadering was en is, was er in de voorgaande jaren weinig veranderd aan het productie proces van deze materialen en hadden ze zeer complexe poreuze structuren. Aangezien elementen van die poreuze structuur, als de poriëngrootte en interconnectiviteit, juist invloed konden uitoefenen op de osteoconductie en osteoinductie eigenschappen, zijn we op zoek gegaan naar een productie methode die deze eigenschappen beter kon sturen. In die tijd was een opkomende en voor ons interessante techniek het z.g.n. rapid prototyping, waarbij vormeigenschappen van de keramische dragers konden worden ontworpen en dus volledig worden gecontroleerd. Dit leidde tot de eerste onderzoeksvraag:

Is het mogelijk met rapid prototyping technologie reproduceerbare gestandaardiseerde keramische dragers te maken met vrijwel identieke macroscopische vormgeving?

De eerste stap om deze vraag te beantwoorden was het ontwerp van een gestandaardiseerde drager. Hierbij werd de kennis over osteoconductieve een osteoinductieve eigenschappen in relatie tot porositeit van de keramieken toegepast, naast de behoefte deze dragers zowel in kleine als grote proefdiermodellen te kunnen gebruiken. Na bestudering van de beschikbare rapid prototyping technieken bleek een indirecte methode, waarbij eerst een tijdelijk wax-model werd gebruikt om de uiteindelijke keramische drager te maken, het meest succesvol en reproduceerbaar. **Hoofdstuk 2** beschrijft het ontwerp en de indirecte rapid prototyping methode van deze gestandaardiseerde HA-dragers. In **Hoofdstuk 4** wordt deze methode uitgebreid, zodat 4 verschillenden

calciumfosfaat dragers kunnen worden gemaakt: HA-dragers gebakken bij lage en hoge oventemperatuur, BCP en TCP dragers. Al deze dragers toonde in essentie eenzelfde macro-porositeit. Alle dragers toonde ook de kleine inkepingen die het gevolg waren van de productiemethode met dezelfde wax-modellen. Deze inkepingen zaten a.g.v. de gelaagde wax-model productie methode alleen op twee overliggende zijde, terwijl de andere zijden juist glad waren. De afmetingen, het volume, het gewicht en de daaruit volgende porositeit waren zeer reproduceerbaar voor de verschillende materialen. Verschillen die werden gemeten tussen de materialen waren het gevolg van een verschillende mate van krimp, welke konden worden toegeschreven aan verschillen in de vaste stof/vloeistof verhouding en benodigde baktemperatuur. Deze verschillen waren dermate klein dat we ze als niet relevante verstoorders hebben geaccepteerd in de verdere studies na de invloed van materiaal type op ectopische botvorming.

Hoofdstuk 6 betreft een poging tot beschrijving en meting van porositeit, interconnectiviteit en toegankelijkheid van macroporiën. Hiervoor gebruikten we een 3D micro-CT methode die was gebaseerd op de traditionele kwik-intrusie porosimetrie. Deze methode gaf vergelijkbare resultaten als de kwikporosimetrie voor macroporeuze polymeren, maar met een betere mogelijkheid om poriën met een diameter groter dan enige honderden micrometers te meten. Daarnaast konden we van poriën die toegankelijk waren via openingen met een diameter onder een bepaalde drempelwaarde het volume visualiseren en meten. Hoewel niet toegepast in het verdere onderzoek van dit proefschrift, kan deze methode zeker gebruikt worden voor calciumfosfaat materialen. Door het niet-destructieve en niet-intrusieve karakter, kan de methode worden gebruikt voor materialen die worden geïmplanteerd of zijn geëxpandeerd in proefdierstudies. Daarom leent de methode zich goed voor onderzoek naar drager eigenschappen van belang voor bot tissue engineering.

Worden de chemische en/of fysische eigenschappen van de keramische materialen beïnvloed door de productie methode?

In **Hoofdstuk 2 en 4** vergeleken we de chemische samenstelling van dragers die waren blootgesteld aan de rapid-prototyping wax-modellen met tegelijkertijd vervaardigde controle dragers. XRD analyse toonde in de experimentele groep het ontstaan van een TCP-fase in de HA en BCP dragers. Elementen analyse met EDX van het materiaal oppervlakten in beide groepen toonde identieke spectra zonder aanwijzingen voor contaminatie door de wax. Waarschijnlijk is het ontstaan van de TCP-fase te wijten aan het inbrengen van de keramieken in de wax-modellen, maar hoe precies is onduidelijk.

Is bot tissue engineering met stromale beenmerg cellen (BMSCs) mogelijk in de gestandaardiseerde dragers?

In **Hoofdstuk 2** laten we door kleuring van vitale en niet-vitale cellen zien dat de cellen goed hechten na zaaien op gestandaardiseerde HA-dragers en dat het aantal levende cellen toenam na 4 en 7 dagen. Zowel gezaaide als vervolgens doorgekweekte constructen lieten consequent botgroei zien na 4 en 6 weken subcutane implantatie in muizen. Deze botvorming was na 4 weken vooral een dun laagje op het HA oppervlakte, maar na 6 weken waren daarbij uitgroeiingen en soms volledige overspanning van de poriën zichtbaar. De uitgroeiing van bot was vooral zichtbaar aan de zijden met de inkepingen. Het percentage bot per beschikbare ruimte (area %) was voor de 4 en 6 weken implantaten gelijk. **Hoofdstuk 3** gaat hierop door met een onderzoek naar cel-activiteit in HA-dragers gezaaid met verschillende hoeveelheden geiten BMSCs en gekweekt voor 7 dagen. Hiervoor is een z.g.n. alamarBlue assay gebruikt. Dit onderzoek laat zien dat de verandering in cel-activiteit afhankelijk is van de initieel gezaaide hoeveelheid cellen. De activiteit in de dragers met de grootste zaaidichtheid (2500.000/drager) nam langzaam af en kwam na 7 dagen samen met de toegenomen activiteit in de 250.000/drager groep. Lagere zaaidichtheden lieten een geringe (25.000/drager) of helemaal geen (2.500 en 250) toename zien. Het samenkomen van de activiteits niveaus van de twee hoge zaaidichtheden suggereert een maximum/equilibrium voor cel activiteit die mogelijk is in een bepaalde drager in bepaalde omgevingscondities. Daarbij wordt dit maximum waarschijnlijk beïnvloed door de dikke laag van cellen en matrix die zich aan de buitenzijde van de drager vormt en daarmee diffusie belemmerd. Doordat de alamarBlue assay niet toxisch is, konden we dezelfde constructen implanteren in het subcutane muizenmodel en vergelijken met controle constructen met 250.000 BMSCs/drager die de alamarBlue assay niet waren ondergaan. Histologisch onderzoek toonde dat de alamarBlue assay weinig effect had op de botvorming, maar kon dit niet uitsluiten. Nog belangrijker was de bevinding van botvorming bij alle zaaidichtheden, met een toename van bot hoeveelheid bij hogere zaaidichtheid.

Samenvattend laten de resultaten van **Hoofdstuk 2, 3 en 4** zien dat onze gestandaardiseerde dragers gemaakt met de indirecte rapid prototyping techniek reproduceerbaar en biocompatibel waren. Daarbij ondersteunde ze bot tissue engineering met in de dragers doorgekweekte geiten BMSCs in het muizen model.

In **Hoofdstuk 5** onderzochten we: *Kunnen we met de gestandaardiseerde dragers de invloed van materiaal type bepalen op ectopische botvorming door tissue engineering*?

Hiervoor werden tissue engineered en lege controles van de gestandaardiseerde dragers: HA (van hoge en lage oventemperatuur), BCP en TCP, zoals beschreven in Hoofdstuk 4, geïmplanteerd in de paraspinale spieren van de geit voor 9 weken. We gebruikte en per-operatieve zaaimethode met ingevroren autologe cellen die eerder had laten zien net zo goed te werken als 7 dagen vooraf kweken.[148, 149] De histologische resultaten van deze studie lieten zien dat zowel het toevoegen van cellen als het materiaaltype als ook het individuele proefdier de botvorming beïnvloedde.

Geen van de controle dragers in deze studie liet botvorming zien. Dit betekende dat deze dragers in dit diermodel niet osteoinductief waren. HA, BCP en TCP bleken in andere studies, ook in het geitenmodel, wel inductief. Hoewel de gestandaardiseerde dragers dezelfde chemische en microporeuze karakteristieken hadden als deze inductieve materialen, zou het relatief kleine volume en/of de toegankelijke gelijkmatige structuur van de poriën de vorming van een geschikt micro-klimaat dat nodig is voor osteoinductie onvoldoende kunnen hebben ondersteund.

Zowel de TCP als de hoge baktemperatuur HA dragers gaven zelfs geen bot wanneer ze waren gezaaid met de BMSCs. Dit terwijl TCP het in de orthotopische modellen besproken in dit proefschrift wel goed deed en algemeen wordt beschouwd als een veelbelovend materiaal voor bot tissue engineering en osteoinductie. Het bleek echter dat de toevoeging van cellen aan de TCP dragers de degradatie hiervan versnelde in vergelijking met de niet gezaaide controles. Negen van de tien gezaaide TCP dragers waren hun structuur vrijwel verloren in tegenstelling tot alle tien de niet gezaaide controle dragers. De toevoeging van cellen leidde ook niet tot botvorming in de hoge baktemperatuur HA dragers wat in contrast staat met de in **Hoofdstuk 2 en 3** beschreven consistente botvorming in dezelfde dragers na 4 weken in het muizenmodel. Hoewel er wel een verschil was in tissue engineering methoden (per-operatief zaaien versus 7 dagen vooraf kweken van de constructen) laat dit zien dat verschillende proefdiermodellen verschillende resultaten kunnen geven en dat de resultaten hiervan dus moeilijk interpreteerbaar en toepasbaar zijn voor de klinische situatie.

De toevoeging van BMSCs aan de gestandaardiseerde lage baktemperatuur HA en BCP dragers resulteerde wel in botvorming. Deze botvorming was vergelijkbaar

in beide materialen en leek op de botvorming door groei vanaf het materiaal oppervlakte zoals die eerder was gezien in het muizenmodel (Hoofdstuk 2) met een vergelijkbare voorkeur voor de oppervlakten met de inkepingen. Opmerkelijk was dat de botvorming afhankelijk was van het proefdier zelf, in de zin dat botvorming altijd in beide dragers werd gezien (in zes van de tien geiten) of helemaal niet. Door toediening van fluorochromen na 3, 5 en 7 weken konden we de dynamiek van botvorming bestuderen. Het vroeg gegeven label werd meestal in kleine botapposities direct tegen het materiaaloppervlakte met de inkepingen gezien. De daaropvolgende labels lieten zien dat het bot hier vanaf groeide, de ruimte van de poriën in.

Screeningsmodellen voor botvorming in posterolaterale spinale fusie

Bij posterolaterale spinale fusie wordt gestreefd naar een benige verbindingsbrug tussen de processi transversus. Veruit de meeste studies hiernaar hebben functionele modellen gebruikt om te beoordelen of er wel of geen fusie optreedt en beoordelen de frequentie van succesvolle fusies. Hoewel deze modellen noodzakelijk zijn voor de ontwikkeling en vergelijking van nieuwe technieken met de huidige standaard, zijn ze zeer inefficiënt om in beginfase van ontwikkeling van nieuwe materialen en technieken meerdere parameters tegelijkertijd te onderzoeken (screening).

Kunnen we een screeningsmodel ontwerpen dat specifiek betrekking heeft op posterolaterale spinale fusie?

Voor een geslaagde posterolaterale fusie is een vitale botbrug tussen twee of meer opeenvolgende processi transversus vereist. Hierbij spelen zowel het bot van de processi als de spieren ertussen een belangrijke rol. Om een fusie te bewerkstelligen worden tijdens een operatie de processi gedecorticeerd tot bloedend bot waarop de botplastiek, die verder in het tussenliggende spierbed ligt, wordt geplaatst. In **Hoofdstuk 7 en 8** beschrijven en valideren we twee varianten van een screeningsmodel in een groot proefdier (geit) dat specifiek rekening houdt met zowel de bot- als de spiercomponent van posterolaterale fusie. Het screeningsmodel maakt gebruik van cassettes met een opening aan de boven en onderzijde. De testmaterialen worden hierin naast elkaar gepositioneerd en hebben contact met de open onder en bovenzijde. Tijdens de operatie worden de lumbale paraspinale spieren stomp geopend en worden de processi transversus gedecorticeerd. Dan worden de cassettes met inhoud op de processi geschroefd en de spieren weer gesloten. De onderzijde van de testmaterialen in de cassette is dan in direct contact met het geaviveerde bot en de bovenzijde met de spieren.

Hierdoor kunnen we efficiënt en gecontroleerd in meerdere materialen tegelijk het vroege botvormingsproces onderzoeken in een omgeving relevant voor posterolaterale fusie. De twee varianten zoals beschreven in dit proefschrift onderzoeken verschillende materiaal oppervlakten en het effect van tissue engineering in klinisch relevante materialen.

In **Hoofdstuk 7** stellen we de vraag: *kunnen we met dit screeningsmodel de invloed van verschillende materialen op orthotopische en ectopische botvorming door tissue engineering onderzoeken?*

Met het screeningsmodel onderzochten we de invloed van materiaaltype alleen op de vroege botvorming. Door dunne schotjes van de materialen met enige ruimte ertussen in de cassette te plaatsen, ontstonden kanaaltjes omgeven door het test materiaal. Per cassette konden zo vijf verschillende conductiekanaaltjes worden gemaakt. Doordat we twee cassettes per proefdier implanteerde konden we tien condities onderzoeken. In tien poefdieren werd dit onderzocht, waarbij we gebruikt maakten van een “randomized block design” voor de locatie van de condities. Door toediening van fluorochromen na 3, 5 en 7 weken en terminatie na 9 weken konden we de dynamiek van botvorming onderzoeken en meten. We onderzochten in tien calciumfosfaat materialen het effect van chemische structuur (HA, BCP en TCP), baktemperatuur (laag, middel en hoog) calcinatie en oppervlakte ruwheid. Het model toonde een duidelijke relatie tussen de verwachtte oplosbaarheid van het materiaal en de botvorming gedurende de implantatie periode. De materialen met een verwachtte hoge oplosbaarheid (TCP en lage baktemperatuur BCP en HA) toonde een duidelijk hogere biologische activiteit met botvorming door conductie van bot direct gebonden aan het materiaal en vaak een grotere totale hoeveelheid bot in de kanaaltjes. Dit effect nam toe tijdens de implantatie periode, wat we konden afleiden uit de maximale hoogte van de opeenvolgende fluorochromen en was het duidelijkst na 9 weken, door meting van de hoeveelheid bot en het contactoppervlakte tussen bot en materiaal. In de minst oplosbare hoge baktemperatuur materialen was het tegenovergestelde zichtbaar, vrijwel geen botvorming door conductie over het materiaal zelf en alleen enige ingroei vanaf het onderliggende bot in het kanaal. Tot slot zagen we ook dat het pre-calcineren van het ruwe basis materiaal, de botvorming verbeterde in het lage baktemperatuur HA. Concluderend blijkt dit model geschikt voor het screenen van verschillende materiaal condities in een posterolaterale fusie omgeving.

In **Hoofdstuk 8** gebruikte we een variant van het cassette model voor de laatste onderzoeksvraag: *Kunnen we met tissue engineering van poreuze calciumfosfaten posterolaterale fusie verbeteren?*

Hiervoor werden de cassettes zo aangepast dat er vier gescheiden blokjes van verschillende materialen in konden. De invloed van tissue engineering met autologe BMSCs werd onderzocht voor poreuze blokjes HA (hoge en lage baktemperatuur), BCP en TCP. 'Hiervoor werd één cassette met en één controle zonder gezaaide cellen geïmplanteerd op de gedecorticeerde lumbale processi transversus. Fluorochromen weren na 3, 5 en 7 weken gegeven en na 9 weken werd het experiment getermineerd. De histologische analyse was gericht op de dynamiek en distributie van botvorming in het bovenste (direct onder de spier), middelste en onderste (direct op het bot) 1/3^{e} deel. Histomorfometrie van de controle groep liet zien dat het bot-materiaalcontact percentage significant lager was voor de HA groepen in vergelijking met BCP en TCP. Dit komt overeen met de bevindingen uit het conductie model beschreven in **Hoofdstuk 7**. De totale hoeveelheid bot was niet significant toegenomen in de HA groepen gezaaid met cellen. Echter, in het bovenste 1/3^{e} deel van de lage baktemperatuur HA met cellen was het bot-contact percentage wel hoger. Tissue engineering zorgde ook voor een hoger contact percentage in de BCP en TCP materialen. Wanneer we naar het effect van de BMSCs in de 3 regio's keken, gaf BCP zonder cellen juist een matig maar significant hoger bot contact, in het middendeel was geen effect van de cellen waarneembaar, maar in het bovenste deel was er een sterk toegenomen botvorming in de BMSCs condities. Deze bevindingen leverde een even verrassende als belangrijke conclusie: In dit model leidde de toevoeging van BMSCs niet tot meer botvorming in gebieden dicht bij het onderliggende bot, (orthotopische omgeving), maar verder van bot verwijderd onder de spieren (meer ectopisch) was het effect van de cellen overduidelijk. Daarom mogen we concluderen dat toevoeging van cellen juist in posterolaterale fusies zinvol kan zijn, omdat de meeste pseudoarthroses juist ontstaan in het meer ectopische gebied tussen de processi transversus. Vervolgstudies zijn daarom een logische stap en op basis van de gegeven van deze studie lijken BCP en TCP goede dragermaterialen.

Conclusies

Het belangrijkste doel van dit proefschrift was de verdere verbetering van tissue engineering voor posterolaterale spinale fusie door onderzoek naar de relatie tussen calciumfosfaat keramische dragers en botvorming door tissue engineering. Dit doel is met de studies uit dit proefschrift op twee manieren bereikt.

Ten eerste werden in de *in vivo* modellen **(Hoofdstuk 4, 7 en 8)** steeds ten minste 4 veelvoorkomende materialen onderzocht HA (hoge en lage-baktemperatuur) BCP en TCP. Steeds werd aangetoond dat hoge baktemperatuur HA de minste bioactiviteit bezat. Daarbij had toevoeging van BMSCs ook het minste effect op dit materiaal. Behalve TCP in het ectopische model (Hoofdstuk 4) waren BCP en TCP het meest bioactief en het meest ontvankelijk voor botvorming door toevoeging van BMSCs. Dit suggereert niet alleen dat BCP en TCP goede materialen zijn voor verdere ontwikkeling, hun waarde wordt temeer bekrachtigd door de stelselmatigheid van de resultaten in de verschillende modellen en de beschikbare literatuur.

Ten tweede bleken de modellen die we hebben ontwikkeld betrouwbaar en efficiënt voor het screenen van meerdere materiaal condities in een relevante biologische omgeving. Hopelijk zullen deze modellen verder worden gebruikt en verbeterd voor onderzoek naar bot tissue engineering in het algemeen en spinale fusie in het bijzonder.

R

References

1. IUPAC Compendium of Chemical Terminology, Electronic version.

2. PDF card no. 9-432. International Centre for Diffraction Data.

3. NIH GUIDE: Tissue Engineering, Biomimetics, and Medical Implant Science. 1997 April 25;26(13).

4. Septic arthritis following anterior cruciate ligament reconstruction using tendon allografts--Florida and Louisiana, 2000. MMWR Morb Mortal Wkly Rep. 2001 Dec 7;50(48):1081-3.

5. Update: allograft-associated bacterial infections--United States, 2002. MMWR Morb Mortal Wkly Rep. 2002 Mar 15;51(10):207-10.

6. Abell AB, Willis KL, Lange DA. Mercury Intrusion Porosimetry and Image Analysis of Cement-Based Materials. J Colloid Interface Sci. 1999 Mar 1;211(1):39-44.

7. Agarwal R, Williams K, Umscheid CA, Welch WC. Osteoinductive bone graft substitutes for lumbar fusion: a systematic review. J Neurosurg Spine. 2009;11(6):729-40.

8. Ahmed SA, Gogal RM, Jr., Walsh JE. A new rapid and simple non-radioactive assay to monitor and determine the proliferation of lymphocytes: an alternative to [3H]thymidine incorporation assay. J Immunol Methods. 1994 Apr 15;170(2):211-24.

9. Albee F. An experimental study on bone growth and the spinal bone transplant. JAMA. 1913;60:1044-52.

10. Anderson JM. The cellular cascades of wound healing. In: Davies JE, editor. Bone Engineering. Toronto: Em Squared; 2000. p. 81-93.

11. Annaz B, Hing KA, Kayser M, Buckland T, Di Silvio L. Porosity variation in hydroxyapatite and osteoblast morphology: a scanning electron microscopy study. J Microsc. 2004;215(Pt 1):100-10.

12. Anselme K, Noel B, Flautre B, Blary MC, Delecourt C, Descamps M, et al. Association of porous hydroxyapatite and bone marrow cells for bone regeneration. Bone. 1999;25(2 Suppl):51S-4S.

13. Arinzeh TL, Peter SJ, Archambault MP, van den Bos C, Gordon S, Kraus K, et al. Allogeneic mesenchymal stem cells regenerate bone in a critical-sized canine segmental defect. J Bone Joint Surg Am. 2003;85-A(10):1927-35.

14. Arinzeh TL, Tran T, McAlary J, Daculsi G. A comparative study of biphasic calcium phosphate ceramics for human mesenchymal stem-cell-induced bone formation. Biomaterials. 2005;26(17):3631-8.

15. Arrington ED, Smith WJ, Chambers HG, Bucknell AL, Davino NA. Complications of iliac crest bone graft harvesting. Clin Orthop Relat Res. 1996(329):300-9.

16. ASTM. ASTM F2150-02e1 Standard Guide for Characterization and Testing of Biomaterial Scaffolds Used in Tissue-Engineered Medical Products. Annual Book of ASTM Standards: ASTM International; 2002.

17. Bab I, Ashton BA, Gazit D, Marx G, Williamson MC, Owen ME. Kinetics and differentiation of marrow stromal cells in diffusion chambers in vivo. J Cell Sci. 1986;84:139-51.

18. Banwart JC, Asher MA, Hassanein RS. Iliac crest bone graft harvest donor site morbidity. A statistical evaluation. Spine. 1995 May 1;20(9):1055-60.

19. Barrere F, van Blitterswijk CA, de Groot K. Bone regeneration: molecular and cellular interactions with calcium phosphate ceramics. Int J Nanomedicine. 2006;1(3):317-32.

20. Barrere F, van der Valk CM, Dalmeijer RA, Meijer G, van Blitterswijk CA, de Groot K, et al. Osteogenecity of octacalcium phosphate coatings applied on porous metal implants. J Biomed Mater Res A. 2003;66(4):779-88.

21. Barrere F, van der Valk CM, Dalmeijer RA, van Blitterswijk CA, de Groot K, Layrolle P. In vitro and in vivo degradation of biomimetic octacalcium phosphate and carbonate apatite coatings on titanium implants. J Biomed Mater Res A. 2003;64(2):378-87.

22. Benglis D, Wang MY, Levi AD. A comprehensive review of the safety profile of bone morphogenetic protein in spine surgery. Neurosurgery. 2008;62(5 Suppl 2):ONS423-31; discussion ONS31.

23. Bentley MD, Ortiz MC, Ritman EL, Romero JC. The use of microcomputed tomography to study microvasculature in small rodents. Am J Physiol Regul Integr Comp Physiol. 2002 May;282(5):R1267-79.

24. Betz RR. Limitations of autograft and allograft: new synthetic solutions. Orthopedics. 2002;25(5 Suppl):s561-70.

25. BioSource International I. alamarBlueTM product booklet.

26. Bloebaum RD, Bachus KN, Momberger NG, Hofmann AA. Mineral apposition rates of human cancellous bone at the interface of porous coated implants. J Biomed Mater Res. 1994 May;28(5):537-44.

27. Boden SD. Overview of the biology of lumbar spine fusion and principles for selecting a bone graft substitute. Spine (Phila Pa 1976). 2002 Aug 16;27(16 Suppl 1):S26-31.

28. Boden SD, Sumner DR. Biologic factors affecting spinal fusion and bone regeneration. Spine. 1995;20(24 Suppl):102S-12S.

29. Boden SD, Titus L, Hair G, Liu Y, Viggeswarapu M, Nanes MS, et al. Lumbar spine fusion by local gene therapy with a cDNA encoding a novel osteoinductive protein (LMP-1). Spine. 1998;23(23):2486-92.

30. Boden SD, Zdeblick TA, Sandhu HS, Heim SE. The use of rhBMP-2 in interbody fusion cages. Definitive evidence of osteoinduction in humans: a preliminary report. Spine. 2000 Feb 1;25(3):376-81.

31. Bouler JM, Trecant M, Delecrin J, Royer J, Passuti N, Daculsi G. Macroporous biphasic calcium phosphate ceramics: influence of five synthesis parameters on compressive strength. J Biomed Mater Res. 1996 Dec;32(4):603-9.

32. Boyce T, Edwards J, Scarborough N. Allograft bone. The influence of processing on safety and performance. Orthop Clin North Am. 1999;30(4):571-81.

33. Bruder SP, Fox BS. Tissue engineering of bone. Cell based strategies. Clin Orthop Relat Res. 1999(367 Suppl):S68-83.

34. Bruder SP, Kraus KH, Goldberg VM, Kadiyala S. The effect of implants loaded with autologous mesenchymal stem cells on the healing of canine segmental bone defects. J Bone Joint Surg Am. 1998;80(7):985-96.

35. Bucholz RW. Nonallograft osteoconductive bone graft substitutes. Clin Orthop Relat Res. 2002 Feb;395(395):44-52.

36. Burger EL, Patel V. Calcium phosphates as bone graft extenders. Orthopedics. 2007 Nov;30(11):939-42.

37. Burkus JK, Gornet MF, Dickman CA, Zdeblick TA. Anterior lumbar interbody fusion using rhBMP-2 with tapered interbody cages. J Spinal Disord Tech. 2002;15(5):337-49.

38. Burwell RG. Studies In The Transplantation Of Bone. Vii. The Fresh Composite Homograft-Autograft Of Cancellous Bone; An Analysis Of Factors Leading To Osteogenesis In Marrow Transplants And In Marrow-Containing Bone Grafts. J Bone Joint Surg Br. 1964;46:110-40.

39. Cancedda R, Mastrogiacomo M, Bianchi G, Derubeis A, Muraglia A, Quarto R. Bone marrow stromal cells and their use in regenerating bone. Novartis Found Symp. 2003;249:133-43; discussion 43-7, 70-4, 239-41.

40. Caplan AI. Mesenchymal stem cells. J Orthop Res. 1991 Sep;9(5):641-50.

41. Caplan AI, Goldberg VM. Principles of tissue engineered regeneration of skeletal tissues. Clin Orthop. 1999 Oct(367 Suppl):S12-6.

42. Carletti E, Motta A, Migliaresi C. Scaffolds for tissue engineering and 3D cell culture. Methods Mol Biol. 2011;695:17-39.

43. Chang BS, Lee CK, Hong KS, Youn HJ, Ryu HS, Chung SS, et al. Osteoconduction at porous hydroxyapatite with various pore configurations. Biomaterials. 2000 Jun;21(12):1291-8.

44. Chang YL, Stanford CM, Keller JC. Calcium and phosphate supplementation promotes bone cell mineralization: implications for hydroxyapatite (HA)-enhanced bone formation. J Biomed Mater Res. 2000 Nov;52(2):270-8.

45. Chim H, Schantz JT. New frontiers in calvarial reconstruction: integrating computer-assisted design and tissue engineering in cranioplasty. Plast Reconstr Surg. 2005 Nov;116(6):1726-41.

46. Chiroff RT, White EW, Weber KN, Roy DM. Tissue ingrowth of Replamineform implants. J Biomed Mater Res. 1975 Jul;9(4):29-45.

47. Chu TM, Halloran JW, Hollister SJ, Feinberg SE. Hydroxyapatite implants with designed internal architecture. J Mater Sci Mater Med. 2001 Jun;12(6):471-8.

48. Chu TM, Orton DG, Hollister SJ, Feinberg SE, Halloran JW. Mechanical and in vivo performance of hydroxyapatite implants with controlled architectures. Biomaterials. 2002 Mar;23(5):1283-93.

49. Cima LG, Vacanti JP, Vacanti C, Ingber D, Mooney D, Langer R. Tissue engineering by cell transplantation using degradable polymer substrates. J Biomech Eng. 1991 May;113(2):143-51.

50. Conrad E, Gretch D, Obermeyer K, Moogk M, Sayers M, Wilson J, et al. Transmission of the hepatitis-C virus by tissue transplantation. J Bone Joint Surg Am. 1995;77(2):214-24.

51. Daculsi G. Biphasic calcium phosphate concept applied to artificial bone, implant coating and injectable bone substitute. Biomaterials. 1998 Aug;19(16):1473-8.

52. Daculsi G, Bouler JM, LeGeros RZ. Adaptive crystal formation in normal and pathological calcifications in synthetic calcium phosphate and related biomaterials. Int Rev Cytol. 1997;172:129-91.

53. Daculsi G, LeGeros RZ, Heughebaert M, Barbieux I. Formation of carbonate-apatite crystals after implantation of calcium phosphate ceramics. Calcif Tissue Int. 1990 Jan;46(1):20-7.

54. Daculsi G, LeGeros RZ, Nery E, Lynch K, Kerebel B. Transformation of biphasic calcium phosphate ceramics in vivo: ultrastructural and physicochemical characterization. J Biomed Mater Res. 1989;23(8):883-94.

55. Daculsi G, Passuti N. Bioactive ceramics, fundamental properties and clinical applications: the osseo-coalescence process. Bioceramics. 1989;2:3-10.

56. Davies JE. Mechanisms of endosseous integration. Int J Prosthodont. 1998;11(5):391-401.

57. Davies JE. Bone bonding at natural and biomaterial surfaces. Biomaterials. 2007;28(34):5058-67. Epub 2007 Aug 13.

58. Davies JE, Hosseini MM. Histodynamics of endosseous wound healing. In: Davies JE, editor. Bone engineering. Toronto: em squared; 2000. p. 1-14.

59. Davis BH, Schroeder T, Yarmolenko PS, Guilak F, Dewhirst MW, Taylor DA. An in vitro system to evaluate the effects of ischemia on survival of cells used for cell therapy. Ann Biomed Eng. 2007;35(8):1414-24. Epub 2007 Apr 7.

60. de Bruijn JD, Bovell YP, van Blitterswijk CA. Structural arrangements at the interface between plasma sprayed calcium phosphates and bone. Biomaterials. 1994;15(7):543-50.

61. de Bruijn JD, Davies JE, Klein CP, de Groot K, van Blitterswijk CA. Biological responses to calcium phosphate ceramics. In: Ducheyne P, Kokubo T, Van Blitterswijk CA, editors. Bone bonding biomaterials. Leiderdorp: Reed Healthcare Communications; 1992. p. 57-72.

62. de Bruijn JD, Klein CP, de Groot K, van Blitterswijk CA. The ultrastructure of the bone-hydroxyapatite interface in vitro. J Biomed Mater Res. 1992 Oct;26(10):1365-82.

63. de Bruijn JD, van Blitterswijk CA, Davies JE. Initial bone matrix formation at the hydroxyapatite interface in vivo. J Biomed Mater Res. 1995 Jan;29(1):89-99.

64. de Bruijn JD, van den Brink I, Bovell YP, van Blitterswijk CA. Tissue engineering of goat bone: osteogenic potential of goat bone marrow cells. Bioceramics. 1998;11:497-500.

65. de Bruijn JD, van den Brink I, Mendes S, Dekker R, Bovell YP, van Blitterswijk CA. Bone induction by implants coated with cultured osteogenic bone marrow cells. Adv Dent Res. 1999;13:74-81.

66. de Bruijn JD, Yuan H, Dekker R, Layrolle P, de Groot K, van Blitterswijk CA. Osteoinductive biomimetic calcium phosphate coatings and their potential use as tissue engineering scaffolds. In: Davies JE, editor. Bone Engineering. Totonto: EM Squared; 2000. p. 421-31.

67. de Bruyn PPH, Kabisch WT. Bone formation by fresh and frozen, autogenous and homogenous transplants of bone, bone marrow and periosteum. American Journal of Anatomy. 1955;96(3):375-417.

68. de Groot K. Bioceramics consisting of calcium phosphate salts. Biomaterials. 1980 Jan;1(1):47-50.

69. de Groot K. Degradable ceramics. In: Williams DF, editor. Biocompatibility of clinical implant materials. Boca Raton, Florida, USA: CRC Press; 1981. p. 199-222.

70. de Groot K. Calcium phosphate ceramics: their current status. In: Boretos JW, Eden M, editors. Contemporary biomaterials. USA: Noyes Publications; 1984. p. 477-92.

71. Delecrin J, Takahashi S, Gouin F, Passuti N. A synthetic porous ceramic as a bone graft substitute in the surgical management of scoliosis: a prospective, randomized study. Spine. 2000 Mar 1;25(5):563-9.

72. Dennis JE, Haynesworth SE, Young RG, Caplan AI. Osteogenesis in marrow-derived mesenchymal cell porous ceramic composites transplanted subcutaneously: effect of fibronectin and laminin on cell retention and rate of osteogenic expression. Cell Transplant. 1992;1(1):23-32.

73. Derubeis AR, Cancedda R. Bone marrow stromal cells (BMSCs) in bone engineering: limitations and recent advances. Ann Biomed Eng. 2004;32(1):160-5.

74. Drespe IH, Polzhofer GK, Turner AS, Grauer JN. Animal models for spinal fusion. Spine J. 2005;5(6 Suppl):209S-16S.

75. Ducheyne P. Bioactive ceramics. J Bone Joint Surg Br. 1994 Nov;76(6):861-2.

76. Ducheyne P, Qiu Q. Bioactive ceramics: the effect of surface reactivity on bone formation and bone cell function. Biomaterials. 1999;20(23-24):2287-303.

77. Ducheyne P, Radin S, King L. The effect of calcium phosphate ceramic composition and structure on in vitro behavior. I. Dissolution. J Biomed Mater Res. 1993;27(1):25-34.

78. Dutta Roy T, Simon JL, Ricci JL, Rekow ED, Thompson VP, Parsons JR. Performance of hydroxyapatite bone repair scaffolds created via three-dimensional fabrication techniques. J Biomed Mater Res A. 2003 Dec 15;67(4):1228-37.

79. Eggli PS, Muller W, Schenk RK. Porous hydroxyapatite and tricalcium phosphate cylinders with two different pore size ranges implanted in the cancellous bone of rabbits. A comparative histomorphometric and histologic study of bony ingrowth and implant substitution. Clin Orthop. 1988 Jul(232):127-38.

80. Eick JD, Good RJ, Newman AW. Thermodynamics of Contact Angles. II. Rough Solid Surfaces. J Colloid Interface Sci. 1975;53:235-48.

81. El-Ghannam A. Bone reconstruction: from bioceramics to tissue engineering. Expert Rev Med Devices. 2005;2(1):87-101.

82. Elliott JC. Structure and Chemistry of the Apatites and Other Calcium Orthophosphates. Amsterdam: Elsevier Science B.V.; 1994.

83. Feiertag MA, Boden SD, Schimandle JH, Norman JT. A rabbit model for nonunion of lumbar intertransverse process spine arthrodesis. Spine. 1996;21(1):27-31.

84. Filmon R, Retailleau-Gaborit N, Grizon F, Galloyer M, Cincu C, Basle MF, et al. Non-connected versus interconnected macroporosity in poly(2-hydroxyethyl methacrylate) polymers. An X-ray microtomographic and histomorphometric study. J Biomater Sci Polym Ed. 2002;13(10):1105-17.

85. Friedenstein AJ, Chailakhjan RK, Lalykina KS. The development of fibroblast colonies in monolayer cultures of guinea-pig bone marrow and spleen cells. Cell Tissue Kinet. 1970;3(4):393-403.

86. Friedenstein AJ, Chailakhyan RK, Gerasimov UV. Bone marrow osteogenic stem cells: in vitro cultivation and transplantation in diffusion chambers. Cell Tissue Kinet. 1987;20(3):263-72.

87. Friedenstein AJ, Petrakova KV, Kurolesova AI, Frolova GP. Heterotopic of bone marrow. Analysis of precursor cells for osteogenic and hematopoietic tissues. Transplantation. 1968;6(2):230-47.

88. Friedenstein AJ, Piatetzky S, II, Petrakova KV. Osteogenesis in transplants of bone marrow cells. J Embryol Exp Morphol. 1966;16(3):381-90.

89. Friedlaender GE, Perry CR, Cole JD, Cook SD, Cierny G, Muschler GF, et al. Osteogenic protein-1 (bone morphogenetic protein-7) in the treatment of tibial nonunions. J Bone Joint Surg Am. 2001;83-A Suppl 1(Pt 2):S151-8.

90. Garboczi EJ, Bentz DP, Martys NS. Chapter 1: Digital images and computer modeling. Experimental methods in the physical sciences: Mehtods in the physics of porous media. San Diego, CA: Academic Press; 1999. p. 1-41.

91. Gauthier O, Bouler JM, Aguado E, Pilet P, Daculsi G. Macroporous biphasic calcium phosphate ceramics: influence of macropore diameter and macroporosity percentage on bone ingrowth. Biomaterials. 1998 Jan-Feb;19(1-3):133-9.

92. Gazdag AR, Lane JM, Glaser D, Forster RA. Alternatives to Autogenous Bone Graft: Efficacy and Indications. J Am Acad Orthop Surg. 1995 Jan;3(1):1-8.

93. Geesink RG, de Groot K, Klein CP. Bonding of bone to apatite-coated implants. J Bone Joint Surg Br. 1988;70(1):17-22.

94. Geuze RE, Kruyt MC, Verbout AJ, Alblas J, Dhert WJ. Comparing various off-the-shelf methods for bone tissue engineering in a large-animal ectopic implantation model: bone marrow, allogeneic bone marrow stromal cells, and platelet gel. Tissue Eng Part A. 2008 Aug;14(8):1435-43.

95. Giannoudis PV, Dinopoulos H, Tsiridis E. Bone substitutes: an update. Injury. 2005;36(Suppl 3):S20-7.

96. Gilbert L, He X, Farmer P, Boden S, Kozlowski M, Rubin J, et al. Inhibition of osteoblast differentiation by tumor necrosis factor-alpha. Endocrinology. 2000 Nov;141(11):3956-64.

97. Gilbert M, Shaw WJ, Long JR, Nelson K, Drobny GP, Giachelli CM, et al. Chimeric peptides of statherin and osteopontin that bind hydroxyapatite and mediate cell adhesion. J Biol Chem. 2000 May 26;275(21):16213-8.

98. Glowacki J. A review of osteoinductive testing methods and sterilization processes for demineralized bone. Cell Tissue Bank. 2005;6(1):3-12.

99. Goshima J, Goldberg VM, Caplan AI. The origin of bone formed in composite grafts of porous calcium phosphate ceramic loaded with marrow cells. Clin Orthop Relat Res. 1991(269):274-83.

100. Goshima J, Goldberg VM, Caplan AI. The osteogenic potential of culture-expanded rat marrow mesenchymal cells assayed in vivo in calcium phosphate ceramic blocks. Clin Orthop. 1991(262):298-311.

101. Gossl M, Bentley MD, Lerman LO. Review--3D micro CT imaging of renal micro-structural changes. Nephron Clin Pract. 2006;103(2):c66-70.

102. Graziano A, d'Aquino R, Cusella-De Angelis MG, De Francesco F, Giordano A, Laino G, et al. Scaffold's surface geometry significantly affects human stem cell bone tissue engineering. J Cell Physiol. 2008;214(1):166-72.

103. Greenwald AS, Boden SD, Goldberg VM, Khan Y, Laurencin CT, Rosier RN. Bone-graft substitutes: facts, fictions, and applications. J Bone Joint Surg Am. 2001;83-A(Suppl 2 Pt 2):98-103.

104. Greenwald AS, Boden SD, Goldberg VM, Yaszemski M, Heim CS. Bone-graft substitutes: facts, fictions and applications. American Acadamy of Orthopaedic Surgeons; March 5 - 9; San Francisco2008.

105. Griffith LG, Naughton G. Tissue engineering--current challenges and expanding opportunities. Science. 2002 Feb 8;295(5557):1009-14.

106. Guda T, Appleford M, Oh S, Ong JL. A cellular perspective to bioceramic scaffolds for bone tissue engineering: the state of the art. Curr Top Med Chem. 2008;8(4):290-9.

107. Guldberg RE, Ballock RT, Boyan BD, Duvall CL, Lin AS, Nagaraja S, et al. Analyzing bone, blood vessels, and biomaterials with microcomputed tomography. IEEE Eng Med Biol Mag. 2003 Sep-Oct;22(5):77-83.

108. Habibovic P, de Groot K. Osteoinductive biomaterials--properties and relevance in bone repair. J Tissue Eng Regen Med. 2007 Jan-Feb;1(1):25-32.

109. Habibovic P, Gbureck U, Doillon CJ, Bassett DC, van Blitterswijk CA, Barralet JE. Osteoconduction and osteoinduction of low-temperature 3D printed bioceramic implants. Biomaterials. 2008 Mar;29(7):944-53.

110. Habibovic P, Kruyt MC, Juhl MV, Clyens S, Martinetti R, Dolcini L, et al. Comparative in vivo study of six hydroxyapatite-based bone graft substitutes. J Orthop Res. 2008 Oct;26(10):1363-70.

111. Habibovic P, Sees TM, van den Doel MA, van Blitterswijk CA, de Groot K. Osteoinduction by biomaterials--physicochemical and structural influences. J Biomed Mater Res A. 2006 Jun 15;77(4):747-62.

112. Habibovic P, Yuan H, van der Valk CM, Meijer G, van Blitterswijk CA, de Groot K. 3D microenvironment as essential element for osteoinduction by biomaterials. Biomaterials. 2005 Jun;26(17):3565-75.

113. Hadjipavlou A, Enker P, Dupuis P, Katzman S, Silver J. The causes of failure of lumbar transpedicular spinal instrumentation and fusion: a prospective study. Int Orthop. 1996;20(1):35-42.

114. Haynesworth SE, Goshima J, Goldberg VM, Caplan AI. Characterization of cells with osteogenic potential from human marrow. Bone. 1992;13(1):81-8.

115. Heslop BF, Zeiss IM, Nisbet NW. Studies on transference of bone. I. A comparison of autologous and homologous bone implants with reference to osteocyte survival, osteogenesis and host reaction. Br J Exp Pathol. 1960;41:269-87.

116. Heughebaert M, LeGeros RZ, Gineste M, Guilhem A, Bonel G. Physicochemical characterization of deposits associated with HA ceramics implanted in nonosseous sites. J Biomed Mater Res. 1988;22(3 Suppl):257-68.

117. Hildebrand T, Rüegsegger P. A new method for the model independent assessment of thickness in three-dimensional images. J Microsc. 1997;185:67-75.

118. Hing KA, Best SM, Bonfield W. Characterization of porous hydroxyapatite. Journal of Materials Science: Materials in Medicine. 1999;10:135-45.

119. Hing KA, Best SM, Tanner KE, Bonfield W, Revell PA. Mediation of bone ingrowth in porous hydroxyapatite bone graft substitutes. J Biomed Mater Res A. 2004 Jan 1;68(1):187-200.

120. Hofmann AA, Bloebaum RD, Bachus KN. Progression of human bone ingrowth into porous-coated implants. Rate of bone ingrowth in humans. Acta Orthop Scand. 1997 Apr;68(2):161-6.

121. Hollinger JO, Brekke J, Gruskin E, Lee D. Role of bone substitutes. Clin Orthop. 1996 Mar(324):55-65.

122. Hollister SJ. Porous scaffold design for tissue engineering. Nat Mater. 2005 Jul;4(7):518-24.

123. Holmes R, Mooney V, Bucholz R, Tencer A. A coralline hydroxyapatite bone graft substitute. Preliminary report. Clin Orthop. 1984 Sep(188):252-62.

124. Holmes RE. Osteoconduction in hydroxyapatite-based materials. In: Brighton CT, Friedlaender G, Lane JM, editors. Bone formation and repair: Rosemont: American Academy of Orthopedic Surgeons; 1994. p. 355-65.

125. Hulbert SF, Young FA, Mathews RS, Klawitter JJ, Talbert CD, Stelling FH. Potential of ceramic materials as permanently implantable skeletal prostheses. J Biomed Mater Res. 1970 Sep;4(3):433-56.

126. Hurley LA, Stinchfield FE, Bassett AL, Lyon WH. The role of soft tissues in osteogenesis. An experimental study of canine spine fusions. J Bone Joint Surg Am. 1959;41-A:1243-54.

127. Hutmacher DW. Scaffolds in tissue engineering bone and cartilage. Biomaterials. 2000 Dec;21(24):2529-43.

128. Hutmacher DW. Scaffold design and fabrication technologies for engineering tissues--state of the art and future perspectives. J Biomater Sci Polym Ed. 2001;12(1):107-24.

129. Pore size distribution and porosity of solid materials by mercury porosimetry and gas adsorption - Part 1: Mercury porosimetry, ISO 15901-1:2005.

130. Jarcho M. Calcium phosphate ceramics as hard tissue prosthetics. Clin Orthop. 1981 Jun(157):259-78.

131. Jin QM, Takita H, Kohgo T, Atsumi K, Itoh H, Kuboki Y. Effects of geometry of hydroxyapatite as a cell substratum in BMP-induced ectopic bone formation. J Biomed Mater Res. 2000 Dec 15;52(4):491-9.

132.Jingushi S. Biological cascades of fracture healing as models for bone-biomaterial interface reactions. In: Davies JE, editor. The Bone Biomaterial Interface. Toronto: Toronto University Press; 1991. p. 250-62.

133.Jones AC, Arns CH, Hutmacher DW, Milthorpe BK, Sheppard AP, Knackstedt MA. The correlation of pore morphology, interconnectivity and physical properties of 3D ceramic scaffolds with bone ingrowth. Biomaterials. 2009;30(7):1440-51. Epub 2008 Dec 16.

134.Kainer MA, Linden JV, Whaley DN, Holmes HT, Jarvis WR, Jernigan DB, et al. Clostridium infections associated with musculoskeletal-tissue allografts. N Engl J Med. 2004;350(25):2564-71.

135.Karageorgiou V, Kaplan D. Porosity of 3D biomaterial scaffolds and osteogenesis. Biomaterials. 2005;26:5474-91.

136.Kawai N, Niwa S, Sato M, Sato Y, Suwa Y, Ichihara I. Bone formation by cells from femurs cultured among three-dimensionally arranged hydroxyapatite granules. J Biomed Mater Res. 1997 Oct;37(1):1-8.

137.Khan SN, Lane JM. Spinal fusion surgery: animal models for tissue-engineered bone constructs. Biomaterials. 2004 Apr;25(9):1475-85.

138.Kleeman TJ, Ahn UM, Talbot-Kleeman A. Laparoscopic anterior lumbar interbody fusion with rhBMP-2: a prospective study of clinical and radiographic outcomes. Spine. 2001 2001 Dec 15;26(24):2751-6.

139.Knabe C, Berger G, Gildenhaar R, Meyer J, Howlett CR, Markovic B, et al. Effect of rapidly resorbable calcium phosphates and a calcium phosphate bone cement on the expression of bone-related genes and proteins in vitro. J Biomed Mater Res A. 2004;69(1):145-54.

140.Kokubo T, Kim HM, Kawashita M. Novel bioactive materials with different mechanical properties. Biomaterials. 2003 Jun;24(13):2161-75.

141.Kon E, Muraglia A, Corsi A, Bianco P, Marcacci M, Martin I, et al. Autologous bone marrow stromal cells loaded onto porous hydroxyapatite ceramic accelerate bone repair in critical-size defects of sheep long bones. J Biomed Mater Res. 2000;49(3):328-37.

142.Kotani Y, Cunningham BW, Cappuccino A, Kaneda K, McAfee PC. The effects of spinal fixation and destabilization on the biomechanical and histologic properties of spinal ligaments. An in vivo study. Spine. 1998;23(6):672-82; discussion 82-3.

143.Kowalski RJ, Ferrara LA, Benzel EC. Biomechanics of bone fusion. Neurosurg Focus. 2001;10(4):E2.

144. Krajewski A, Ravaglioli A, di Sanseverino LR, Marchetti F, Monticelli G. The behaviour of apatite-based ceramics in relation to the critical 1150 degrees-1250 degrees C temperature range. Biomaterials. 1984 Mar;5(2):105-8.

145. Krebsbach PH, Kuznetsov SA, Satomura K, Emmons RVB, Rowe DW, Robey PG. Bone Formation in Vivo: Comparison of Osteogenesis By Transplanted Mouse and Human Marrow Stromal Fibroblasts. Transplantation. 1997 27 April;63(8):1059-69.

146. Kruyt M, de Bruijn J, Rouwkema J, van Blitterswijk C, Oner C, Verbout A, Dhert W. Analysis of the dynamics of bone formation, effect of cell seeding density, and potential of allogeneic cells in cell-based bone tissue engineering in goats. Tissue Eng Part A. 2008 Jun;14(6):1081-8.

147. Kruyt MC, de Bruijn JD, Wilson CE, Oner FC, van Blitterswijk CA, Verbout AJ, Dhert WJ. Viable osteogenic cells are obligatory for tissue-engineered ectopic bone formation in goats. Tissue Eng. 2003 Apr;9(2):327-36.

148. Kruyt MC, de Bruijn JD, Yuan H, van Blitterswijk CA, Verbout AJ, Oner FC, Dhert WJ. Optimization of bone tissue engineering in goats: a peroperative seeding method using cryopreserved cells and localized bone formation in calcium phosphate scaffolds. Transplantation. 2004;77(3):359-65.

149. Kruyt MC, Dhert WJ, Oner C, van Blitterswijk CA, Verbout AJ, de Bruijn JD. Optimization of bone-tissue engineering in goats. J Biomed Mater Res. 2004 May 15 ;69B(2):113-20.

150. Kruyt MC, Dhert WJ, Oner FC, van Blitterswijk CA, Verbout AJ, de Bruijn JD. Analysis of ectopic and orthotopic bone formation in cell-based tissue-engineered constructs in goats. Biomaterials. 2007 Apr;28(10):1798-805.

151. Kruyt MC, Dhert WJ, Yuan H, Wilson CE, van Blitterswijk CA, Verbout AJ, de Bruijn JD. Bone tissue engineering in a critical size defect compared to ectopic implantations in the goat. J Orthop Res. 2004 May;22(3):544-51.

152. Kruyt MC, van Gaalen SM, Oner FC, Verbout AJ, de Bruijn JD, Dhert WJ. Bone tissue engineering and spinal fusion: the potential of hybrid constructs by combining osteoprogenitor cells and scaffolds. Biomaterials. 2004 Apr;25(9):1463-73.

153. Kruyt MC, Wilson CE, de Bruijn JD, van Blitterswijk CA, Oner CF, Verbout AJ, Dhert WJ. The effect of cell-based bone tissue engineering in a goat transverse process model. Biomaterials. 2006 Oct;27(29):5099-106.

154. Kuboki Y, Takita H, Kobayashi D, Tsuruga E, Inoue M, Murata M, et al. BMP-induced osteogenesis on the surface of hydroxyapatite with geometrically feasible and nonfeasible structures: topology of osteogenesis. J Biomed Mater Res. 1998 Feb;39(2):190-9.

155. Kuhne JH, Bartl R, Frisch B, Hammer C, Jansson V, Zimmer M. Bone formation in coralline hydroxyapatite. Effects of pore size studied in rabbits. Acta Orthop Scand. 1994 Jun;65(3):246-52.

156. Laib A, Barou O, Vico L, Lafage-Proust MH, Alexandre C, Rüegsegger P. 3D micro-computed tomography of trabecular and cortical bone architecture with application to a rat model of immobilisation osteoporosis. Med Biol Eng Comput. 2000 May;38(3):326-32.

157. Lampin M, Warocquier C, Legris C, Degrange M, Sigot-Luizard MF. Correlation between substratum roughness and wettability, cell adhesion, and cell migration. J Biomed Mater Res. 1997 Jul;36(1):99-108.

158. Le Gros MA, McDermott G, Larabell CA. X-ray tomography of whole cells. Curr Opin Struct Biol. 2005 Oct;15(5):593-600.

159. Le HM, Holmes RE, Shors E, Rosenstein DA. Computerized quantitative analysis of the interconnectivity of porous biomaterials. Acta Stereologica. 1992;11S1:267-72.

160. Le Huec JC, Lesprit E, Delavigne C, Clement D, Chauveaux D, Le Rebeller A. Tri-calcium phosphate ceramics and allografts as bone substitutes for spinal fusion in idiopathic scoliosis as bone substitutes for spinal fusion in idiopathic scoliosis: comparative clinical results at four years. Acta Orthop Belg. 1997 Sep;63(3):202-11.

161. LeGeros RZ. Calcium Phosphates in Oral Biology and Medicine. New York, NY: Karger; 1991.

162. LeGeros RZ. Properties of osteoconductive biomaterials: calcium phosphates. Clin Orthop Relat Res. 2002;395:81–98.

163. LeGeros RZ, LeGeros JP. Calcium phosphate biomaterials in medical applicaitons. Bioceramics. 1996;9:7-10.

164. LeGeros RZ, LeGeros JP, Daculsi G, Kijkowska R. Calcium phosphate biomaterials: preparation, properties and biodegradation. In: Wise DLea, editor. Encyclopedic handbook of biomaterials engineering Part A: Materials. New York: M. Dekker; 1995. p. 1429-63.

165. Lemon G, Reinwald Y, White LJ, Howdle SM, Shakesheff KM, King JR. Interconnectivity analysis of supercritical CO(2)-foamed scaffolds. Comput Methods Programs Biomed. 2010(In Press, Corrected Proof).

166. Leon y Leon CA. New perspectives in mercury porosimetry. Adv Colloid Interface Sci. 1998;76-77:341-72.

167.Levy RA, Chu TM, Halloran JW, Feinberg SE, Hollister S. CT-generated porous hydroxyapatite orbital floor prosthesis as a prototype bioimplant. AJNR Am J Neuroradiol. 1997 Sep;18(8):1522-5.

168.Lewis MC, Macarthur BD, Malda J, Pettet G, Please CP. Heterogeneous proliferation within engineered cartilaginous tissue: the role of oxygen tension. Biotechnol Bioeng. 2005;91(5):607-15.

169.Li SH, De Wijn JR, Layrolle P, De Groot K. Synthesis of macroporous hydroxyapatite scaffolds for bone tissue engineering. Journal of Biomedical Materials Research. 2002;61(1):109-20.

170.Lin AS, Barrows TH, Cartmell SH, Guldberg RE. Microarchitectural and mechanical characterization of oriented porous polymer scaffolds. Biomaterials. 2003;24:481-9.

171.Lin FH, Liao CJ, Chen KS, Sun JS, Lin CY. Preparation of betaTCP/HAP biphasic ceramics with natural bone structure by heating bovine cancellous bone with the addition of (NH(4))(2)HPO(4). J Biomed Mater Res. 2000 Aug;51(2):157-63.

172.Lu X, Leng Y. Quantitative analysis of osteoblast behavior on microgrooved hydroxyapatite and titanium substrata. J Biomed Mater Res A. 2003;66(3):677-87.

173.Ma PX, Choi JW. Biodegradable polymer scaffolds with well-defined interconnected spherical pore network. Tissue Eng. 2001 Feb;7(1):23-33.

174.Malda J, Rouwkema J, Martens DE, Le Comte EP, Kooy FK, Tramper J, et al. Oxygen gradients in tissue-engineered PEGT/PBT cartilaginous constructs: measurement and modeling. Biotechnol Bioeng. 2004;86(1):9-18.

175.Maquet V, Blacher S, Pirard R, Pirard JP, Vyakarnam MN, Jerome R. Preparation of macroporous biodegradable poly(L-lactide-co-epsilon-caprolactone) foams and characterization by mercury intrusion porosimetry, image analysis, and impedance spectroscopy. J Biomed Mater Res A. 2003 Aug 1;66(2):199-213.

176.Mastrogiacomo M, Scaglione S, Martinetti R, Dolcini L, Beltrame F, Cancedda R, et al. Role of scaffold internal structure on in vivo bone formation in macroporous calcium phosphate bioceramics. Biomaterials. 2006 Jun;27(17):3230-7.

177.Mata A, Boehm C, Fleischman AJ, Muschler GF, Roy S. Connective tissue progenitor cell growth characteristics on textured substrates. Int J Nanomedicine. 2007;2(3):389-406.

178. Mawatari T, Miura H, Higaki H, Kurata K, Moro-oka T, Murakami T, et al. Quantitative analysis of three-dimensional complexity and connectivity changes in trabecular microarchitecture in relation to aging, menopause, and inflammation. J Orthop Sci. 1999;4(6):431-8.

179. Meijer GJ, de Bruijn JD, Koole R, van Blitterswijk CA. Cell-Based Bone Tissue Engineering. PLoS Med. 2007;4(2):e9.

180. Melchels FP, Barradas AM, van Blitterswijk CA, de Boer J, Feijen J, Grijpma DW. Effects of the architecture of tissue engineering scaffolds on cell seeding and culturing. Acta Biomater. 2010 Nov;6(11):4208-17.

181. Mizuno K, Mineo K, Tachibana T, Sumi M, Matsubara T, Hirohata K. The osteogenetic potential of fracture haematoma. Subperiosteal and intramuscular transplantation of the haematoma. J Bone Joint Surg Br. 1990;72(5):822-9.

182. Moore MJ, Jabbari E, Ritman EL, Lu L, Currier BL, Windebank AJ, et al. Quantitative analysis of interconnectivity of porous biodegradable scaffolds with micro-computed tomography. J Biomed Mater Res. 2004;71A:258-67.

183. Moore WR, Graves SE, Bain GI. Synthetic bone graft substitutes. ANZ J Surg. 2001 Jun;71(6):354-61.

184. Mroz TE, Joyce MJ, Lieberman IH, Steinmetz MP, Benzel EC, Wang JC. The use of allograft bone in spine surgery: is it safe? Spine J. 2009;9(4):303-8. Epub 2008 Sep 19.

185. Murphy WL, Dennis RG, Kileny JL, Mooney DJ. Salt fusion: an approach to improve pore interconnectivity within tissue engineering scaffolds. Tissue Eng. 2002 Feb;8(1):43-52.

186. Muschler GF, Nitto H, Matsukura Y, Boehm C, Valdevit A, Kambic H, et al. Spine fusion using cell matrix composites enriched in bone marrow-derived cells. Clin Orthop Relat Res. 2003(407):102-18.

187. Ohgushi H, Caplan AI. Stem cell technology and bioceramics: from cell to gene engineering. J Biomed Mater Res. 1999;48(6):913-27.

188. Ohgushi H, Miyake J, Tateishi T. Mesenchymal stem cells and bioceramics: strategies to regenerate the skeleton. Novartis Found Symp. 2003;249:118-27; discussion 27-32, 70-4, 239-41.

189. Ohgushi H, Okumura M, Tamai S, Shors EC, Caplan AI. Marrow cell induced osteogenesis in porous hydroxyapatite and tricalcium phosphate: a comparative histomorphometric study of ectopic bone formation. J Biomed Mater Res. 1990 Dec;24(12):1563-70.

190. Okumura M, Ohgushi H, Tamai S. Bonding osteogenesis in coralline hydroxyapatite combined with bone marrow cells. Biomaterials. 1991;12(4):411-6.

191. Parekkadan B, Milwid JM. Mesenchymal Stem Cells as Therapeutics. Annual Review of Biomedical Engineering. 2010 Aug 15;12:87-117.

192. Patel N, Gibson IR, Ke S, Best SM, Bonfield W. Calcining influence on the powder properties of hydroxyapatite. J Mater Sci Mater Med. 2001 Feb;12(2):181-8.

193. Peterson B, Iglesias R, Zhang J, Wang JC, Lieberman JR. Genetically modified human derived bone marrow cells for posterolateral lumbar spine fusion in athymic rats: beyond conventional autologous bone grafting. Spine. 2005;30(3):283-9.

194. Peterson B, Whang PG, Iglesias R, Wang JC, Lieberman JR. Osteoinductivity of commercially available demineralized bone matrix. Preparations in a spine fusion model. J Bone Joint Surg Am. 2004;86-A(10):2243-50.

195. Petite H, Viateau V, Bensaid W, Meunier A, de Pollak C, Bourguignon M, et al. Tissue-engineered bone regeneration. Nat Biotechnol. 2000;18(9):959-63.

196. Pirard R, Alié C, Pirard J. Characterization of porous texture of hyperporous materials by mercury porosimetry using densification equation. Powder Technol. 2002;128:242-7.

197. Pirard R, Blacher S, Brouers F, Pirard J. Interpretation of mercury porosimetry applied to aerogels. J Mater Res. 1995;10(8):2114-9.

198. Pirard R, Sahouli B, Blacher S, Pirard J. Sequentially Compressive and Intrusive Mechanisms in Mercury Porosimetry of Carbon Blacks. J Colloid Interface Sci. 1999 Sep 1;217(1):216-7.

199. Radin SR, Ducheyne P. The effect of calcium phosphate ceramic composition and structure on in vitro behavior. II. Precipitation. J Biomed Mater Res. 1993;27(1):35-45.

200. Radisic M, Malda J, Epping E, Geng W, Langer R, Vunjak-Novakovic G. Oxygen gradients correlate with cell density and cell viability in engineered cardiac tissue. Biotechnol Bioeng. 2006;93(2):332-43.

201. Ramay HR, Zhang M. Preparation of porous hydroxyapatite scaffolds by combination of the gel-casting and polymer sponge methods. Biomaterials. 2003;24(19):3293-302.

202. Ransford AO, Morley T, Edgar MA, Webb P, Passuti N, Chopin D, et al. Synthetic porous ceramic compared with autograft in scoliosis surgery. A

prospective, randomized study of 341 patients. J Bone Joint Surg Br. 1998 Jan;80(1):13-8.

203. Redey SA, Nardin M, Bernache-Assolant D, Rey C, Delannoy P, Sedel L, et al. Behavior of human osteoblastic cells on stoichiometric hydroxyapatite and type A carbonate apatite: role of surface energy. J Biomed Mater Res. 2000;50(3):353-64.

204. Rejda BV, Peelen JG, de Groot K. Tri-calcium phosphate as a bone substitute. J Bioeng. 1977 Jan;1(2):93-7.

205. Ripamonti U. Bone induction in nonhuman primates. An experimental study on the baboon. Clin Orthop. 1991 Aug(269):284-94.

206. Ripamonti U. Osteoinduction in porous hydroxyapatite implanted in heterotopic sites of different animal models. Biomaterials. 1996 Jan;17(1):31-5.

207. Ripamonti U, Ma S, Reddi AH. The critical role of geometry of porous hydroxyapatite delivery system in induction of bone by osteogenin, a bone morphogenetic protein. Matrix. 1992 Jun;12(3):202-12.

208. Ritman EL. Molecular imaging in small animals--roles for micro-CT. J Cell Biochem Suppl. 2002;39:116-24.

209. Ritman EL. Micro-computed tomography of the lungs and pulmonary-vascular system. Proc Am Thorac Soc. 2005;2(6):477-80.

210. Ritman EL, Bolander ME, Fitzpatrick LA, Turner RT. Micro-CT imaging of structure-to-function relationship of bone microstructure and associated vascular involvement. Technol Health Care. 1998 Dec;6(5-6):403-12.

211. Roy DM, Linnehan SK. Hydroxyapatite formed from coral skeletal carbonate by hydrothermal exchange. Nature. 1974 Jan 25;247(438):220-2.

212. Russ JC, Dehoff RT. Practical stereology. 2nd ed. New York2000.

213. Sandhu HS. Anterior lumbar interbody fusion with osteoinductive growth factors. Clin Orthop Relat Res. 2000(371):56-60.

214. Sandhu HS, Boden SD, An H, Kang J, Weinstein J. BMPs and gene therapy for spinal fusion: summary statement. Spine. 2003 Aug 1;28(15 Suppl):S85.

215. Sandhu HS, Kanim LEA, Girardi F, Cammisa FP, Dawson EG. Animal models of spinal instability and spinal fusion. In: An YH, Friedman RJ, editors. Animal models in orthopaedic research. Boca Raton: CRC Press; 1999. p. 505-26.

216. Sandhu HS, Khan SN. Animal models for preclinical assessment of bone morphogenetic proteins in the spine. Spine (Phila Pa 1976). 2002 Aug 15;27(16 Suppl 1):S32-8.

217.Schimandle JH, Boden SD. Spine update. The use of animal models to study spinal fusion. Spine (Phila Pa 1976). 1994 Sep 1;19(17):1998-2006.

218.Schliephake H, Neukam FW, Klosa D. Influence of pore dimensions on bone ingrowth into porous hydroxylapatite blocks used as bone graft substitutes. A histometric study. Int J Oral Maxillofac Surg. 1991 Feb;20(1):53-8.

219.Seitz H, Rieder W, Irsen S, Leukers B, Tille C. Three-dimensional printing of porous ceramic scaffolds for bone tissue engineering. J Biomed Mater Res B Appl Biomater. 2005 Aug;74(2):782-8.

220.Sepulveda P, Binner JG, Rogero SO, Higa OZ, Bressiani JC. Production of porous hydroxyapatite by the gel-casting of foams and cytotoxic evaluation. J Biomed Mater Res. 2000 Apr;50(1):27-34.

221.Shimer AL, Oner FC, Vaccaro AR. Spinal reconstruction and bone morphogenetic proteins: open questions. Injury. 2009;40(Suppl 3):S32-8.

222.Simon JL, Dutta Roy T, Parsons JR, Rekow ED, Thompson VP, Kemnitzer J, et al. Engineered cellular response to scaffold architecture in a rabbit trephine defect. J Biomed Mater Res. 2003;66A(2):275-82.

223.Spivak JM, Blumenthal NC, Ricci JL, Alexander H. A new canine model to evaluate the biological effects of implant materials and surface coatings on intramedullary bone ingrowth. Biomaterials. 1990 Jul;11:79-82.

224.Srouji S, Kizhner T, Livne E. 3D scaffolds for bone marrow stem cell support in bone repair. Regen Med. 2006;1(4):519-28.

225.Steffen T, Tsantrizos A, Fruth I, Aebi M. Cages: designs and concepts. Eur Spine J. 2000;9(Suppl 1):S89-94.

226.Taboas JM, Maddox RD, Krebsbach PH, Hollister SJ. Indirect solid free form fabrication of local and global porous, biomimetic and composite 3D polymer-ceramic scaffolds. Biomaterials. 2003;24:181-94.

227.Takemoto M, Fujibayashi S, Otsuki B, Matsushita T, Kokubo T, Nakamura T. 3-D analysis of pore structure of porous biomaterials using micro focus X-ray computed tomography. Bioceramics. 2006;18:1095-8.

228.Tamai N, Myoui A, Tomita T, Nakase T, Tanaka J, Ochi T, et al. Novel hydroxyapatite ceramics with an interconnective porous structure exhibit superior osteoconduction in vivo. J Biomed Mater Res. 2002 Jan;59(1):110-7.

229.Tancred DC, McCormack BA, Carr AJ. A synthetic bone implant macroscopically identical to cancellous bone. Biomaterials. 1998 Dec;19(24):2303-11.

230.Thomsen JS, Laib A, Koller B, Prohaska S, Mosekilde L, Gowin W. Stereological measures of trabecular bone structure: comparison of 3D micro

computed tomography with 2D histological sections in human proximal tibial bone biopsies. J Microsc. 2005 May;218(Pt 2):171-9.

231. Tomford WW. Transmission of disease through transplantation of musculoskeletal allografts. J Bone Joint Surg Am. 1995;77(11):1742-54.

232. Toribatake Y, Hutton WC, Tomita K, Boden SD. Vascularization of the fusion mass in a posterolateral intertransverse process fusion. Spine. 1998;23(10):1149-54.

233. Tsuruga E, Takita H, Itoh H, Wakisaka Y, Kuboki Y. Pore size of porous hydroxyapatite as the cell-substratum controls BMP-induced osteogenesis. J Biochem (Tokyo). 1997 Feb;121(2):317-24.

234. Underwood ED. Quantitative Stereology. Reading, Massachusetts: Addison-Wesley; 1970.

235. Urist MR, Silverman BF, Buring K, Dubuc FL, Rosenberg JM. The bone induction principle. Clin Orthop. 1967 Jul-Aug;53:243-83.

236. van Lenthe GH, Hagenmuller H, Bohner M, Hollister SJ, Meinel L, Muller R. Nondestructive micro-computed tomography for biological imaging and quantification of scaffold-bone interaction in vivo. Biomaterials. 2007 May;28(15):2479-90.

237. Wake MC, Patrick CW, Jr., Mikos AG. Pore morphology effects on the fibrovascular tissue growth in porous polymer substrates. Cell Transplant. 1994 Jul-Aug;3(4):339-43.

238. Wang C, Duan Y, Markovic B, Barbara J, Howlett CR, Zhang X, et al. Phenotypic expression of bone-related genes in osteoblasts grown on calcium phosphate ceramics with different phase compositions. Biomaterials. 2004;25(13):2507-14.

239. Wang YC, Lin MC, Wang da M, Hsieh HJ. Fabrication of a novel porous PGA-chitosan hybrid matrix for tissue engineering. Biomaterials. 2003 Mar;24(6):1047-57.

240. Washburn EW. Note on a method of determining the distribution of pore sizes in a porous material. Proc Natl Acad Sci. 1921;7:115-6.

241. Webb PA. An Introduction to the physical characterization of materials by mercury intrusion porosimetry with emphasis on reduction and presentation of experimental data. Norcross, Georgia: Micromeritics Instrument Corp.; 2001; Available from: http://www.micromeritics.com/.

242. White RA, Weber JN, White EW. Replamineform: a new process for preparing porous ceramic, metal, and polymer prosthetic materials. Science. 1972 May 26;176(37):922-4.

243. Williams BJ, Smith JS, Fu KM, Hamilton DK, Polly DW, Jr., Ames CP, et al. Does BMP increase the incidence of perioperative complications in spinal fusion? A comparison of 55,862 cases of spinal fusion with and without BMP. Spine. 2011;2011:9.

244. Wilson C, van Blitterswijk C, Verbout A, Dhert W, de Bruijn J. Scaffolds with a standardized macro-architecture fabricated from several calcium phosphate ceramics using an indirect rapid prototyping technique. J Mater Sci Mater Med. 2010;22(1):97-105.

245. Wilson CE, De Bruijn JD, van Blitterswijk CA, Kruyt M, van Gaalen S, Dhert WJ, et al., editors. Preliminary Evaluation of Porous Hydroxyapatite Scaffolds for Bone Tissue Engineering Designed and Fabricated Using Rapid Prototyping Techniques. 27th Annual Meeting of the Society For Biomaterials; 2001; Saint Paul.

246. Wilson CE, de Bruijn JD, van Blitterswijk CA, Verbout AJ, Dhert WJ. Design and fabrication of standardized hydroxyapatite scaffolds with a defined macro-architecture by rapid prototyping for bone-tissue-engineering research. J Biomed Mater Res. 2004 Jan 1;68A(1):123-32.

247. Wilson CE, Kruyt MC, de Bruijn JD, van Blitterswijk CA, Oner FC, Verbout AJ, et al. A new in vivo screening model for posterior spinal bone formation: Comparison of ten calcium phosphate ceramic material treatments. Biomaterials. 2006 Jan;27(3):302-14.

248. Winslow DN, Diamond S. A Mercury Porosimetry Study of the Evolution of Porosity in Portland Cement. Journal of Materials, JMLSA. 1970;5(3):564-85.

249. Woodfield TB, Bezemer JM, Pieper JS, van Blitterswijk CA, Riesle J. Scaffolds for tissue engineering of cartilage. Crit Rev Eukaryot Gene Expr. 2002;12(3):209-36.

250. Woyansky JS, Scott CE, Minnear WP. Processing of porous ceramics. Am Ceram Soc Bull. 1992;71:1674-82.

251. Yang S, Leong KF, Du Z, Chua CK. The design of scaffolds for use in tissue engineering. Part I. Traditional factors. Tissue Eng. 2001 Dec;7(6):679-89.

252. Yang S, Leong KF, Du Z, Chua CK. The Design of Scaffolds for Use in Tissue Engineering. Part II. Rapid Prototyping Techniques. Tissue Eng. 2002 Feb;8(1):1-11.

253. Yang ZJ, Yuan H, Zou P, Tong W, Qu S, Zhang XD. Osteogenic responses to extraskeletally implanted synthetic porous calcium phosphate ceramics: an early stage histomorphological study in dogs. J Mater Sci Mater Med. 1997;8(11):697-701.

254. Yoshikawa T, Ohgushi H, Nakajima H, Yamada E, Ichijima K, Tamai S, et al. In vivo osteogenic durability of cultured bone in porous ceramics: a novel method for autogenous bone graft substitution. Transplantation. 2000;69(1):128-34.

255. Younger EM, Chapman MW. Morbidity at bone graft donor sites. J Orthop Trauma. 1989;3(3):192-5.

256. Yuan H, de Bruijn JD, Zhang X, van Blitterswijk CA, de Groot K. Bone induction by porous glass ceramic made from Bioglass (45S5). J Biomed Mater Res. 2001 May 1;58(3):270-6.

257. Yuan H, Fernandes H, Habibovic P, de Boer J, Barradas AM, de Ruiter A, et al. Osteoinductive ceramics as a synthetic alternative to autologous bone grafting. Proc Natl Acad Sci. 2010 Aug 3;107(31):13614-9.

258. Yuan H, Kurashina K, de Bruijn JD, Li Y, de Groot K, Zhang X. A preliminary study on osteoinduction of two kinds of calcium phosphate ceramics. Biomaterials. 1999 Oct;20(19):1799-806.

259. Yuan H, Van Den Doel M, Li S, Van Blitterswijk CA, De Groot K, De Bruijn JD. A comparison of the osteoinductive potential of two calcium phosphate ceramics implanted intramuscularly in goats. J Mater Sci Mater Med. 2002;13(12):1271-5.

260. Yuan H, van den Doel M, van Blitterswijk CA, de Groot K, De Bruij JD, editors. 28th Annual Meeting of the Society for Biomaterials; 2002; Tampa, USA.

261. Yuan H, Yang Z, De Bruij JD, De Groot K, Zhang X. Material-dependent bone induction by calcium phosphate ceramics: a 2.5-year study in dog. Biomaterials. 2001 Oct;22(19):2617-23.

262. Yubao L, Klein CP, Zhang X, de Groot K. Formation of a bone apatite-like layer on the surface of porous hydroxyapatite ceramics. Biomaterials. 1994;15(10):835-41.

263. Zdeblick TA, Phillips FM. Interbody cage devices. Spine (Phila Pa 1976). 2003 Aug 1;28(15 Suppl):S2-7.

264. Zeltinger J, Sherwood JK, Graham DA, Mueller R, Griffith LG. Effect of pore size and void fraction on cellular adhesion, proliferation, and matrix deposition. Tissue Eng. 2001 Oct;7(5):557-72.

A

Acknowledgements

Knowledge is in the end based on acknowledgement.
– Ludwig Wittgenstein –

I must first admit that I cannot adequately acknowledge all of the people who have influenced the progression of my research and this thesis. Rest assured that the contribution of all is appreciated. Thank you for the guidance, patience, contribution, diversion, criticism, perspective, amusement and support.

In particular:

I thank my promoters for their advice, encouragement and endurance.

I thank all of my friends and colleagues from CellCoTec, UMC Utrecht, University of Twente and the former IsoTis.

I thank my parents for instilling in me the belief that I could accomplish such things.

And finally, I thank my wife Susan. I did not know our journey would lead us here and I do not know where it will take us but I do know that without you I would not be who I am today.

CV

Curriculum Vitae

Clayton Ellis Wilson was born on April 14th, 1967 in Prosser, Washington, in The United States of America. He grew up and attended primary and high school in the small farming community of Bickleton, Washington. In 1985, he began his higher education at Washington State University. Midway through his engineering studies he joined the United States Navy and served several years as an analytical chemist onboard a nuclear powered submarine. Following his military service he continued his education, first at the Community College of Philadelphia, and subsequently at Rensselaer Polytechnic Institute in Troy, New York. Fascinated by both medicine and engineering, he enrolled in the Biomedical Engineerng program at Rensselaer Polytechnic obtaining a Bachelor of Science in 1995 and a Master of Science in 1999. Following his Masters, he worked for one year at the Bone and Joint Center at Henry Ford Hospital in Detroit, Michigan. In January 2000 he moved to The Netherlands and started as a PhD student on the research project "Tissue engineered hybrid bone for spinal fusion", a Dutch Technology Foundation sponsored collaboration between the Department of Orthopaedics at the University Medical Center Utrecht and IsoTis in Bilthoven. The work on this project was conducted alongside fellow PhD students Moyo Kruyt and Steven van Gaalen and under the supervision of prof. dr. Ab Verbout, prof. dr. Wouter Dhert, prof. dr. Clemens van Blitterswijk and prof. dr. Joost de Bruijn. During the course of this work, Wouter Dhert and Joost de Bruijn were promoted to professors and became promoters of this thesis together with Clemens van Blitterswijk. With support of the BioPartner program, Clayton, along with colleagues Jiaping Li and Tim Woodfield, founded PoroGen B.V. to commercialize technologies related to the manufacture of porous biomaterials. In 2008, Clayton joined CellCoTec B.V. to help bring the 3-D printing of porous polymer scaffolds from the research bench to the clinic. The manufacture of clinical scaffolds was initiated at CellCoTec in 2009 followed by application in the first patient in 2010.

Clayton has been married to Susan Wilson since 2001. They reside in Zeist, The Netherlands, with their daughter, Mackenzie.

CF

Color Figures

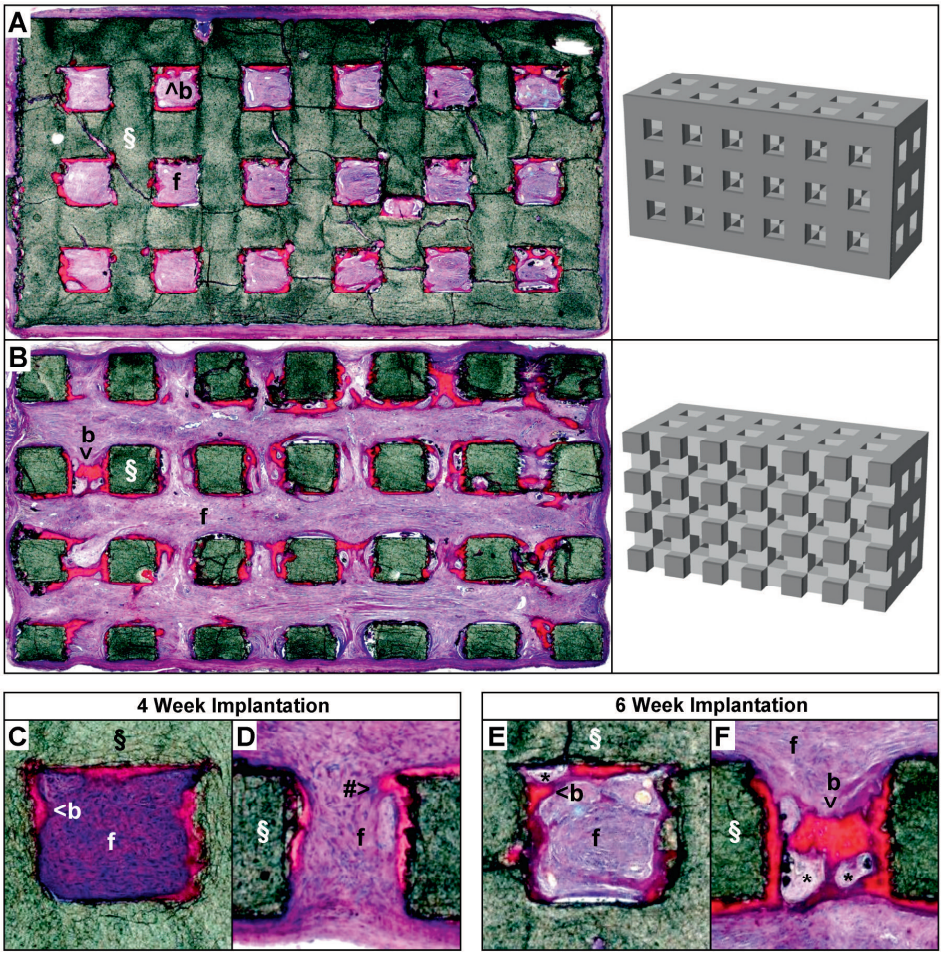

Figure 2.9: Light micrographs of methylene blue/basic fuchsine stained histological sections. Pores/channels are approximately 350 to 400 µm across. **A** and **B**, full sections from mouse 3 (see Table 4) after 6 weeks implantation with schematic representations of the sections to the right. Scaffold material (gray, **§**), fibrous tissue (purple, **f**), and mineralized bone tissue (red, **b>**) are visible. **C** and **D**, enlargements of 4 week histology. Bone tissue is primarily on scaffold surfaces with some early indications of bone budding away from surface (**#>**). **E** and **F**, enlargements of 6 week histology. Surface bone formation most common with frequent budding away from surface and encapsulation of fat or marrow like tissue (*).

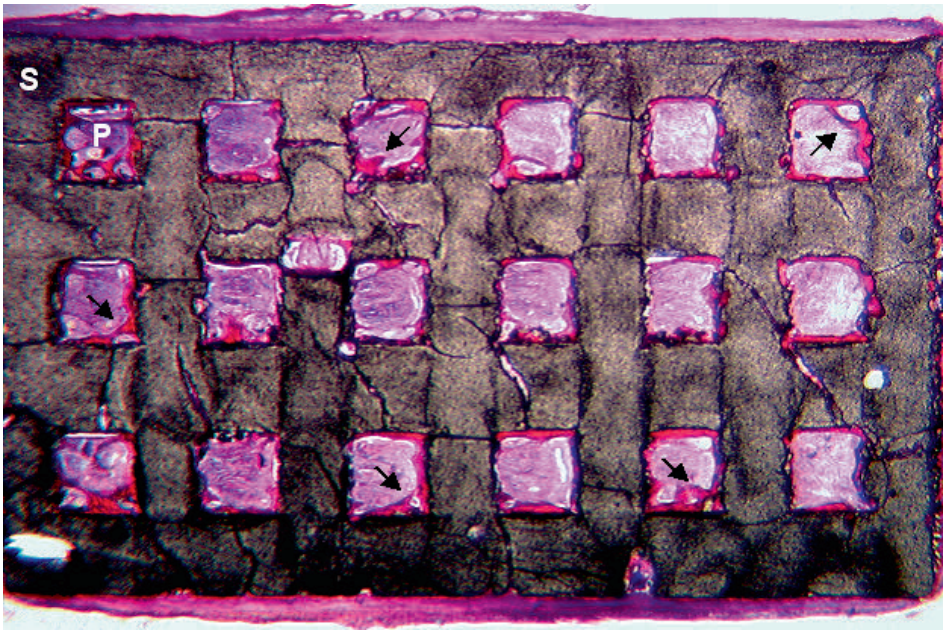

Figure 3.2: Example of histology. The scaffolds (S) forms a continuous lattice containing a 3x6 array of pores (P). Bone is present on the periphery of all pores. Some of this bone is indicated by the black arrows.

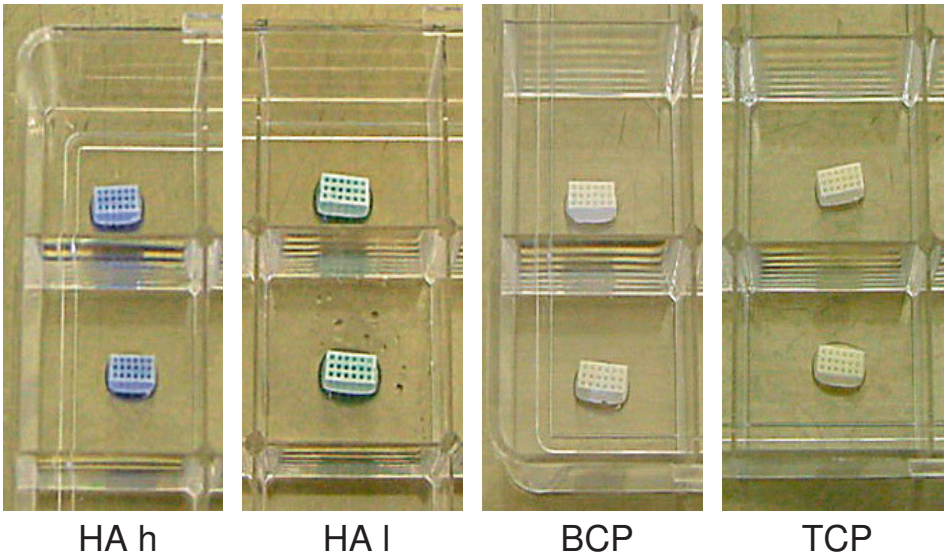

Figure 4.2: The four ceramic compositions all in 25 well plates. Note the similarity of the scaffold structures and the differences in the scaffold colors.

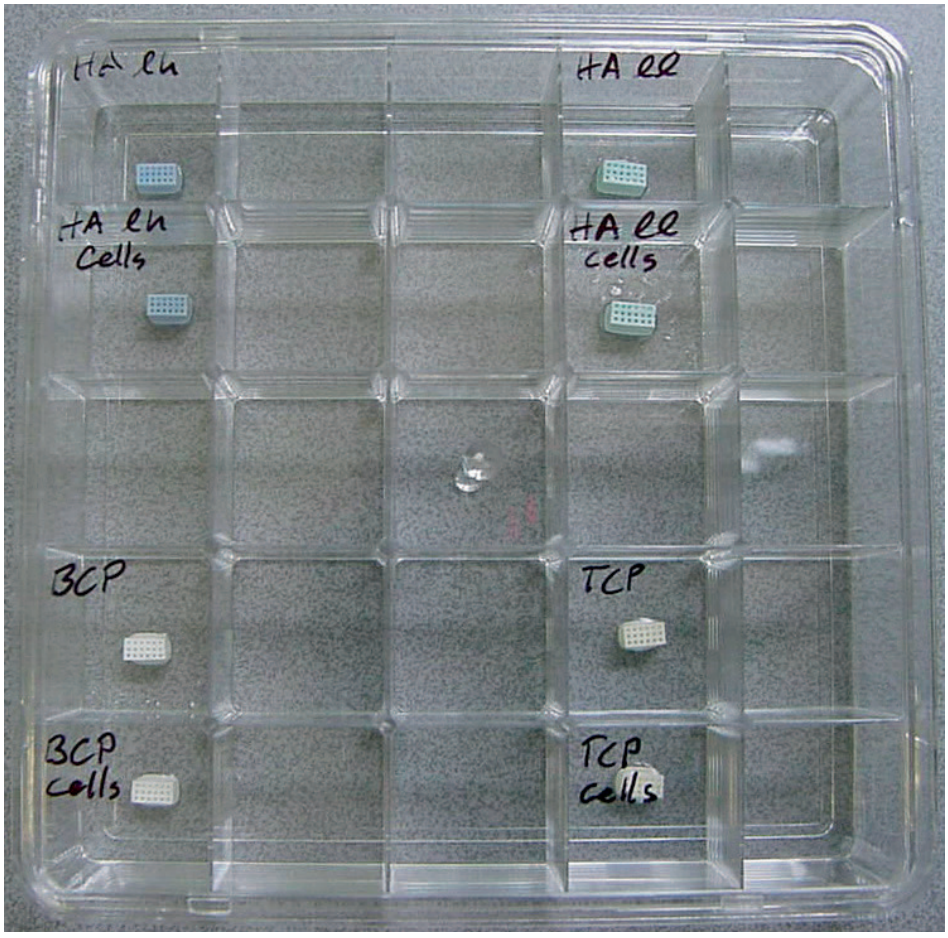

Figure 5.1: The four ceramic compositions in a 25 well plate. Note the similarity of the scaffold structures and the differences in the scaffold colors.

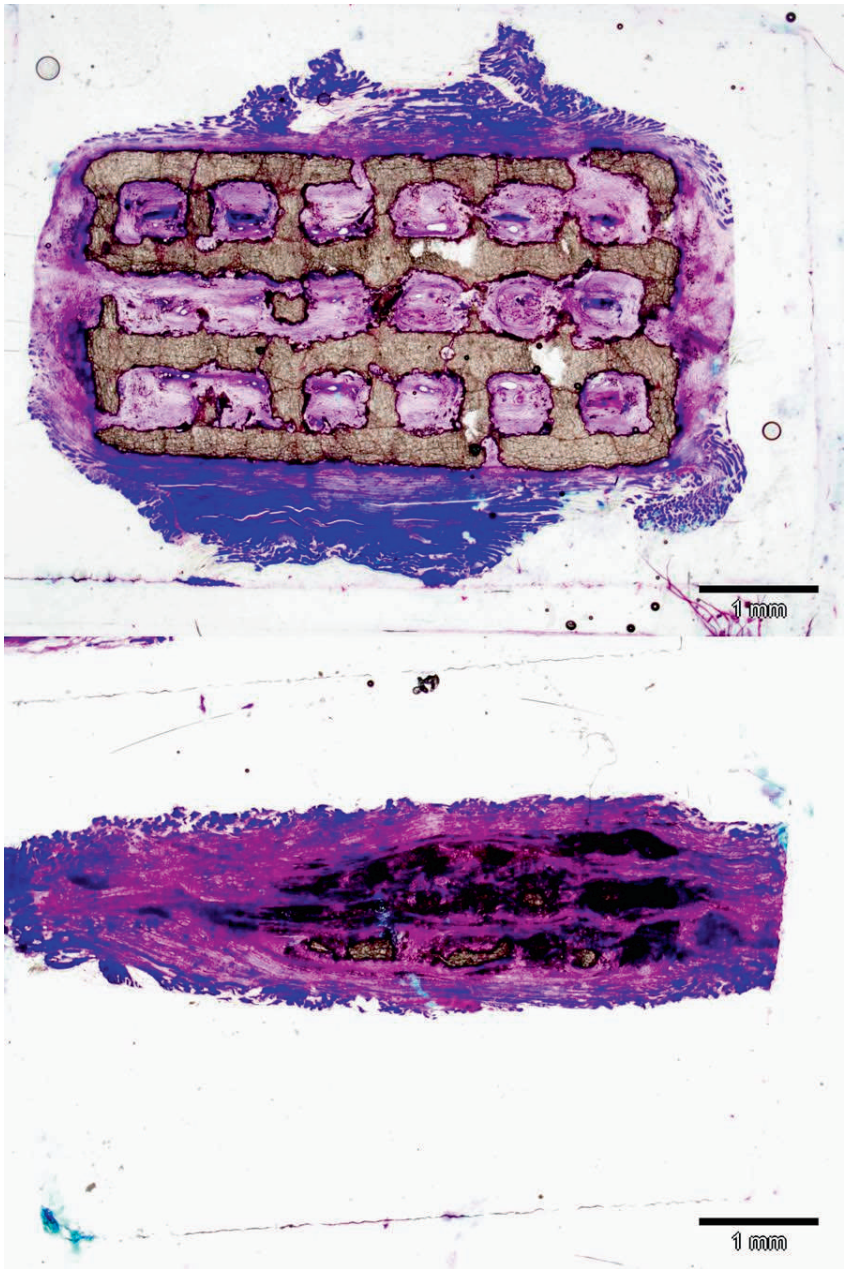

Figure 5.3: Light micrographs of methylene blue/basic fuchsin stained histological sections of TCP scaffolds with (top) and without (bottom) cells. This pattern of degradation was present in 9 of 10 pairs of TCP scaffolds.

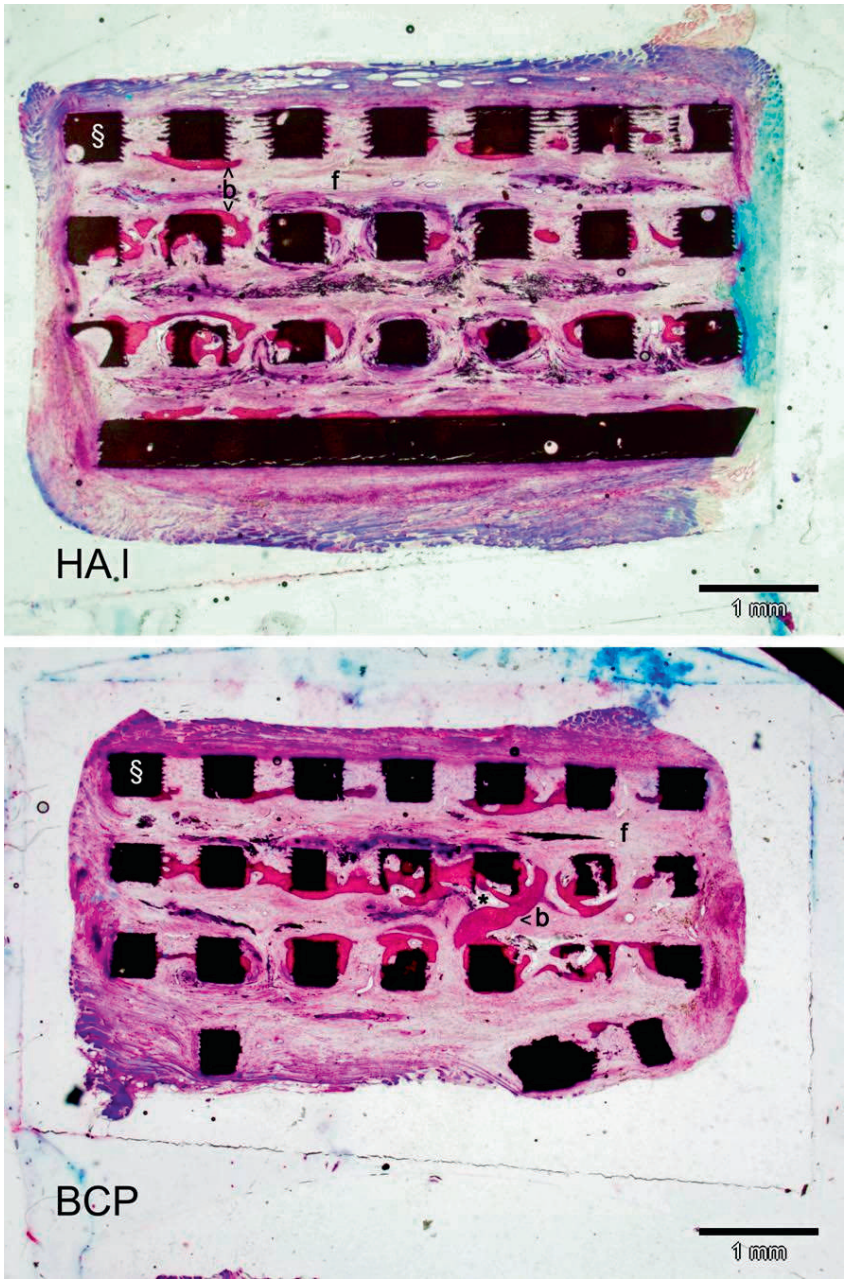

Figure 5.4: Representative light micrographs of methylene blue/basic fuchsin-stained histologic sections of bone formation in HA I (top) and BCP (bottom) scaffolds. Scaffold material (dark gray, §), fibrous tissue (purple, f), and mineralized bone tissue (red, b) are visible. Surface bone formation is most common, with frequent budding away from surface and encapsulation of fat or marrow-like tissue (*).

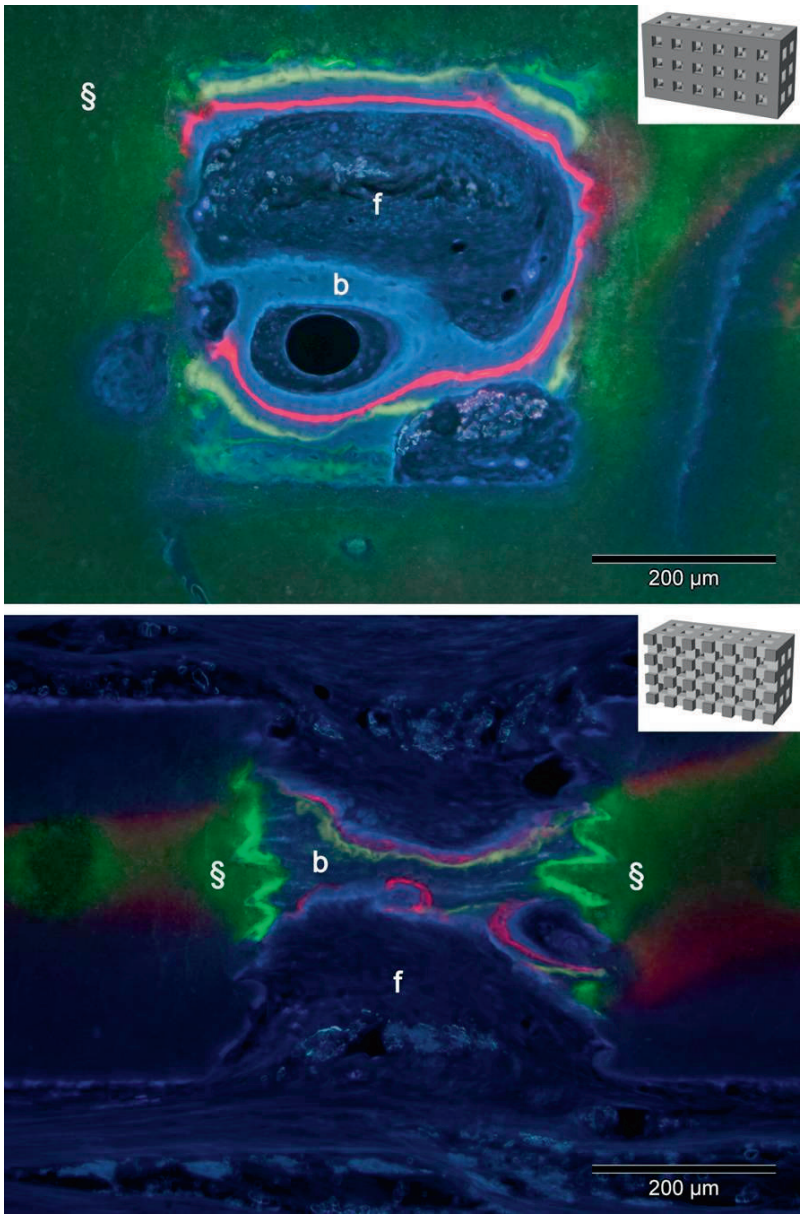

Figure 5.5: Epifluorescent microscopy images of fluorochrome markers. Top image shows a single pore containing fibrous tissue (f) and bone (b) that is completely surrounded by scaffold (§). The bottom image shows bone (b) between two scaffold struts. In both images the earliest label is green (3 weeks, calcein green), the intermediate label is yellow (5 weeks, oxytetracyclin) and the final label is orange (7 weeks, xylenol orange). Diffuse labeling of the scaffold material is also present. Inset drawings demonstrate general section configuration of the two images.

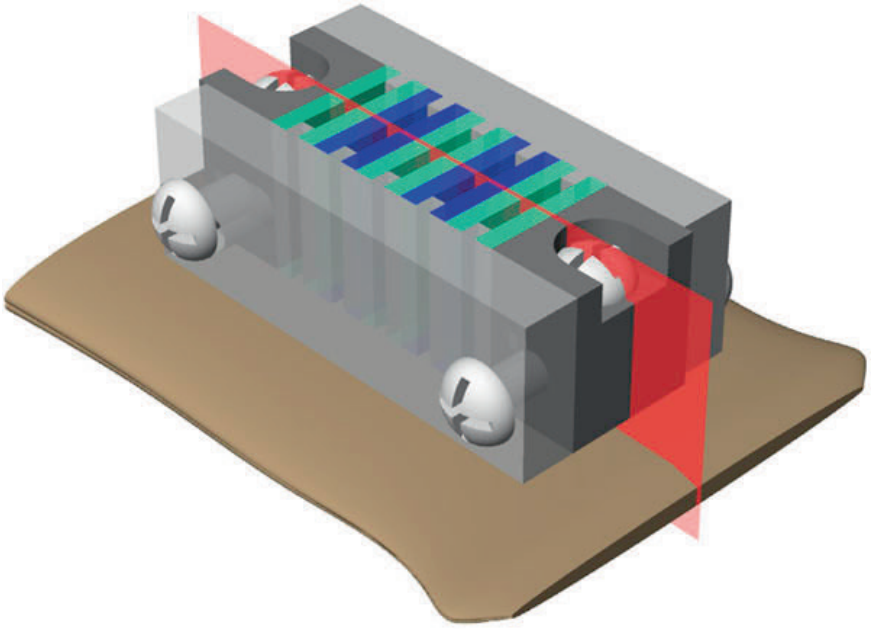

Figure 7.1: Computer generated image of conduction cage placed on a transverse process. The sectioning plane used for histology is indicated.

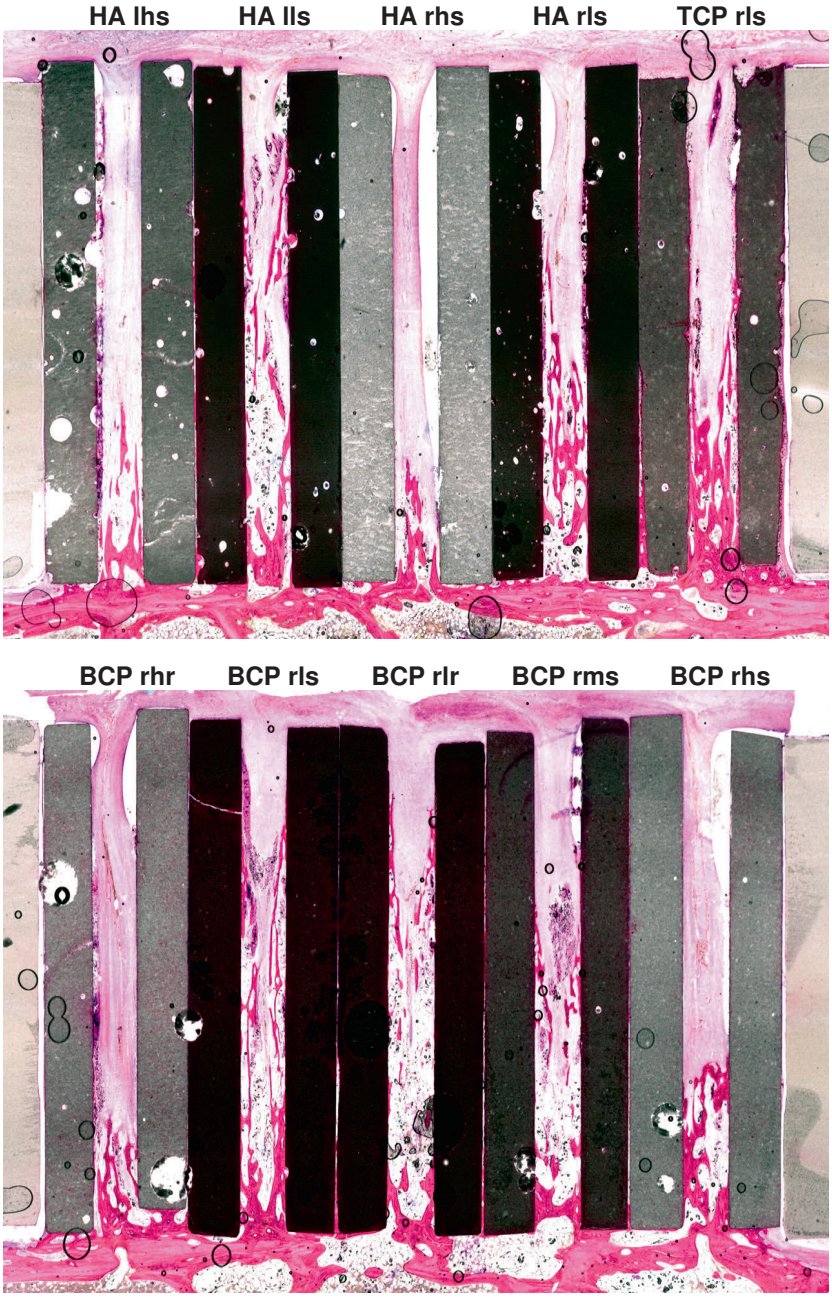

Figure 7.3: Stained (methylene blue/basic fuchsine) histological sections. Bone is stained pink/red and the ceramic plates light to dark gray. The transverse processes are at the bottom the images and the polymer cage is visible at the extreme right and left of the images. Material treatment label (ref. table 1) is indicated above the conduction channels created by pairs of material plates.

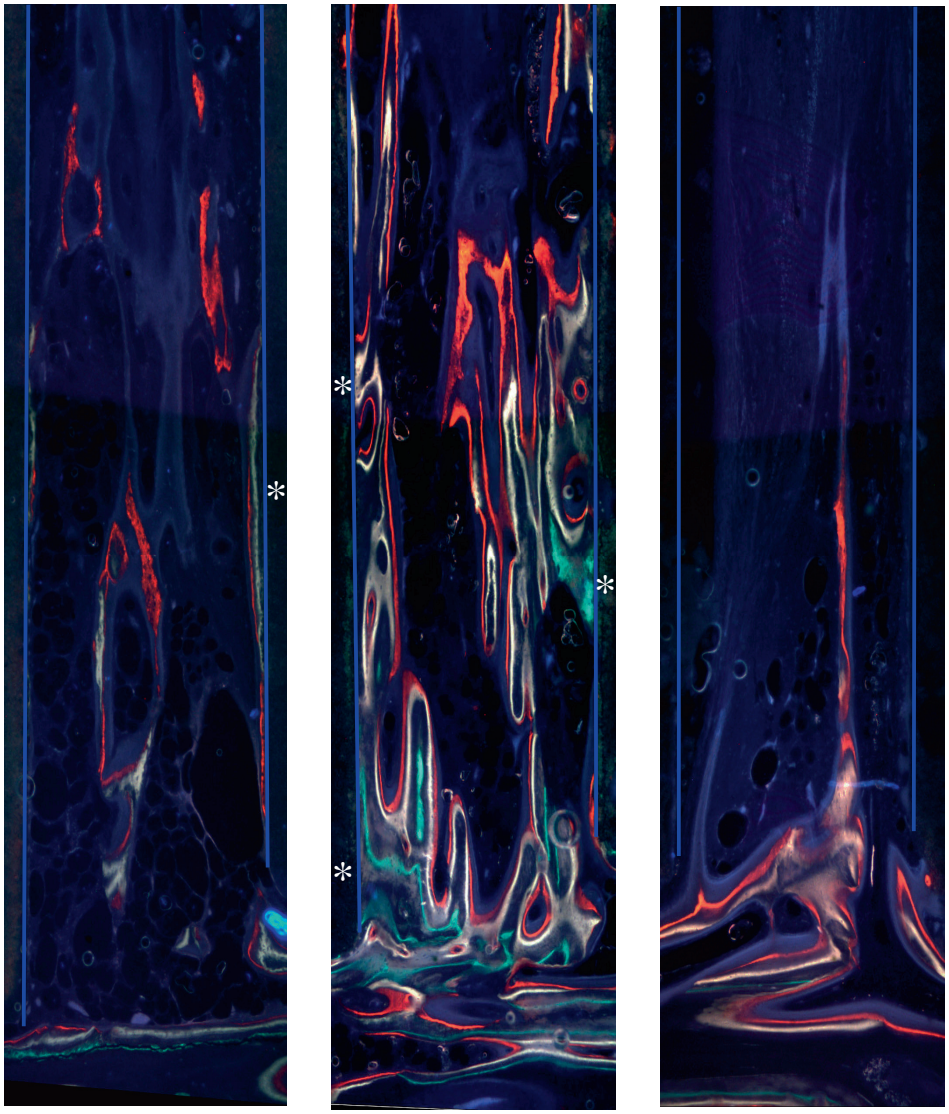

Figure 7.4: Epifluorescent microscopy images of fluorochrome markers. Label at bottom of each image indicates the goat number and material treatment. In all three images the earliest label is green (3 weeks, calcein green), the middle label is yellow (5 weeks, oxytetracyclin) and the final label is orange (7 weeks, xylenol orange). Vertical blue lines indicate the approximate location of the ceramic surface. Examples of bonding osteogenesis are indicated by an *.

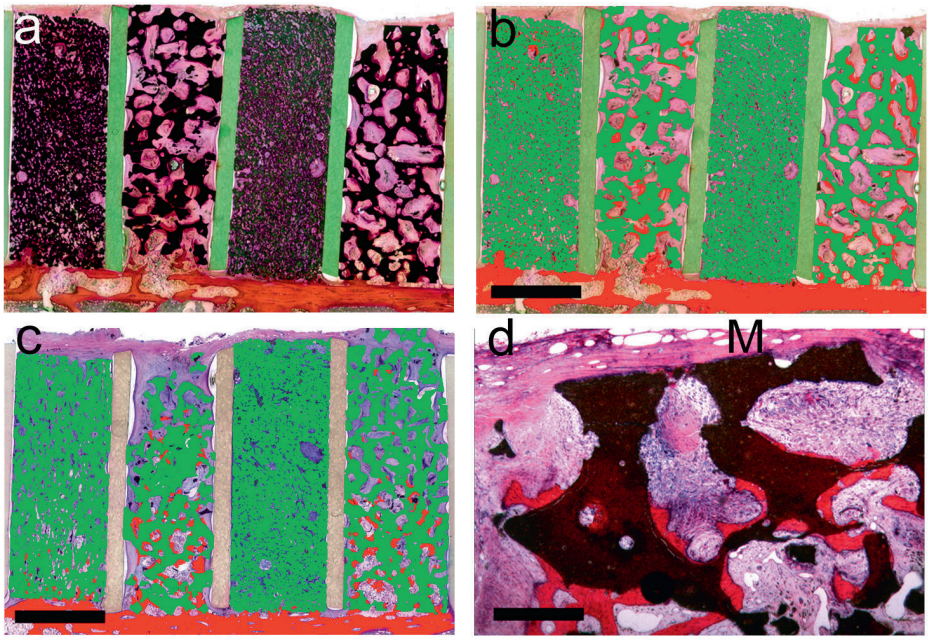

Figure 8.3: Histology. (a) Low-magnification image of the midsection through a BMSC-impregnated cassette. All four ceramic blocks separated by Teflon sheets can be discerned. From left to right: HA1150; TCP; HA1250 and BCP. An obvious difference in pore size can be observed, as well as a preference of bone (red) for apposition in the larger pores. Note the good integration of all materials from the underlying transverse process (Bar = 3 mm). (b) Pseudocolored version of image 8.3a (green = scaffold, red = bone). Note the homogeneous distribution of bone throughout the BCP and TCP scaffolds (Bar = 3 mm). (c) Pseudocolored image of the control cassette (not seeded with BMSCs) in the same animal. The order of materials is the same. Note bone is much less in the upper parts (Bar = 3 mm). (d) High-magnification image of the upper part of TCP with BMSCs. Abundant bone (red) is present within the concavities Typically no bone was found at the peripheral straight surface next to muscle (M) (Bar = 600 µm).

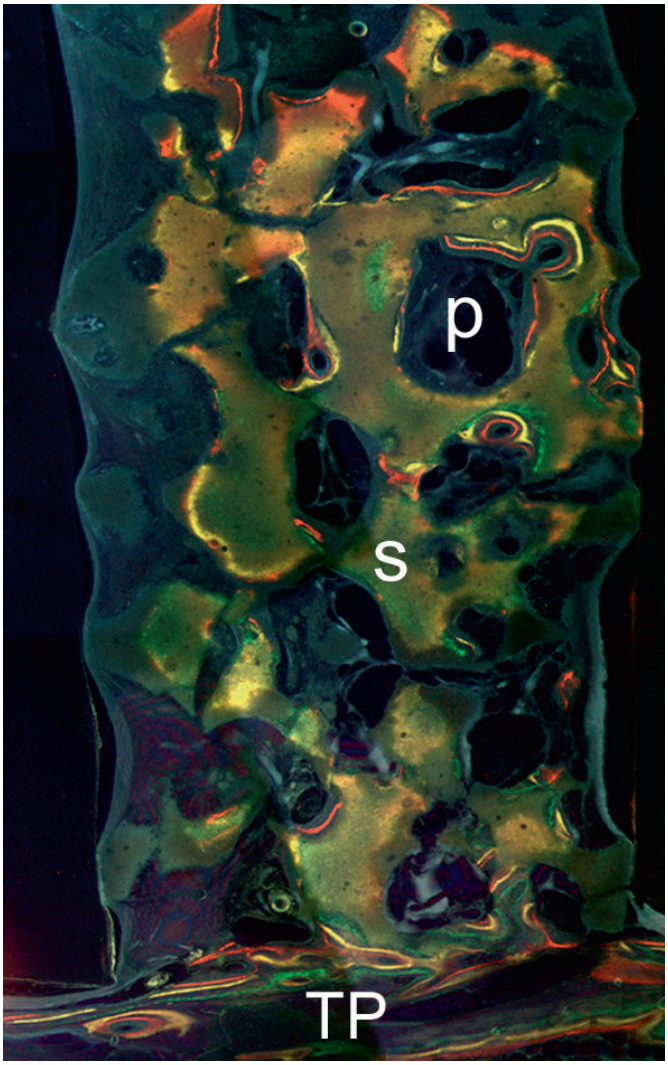

Figure 8.4: Fluorescent microscopy. Composite image of the lower half of a BCP scaffold (s) without BMSCs. The green (3 weeks) yellow (5 weeks) and orange (7 weeks) labels are present in the lower area and in the underlying transverse process (TP) In the highest areas only the orange label is present indicating bone had grown by conduction. (p = pore).